

UNCLASSIFIED

AD 4 2 3 0 6 3

DEFENSE DOCUMENTATION CENTER

FOR

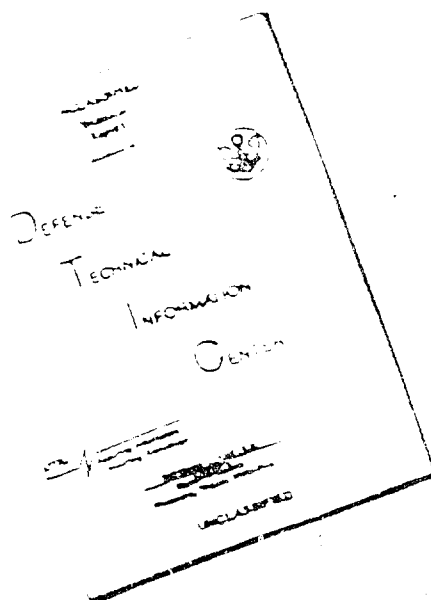
SCIENTIFIC AND TECHNICAL INFORMATION

CAMERON STATION ALEXANDRIA, VIRGINIA



UNCLASSIFIED

# DISCLAIMER NOTICE



THIS DOCUMENT IS BEST  
QUALITY AVAILABLE. THE COPY  
FURNISHED TO DTIC CONTAINED  
A SIGNIFICANT NUMBER OF  
PAGES WHICH DO NOT  
REPRODUCE LEGIBLY.

REPRODUCED FROM  
BEST AVAILABLE COPY

THIS DOCUMENT CONTAINED  
BLANK PAGES THAT HAVE  
BEEN DELETED

NOTICE: When government or other drawings, specifications or other data are used for any purpose other than in connection with a definitely related government procurement operation, the U. S. Government thereby incurs no responsibility, nor any obligation whatsoever; and the fact that the Government may have formulated, furnished, or in any way supplied the said drawings, specifications, or other data is not to be regarded by implication or otherwise as in any manner licensing the holder or any other person or corporation, or conveying any rights or permission to manufacture, use or sell any patented invention that may in any way be related thereto.

PROCEEDINGS  
OF THE  
**SIXTH SYMPOSIUM ON  
HYPERVELOCITY IMPACT**



VOLUME II  
PART I

AUGUST 1963



**PROCEEDINGS  
OF THE  
SIXTH SYMPOSIUM ON  
HYPERVELOCITY IMPACT**

**CLEVELAND, OHIO  
APRIL 30, MAY 1, 2, 1963**

*Sponsored by:*

U.S. Army  
U.S. Air Force  
U.S. Navy

*Tri-Service Committee:*

R. J. Eichelberger, Army, BRL, Chairman  
W. H. Dittrich, Air Force, Det. 4, ASD  
W. W. Atkins, Navy, NRL

**Contract No.**

**DA-31-124-ARO(D)-16**

**VOLUME II  
PART I**

**AUGUST, 1963**

**The Firestone Tire & Rubber Co. (Conference Host)**

Volume II of the Sixth Symposium on Hypervelocity Impact appears in two parts. Part 1 contains pages 1 through 336; Part 2 contains pages 337 through 709.

The views, conclusions and recommendations expressed herein do not necessarily reflect the official views or policies of either the United States Army, United States Navy or the United States Air Force.

## TABLE OF CONTENTS

### VOLUME I PROJECTION TECHNIQUES

TABLE OF CONTENTS	iii
UNPUBLISHED PRESENTATIONS	
A CRITIQUE OF ACCELERATOR TECHNIQUES FOR HYPERVELOCITY IMPACT (Introductory Paper) A. C. Charters	1
EXPERIMENTAL AND THEORETICAL STUDIES ON THE INTERIOR BALLISTICS OF LIGHT GAS GUNS Paul G. Baer and Horace C. Smith	41
AN INVESTIGATION OF THE PERFORMANCE OF A COMPRESSION HEATER FOR USE WITH GUN TUNNELS OR HYPERVELOCITY LAUNCHERS Bo Lemcke	107
COMPUTER ANALYSIS OF TWO-STAGE HYPERVELOCITY MODEL LAUNCHERS R. Placesi, D. F. Gates, and A. E. Seigel	155
NRL HYPERVELOCITY ACCELERATOR DEVELOPMENT H. F. Swift, C. D. Porter, J. J. Condon, and J. R. Baker	175
PERFORMANCE OF A THREE STAGE ARC HEATED LIGHT GAS GUN J. Eckerman and W. L. McKay	247
HYPERVELOCITY AUGMENTATION TECHNIQUES William G. Howell, Rodney F. Recht, and Thomas W. Ipson	305

THE MAGNETOHYDRODYNAMIC HYPERVELOCITY GUN R. L. Chapman, D. E. Harms, and G. P. Sorenson	317
INHIBITED JET CHARGE S. Kronman and A. Merendino	331
SPECIAL EXPLOSIVE PROJECTORS: I. SHAPED CHARGE ACCELERATOR; II. TARGET PLATE ACCELERATOR K. N. Kreyenhagen, J. E. Ferguson, R. R. Randall, and J. P. Joyce	349
(Confidential) ARMOUR RESEARCH FOUNDATION TRAVELING CHARGE GUN (U) Louis A. C. Barbarek	Vol. IV, 395
SUMMARY REMARKS H. F. Swift	375
ATTENDANCE ROSTER	379
AUTHOR INDEX	387

VOLUME II - Part I  
THICK TARGET CRATERING AND IONIZATION

TABLE OF CONTENTS	111
REVIEW OF PHYSICAL PROCESSES IN HYPERVELOCITY IMPACT AND PENETRATION (Introductory Paper) Robert L. Bjork	1
HYDRODYNAMICS OF HYPERVELOCITY IMPACT J. M. Walsh and J. H. Tillotson	59
VISCO-PLASTIC SOLUTION OF HYPERVELOCITY IMPACT CRATERING PHENOMENON T. E. Riney	105
THE CALCULATION OF STRESS WAVES IN SOLIDS Mark L. Wilkins and Richard Giroux	141
A HYPERVELOCITY IMPACT MODEL FOR COMPLETELY DEFORMING PROJECTILES J. L. Luttrell	157
A BLAST-WAVE THEORY OF CRATER FORMATION IN SEMI-INFINITE TARGETS William J. Rae and Henry P. Kirchner	163
SPHERICAL SHOCK WAVES AND CAVITY FORMATION IN METALS N. Davids, H. H. Calvit, and O. T. Johnson	229
PROPERTIES OF SPHERICAL SHOCK WAVES PRODUCED BY HYPERVELOCITY IMPACT Ray Kinslow	273
SHOCK FRONT VARIATION IN TIME FOR HIGH SPEED IMPACT INTO WATER James F. Heyda	321

## VOLUME II - Part 2

<b>HYPERVELOCITY CRATERING DATA AND A CRATER- DEPTH MODEL FOR THE REGIME OF FLUIDITY</b> Olive G. Engel	337
<b>FLUID IMPACT CRATERS AND HYPERVELOCITY - - HIGH-VELOCITY IMPACT EXPERIMENTS IN METALS AND ROCKS</b> H. J. Moore, R. W. MacCormack, and D. E. Gault	367
<b>ENERGY BALANCES IN HYPERVELOCITY PENETRATION</b> R. B. Pond, C. Mobley, and C. M. Glass	401
<b>THE PARTITION OF ENERGY FOR HYPERVELOCITY IMPACT CRATERS FORMED IN ROCK</b> Donald E. Gault and Ezra D. Heitowit	419
<b>TRANSIENT OBSERVATIONS OF CRATER FORMATION IN SEMI-INFINITE TARGETS</b> J. H. Kineke, Jr., and Richard Vitali	457
<b>INFLUENCE OF TARGET STRENGTH ON HYPERVELOCITY CRATER FORMATION IN ALUMINUM</b> J. H. Kineke, Jr., and L. G. Richards	513
<b>SOME PHENOMENA ASSOCIATED WITH IMPACTS INTO ALUMINUM</b> S. M. Halperson	525
<b>PARTICLE-SOLID IMPACT PHENOMENA</b> E. H. Goodman and C. D. Liles	543
<b>INVESTIGATION OF THE IMPACT OF COPPER FILAMENTS INTO ALUMINUM TARGETS AT VELOCITIES TO 16,000 FEET PER SECOND</b> C. Robert Nysmith, James L. Summers, and B. Pat Denardo	577
<b>IONIZATION ASSOCIATED WITH HYPERVELOCITY IMPACT</b> J. F. Friichtenicht and J. C. Slattery	591

INVESTIGATION OF IMPACT FLASH AT LOW AMBIENT PRESSURES Robert W. MacCormack	613
AN INVESTIGATION OF THE PHENOMENA OF IMPACT FLASH AND ITS POTENTIAL USE AS A HIT DETECTION AND TARGET DISCRIMINATION TECHNIQUE J. W. Gehring and R. L. Warnica	627
SUMMARY: THEORETICAL AND EXPERIMENTAL STUDIES OF CRATER FORMATION R. J. Eichelberger	683
AUTHOR INDEX	707

## TABLE OF CONTENTS

### VOLUME III THIN TARGET PERFORATIONS AND PROTECTION

TABLE OF CONTENTS	iii
INTRODUCTORY PAPER - EXPERIMENTATION L. Zernow	1
TWO DIMENSIONAL ANALYSIS OF A HYPERVELOCITY IMPACT UPON A VISCO-PLASTIC PLATE H. Kraus	13
A METEOROID BUMPER DESIGN CRITERION P. E. Sandorff	41
EXPERIMENTAL AND THEORETICAL RESULTS CONCERNING THE PROTECTIVE ABILITY OF A THIN SHIELD AGAINST HYPERVELOCITY PROJECTILES C. J. Maiden	69
EFFECTS OF 3 TO 12 KM/SEC IMPACTS ON FINITE TARGETS R. B. Mortenson, J. E. Ferguson, J. P. Joyce, and K. N. Kreyenhagen	157
THIN PLATE PERFORATION STUDIES WITH PROJECTILES IN THE VELOCITY RANGE FROM 2 TO 5 KM/SEC R. W. Watson, K. R. Becker, and F. C. Gibson	207
A NEW SYSTEM OF PROTECTION FROM HYPERVELOCITY PARTICLES B. W. Reynolds and R. H. Emmons	249
HYPERVELOCITY PUNCTURING OF SELF-SEALING STRUCTURES Philip J. D'Anna	281
AN INVESTIGATION OF THE PENETRATION OF HYPER- VELOCITY PROJECTILES INTO COMPOSITE LAMINATES A. R. McMillan	309



METEOROID EFFECTS ON NUCLEAR ROCKET SPACE VEHICLE MISSION SUCCESS William H. Sterbentz and Loren L. Long	357
SUMMARY: THIN PLATE PERFORATION AND PROTECTION Dale M. Davis	387
AUTHOR INDEX	393

**VOLUME IV  
APPLICATIONS**

<b>TABLE OF CONTENTS</b>	<b>111</b>
(Secret) APPLICATION ASPECTS OF HYPERVELOCITY IMPACT - 1963 (U) (Introductory Paper) J. M. Brown and P. K. Margolis	1
(Confidential) JET PELLET PROJECTION TECHNIQUE (U) S. Kronman	21
(Confidential) HYPERVELOCITY PROJECTILE INVESTIGATION FOR MULTIPLE THIN PLATE PENETRATION (U) R. L. Chandler, T. Watmough, and F. J. Zimmerman	37
(Secret) LETHALITY OF HOLLOW SHAPES (U) W. H. Dietrich, D. R. Christman J. W. Gehring, K. N. Kreyenhagen, and R. B. Mortensen	101
(Confidential) A WARHEAD CONCEPT FOR DEFEAT OF HARD TARGETS IN SPACE (U) Dale M. Davis	151
(Secret) AIMED WARHEAD CONCEPTS (U) Samuel D. Stein, George M. Gaydos, and Edmund M. Harrity	167
(Confidential) HYPERVELOCITY IMPACT EXPERIMENTS WITH LAMINATED COMPLEX TARGETS (U) C. M. Cox and E. S. Thorn	193
(Secret-No Foreign) HYPERVELOCITY IMPACTS INTO ABLATIVE MATERIALS (U) Mario A. Persechino	235
(Confidential) DETERMINATION OF PERFORATION ENERGIES FOR COMPOSITE TARGETS (U) Murray Rockowitz and Charles A. Carey	271

(Secret) A SHORT REVIEW OF THE STATUS OF THE AERO-THERMAL PHASE OF THE HYPERVELOCITY KILL MECHANISMS PROGRAM (U) Coleman duP. Donaldson	305
(Secret-No Foreign) LETHALITY OF SMALL FRAGMENTS VERSUS ICBM RE-ENTRY VEHICLES (U) James J. Dailey	329
(Secret-No Foreign) VULNERABILITY OF LARGE MISSILE SYSTEMS DURING THE LAUNCH PHASE (U) H. S. Zimney, R. B. Mortensen, W. A. Rhea, and R. B. Coley	345
(Confidential) FREE, A HYPERVELOCITY ROCKET WEAPON (U) D. C. Lane	373
(Secret) SUMMARY: APPLICATIONS (U) W. W. Atkins	385
(Confidential) ARMOUR RESEARCH FOUNDATION TRAVELING CHARGE GUN (U) Louis A. C. Barbarek	395
AUTHOR INDEX	417
ATTENDANCE ROSTER	421

**MEMORANDUM**

**RM-3529-PR**

**JULY 1963**

**REVIEW OF PHYSICAL PROCESSES IN  
HYPERVELOCITY IMPACT AND PENETRATION**

**Robert L. Bjork**

This research is sponsored by the United States Air Force under Project RAND—contract No. AF 49(638)-700 monitored by the Directorate of Development Planning, Deputy Chief of Staff, Research and Development, Hq USAF. Views or conclusions contained in this Memorandum should not be interpreted as representing the official opinion or policy of the United States Air Force.

---

*The* **RAND** *Corporation*  
1700 MAIN ST • SANTA MONICA • CALIFORNIA

# IMPACT PHYSICAL PROCESSES REVIEW

## PREFACE

A continuing effort has been conducted on hypervelocity impact within RAND for several years. Applications of the results have been made to the problems of the meteoroid hazard, satellite vulnerability, and ICBM defense. This Memorandum presents some new information in this area and compares some of the earlier work with recent experimental data.

## IMPACT PHYSICAL PROCESSES REVIEW

### SUMMARY

The so-called volume-energy law, or two-thirds law, is an empirical fit which has been used by many writers to predict penetration by hypervelocity fragments. A comparison is drawn between this law and well-controlled high-velocity experimental results which have been obtained recently. The comparison reveals that the data fit the law satisfactorily at relatively low velocities but deviate from it in a marked way as impact velocities increase. It is therefore incorrect to extrapolate this law to predict impact effects in the meteor-velocity range.

The experimental data are shown to agree well with the author's earlier impact predictions based on a hydrodynamic model.\* The agreement of penetration by aluminum spheres impacting 1100-F aluminum targets is particularly good. Penetration of the same spheres into 2024 alloy is less in all cases at corresponding velocities. It is observed that the ratio of the penetration in the two alloys increases with impact velocity, ranging from about 50 per cent at 3 km/sec to 75 per cent at 7.5 km/sec, which suggests that the relative importance of strength wanes with waxing velocity. The 25 per cent change in penetration occasioned by increasing the strength by a factor of 7.5 emphasizes the insensitivity to strength at high impact velocities.

Irreversible heating, accompanied by the creation of entropy, always occurs in a shock. Transit of the target by the shock system produced in hypervelocity impacts leaves the target material in a heated state. It is shown that impacts in the meteor-velocity range create enough heat by this mechanism to vaporize and liquefy portions

---

\* Published in RAND P-1662, Effects of a Meteoroid Impact on Steel and Aluminum in Space.

## IMPACT PHYSICAL PROCESSES REVIEW

presented scaling laws to account for projectile-material influence on a shock-impedance model. Publications are cited which deny the existence of this effect. Comparisons are drawn between the two theoretical predictions and recent well-controlled experimental results. The effect of projectile material is unambiguously demonstrated, and excellent agreement with the shock-impedance law is found. The agreement is found to extend over a wide range of projectile materials, from copper and steel on the one hand to plastics having specific gravity less than unity on the other. It is concluded that by combining the shock-impedance law with the earlier predictions on the hydrodynamic model, the penetration by projectiles of any material into aluminum targets may be predicted up to velocities of about 20 km/sec. Above this impact velocity, the effects of melting and vaporization are expected to become important in establishing the crater dimensions. The role of projectile material in this physical regime has not been studied as yet.

## IMPACT PHYSICAL PROCESSES REVIEW

### CONTENTS

PREFACE .....	2
SUMMARY .....	3
SYMBOLS .....	7
Section	
I. CRATERING IN THICK TARGETS .....	8
Volume Versus Energy .....	8
Hydrodynamic Penetration .....	18
Strength Effects .....	22
II. MELTING AND VAPORIZATION .....	26
Shock Heating as a Function of Particle Velocity .....	26
Effect of Target Melting on Crater Size .....	29
III. PHYSICS OF THIN-TARGET PENETRATION .....	32
IV. SCALING LAW FOR DISSIMILAR-MATERIAL IMPACTS .....	39
REFERENCES .....	58



## IMPACT PHYSICAL PROCESSES REVIEW

### SYMBOLS

- $a$  = constant used in fit
- $B, \text{BIN}$  = Brinell hardness number
- $B-A$  = subscript indicating projectile of material B incident on target of material A
- $b$  = constant used in fit
- $D_h$  = hole diameter
- $d$  = projectile characteristic dimension
- $E$  = projectile kinetic energy
- $e$  = base of Napierian logarithms
- $F$  = normalized penetration ratio (defined on p. 40)
- $m$  = constant used as exponent
- $n$  = constant used as exponent
- $P$  = pressure
- $p$  = penetration
- $r$  = radial distance in cylindrical coordinate system
- $t$  = target thickness
- $u$  = particle velocity
- $V$  = crater volume
- $v$  = impact velocity
- $x$  = distance parallel to axis in cylindrical coordinate system
- $\beta$  = exponent in fit of penetration as a function of density
- $\pi$  = normalized penetration ( $p/d$ )
- $\rho_A, \rho_B$  = density of materials A and B, respectively
- $\rho_p$  = projectile density
- $\rho_t$  = target density
- $\sigma_o$  = material yield strength

## IMPACT PHYSICAL PROCESSES REVIEW

### I. CRATERING IN THICK TARGETS

#### VOLUME VERSUS ENERGY

The idea has been put forth by many writers that the volume of the crater produced in a thick target is proportional to the kinetic energy of the projectile which produced it. If one assumes also that the crater geometry remains similar throughout a region of the velocity spectrum, then the two assumptions taken together lead to the hypothesis that penetration is proportional to the two-thirds power of the impact velocity. In practice, both assumptions encounter difficulties.

For impacts between projectiles and targets of like materials, the similar-geometry assumption is usually well founded in the hyper-velocity regime, the craters being approximately hemispherical. However, for impacts between unlike materials, substantial deviations from hemisphericity are observed, and the geometries do not remain similar as the impact velocity is changed. For example, iron or copper spheres striking aluminum targets at 2 or 3 km/sec produce craters whose depths are about equal to their diameter. At about 7 km/sec, these spheres yield craters whose depths are about 80 per cent of their diameters. The ratio for hemispherical craters would be 50 per cent.

Projectile geometry can also produce departures from hemisphericity, even for like-material collisions at very high velocities. For example, aluminum jet pellets impacting 2024 aluminum targets at 10 km/sec are found to produce craters whose depths are 80 per cent of their diameter.\* The pellets have lengths about three times their

---

\* Personal communication from J. Kineke.

## IMPACT PHYSICAL PROCESSES REVIEW

diameter. The variation of crater geometry with impact velocity for this type of projectile has not been thoroughly investigated.

The assumption that crater volume is proportional to projectile kinetic energy encounters difficulty at any fixed velocity when one considers projectiles of various materials impacting on a given target material. More and more experimental data are accumulating which demonstrate that projectiles of the denser materials are more efficient in producing craters, in that they produce a greater crater volume per unit kinetic energy. If one wishes to take account of these experimental data and still retain the physical flavor of the "volume-proportional-to-kinetic-energy" hypothesis, he must choose a different constant of proportionality for each set of projectile and target materials. Several attempts have been made to fit the variation of the proportionality constant by correction factors of the form

$$p \sim \left( \frac{\rho_p}{\rho_t} \right)^n v^{2/3}$$

In such fits,  $n$  is an empirically determined constant. In Ref. 1, we propose a physical basis for the success of such density corrections, but it is shown there that  $n$  has a slight velocity dependence. Of course, the  $v^{2/3}$  dependence is an empirical fit which is valid only over a limited portion of the velocity spectrum.

Examination of log-log plots of penetration versus impact velocity reveals the power of velocity on which the penetration depends. The power is given by the slope of such plot. Typical plots show a linear dependence of penetration on velocity at low velocities. The slope of the curves generally decreases with waxing velocity, and for

## IMPACT PHYSICAL PROCESSES REVIEW

many metals becomes approximately  $2/3$  in the velocity range of 3 to 5 km/sec. This velocity range has been extensively investigated in the last few years, and the  $2/3$  value of the slope has been cited as substantiating evidence for the volume-energy law. Such arguments ignore the difficulties cited above.

Experimental data have recently been accumulated in the velocity range of about 6 to 9 km/sec. These data quite clearly demonstrate that the penetration increases with a power of velocity less than  $2/3$ . In addition, actual measurement of the crater volumes indicates that they increase less than linearly with projectile kinetic energy.

It should be emphasized that the "two-thirds law" is only an empirical fit. No defensible physical theory has been set forth to support it. An early attempt in this direction was made by Whipple, who proposed that the kinetic energy of the projectile was used to melt the material in the crater as well as the projectile. Under this assumption, all the material in the crater receives exactly enough internal energy to melt it, and the volume of the melted material is thus proportional to the kinetic energy of the projectile. However, the physical understanding which we now have of the process indicates that the average internal energy imparted to the crater material increases with impact velocity. Thus, to assume that the projectile energy goes almost entirely into heating would lead to the prediction that the penetration increases with a power of the velocity which was less than two-thirds. Moreover, Whipple's theory does not explain the pronounced effect of projectile density on the crater dimension.

## IMPACT PHYSICAL PROCESSES REVIEW

Another notion proposed was that in expanding, the crater did work against a yield strength,  $\sigma_0$ , of the metal being deformed. Thus, the work done in forming the crater is  $V\sigma_0$ , this work being supplied by the projectile's kinetic energy. Under this model, the constant of proportionality between kinetic energy and volume is just  $\sigma_0$ , which should be a characteristic of the target material only. Again, the dependence of crater dimension on projectile material is not explained.

Despite the difficulties which the volume-energy law encounters in the lower-velocity range, and its lack of theoretical justification, it has become common practice for writers to extrapolate the law to cover the meteor-velocity range of 11 to 72 km/sec. The practice has become so common that a worker in another field who surveys the literature is liable to accept the validity of the extrapolated volume-energy relation only on the basis of the number of writers who have made this extrapolation.

Recent carefully controlled experiments at the higher velocities have been conducted which demonstrate that the volume-energy law is not being followed. For each combination of projectile-target materials, it is found that the volume increases more slowly than the energy, with the result that the ratio,  $V/E$ , decreases as impact velocity rises. Some examples will be given to illustrate this fact.

For the purpose of drawing comparisons, we will consider the penetration law recently proposed by Eichelberger and Gehring,<sup>(2)</sup> which states that in thick target impacts, hemispherical craters will be formed for which

$$V = 4 \times 10^{-9} \frac{E}{B} \quad (1)$$

## IMPACT PHYSICAL PROCESSES REVIEW

where  $V$  is the crater volume in cubic centimeters,  $E$ , the projectile kinetic energy in ergs, and  $B$ , the Brinell hardness number of the target material in kilograms per square millimeter. This relation is asserted to be valid over the meteor-velocity range and to hold for projectiles of any material.

Figure 1 shows the values predicted by Eq. (1) for penetration of aluminum projectiles into the 1100-F alloy of aluminum, compared with experimental results. The experiments were conducted by Atkins<sup>(3)</sup> and Liles and Goodman<sup>(4)</sup>. Both sets of experiments utilized spherical projectiles fired from light-gas guns, and the projectiles were fired in sabots to prevent erosion in the gun barrel. Liles and Goodman reported the Brinell hardness numbers of their targets to lie in the range of 15.9 to 17.8 kg/mm<sup>2</sup>. The average value of 16.85 was used in evaluating Eq. (1) in order to plot it in Fig. 1. The prediction of the author, which was calculated on a hydrodynamic model,<sup>(5)</sup> is shown as the shaded region in Fig. 1.

At the lower experimental velocities, Eichelberger and Gehring obtain good agreement with the data. However, above about 5 km/sec the experimental results deviate from their prediction. The reason for the deviation becomes evident if we consider the variation of the energy-volume ratio as a function of impact velocity. This is plotted in Fig. 2. Liles and Goodman<sup>(4)</sup> measured the crater volumes individually by accurately metering a liquid into them. Eichelberger and Gehring predict a constant  $V/E$  ratio of  $2.42 \times 10^{-10}$  cc/erg, whereas the midpoint of the experimental data goes from about  $1.8 \times 10^{-10}$  at 3 km/sec to about  $1.1 \times 10^{-10}$  at 7.5 km/sec.

# IMPACT PHYSICAL PROCESSES REVIEW

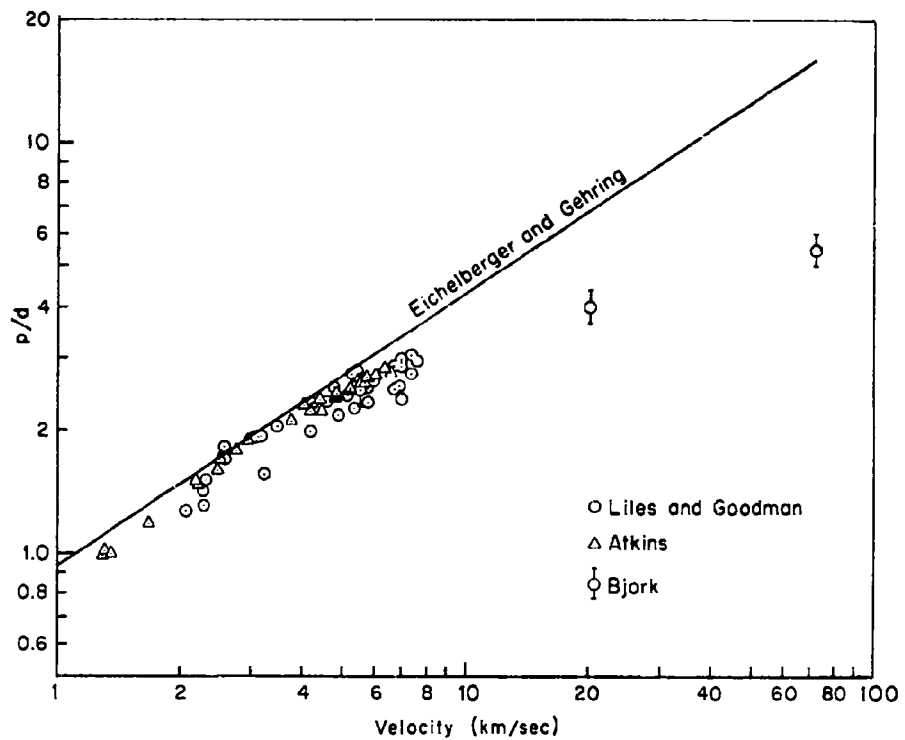


Fig. 1—Penetration of aluminum projectiles into 1100-F aluminum targets (The theoretical point at 5.5 km/sec is nearly obscured by the experimental data)

# IMPACT PHYSICAL PROCESSES REVIEW

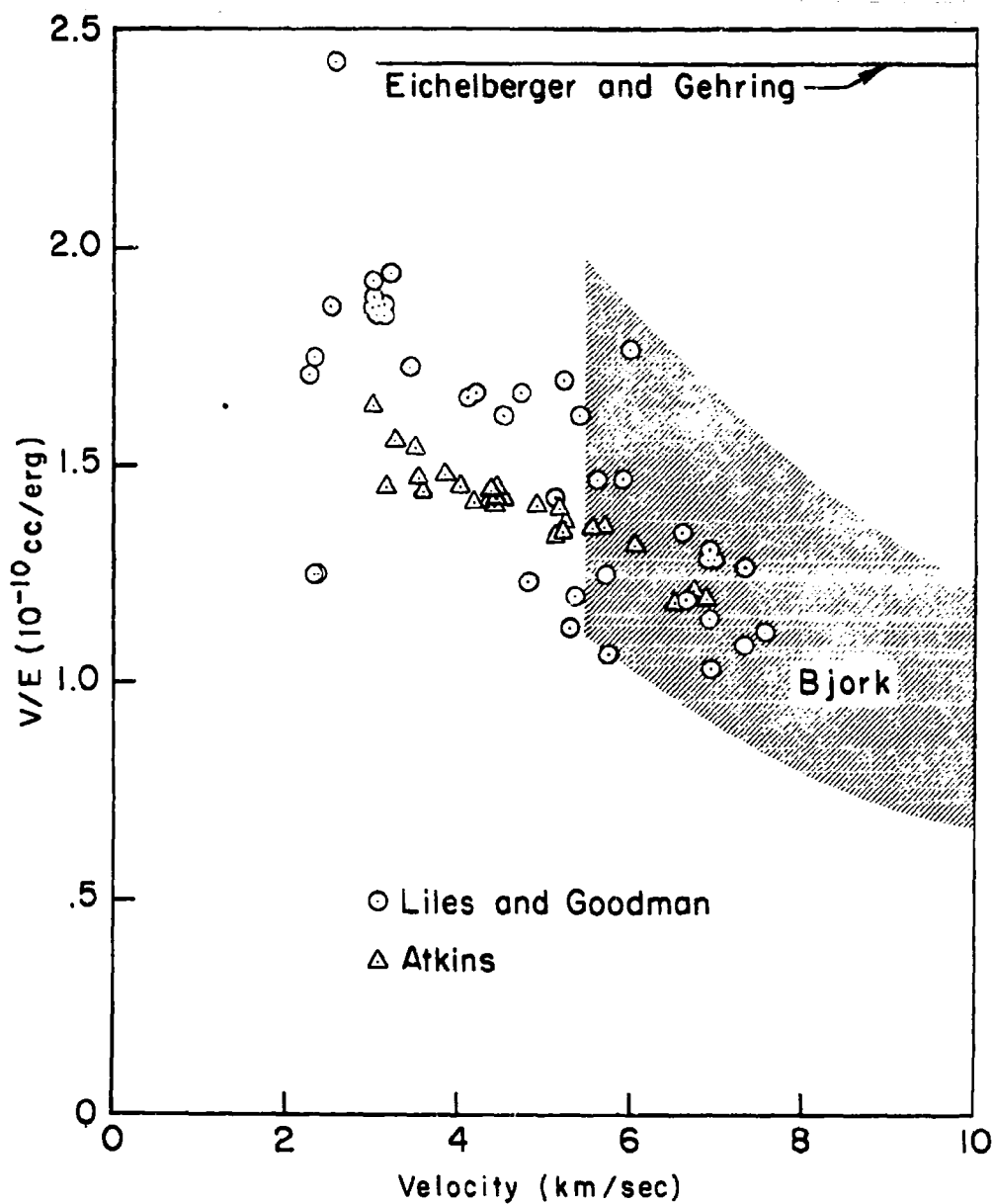


Fig.2— Ratio of crater volume to projectile kinetic energy as a function of impact velocity for aluminum spheres on 1100F aluminum targets



## IMPACT PHYSICAL PROCESSES REVIEW

The values of  $V/E$  measured by Liles and Goodman<sup>(4)</sup> for copper spheres impacting on 1100-F aluminum targets are shown in Fig. 3 as functions of impact velocity.\* The values are notably higher than for aluminum projectiles, running from about  $2.6 \times 10^{-10}$  cc/erg at 3 km/sec to about  $1.9 \times 10^{-10}$  at 6.5 km/sec. The model of Eichelberger and Gehring, which does not differentiate among projectile materials, still predicts the constant value of  $2.42 \times 10^{-10}$  cc/erg. For this particular combination of projectile and target materials, Eichelberger and Gehring obtain fair agreement at the lower impact velocities but again depart seriously from experiment as the experimental values of  $V/E$  decrease with velocity.

For completeness, the volume-energy ratio found by Liles and Goodman<sup>(4)</sup> for copper targets is plotted in Fig. 4 as a function of velocity.\* In this case also, the volume-energy ratio is found to decrease with velocity, and the ratio for copper projectiles is substantially higher than that for aluminum projectiles at the same velocity.

For these targets, which have Brinell hardness numbers ranging from 48.9 to 50.9, the equation of Eichelberger and Gehring predicts a constant  $V/E$  of  $0.802 \times 10^{-10}$  for both projectile materials. Their prediction is plotted in Fig. 4 as the flat line. Besides failing to make the important distinction between projectile materials, their prediction departs seriously from the experimental results as the impact velocity increases.

---

\*The straight lines bracketing the data groups in Figs. 3 and 4 have been inserted only to illustrate the data trend. They should not be extrapolated.

# IMPACT PHYSICAL PROCESSES REVIEW

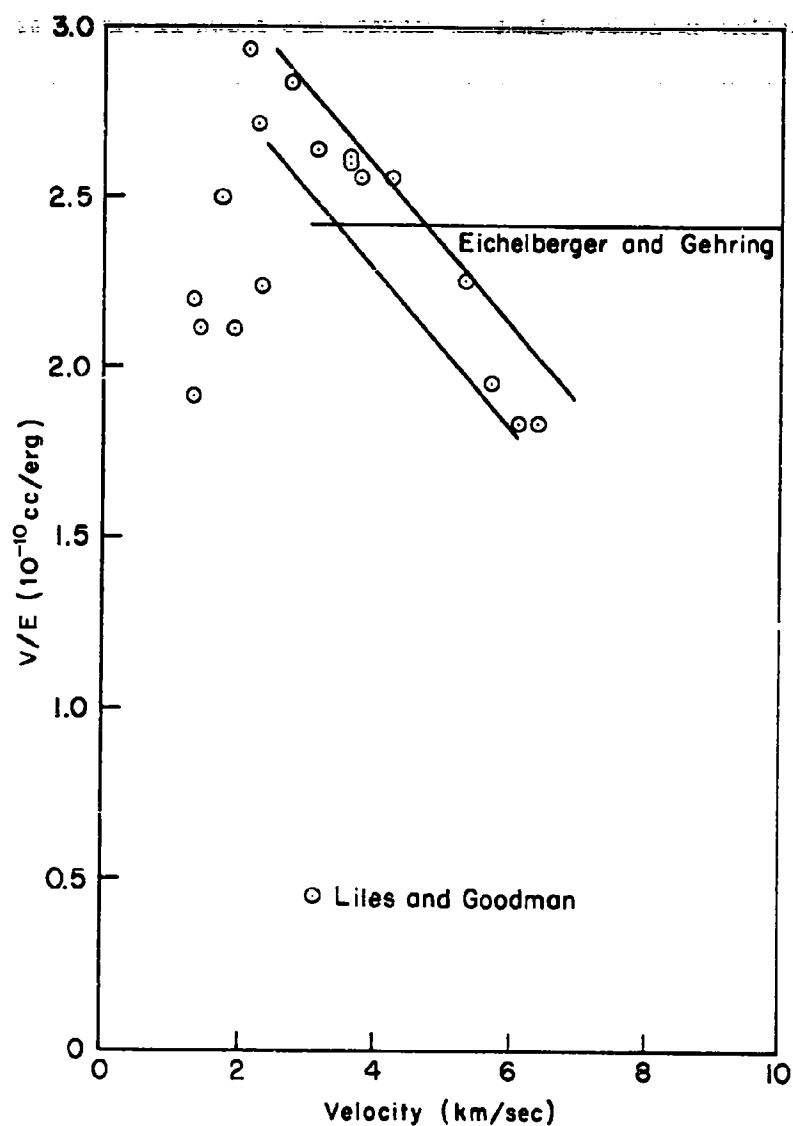


Fig. 3—Ratio of crater volume to projectile kinetic energy as a function of impact velocity for copper spheres on 1100-F aluminum targets

# IMPACT PHYSICAL PROCESSES REVIEW

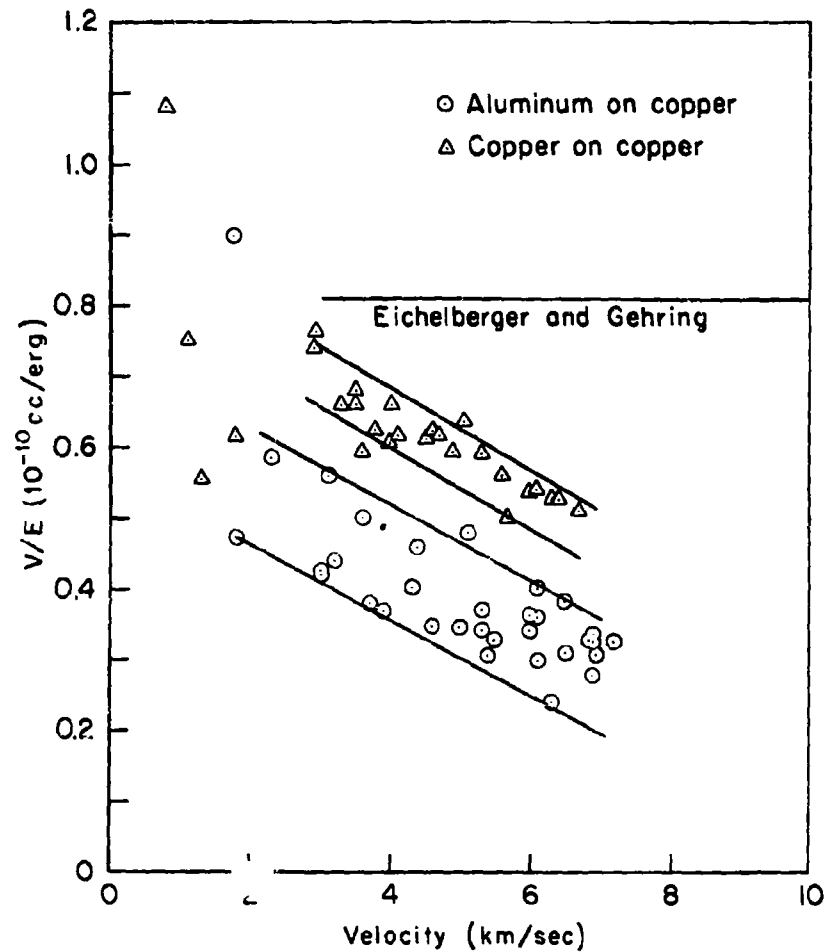


Fig. 4—Ratio of crater volume to projectile kinetic energy as a function of impact velocity for aluminum and copper spheres on copper targets  
(Data due to Liles and Goodman (4))

## IMPACT PHYSICAL PROCESSES REVIEW

The hypothesis that crater volume is directly proportional to projectile kinetic energy rests solely on empirical grounds. In the lower velocity range, where the hypothesis holds fairly well, the constant of proportionality is a function of both the projectile and target materials. There is no theoretical justification for extrapolating the relation outside the regime where the empirical fit was obtained. Indeed, for copper and 1100-F aluminum targets, where well-controlled experimental data at very high impact velocities exist, the hypothesis of constant volume-energy ratio is found to be incorrect.

### HYDRODYNAMIC PENETRATION

Penetration of aluminum projectiles into aluminum targets at velocities of 5.5, 20, and 72 km/sec were calculated on the hydrodynamic model and published by the author in 1958.<sup>(5)</sup> The projectile geometry considered in these calculations was that of a square cylinder (length equal to diameter), which moved along its axis of symmetry. The results are plotted as the shaded region in Fig. 1. The ordinate in this figure is the normalized penetration,  $p/d$ , where  $p$  is the penetration depth and  $d$  is the length of the projectile.

Since no other projectile geometries have been treated theoretically, one must examine experimental data to determine how to apply the theory to other projectile shapes.

A way of comparing the penetrations of spheres and square cylinders was suggested by Collins and Kinard<sup>(6)</sup> based on their experiments with both types of projectiles. For a given set of projectile-target materials they found that the penetration depended only on the projectile length, rather than on the projectile mass. Choosing the cylinder

## IMPACT PHYSICAL PROCESSES REVIEW

length (which equals its diameter) and the sphere diameter as characteristic dimensions,  $d$ , led to plots of  $p/d$  versus impact velocity which were identical for their data. The surprising conclusion is that a sphere of given diameter produces the same penetration as a square cylinder which has the same characteristic dimension, but which weighs 50 per cent more. Their data included cases of aluminum-on-aluminum impacts.

A possible criticism of their data is that it was apparently taken with unsaboted projectiles, and that aluminum projectiles have been found to lose a substantial fraction of their mass by erosion during flight through the launch tube.

On the other hand, Halperson and Atkins have presented data taken with aluminum spheres and cylinders fired in sabots.<sup>(7)</sup> For penetrations into the 1100-F aluminum alloy, their conclusion is that at a given impact velocity, the crater volume per unit projectile mass is the same for both geometries. The projectile masses were reported as 1.27 gm, but the dimensions of neither the cylinder nor its crater were specified. For this reason, one cannot be certain whether their result is in agreement with Collins and Kinard or not. Any disagreement is likely to be on the order of 10 per cent in penetration, which is comparable with the theoretical uncertainty and the scatter in even the best experiments, as illustrated in Fig. 1.

For irregular geometries, where one dimension greatly exceeds another, it is difficult to assign a characteristic dimension. In this case, some success has been obtained by choosing the equivalent sphere diameter as the characteristic dimension, i.e., the diameter of the sphere having the same mass as the projectile. In Section IV

## IMPACT PHYSICAL PROCESSES REVIEW

we will show that this yields a satisfactory treatment of flat disks, for example, the steel disks accelerated by the Ballistic Research Laboratories (BRL) explosive accelerator, and the plastic disks fired by the Ames Research Center light-gas gun.

However, even this treatment breaks down for the case of short, oriented rods. To exemplify this, the jet pellets fired by BRL at 10 km/sec have a length about 3 times their diameter and strike the target oriented end-on. The normalized penetration calculated using the equivalent sphere diameter greatly exceeds that expected from spherical projectiles striking at the same speed. The craters produced by the jet pellets are deeper and narrower than hemispherical, which is probably the source of the difficulty. However, they are not deep and narrow enough to be treated on the basis of shaped-charge jet theory. It is felt that more theoretical work is necessary in order to explain the penetration of short, oriented rods.

The theoretical craters were felt to contain a possible error of  $\pm 10$  per cent, which is denoted by the height of the shaded region. The portion of the theoretical craters below the original target surface was observed to be hemispherical within the limit of the error. It was also noted that the three calculated points could be fitted within the limits of the error by a curve having the form

$$\frac{p}{d} \sim v^{1/3}$$

In view of the fact that the fastest experimental shots at that time lay in the range of 15,000 to 17,000 ft/sec (and there were very few of these), and that the experimental results differed among themselves

## IMPACT PHYSICAL PROCESSES REVIEW

by a factor of two or more, the error cited seemed small indeed, and a more refined fit did not seem justified. However, the excellent agreement of the theoretical points with recent experimental data, which extends into the velocity range treated theoretically, justifies a more careful treatment. Accordingly, the theoretical points are connected in Fig. 1, and in the following figures of the same type, by a smooth curve.

The equation of the curve is

$$\frac{p}{d} = 11.02 \exp \left\{ \frac{-2.457}{v^{0.295}} \right\} \quad (2)$$

where  $v$ , the impact velocity, is given in km/sec. The form of the fit was chosen to produce a smooth change of curvature on a log-log plot of  $p/d$  versus  $v$ . It is noteworthy that this fit agrees with both the magnitude and slope of the experimental data. For a given value of velocity, the possible error in  $p/d$  should still be taken to be 10 per cent. For 1100-F targets, it is believed that this equation will be accurate to within the limits of error prescribed for the velocity range of 5.5 to 20 km/sec. At lower velocities, the equation will overestimate the penetration because of material-strength effects which the hydrodynamic model does not consider. At higher velocities, for reasons discussed in the section on melting and vaporization, the equation will underestimate the penetration. It is anticipated that penetrations will be about 40 per cent higher than predicted by the equation at impact velocities of 72 km/sec.

Assuming that the craters are hemispherical and employing Eq.

## IMPACT PHYSICAL PROCESSES REVIEW

(2) leads one to the relation

$$\frac{V}{E} = \frac{3969}{v^2} \exp \left\{ \frac{-7.371}{v^{0.295}} \right\} \quad (3)$$

for the volume-energy ratio. Since the equation for  $p/d$  is cubed to obtain this expression, the limits of error are now  $\pm 33$  per cent. The shaded region in Fig. 2 shows the volume-energy ratio specified by Eq. (3). All the experimental points are encompassed by the theoretical region. Despite the large uncertainty, it is clear that a substantial reduction in  $V/E$  with increasing velocity is predicted and verified by the experimental data.

### STRENGTH EFFECTS

Since the hydrodynamic model neglects material strength, the question naturally arises as to how well it simulates the actual physical process of an impact in a metal. Most investigators feel intuitively that the material strength must play an essential role in determining crater size.

In order to gain an insight into this question, we may consider penetrations into the various alloys of aluminum. These alloys are interesting in that they have essentially the same elastic properties, such as Young's modulus, sound velocity, and bulk modulus, but widely varying strength parameters. For example, the Brinell hardness number of the 1100-F alloy (commercially pure aluminum) is about 16, whereas the BHN for the 2024-T3 alloy is about 7.5 times as large, or 120.

In Fig. 5, the penetration of aluminum spheres in the two alloys



# IMPACT PHYSICAL PROCESSES REVIEW

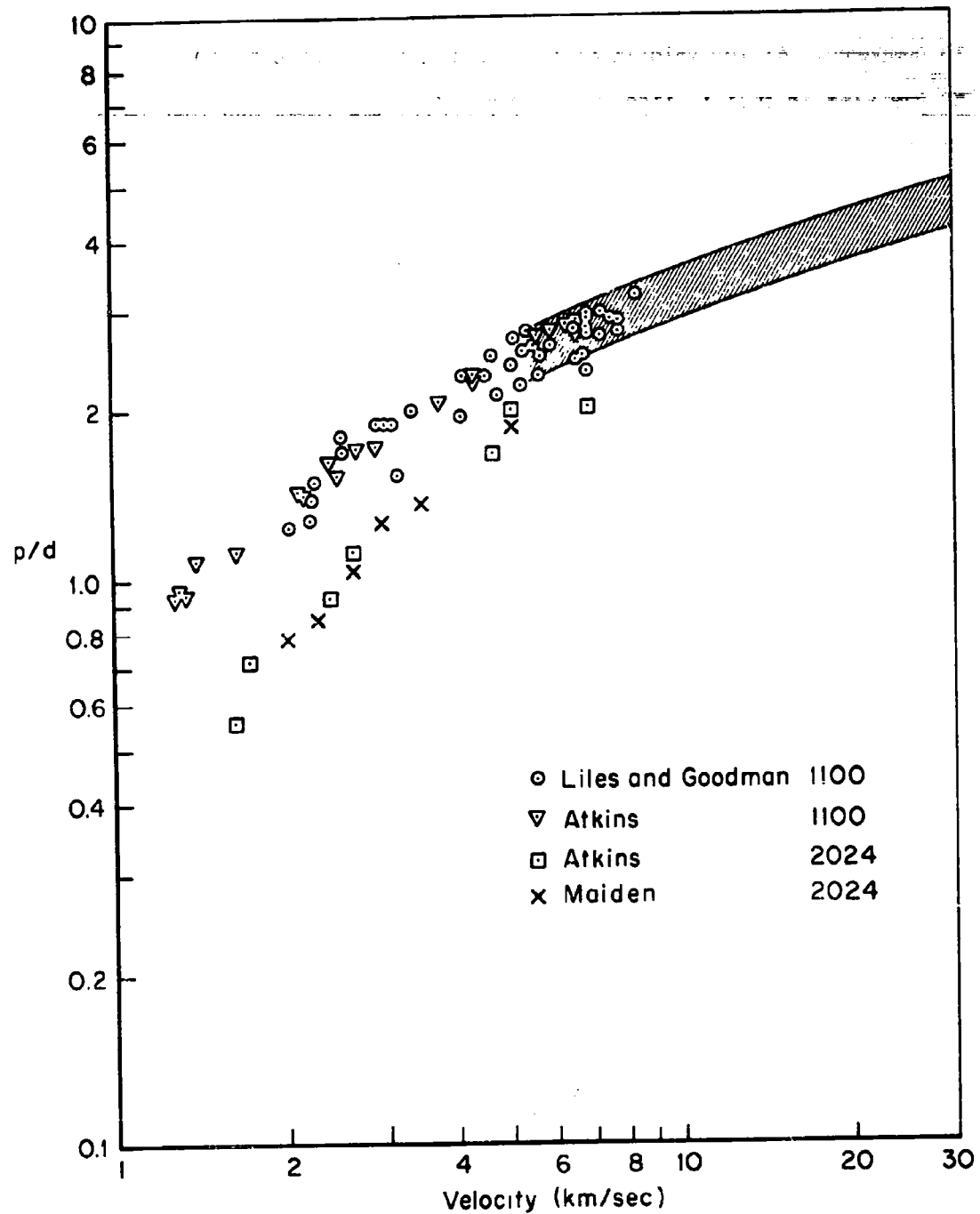


Fig. 5 — Normalized penetration ( $p/d$ ) as a function of impact velocity for aluminum projectiles into 1100-F and 2024-T3 aluminum targets

## IMPACT PHYSICAL PROCESSES REVIEW

is compared. At low velocities the penetration in 2024-T3 is about 50 per cent of that in 1100-F. At 7.5 km/sec the ratio has increased to 74 per cent. These experimental results strongly suggest that the ratio of penetrations in the two alloys is drawing closer to unity as the impact velocity is increased. The theoretical considerations on target melting discussed in Section III indicate that at 20 km/sec and above the ratio will be essentially unity.

The experimental penetrations in the low-strength 1100-F alloy are seen to be in excellent agreement with those predicted by the hydrodynamic model<sup>(5)</sup> which is shown as the shaded region.

Since the two alloys are identical in almost all respects except strength, the reduced penetration in 2024-T3 must be ascribed to a strength effect. At the present time no satisfactory theory exists to calculate the penetration reduction due to material strength. We will discuss two considerations which suggest that the formulation of such a theory will be extremely difficult.

First, the penetration is already very insensitive to strength at 7.5 km/sec, an increase of BHN by a factor of 7.5 causing a reduction of only 26 per cent in penetration. If one sought to fit the penetration in various alloys by a factor involving some power of BHN, e.g.

$$p/d \sim (\text{BHN})^m$$

or by linear interpolation

$$p/d \sim a + b(\text{BHN})$$

he would obtain nearly the same result because of the insensitivity.

## IMPACT PHYSICAL PROCESSES REVIEW

Moreover, if he chose any other strength parameter, e.g., shear strength or tensile strength, he could obtain nearly the same results, since the various strength parameters correlate quite well among themselves. Therefore, it is anticipated that experimental data will not distinguish definitively among the various strength parameters and their functional relation to penetration reductions.

A more basic difficulty arises from the fact that the final stages of crater formation occur in target material which has been conditioned by the initial shock.<sup>(8)</sup> At least one physical parameter is definitely known to be altered by this conditioning, namely, the temperature. One can easily imagine that others might be also, in view of the severe compression and re-expansion which the material has suffered. Thus the notion of using a normal-temperature strength parameter to scale high-velocity penetration is open to serious question. The parameter modification by shock-conditioning must be taken into account.

With the experimental results before us, however, it is probably safe to scale over the small penetration range by an expression of the form

$$p/d = 2.75 \left\{ \frac{16}{\text{BHN}} \right\}^{0.15}$$

which may be expected to predict penetrations in the various aluminum alloys at 7.5 km/sec.

## IMPACT PHYSICAL PROCESSES REVIEW

### II. MELTING AND VAPORIZATION

#### SHOCK HEATING AS A FUNCTION OF PARTICLE VELOCITY

When a hypervelocity projectile encounters a target surface, it generates a shock wave in the target. The shock propagates into the target material with supersonic velocity and is the first physical manifestation of impact which any element of the target feels. The shock's passage sets the target material into motion and heats it. In view of the creation of entropy in the shock front, the target material is left heated even after expanding back to zero pressure. Figure 6 shows the temperatures produced in four metals as a function of shock pressure. The numbers plotted in the figure pertain to material that is initially at zero pressure, is acted upon by a single shock of maximum pressure  $P$ , and then expands adiabatically back to zero pressure. The temperature after release is plotted as a function of the peak pressure.

For a given material, the pressure behind a shock may be expressed as a function of only the change in particle velocity across the shock. (Particle velocity is defined as the velocity of each material element.) In hypervelocity impact, it is common to consider the target as being at rest, so that the peak pressure may be expressed as a function of only the particle velocity behind the shock. In that case the release temperature may also be expressed as a function of particle velocity only. This is done for aluminum in Fig. 7, where the left ordinate scale gives particle velocity in km/sec, and the right ordinate scale gives the release temperature as well as the state to which the material reverts.

## IMPACT PHYSICAL PROCESSES REVIEW

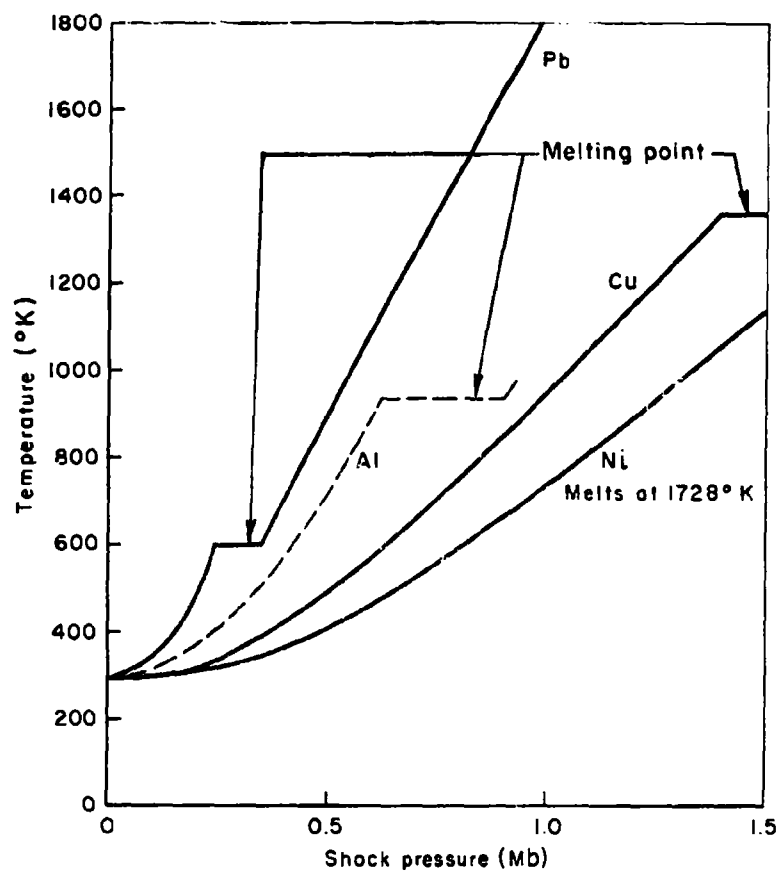


Fig. 6 — Release temperature as a function of shock pressure for four metals

# IMPACT PHYSICAL PROCESSES REVIEW

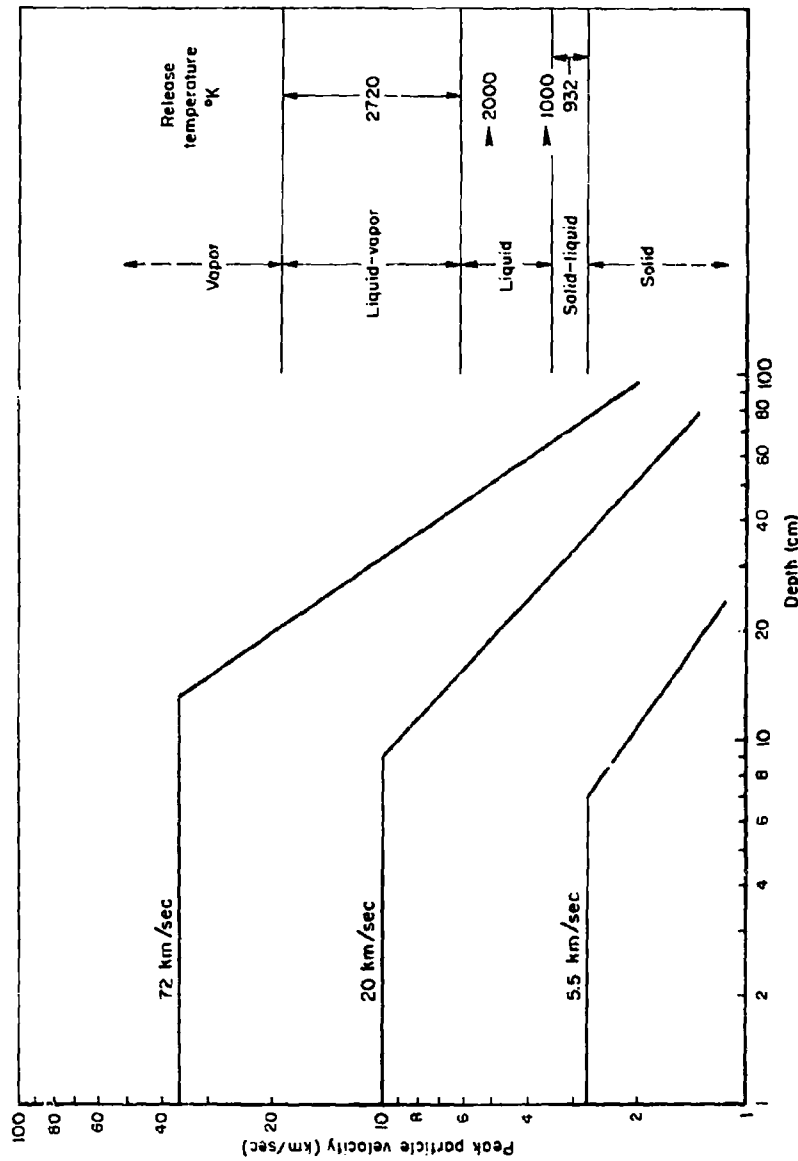


Fig. 7—Left scale: peak particle velocity as a function of depth along axis of symmetry for 10x10-cm aluminum cylinders striking end-on on semi-infinite aluminum targets  
Right scale: release temperature and material state for same cases

## IMPACT PHYSICAL PROCESSES REVIEW

The curves in Fig. 7 show the peak particle velocity as a function of depth along the axis of symmetry as calculated in Ref. 5.

The curves in the figure are indexed by the impact velocity. Since these calculations referred to the impact of aluminum projectiles on aluminum targets, the initial particle velocity is half the impact velocity. Thus, the curve pertaining to an impact at 72 km/sec shows a particle velocity of 36 km/sec for small depths. Because the solution along the axis remains one-dimensional in nature until rarefaction waves from the target surface reach the axis, the curves all remain flat for a considerable depth. After this point, the peak particle velocity decreases with depth. Either the particle velocity or the release temperature may be read from the graph as a function of depth.

### EFFECT OF TARGET MELTING ON CRATER SIZE

For the impact at 20 km/sec, it may be seen that the target material is melted to nearly the crater depth of 40 cm predicted purely on the basis of hydrodynamic flow. Thus, at about this impact velocity, one may expect that craters in all alloys of aluminum will have about the same depth, since the material strength does not influence the shock to a measurable degree at depths of less than 40 cm, and the melting characteristics of the various commercial alloys are similar. At impact velocities greater than 20 km/sec, the melted region will extend below the predicted craters. For example, at 72 km/sec the melted region is seen to extend to about 78 cm, which may be compared with the 55-cm penetration predicted in Ref. 5.

## IMPACT PHYSICAL PROCESSES REVIEW

The numbers quoted should be considered preliminary estimates, which might be revised when a more thorough investigation is conducted. To reflect this fact, the estimated crater depth is shown as a dashed line in Figs. 18 and 19. However, it is possible to make some observations on the physics of the cratering process with more certainty. At impact velocities above 20 km/sec, the crater dimensions are determined essentially by the extent of the melted region. The fact that a new physical mechanism becomes important at higher velocities stands in contrast with the belief of Eichelberger and Gehring<sup>(2)</sup> that the physical mechanisms they considered were the only important ones over the meteoric-velocity regime.

The notion that material melting determines the crater size is strongly reminiscent of Whipple's hypothesis discussed in Section I, and the question logically arises as to whether Whipple might be correct for high velocities. The answer to this question comes from an examination of Fig. 7. Consider the case of an impact at 72 km/sec. The melted zone extends to about 78 cm, which we estimate to be the depth of the crater. However, the graph shows that the target material is completely vaporized to a depth of about 20 cm, is a mixture of liquid and vapor at a temperature of  $2720^{\circ}\text{K}$  to a depth of 45 cm, is liquid at a temperature substantially above the melting point down to about 66 cm, and is a mixture of liquid and solid at  $932^{\circ}\text{K}$  down to the final crater depth. In short, the average specific internal energy to which the crater material finally reverts is much greater than the heat of fusion. In addition, energy is delivered to other sources, e.g., kinetic energy and heating the material outside the crater.



## IMPACT PHYSICAL PROCESSES REVIEW

Thus, a consideration of the energetics of the process indicates that Whipple must considerably overestimate the crater at the higher velocities.

Although the depths delineating the various state regimes may be slightly revised in the future, the qualitative physical observations are still expected to apply.

For impacts at velocities below 20 km/sec, the initial shock heating reduces the material strength and enhances the validity of the hydrodynamic model used in calculating the crater sizes. The reduction in strength may be expected to bring the craters in 1100 and 2024 alloys into closer and closer correspondence as the impact velocity is increased.

## IMPACT PHYSICAL PROCESSES REVIEW

### III. PHYSICS OF THIN-TARGET PENETRATION

Calculations based on the hydrodynamic model were made for aluminum cylinders striking aluminum plates at a velocity of 20 km/sec. The cylinder was chosen to be 10 cm long and 10 cm in diameter. Two target thicknesses were considered, namely, 1 and 2 cm. Although specific dimensions are prescribed in these examples, the problem is scalable, so that only the ratios of the dimensions are physically significant. Thus the results correctly describe the process where a square (length equals diameter) cylinder impacts targets whose thicknesses are one-tenth and one-fifth its length.

Figure 8 illustrates conditions 2.56  $\mu$ sec after initial impact. In this figure and the following similar ones the x-axis is the axis of cylindrical symmetry, so that the target plate is depicted by the two parallel lines,  $x = 0$  and  $x = 2$  cm. An arrow in the figures denotes the particle velocity at the arrow's tail. The dashed line is the interface between projectile and target material. Pressure contours for the pressure values of 0.1, 1, 2, and 3 megabars are also shown.

Upon impact, two shocks are created, one moving into the target material and one moving upstream in the projectile material. For this particular set of conditions the shock moves upstream at about the same rate that the projectile moves forward, with the result that the shock remains nearly stationary relative to the target. In other words, the shock moves backward at about 20 km/sec relative to the projectile material, and the projectile material moves forward at 20 km/sec until it encounters the shock.

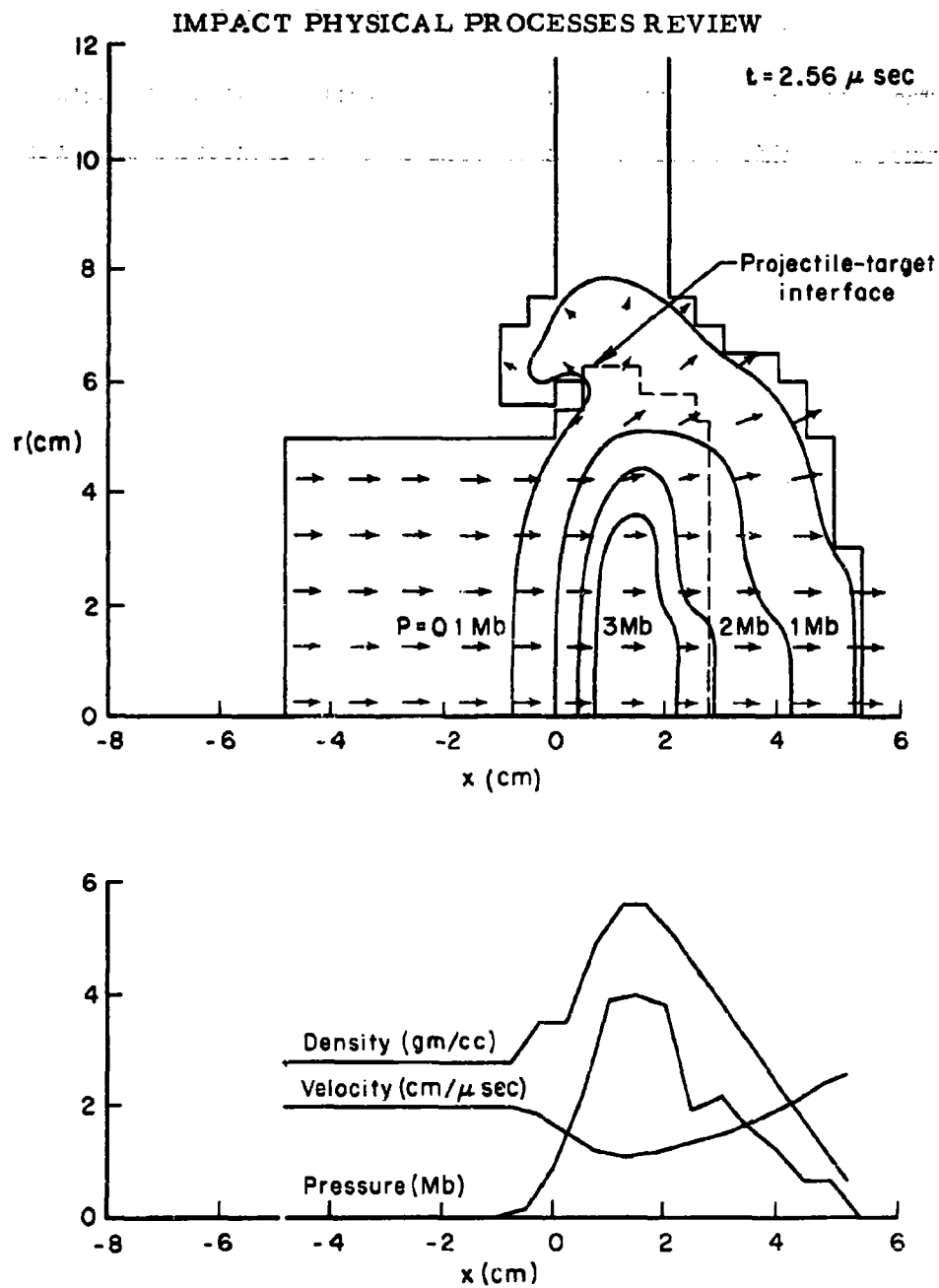


**Fig. 8 — Aluminum cylinder (10-cm diameter, 10-cm length) striking 2-cm aluminum plate at 20-km/sec. Conditions:  $2.56 \mu \text{ sec}$  after initial contact**

## IMPACT PHYSICAL PROCESSES REVIEW

The bottom half of Fig. 8 illustrates conditions along the axis of symmetry at this time. It may be seen that the projectile material moves unimpeded at a velocity of 20 km/sec until it reaches the left shock. In these calculations, the shock is purposely smeared out somewhat. The smearing is necessary in order that the numerical equations used be stable. In the actual impact, the shock would represent a discontinuity in velocity, pressure, and density at about  $x = 0$ , whereas the figure illustrates that these variables undergo a rapid, but continuous, change between about  $x = -1$  and  $x = 1$ . On crossing the shock front, the material velocity is reduced to 10 km/sec, the density is raised to about 5.6 gm/cc, and the pressure is raised to about 5 megabars.

At the time of 2.56  $\mu$ sec represented in the figure, the shock moving into the target has encountered the rear target surface and blown it off. As a result, a rarefaction wave moves into the shocked material. As may be seen, the material velocity increases smoothly in the rarefaction wave, and the pressure and density undergo a smooth decrease to zero values. The smooth variation corresponds to physical reality in this case. Reference to Fig. 7 shows that the shock is sufficiently strong to partly vaporize the target material. The material in the rarefaction wave will thus consist of a mixture of aluminum vapor and molten droplets, so that the pressure and density in the rarefaction must decrease smoothly in manner illustrated.

As the process progresses, the rarefaction wave will overtake the left shock and decrease its strength. That is, we may expect to see smaller peak pressures behind the left shock, we may expect to see a

## IMPACT PHYSICAL PROCESSES REVIEW

smaller velocity drop as projectile material crosses the shock, and we may expect to see smaller densities. In effect, a race is occurring between the shock and the rarefaction overtaking it. If the shock maintains sufficient strength when the rear surface of the projectile reaches it, the rear surface will be thoroughly shattered and dispersed. If not, large fragments of the rear portions of the projectile will survive and continue their flight unimpeded through the hole punched in the target by the front portions of the projectile.

In addition to the rarefaction due to the back face of the target, lateral expansion of the projectile is occurring which also generates rarefaction waves. The pressures in the shock are high enough to move the target material laterally, as is shown by the arrows moving upward into the target material. Behind the target, the material can expand laterally into a void, and so the expansion proceeds faster there. The region influenced by the lateral expansion can be identified by the velocities which have acquired an r-component of velocity.

The continuation of the process described is shown in Fig. 9, which pertains to the time of 4.2  $\mu$ sec. Both rarefactions have eaten into the shocked region, reducing the pressures there. In spite of the pressure reduction which has occurred at this point, it is interesting to note that the projectile, which was originally 10 cm in length, is at this time compressed into the region between  $x = 5.3$  cm and  $x = -1.6$  cm. The pressures in the shock, which is about to encounter the back of the projectile, range from about 2 megabars on the axis to about 0.2 megabars at the cylinder periphery. This is sufficient to thoroughly shatter the projectile.

# IMPACT PHYSICAL PROCESSES REVIEW

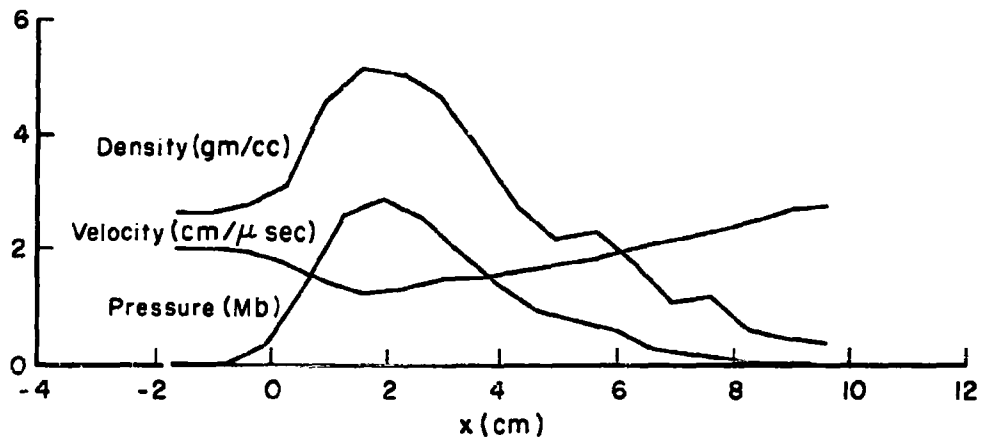
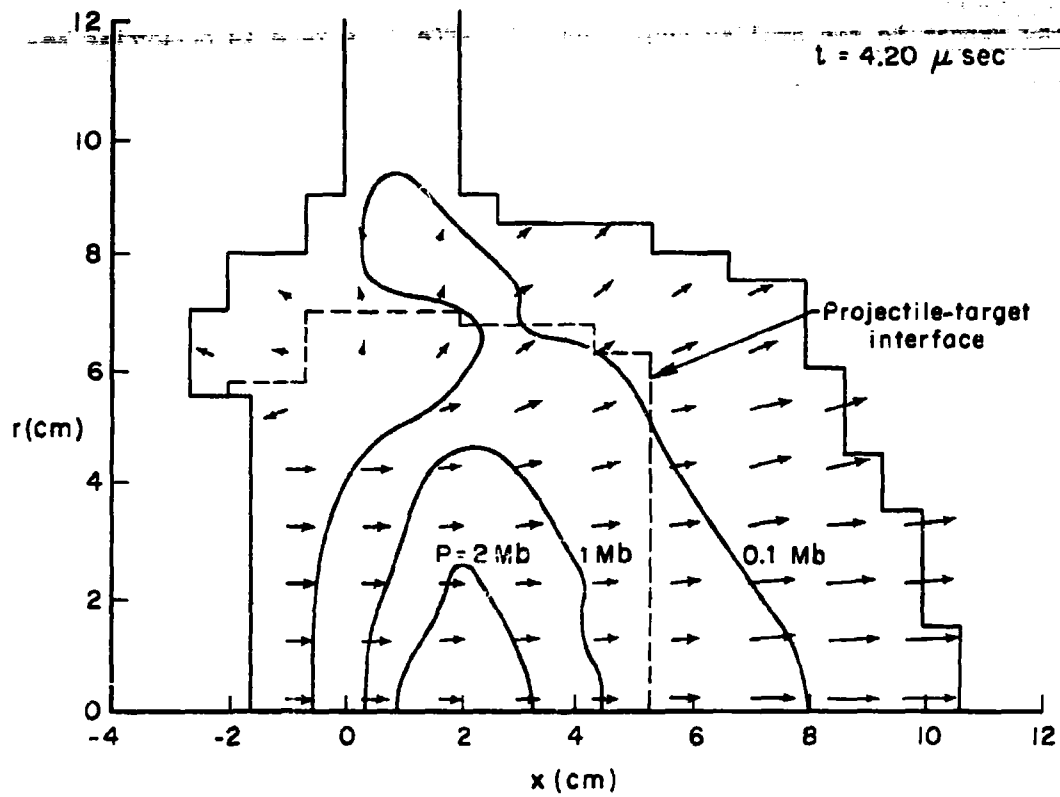


Fig. 9 — Aluminum cylinder (10-cm diameter, 10-cm length) striking 2-cm aluminum plate at 20 km/sec.  
Conditions:  $4.20 \mu \text{ sec}$  after initial contact

## IMPACT PHYSICAL PROCESSES REVIEW

The final stage of the process is shown in Fig. 10. At this time of 9.86  $\mu$ sec, sufficient expansion of the material has occurred to render all pressures zero. Density contours are plotted instead of pressure contours. On the model used in the calculation, the material is represented as a continuum, and the density is calculated on that basis. In reality, the material has undoubtedly broken up into particles at this time. The density reported may be expected to give quite accurately the density, averaged over particles and voids.

Unfortunately, there is no known method of estimating the particle sizes present in the diverging spray shown in Fig. 10. Were such an estimate possible, a complete description of the damage to be expected from this spray might be given. Available experimental evidence indicates that for a given projectile-target system the spray particles become smaller with increasing impact velocity. A qualitative discussion of the expected damage will be given later in this Memorandum.

One can see from Fig. 10 that the velocity field essentially radiates from a single point, the point being on the axis of symmetry at -8.8 cm. That is to say, if each velocity vector were projected backward to the axis of symmetry, it would intersect the axis at about -8.8 cm. One such constructed line is shown dashed in the figure. The flow is thus conical in nature, and further inspection shows that along a ray from the cone's apex, there is a positive velocity gradient, so that in flight the spray is elongating as well as expanding laterally. This implies that each particle will proceed with unchanged velocity from this time forward because there are no pressure forces and no material will accumulate in the future to create any, in view of the positive velocity gradient.

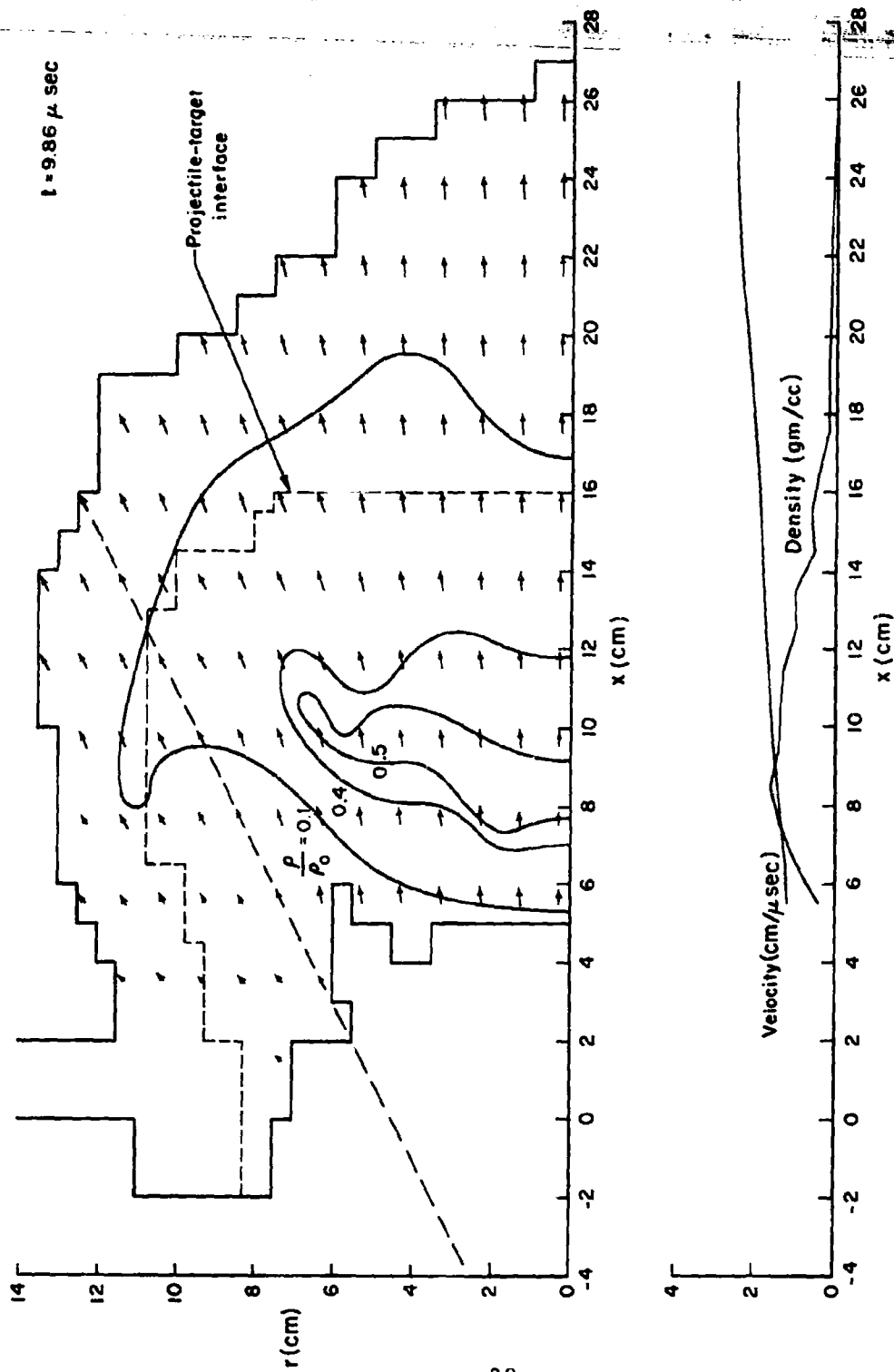


Fig. 10—Aluminum cylinder (10-cm diameter, 10-cm length) striking 2-cm aluminum plate at 20 km sec. Conditions: 9.86  $\mu$  sec after initial contact



## IMPACT PHYSICAL PROCESSES REVIEW

Because of the conical nature of the flow, it is physically meaningful to prescribe the momentum per unit solid angle about the cone's apex. This quantity will remain fixed no matter how far the spray flies. One should note that this may be said only of a conical-type flow. In Fig. 11 the momentum per unit solid angle about the conical apex is shown as a function of angle from the axis of symmetry. To calculate these numbers, cones having 5-deg increments in apex half angle were laid out, and the momentum of material contained between them was summed. This momentum was then divided by the solid angle bounded by the two cones. The number thus obtained is plotted at the angle halfway between the two cones. The points are then connected by straight lines.

The results from both the 1- and 2-cm targets are shown, and the effect of target thickness is obvious. The spray from the thin target is more concentrated at the smaller angles, and the maximum dispersion angle is smaller. The physical reason for this will now be discussed.

In the series of Figs. 12 to 14, the impact of the same cylinder with a 1-cm target is presented. The qualitative features of the process are exactly the same. Quantitatively, a few differences appear. In Fig. 12, which pertains to a time of 2.75  $\mu$ sec, it may be noticed that the left shock has been carried forward slightly. The reason for this is that the shock propagation velocity increases with shock strength, and the rarefaction from the rear of the target weakens the shock more quickly than in the case of the thicker target. For this reason, the shock will be weaker at corresponding times than the shock in the other case.

The lower pressures from this source lead to less lateral expansion.

## IMPACT PHYSICAL PROCESSES REVIEW

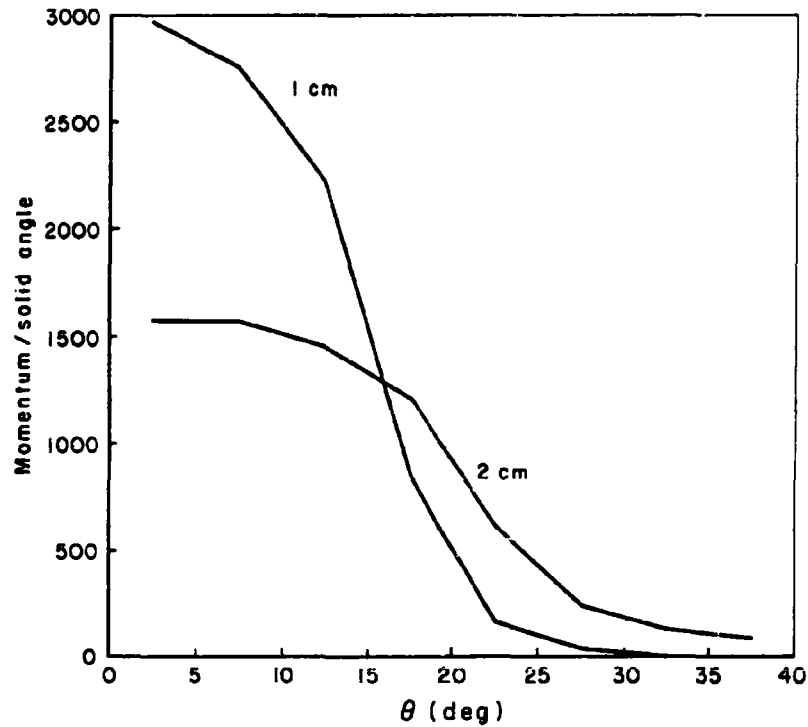


Fig. 11—Momentum per unit solid angle contained in the spray resulting from cylinder (length = diameter = 10 cm) striking aluminum plates of thickness 1 and 2 cm

# IMPACT PHYSICAL PROCESSES REVIEW

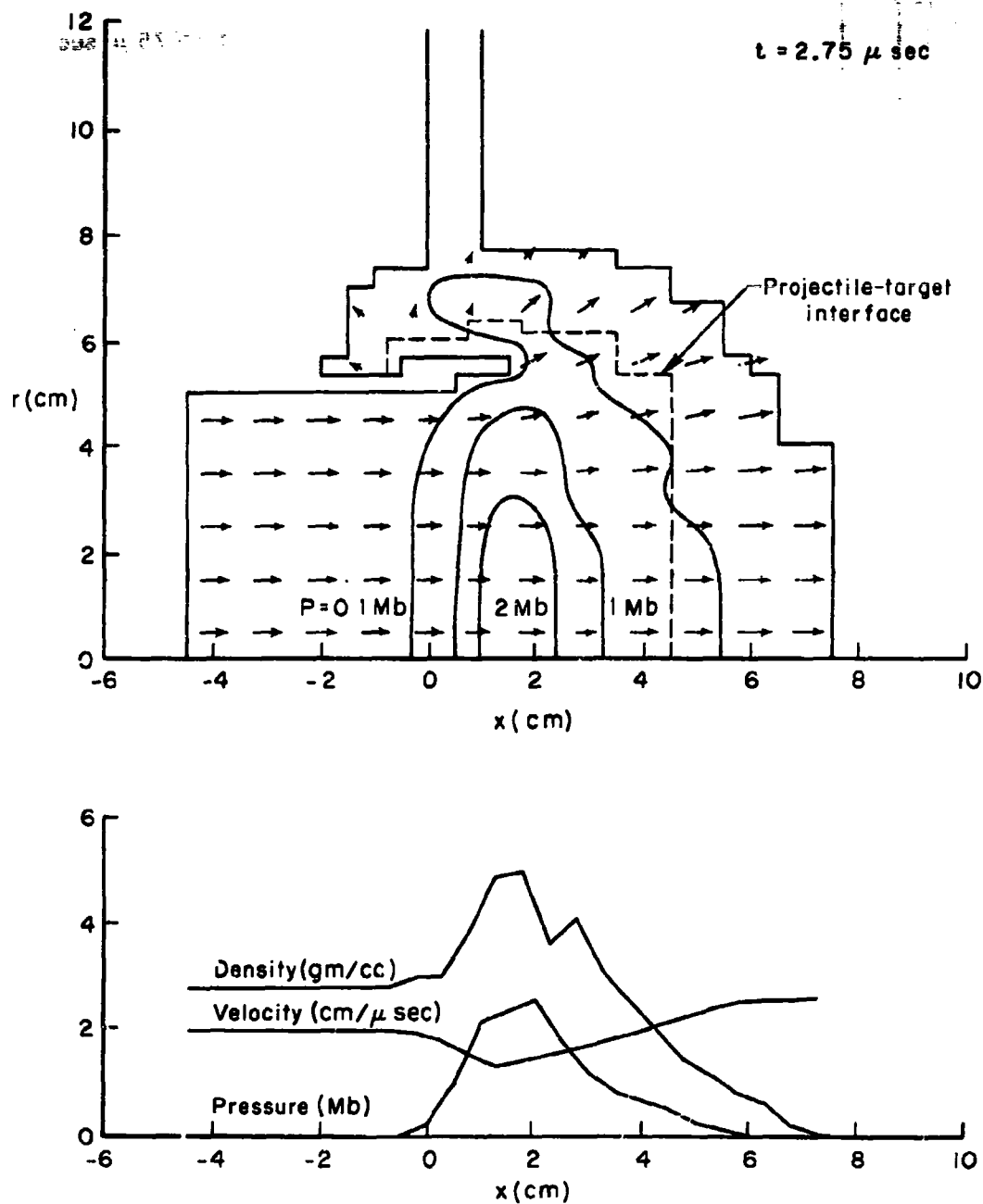


Fig. 12— Aluminum cylinder (length = diameter = 10 cm) striking 1-cm aluminum plate. Conditions: 2.75  $\mu \text{ sec}$  after initial contact

# IMPACT PHYSICAL PROCESSES REVIEW

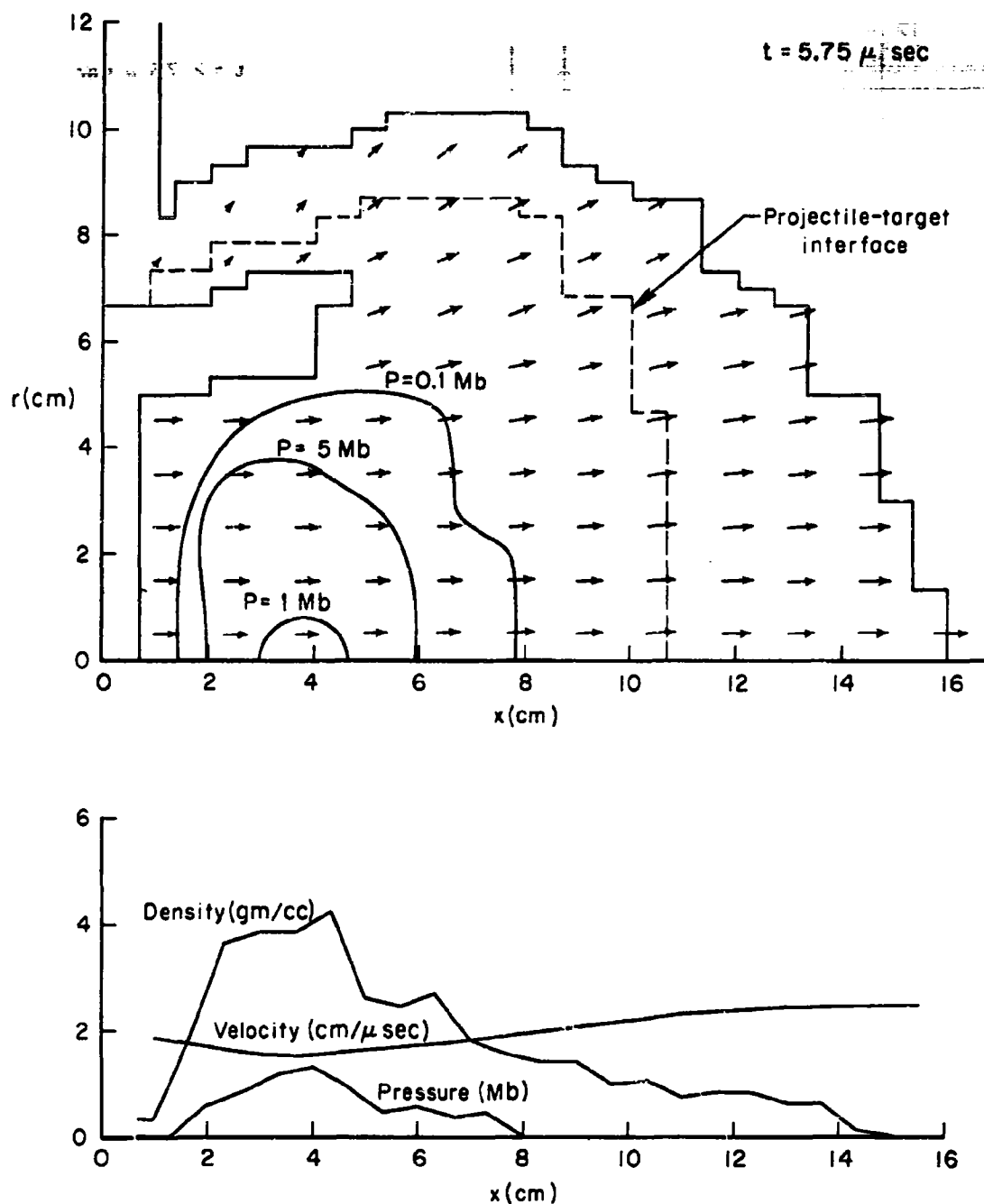


Fig. 13—Aluminum cylinder (10-cm diameter, 10-cm length) striking 1-cm aluminum plate at 20 km/sec.  
Conditions:  $5.75 \mu\text{sec}$  after initial contact

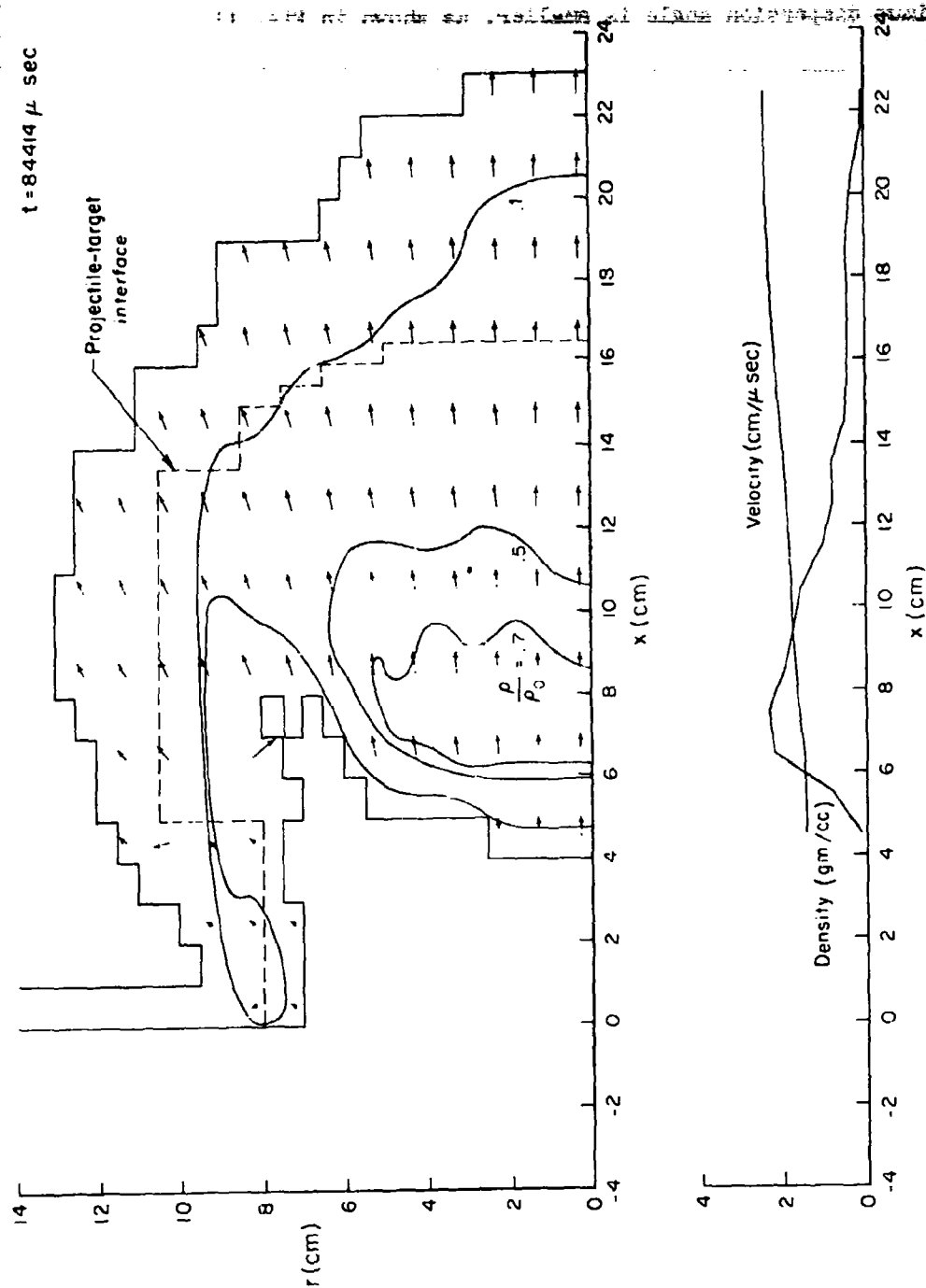


Fig. 14—Aluminum cylinder (10-cm diameter, 10-cm length) striking 2-cm aluminum plate at 20 km/sec. Conditions: 8.44  $\mu$  sec after initial contact

## IMPACT PHYSICAL PROCESSES REVIEW

This explains why more mass is carried in the forward direction and the maximum dispersion angle is smaller, as shown in Fig. 11.

For the same reason, the strength of the shock which reaches the rear projectile surface is also smaller, ranging from 1 megabar to somewhat less than 0.2 megabar in this case. These pressures should still be sufficient to thoroughly shatter the projectile.

Finally, a smaller hole will be produced in the thinner target, since less impulse per unit lateral area is applied to it, and the pressure in the thinner plate is more rapidly relieved by rarefaction waves. The final hole radius is estimated from these calculations to be about 9 cm for the thin target and about 12 cm for the thicker one.

It is clear from these considerations that the diameter of a hole created in a thin target will always be smaller than the crater diameter produced in a thick target. Figure 15 shows roughly how the hole diameter in a thin target will vary as a function of target thickness. The ordinate of the figure is  $D_h/d$ , where  $D_h$  is the hole diameter and  $d$  is the characteristic dimension of the projectile. The abscissa,  $t/d$ , is the target thickness in units of the projectile dimension. The figure indicates that in the limit of zero target thickness, the hole diameter approaches the projectile diameter, so that  $D_h/d$  approaches unity. As the target thickness is increased, the hole diameter increases rapidly until it reaches the limiting diameter, corresponding to the thick-target crater diameter. This limit is reached when the target thickness is of the order of the projectile dimension. After this point, the hole diameter on the entrance surface will remain essentially constant, but with further increase in target thickness a

# IMPACT PHYSICAL PROCESSES REVIEW

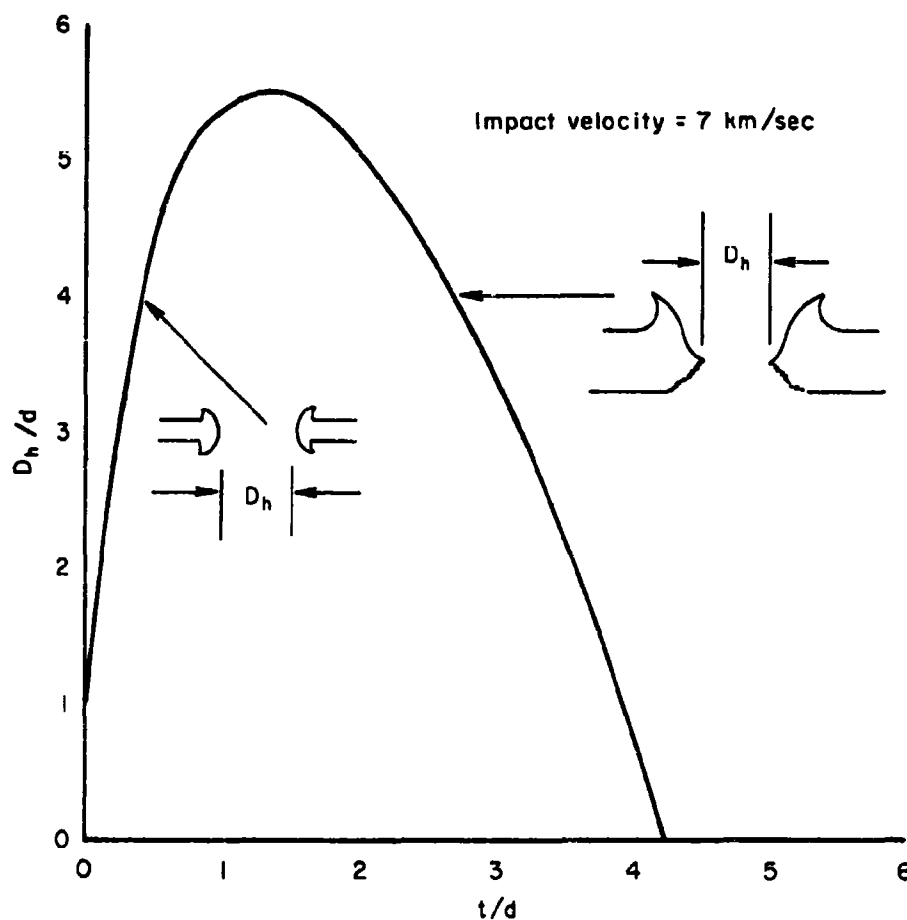


Fig. 15 — Expected hole diameter ( $D_h$ ) at constant impact velocity as a function of target thickness ( $t$ ) for 1100-F aluminum targets. Quantities are expressed in units of projectile dimension ( $d$ )

## IMPACT PHYSICAL PROCESSES REVIEW

constriction will appear below the entrance surface. This is illustrated in the inset in Fig. 15. Below the constriction the hole enlarges due to spallation of the rear surface. The portion of the hole due to spallation will vary erratically from sample to sample and will also depend on such factors as the strength and brittleness of the sample. As the target thickness is further increased, the diameter of the constriction will decrease, finally becoming zero when the target attains a thickness of about three-quarters of the thick-target crater diameter. Figure 15 is sketched for the case of aluminum striking aluminum at 7 km/sec, a reasonable satellite orbital velocity. For this case, the thick-target penetration is about 2.75 projectile diameters. Therefore, the maximum hole diameter is about  $5.5d$ , and the closure of the constriction occurs for a target thickness of about  $4.1d$ .

The discussion of the physical process of thin-plate perforation has disclosed that such plates are amazingly efficient in shattering a hypervelocity projectile. Of course, the plate pays the penalty of having a hole blown in it during the process, and the hole dimensions have been discussed in the preceding section. We will now consider the damage which the spray of fine particles emerging from the rear surface may be expected to cause.

The damage will be a function of standoff--the separation between the back of the first plate and the next surface to be encountered. At small standoffs, the impact craters of the individual spray particles will overlap, with the result that a single rather deep crater would be produced in a thick target. In a thin target at small standoff, a clean perforation may be expected. The criterion for this type of



## IMPACT PHYSICAL PROCESSES REVIEW

perforation is that a sufficiently high pressure be built up in the second target to occasion behavior of the hydrodynamic type. The shock, upon reaching the rear of the second plate, must blow it off and allow the momentum to proceed through in the manner just discussed for the first plate. If this occurs, almost all of the momentum passes through the second sheet, leaving only a clean perforation, and producing very little bulging or other distortion of the plate. At larger standoffs, the individual impact craters produced by the spray particles cease to overlap, and in a thick target, only the dimpling of the individual craters will be apparent. In a thin target, however, if the individual craters do not perforate the sheet, the momentum of the spray particle is entirely trapped within the plate. It may even be somewhat enhanced because of producing back splash. For such cases the behavior of the plate may be deduced by calculating the pressure pulse (pressure as a function of time and position) which acts upon it and solving the resulting problem in mechanics. The pressure is equal to the time rate of momentum arrival per unit area, a quantity which may be calculated from the theoretical data presented in Figs. 10 and 14.

Some general observations may be made on the nature of the pressure pulse received by the second plate. At any given angle,  $\theta$ , the total momentum per unit area received by the second plate is a function of standoff, since it varies inversely as the square of the distance from the apex of the conical flow. Because of the velocity gradient along a given ray, the time required to impart this momentum will increase linearly with distance from the apex point. Thus, the peak pressure at any given angle may be expected to fall off inversely as the cube of the distance from the apex point.

## IMPACT PHYSICAL PROCESSES REVIEW

At very great standoffs, the plate will withstand the effects of the pressure pulse very well, and the only damage expected is the pitting due to the individual fragments present in the spray. The depth of these pits will vary linearly with the dimension of the fragment which produces them. Therefore, an assessment of the damage from this source requires a knowledge of the fragment sizes present in the spray. As standoff is decreased, the pressure pulse will produce a bulge in the plate, whose severity increases with shorter standoff. The bulging deformation produces tension in the plate and stretches the material so that it thins out. At some critical standoff, the material in the bulge fails in tension, the failure originating at the crown. This failure is accompanied by cracks which propagate down the sides of the bulge as the sides flare out, forming large petals. The effects of standoff are very critical in this region, the bulge either remaining intact if no tensile failure occurs or petalling fully in the event of failure. The petalling failure usually produces much larger holes in the second plate than the primary projectile would produce in the absence of the first plate.

## IMPACT PHYSICAL PROCESSES REVIEW

While scaling by means of the F-factors is regarded as most accurate, a rougher but more convenient scaling is also possible. An empirical fit to the results of F-scaling may be written in the form

$$\frac{x_{B-A}(v)}{x_{A-A}(v)} = \left( \frac{\rho_B}{\rho_A} \right)^{\beta_A(v) + 1/3} \quad (10)$$

where  $\beta_A(v)$  pertains to targets of material A. The functions,  $\beta_A$ , may all be presented on one graph, as in Fig. 16. In general,  $\beta$ -scaling agrees with the more accurate F-scaling to within 10 per cent. Calculation of the F-factors demands the knowledge of the shock Hugoniot of the projectile material at the impact velocities of interest. Where this information is not available, one may still use  $\beta$ -scaling to give a reasonable first estimate. The F-factors for aluminum targets are shown in Fig. 17.

In Fig. 18 the scaling law is tested against recent experimental data. All of the data in the figure pertain to 1100F aluminum targets. The data of Atkins, shown as circles in the figure, were obtained by firing sabot aluminum spheres. The data are presented unscaled in the figure, and good agreement with the author's theoretical results is obtained, as previously noted. The data of Liles and Goodman,<sup>(4)</sup> shown as triangles, pertain to sabot copper spheres impacting 1100-F aluminum. These data have been scaled down by the appropriate F-factor, shown in Fig. 17. If the scaling law is correct, the two sets of data should be brought to the same curve by this treatment. The scaling law gives remarkably exact agreement with the experimental data.

# IMPACT PHYSICAL PROCESSES REVIEW

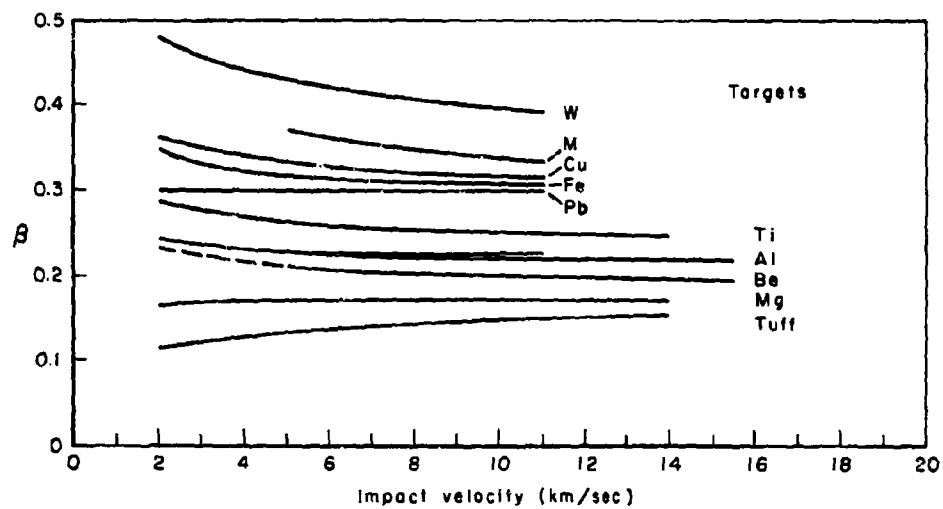


Fig. 16 — Values of  $\beta$  deduced from the normalized penetration-ratio curves

# IMPACT PHYSICAL PROCESSES REVIEW

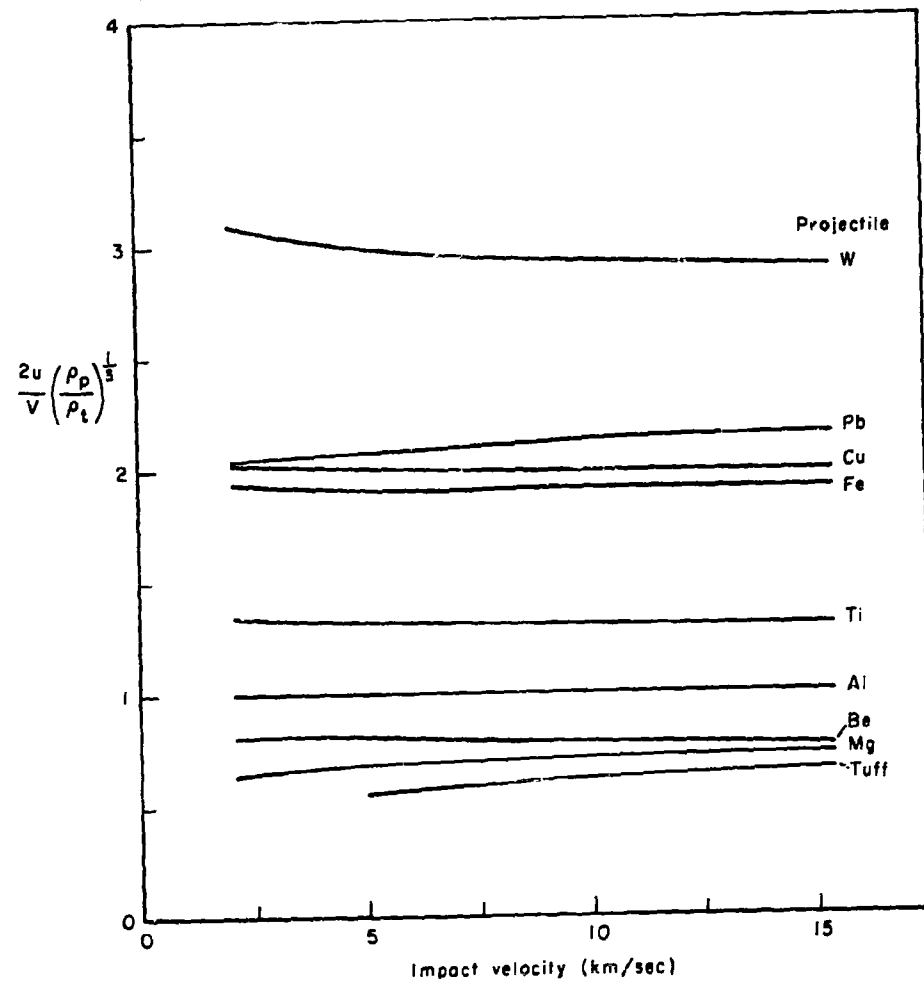


Fig. 17 — Normalized penetration ratios versus impact velocity for aluminum targets

# IMPACT PHYSICAL PROCESSES REVIEW

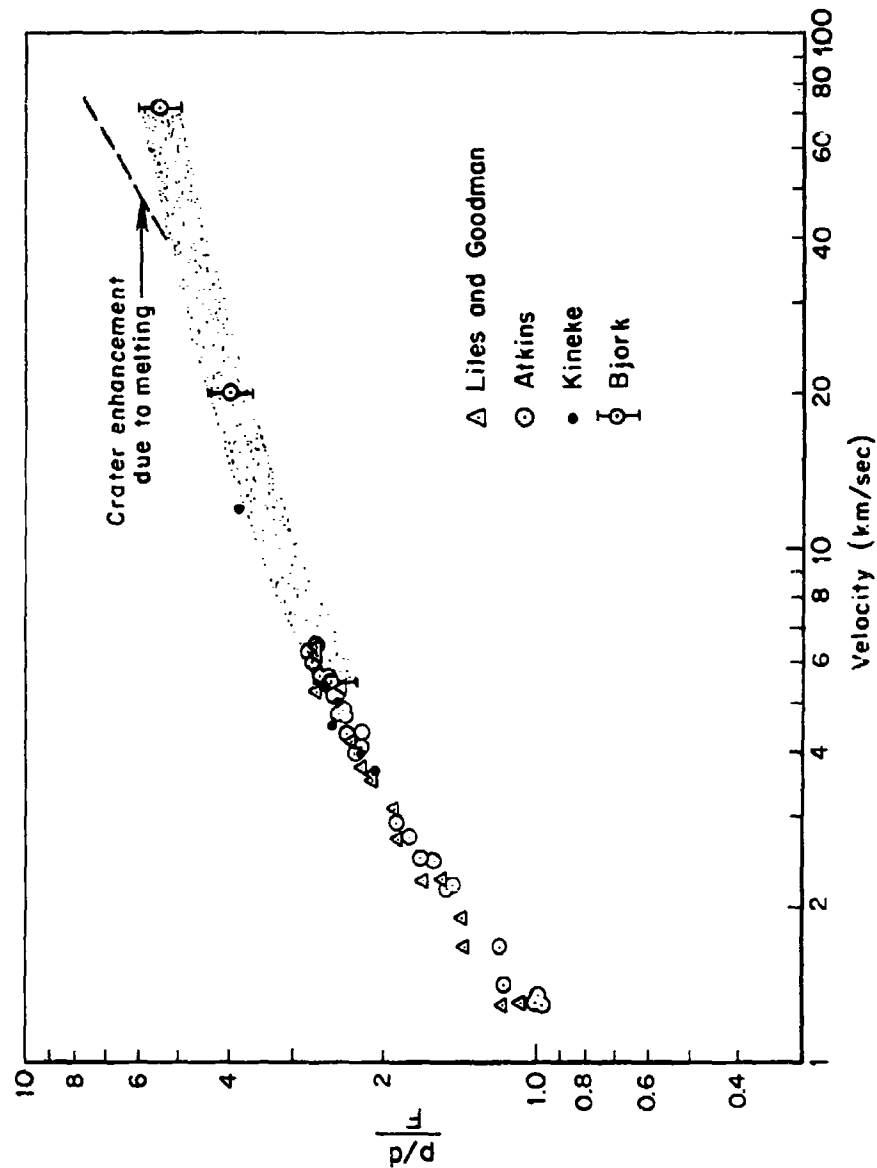


Fig. 18—Dissimilar-material scaling law compared with experimental data for 1100-F aluminum targets. Aluminum projectile points (Atkins) shown unscaled. Copper projectile (Liles and Goodman) and steel projectile (Kineke) points reduced by factor given in Fig. 17

## IMPACT PHYSICAL PROCESSES REVIEW

The preceding constitutes a well-controlled test of the scaling law, since the mass, geometry, and velocity of all the data were well known. In particular, there is an unambiguous characteristic dimension to use for the projectile, namely, the sphere diameter.

The data of Kineke are shown as the dark dots in Fig. 18. While the agreement is apparently good, more treatment was required before plotting. Kineke accelerates flat steel discs by explosive means. The characteristic dimension of these projectiles was taken to be the diameter of the equivalent sphere, that is, the steel sphere which has the same mass as his projectiles. It may be observed that such treatment brings his data into extremely good correspondence with the other two better-controlled sets. The agreement of his fastest point with the theoretical prediction of the author is encouraging.

In Fig. 19 the scaling law is tested for the case of 2024-T3 targets. The data have been treated in the same way, the aluminum projectile points being presented unscaled, and the other projectile points being scaled so as to bring them onto the aluminum curve. The data all lie below the theoretical prediction of the author, as discussed in the section on strength effects. There is more scatter at lower velocities for this target material, but the different data sets are coalescing satisfactorily at the higher velocities.

The shock Hugoniot data for the plastic projectiles are not available at the experimental velocities shown, so that  $\beta$ -scaling was required. At 7 to 10 km/sec. the data for plastic, aluminum, and steel projectiles--materials that span a large part of the projectile-material spectrum--are brought together satisfactorily.

# IMPACT PHYSICAL PROCESSES REVIEW

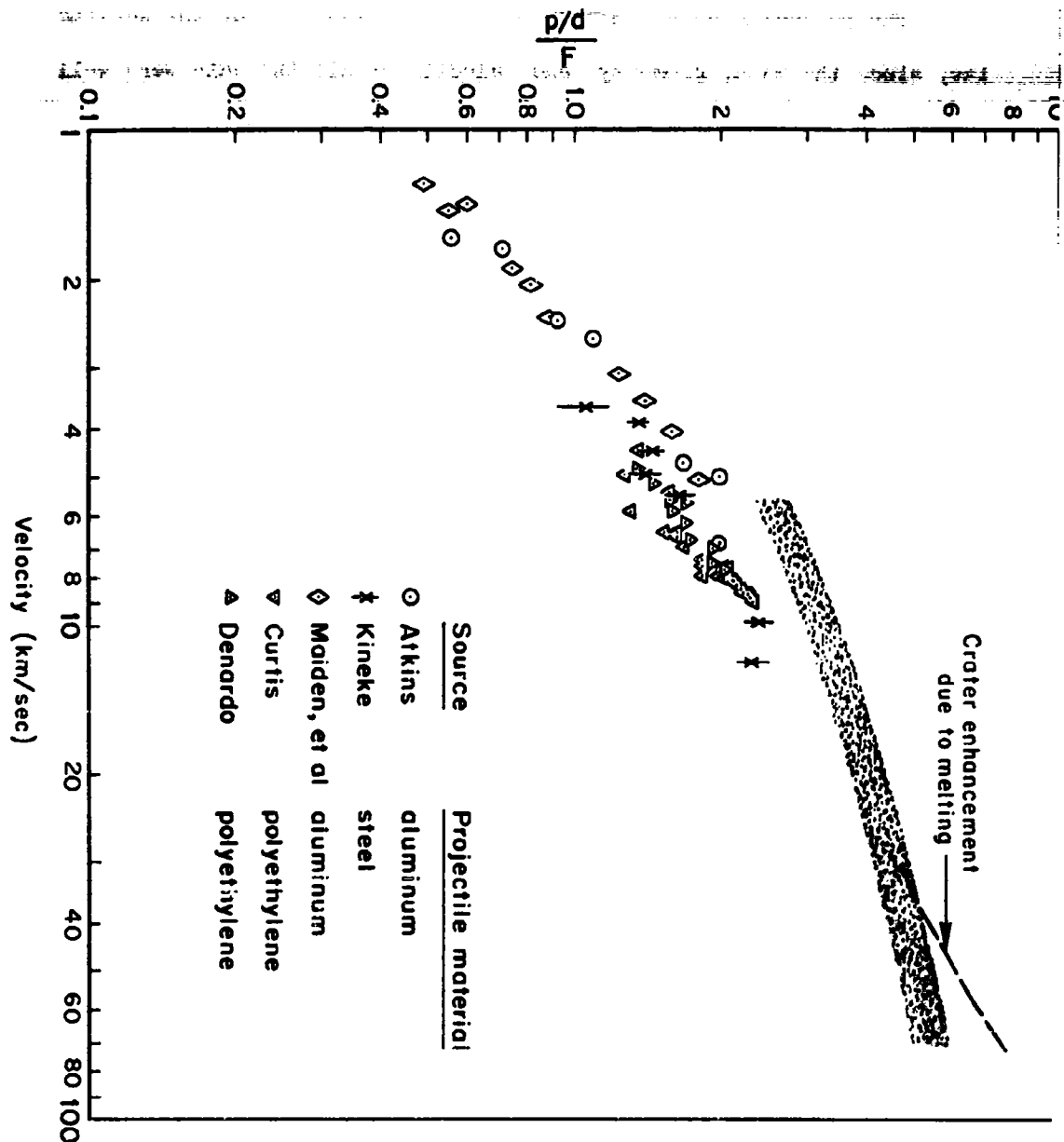


Fig. 19 — Dissimilar-material scaling law compared with experimental data for 2024-T3 targets.

Aluminum points are presented unscaled.

Steel points reduced by factor given in Fig. 17.

Polyethylene points increased by factor given in Fig. 16



## IMPACT PHYSICAL PROCESSES REVIEW

It is believed that using the theoretical predictions of the author for aluminum-aluminum and iron-iron impacts and deriving the penetrations of other projectile materials in these targets by means of the scaling law just discussed will give an accurate estimate of any projectile penetration into these structural materials up to a velocity of 20 km/sec. Above that velocity, the possible effects of target melting must be taken into account.

## IMPACT PHYSICAL PROCESSES REVIEW

### REFERENCES

1. Bjork, R. L., and A. E. Olshaker, A Proposed Scaling Law for Hypervelocity Impacts Between a Projectile and a Target of Dissimilar Material, The RAND Corporation, RM-2926-PR (to be published).
2. Eichelberger, R. J., and J. W. Gehring, "Effects of Meteoroid Impacts on Space Vehicles," ARS J., Vol. 32, No. 10, October 1962, p. 1583.
3. Atkins, W. W., Proceedings of the Fourth Symposium on Hypervelocity Impact, Air Proving Ground Center, Air Research and Development Command, Eglin Air Force Base, Florida, September 1960.
4. Liles, C. D., and J. H. Goodman, Particle-Solid Impact Phenomena, Arnold Engineering Development Center, AEDC-TDR-62-202, November 1962.
5. Bjork, R. L., Effects of a Meteoroid Impact on Steel and Aluminum in Space, The RAND Corporation, P-1662, December 16, 1958.
6. Collins, R. D., Jr., and W. H. Kinard, The Dependency of Penetration on the Momentum Per Unit Area of the Impacting Projectile and the Resistance of Materials to Penetration, NASA TN D-238, May 1960.
7. Halperson, S. M., and W. W. Atkins, Proceedings of the Fifth Symposium on Hypervelocity Impact, Colorado School of Mines, Golden, Colorado (Host organization), November 1961.
8. Bjork, R. L., and A. E. Olshaker, The Role of Melting and Vaporization in Hypervelocity Impact, The RAND Corporation, RM-3490-PR (to be published).

**GENERAL ATOMIC**  
DIVISION OF  
**GENERAL DYNAMICS**

JOHN JAY HOPKINS LABORATORY FOR PURE AND APPLIED SCIENCE  
P.O. BOX 608, SAN DIEGO 12, CALIFORNIA

GA-3827

**HYDRODYNAMICS OF HYPERVELOCITY IMPACT\***

by

J. M. Walsh and J. H. Tillotson

\*This research is a part of Project DEFENDER, sponsored  
by the Advanced Research Projects Agency, Department of Defense.

Air Force Special Weapons Center  
Air Force Systems Command  
Contract AF29(601)-4759  
Advanced Research Projects Agency  
ARPA Order No. 251-61

# HYDRODYNAMICS OF HYPERVELOCITY IMPACT

## CONTENTS

I. INTRODUCTION . . . . .	62
II. THE CONSTITUTIVE EQUATIONS; SIMPLE LINEAR SCALING . . . . .	64
III. EQUATIONS OF STATE . . . . .	66
IV. A TYPICAL IMPACT AND RELEVANT CODE CONSIDERATIONS . . . . .	70
V. DIMENSIONAL ANALYSIS; SCALING RELATIONS FOR METALS . . . . .	83
VI. IMPACT ON THICK TARGETS; THE LATE-STAGE ASYMPTOTIC SOLUTION . .	94
VII. CONCLUSION . . . . .	100
REFERENCES . . . . .	104

## HYDRODYNAMICS OF HYPERVELOCITY IMPACT

### ABSTRACT

Numerical techniques have been used to treat the hydrodynamic phase of axisymmetric hypervelocity impact. A series of iron-on-iron impact calculations are discussed in which the projectile velocity and target thickness are each varied over a wide range. An equation-of-state correlation and dimensional analysis then lead to a general description of like-metal impacts. Further, an observed late time asymptotic solution within the stages of the interaction for which the hydrodynamic approximation is valid is used to predict the dependence of crater size upon impact velocity. For velocities between about  $5(10)^5$  and  $2.5(10)^7$  cm/sec crater dimensions increase as the 0.62 power of impact velocity.

# HYDRODYNAMICS OF HYPERVELOCITY IMPACT

## I. INTRODUCTION

At sufficiently high impact velocities the pressures which arise in the early stages of a projectile-target interaction are very large compared to the material yield strength. During this phase of the interaction, it is appropriate to neglect strength of materials and to treat the problem as one in hydrodynamics. A satisfactory description of the material flow in hypervelocity impact must include a realistic equation of state for the target and projectile materials; for the hydrodynamics problem, the necessary equation of state information can be formulated as a relation among the scalar pressure, the density, and the specific internal energy.

In the later stages of the interaction, as the disturbance engulfs more target material, the hydrodynamic pressures become comparable to yield stresses. It is then inappropriate to neglect material strength, and the hydrodynamic approximation ceases to provide a valid solution to the problem. In this case an elastic-plastic material, for example, should be represented by a suitable relation among the stress tensor, the strain tensor, and the specific internal energy; also the yield strength must be specified as a function of the state of the material. Such a formulation would then replace the scalar equation of state that is applicable in the hydrodynamic regime.

A complete material description for all of the states of interest, and its successful application to the impact process, would be very satisfying. Such a program would provide a direct comparison between theoretically determined impact craters and those which have been reported extensively from experimental programs. On the other hand, the hydrodynamic phase of the interaction is considerably less difficult to analyze than the strength-dependent phase. Also, the hydrodynamic equation of state is relatively free from uncertainties in material properties. It therefore seems desirable, both for reasons of simplicity and accuracy, to concentrate first on the hydrodynamic part of the interaction and the conclusions which can be drawn therefrom. The present paper is devoted to this objective. While the hydrodynamic approximation precludes the explicit treatment of the final

## HYDRODYNAMICS OF HYPERVELOCITY IMPACT

stages of crater formation, it nevertheless proves possible to establish relations by which the experimental crater data at attainable velocities can be extrapolated to the highest velocities of interest.

For simplicity, only like-material impacts are considered in the present discussion, and the projectile geometry is kept constant as a right circular cylinder of aspect ratio unity. Several parameters of the system are studied, the most important of which are projectile velocity, the equation of state of the interacting material, and the relative thickness of the target plate.

The basic approach has been to develop and solve numerically a system of finite difference equations which correspond to the appropriate hydrodynamic equations of compressible fluids. This is accomplished by means of the SPEAR hydrodynamic code using the IBM 7090 computer. The Eulerian form of the difference equations, in which the independent space variables define a fixed axisymmetric coordinate system through which the mass moves, has been adopted for solving two-dimensional, time-dependent impact problems. The differencing method consists of dividing the Eulerian space into a finite number of small cells (having rectangular cross sections and axial symmetry) through which the mass, represented by many discrete mass points, moves and interacts in accord with the usual conservation equations and the material equation of state. Pressure, velocity, density, and specific internal energy are given for each cell in periodic printouts; also pictorial displays of the mass distribution and the velocity field or subregions thereof are afforded by computer plotting routines. Solutions obtained with the SPEAR code are in good agreement with available analytical results on flows involving shock and rarefaction waves, the differences being attributed to the above finite difference approximations in the partitioned space and discrete mass representations. The present SPEAR code is the product of a continuing development program to improve the accuracy and economy of two-dimensional hydrodynamic computations. An excellent discussion of the general logic underlying an Eulerian discrete mass point representation is to be found in the PIC literature by F. Harlow and associates.<sup>(1)</sup>

The first reported work on the time-dependent hydrodynamics of impact, other than analytical models based on rough approximations, was

## HYDRODYNAMICS OF HYPERVELOCITY IMPACT

by R. L. Bjork.<sup>(2)</sup> Bjork employed a computational scheme which was similar to the present one and has reported results, in particular, for aluminum projectiles striking aluminum targets and for similar iron-on-iron impacts. The approach differs from the present one, however, in that the hydrodynamic approximation was used to describe the entire interaction, so that strength effects were necessarily invoked somewhat artificially to arrest the flow when pressures became small. This led to a crater size which, for the lowest velocities considered, was actually in fair agreement with high-velocity experimental results. The consequent crater volume, however, was proportional to projectile momentum. The experimental data at high velocities, and also the results of the present investigation, indicate a crater volume which is very nearly proportional to projectile kinetic energy.

Section II of this report is devoted to specifying the appropriate governing equations for impact hydrodynamics. Section III is a discussion of the metallic equations of state that were used in the computations. Section IV is a detailed description of results from a typical impact problem--namely, the interaction of a 4 cm/ $\mu$ sec iron projectile with an iron plate. Section V is an application of dimensional analysis to develop scaling relations by which the known impact hydrodynamics of one metal can be transformed to a general description of like-material impacts. Section VI is devoted to impact on thick targets, with particular emphasis on the late-stage hydrodynamic equivalence and the consequent determination of crater size as a function of velocity. Finally, Section VII consists of some summarizing remarks.

### II. THE CONSTITUTIVE EQUATIONS; SIMPLE LINEAR SCALING

The first step in the analysis of hypervelocity impact is that of defining the important physical processes and associated constitutive equations which should be included in a theory of impact. The neglect of strength, already indicated in the previous discussion, makes possible the use of a simple pressure, density, energy equation of state, and is justified in the present application by the fact that the pressures of interest are typically two or more orders of magnitude greater than yield strengths.



## HYDRODYNAMICS OF HYPERVELOCITY IMPACT

The neglect of thermal conduction is justified by a simple calculation: For a projectile of typical linear dimension  $l$  and velocity  $v_0$ , the time for the hydrodynamic phase of the interaction is of the order  $10l/v_0$ . The thermal diffusion distance in this time, using a typical metal diffusivity of  $h = 0.5 \text{ cm}^2/\text{sec}$ , is of the order  $x = \sqrt{ht} = \sqrt{(0.5) 10l/v_0}$ . Hence, the ratio of diffusion distance to  $l$  is  $x/l = \sqrt{5/v_0 l}$ , and using  $v_0 = 10^6 \text{ cm/sec}$  shows that  $x/l$  is as large as 0.6 only if  $l$  is less than  $5 \times 10^{-4} \text{ cm}$ . For larger projectiles, thermal conduction is not significant as a perturbation to the hydrodynamics.

The magnitude of the viscosity which is appropriate for impact work is much more uncertain than the thermal diffusivity or the yield strength, and the justification for excluding viscous phenomena from the theory is accordingly somewhat less direct. First, very large viscosities can be excluded on the grounds that the consequent thick shock fronts would be observed in shock-wave experiments as a continuous acceleration of the free surface upon shock arrival. Such evidence can lead to the conclusion that viscous phenomena are not important unless projectile dimensions are less than about 0.1 cm, but the considerations leave open the possibility that this critical size may be substantially smaller. A much smaller projectile size for the viscosity threshold is, in fact, indicated by experimental impact data and is discussed in connection with scaling in the following paragraph.

If thermal conduction and viscous effects are negligible within the hydrodynamics, the results are subject to simple linear scaling. Specifically, the solution for a problem in which a typical length  $l$  can be scaled to larger or smaller sizes by the use of a scale factor  $F$  on all lengths and times; i.e.,  $l \rightarrow Fl$ ,  $t \rightarrow Ft$ , and the dependent variables  $P$ ,  $p$ ,  $\bar{u}$  are not affected by the transformation. The validity of simple linear scaling follows directly from the fact that the governing Rankine-Hugoniot and continuous flow equations (below) are homogeneous in the distance and time variables. The inclusion of viscosity or conduction terms, on the other hand, introduces second derivatives in the continuous flow equations and the scaling no longer applies. As has been indicated above, these terms will dominate the interaction for sufficiently small geometries. It is

## HYDRODYNAMICS OF HYPERVELOCITY IMPACT

therefore of interest to inquire whether experimental impact data exhibit departures from simple scaling. The question has been answered by several authors in recent correlations of the available impact data.<sup>(3,4)</sup> Present evidence indicates that the scaling remains valid down to the smallest projectiles studied. Eichelberger and Gehring,<sup>(4)</sup> in particular, cite data for projectile masses ranging from  $10^{-11}$  to 10 grams, or projectile dimensions in the range  $10^{-4}$  to 1 cm. Thus, the present data indicate that viscous phenomena (or thermal conduction) are not seriously affecting impact results for projectiles of  $10^{-11}$  g, i.e., linear dimensions of the order of  $10^{-4}$  cm. It is therefore appropriate to neglect viscosity in the treatment of impact problems involving larger projectiles.

The exclusion of strength, conduction, and viscous effects from the theory leaves us with a hydrodynamics which is composed of shock-wave compressions, satisfying the Rankine-Hugoniot jump conditions, and compressible continuous flow (usually expansions) during which the entropy of a mass element remains constant and the governing equations are:

$$\frac{\partial \rho}{\partial t} + \nabla \cdot (\rho \vec{u}) = 0$$

$$\frac{\partial \vec{u}}{\partial t} + (\vec{u} \cdot \nabla) \vec{u} + \nabla P = 0$$

$$\frac{\partial E}{\partial t} + \vec{u} \cdot \nabla E = -P \left( \frac{\partial V}{\partial t} + \vec{u} \cdot \nabla V \right)$$

The SPEAR hydrodynamics code is formulated for describing such interactions, and results therefrom can be scaled in accordance with the simple linear scaling laws defined above.

### III. EQUATIONS OF STATE

In the present study, materials are subjected to shock pressures which range from a few tenths of a megabar to about 1000 megabars, and are subsequently free to expand as the pressures are relieved by rarefaction waves and by flow divergence. For accurate calculations, it is necessary to have a realistic thermodynamic description of the material for the entire range of interest.

## HYDRODYNAMICS OF HYPERVELOCITY IMPACT

The formulation of a suitable equation of state has been given previously<sup>(5)</sup> by one of the authors. This equation of state has the form

$$P = \left[ a + \frac{b}{\frac{E}{E_0} \eta^2 + 1} \right] E_0 \rho + A\mu + B\mu^2 ,$$

for condensed states of the material, and

$$P = aE\rho + \left[ \frac{bE\rho}{\frac{E}{E_0} \eta^2 + 1} + A\mu e^{-\beta(V/V_0 - 1)} \right] e^{-\alpha(V/V_0 - 1)^2}$$

for expanded states, where  $P$ ,  $E$ ,  $\rho = 1/V$  are pressure, specific internal energy, and density, respectively, and  $\eta = \rho/\rho_0$ ,  $\mu = \eta - 1$ .

The parameters  $\alpha, \beta$  are constants controlling the rate of convergence to the ideal gas form,  $P = aE\rho$ , which is assumed valid for highly expanded states. The other five parameters are different for each material and are chosen to provide good agreement with experimental shock-wave data at low pressures and, at high pressures, with theoretical results obtained by Cowan from the Thomas-Fermi-Dirac model of the atom. The equation-of-state results for aluminum are plotted as Figs. 1 and 2. Other metals for which the equation of state has been formulated are W, Cu, Fe, Be, Ti, Ni, Mo, and Th.

A simple approximate representation of vaporization is given by an appropriate choice of the states to be represented by the condensed and expanded formulations. The condensed form is used for all states  $V < V_0$ , and also for  $V_s > V > V_0$  provided  $E \leq E_s$ . Here,  $V_s$  is the specific volume and  $E_s$  is the specific internal energy for the liquid at the  $P = 0$  vaporization point. The expanded formulation is employed for the remaining states  $V > V_0$ ,  $E > E_s$ . The representation leads correctly to an infinite expansion when shock-heating is sufficient to cause vaporization. A similar distinction between solid and liquid is unnecessary in the present hydrodynamics approximation.

In the case of iron, a polymorphic transition at low pressure (0.13 megabars) has been ignored in the equation-of-state formulation.

# HYDRODYNAMICS OF HYPERVELOCITY IMPACT

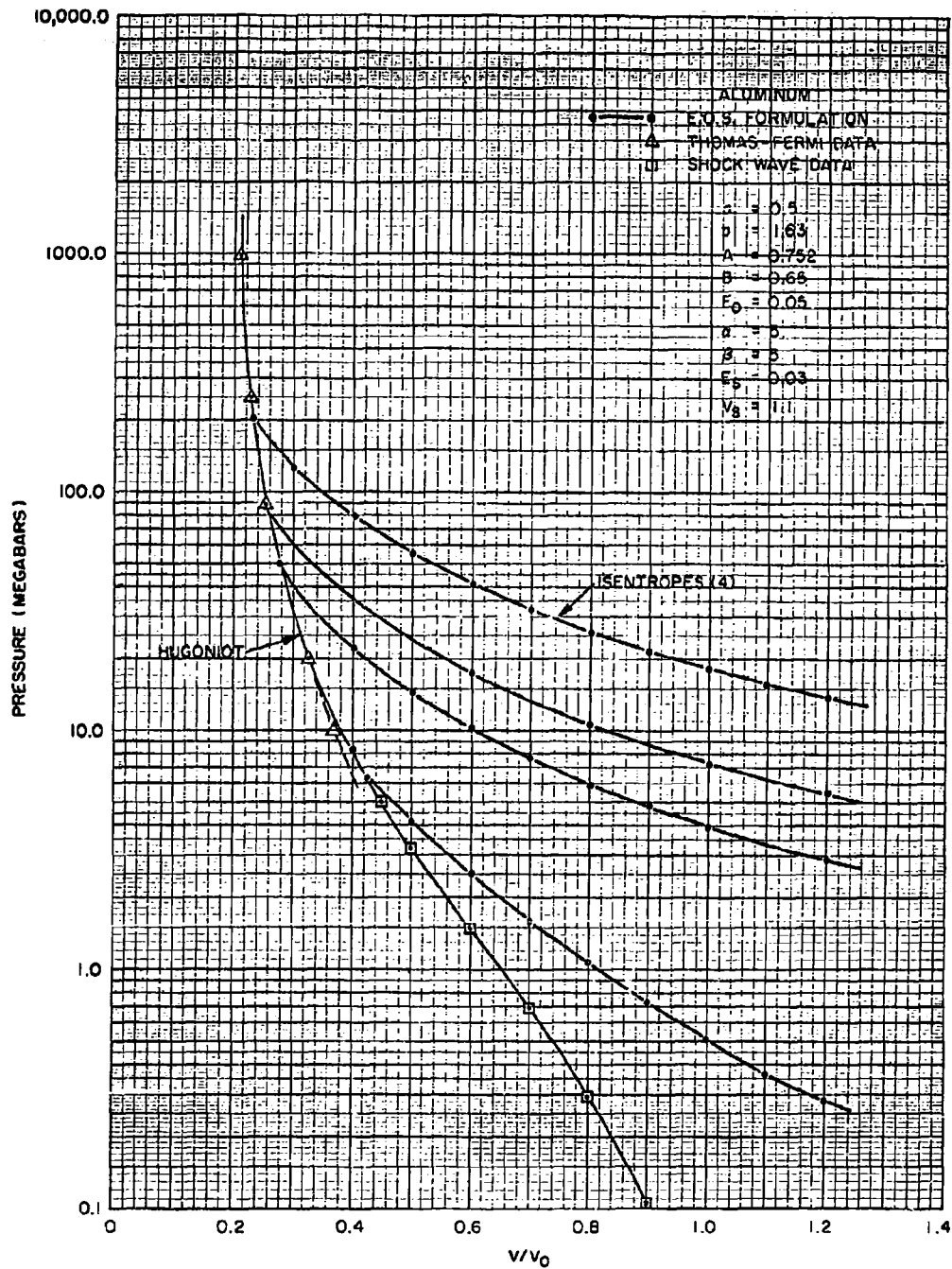


Fig. 1--Hugoniot curve and isentropes for aluminum

# HYDRODYNAMICS OF HYPERVELOCITY IMPACT

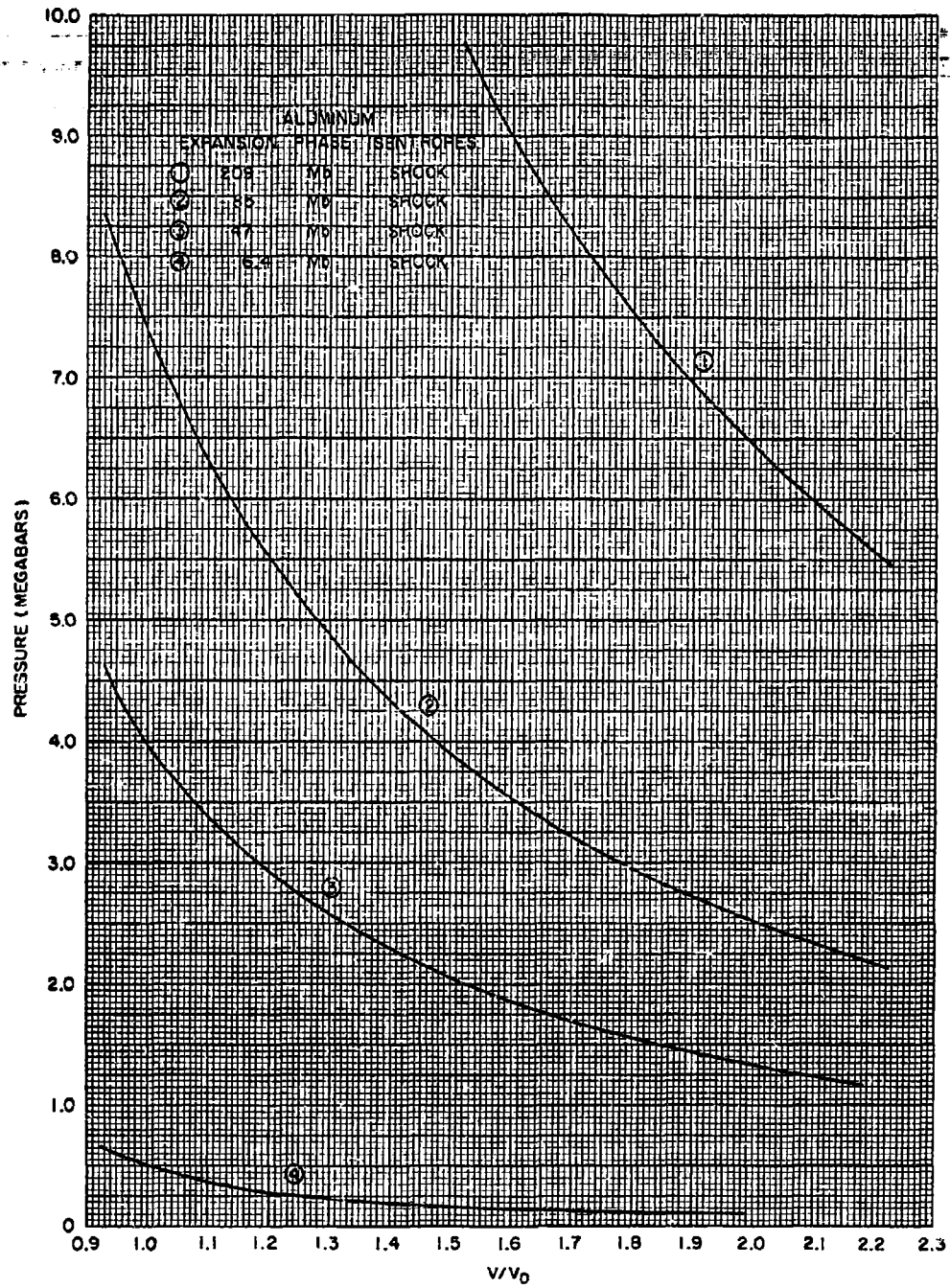


Fig. 2--Isentropes for aluminum

## HYDRODYNAMICS OF HYPERVELOCITY IMPACT

Experimental shock-wave data between about 0.3 megabars and 5 megabars and Thomas-Fermi-Dirac results at higher pressures are, however, reproduced by the present formulation. While the polymorphic transition is known to lead to interesting effects which are peculiar to iron, these do not occur at the high pressures (0.5 megabars and above) of interest in the present investigation.

### IV. A TYPICAL IMPACT AND RELEVANT CODE CONSIDERATIONS

The typical impact of a cylindrical iron pellet, having a diameter (1.842 cm) equal to its length, and an iron target, having a thickness of several pellet diameters, is shown for various times as Figs. 3 through 10. The left-hand border of each figure is the axis of symmetry, which coincides with the projectile's line of flight. In this problem, the impact velocity is 4 cm/ $\mu$ sec and is positive upward. For each time shown, there are two pictures, one of which gives the mass distribution as discrete points and the other shows the corresponding velocity field. Both representations are superimposed on a rectangular grid, through which the mass particles are moved in accord with the usual energy, momentum, and mass conservation equations and the equation of state. The problem is solved numerically with the SPEAR code, which relates these equations, expressed in conservative finite difference form, to the system of cylindrical cells of rectangular cross section defined by the grid. Complete energy conservation has been of great value in the code development program and provides a continuous energy check during computation for detecting instability and round-off errors. All of the quantities entering the difference equations are averages over the corresponding cell volume and may be considered as representing the values at the geometrical center of the cell.

Two rather important parameters which influence the accuracy of the results are the number of discrete mass points per cell and the relative size of the cells. In zoning a problem, the number of particles per cell in an initial configuration can range from 1 to 81. Maximizing this quantity, although desirable for optimum mass resolution, is usually prohibitive because of increased computing time and resulting higher costs. Sufficient accuracy in the present investigation has been obtained by using

## HYDRODYNAMICS OF HYPERVELOCITY IMPACT

### Figs. 1 through 10

Several stages in the impact of a 4 cm/ $\mu$ sec iron projection on an iron plate. In each stage both the mass distribution and velocity field (plotted as vectors from cell centers) are shown. Note that the velocity plot is depicted on a slightly enlarged space scale. Times for the various pictures are:

	<u>TOP</u>	<u>BOTTOM</u>
Fig. 3	0.0 $\mu$ sec	0.21 $\mu$ sec
Fig. 4	0.42	0.63
Fig. 5	0.84	1.04
Fig. 6	1.25	1.46
Fig. 7	1.66	1.88
Fig. 8	2.26	3.02
Fig. 9	3.81	4.60
Fig. 10	5.39	6.18

In these and the subsequent plots of mass and velocity distributions, the interaction is axisymmetric about the left-hand axis, and the projectile strikes the plate from below.

# HYDRODYNAMICS OF HYPERVELOCITY IMPACT

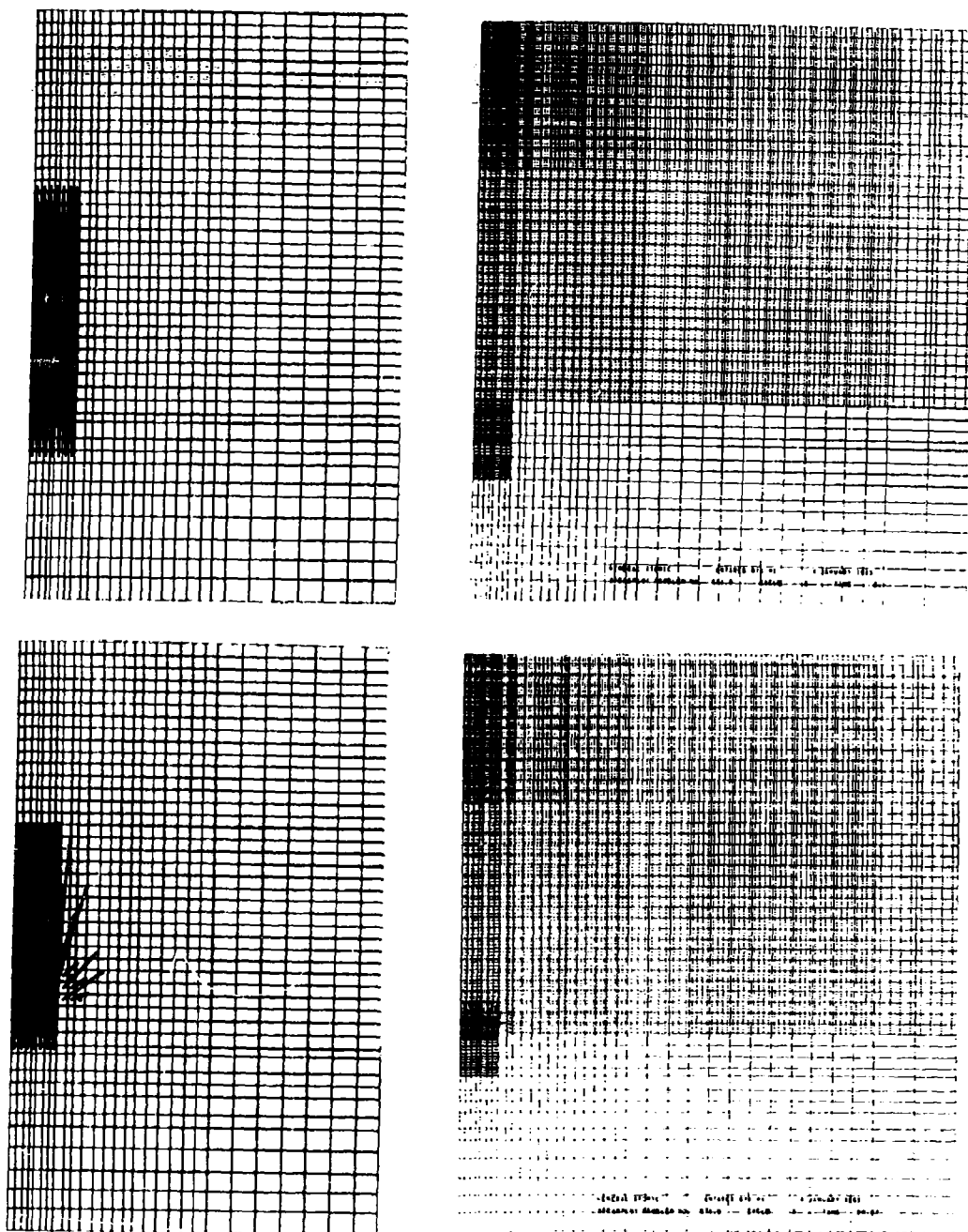


Fig. 3



# HYDRODYNAMICS OF HYPERVELOCITY IMPACT

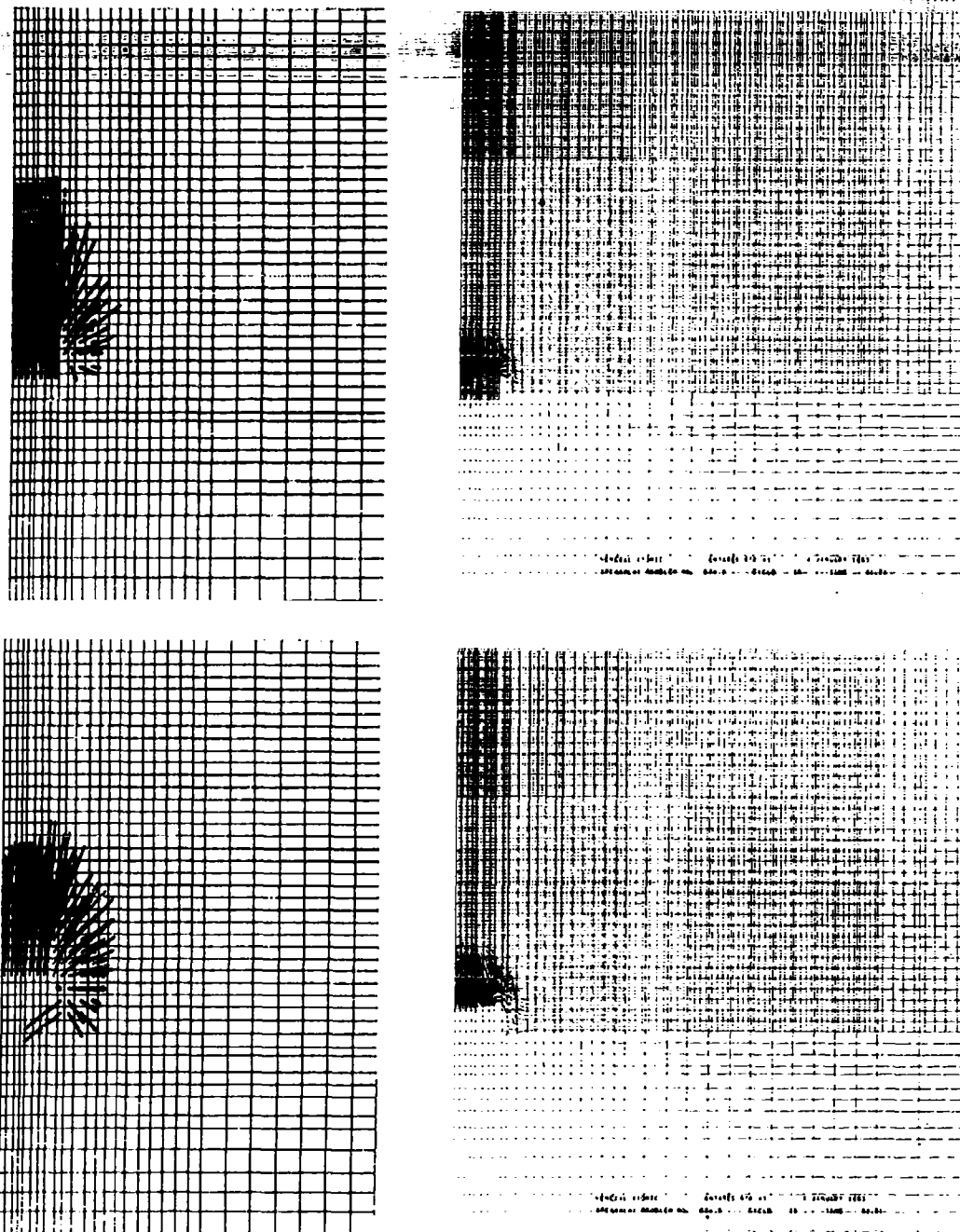


Fig. 4

# HYDRODYNAMICS OF HYPERVELOCITY IMPACT

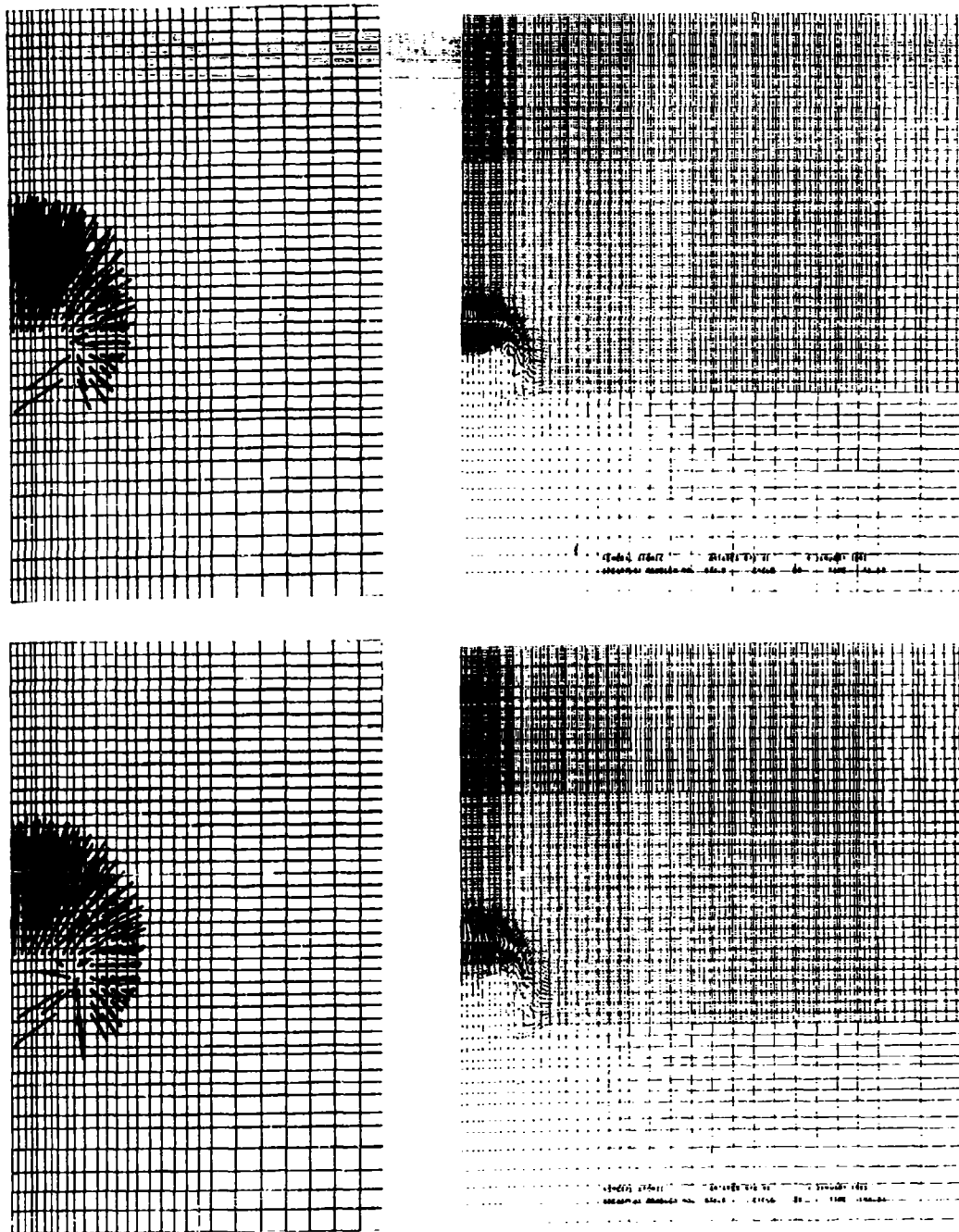


Fig. 5

# HYDRODYNAMICS OF HYPERVELOCITY IMPACT

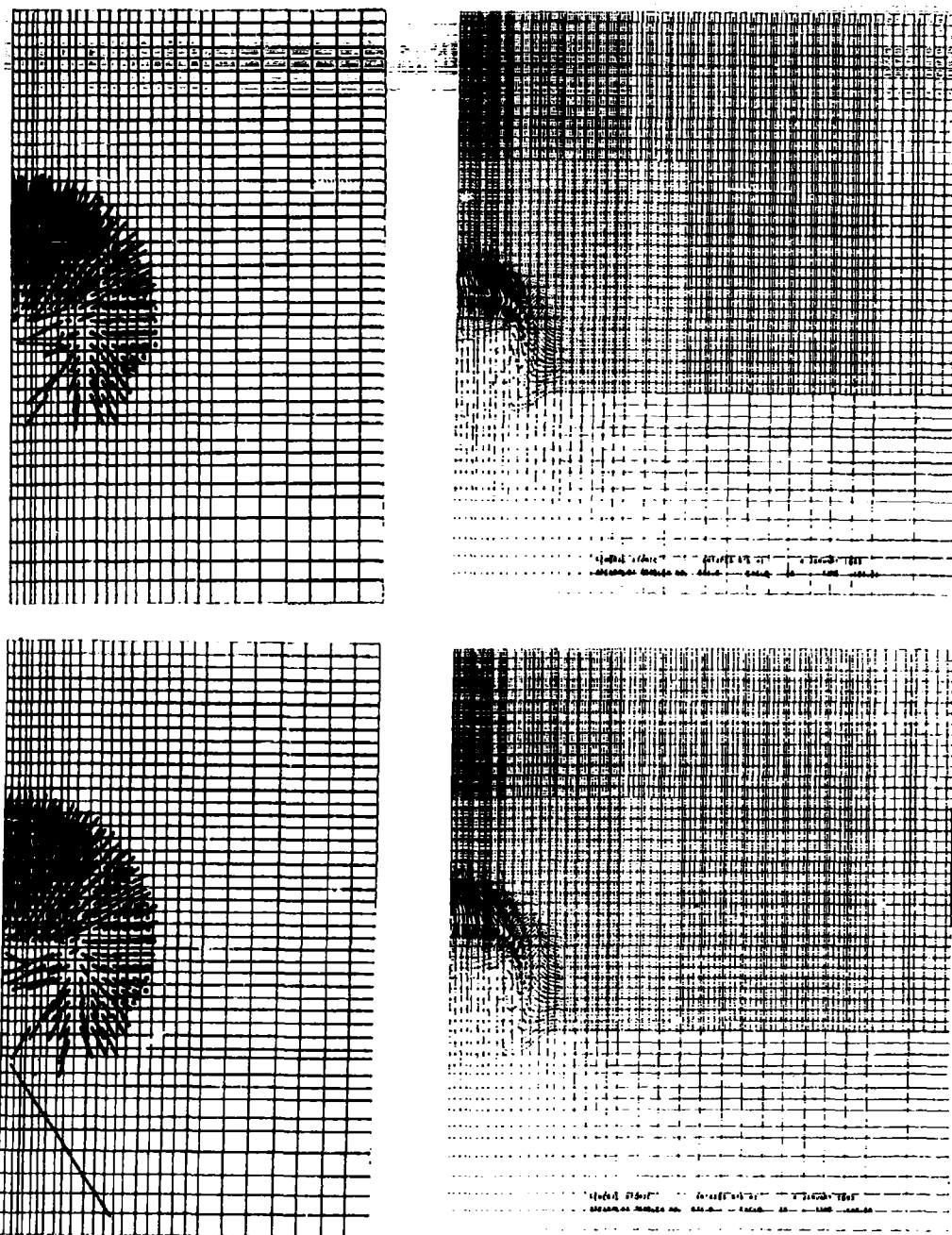


Fig. 6

# HYDRODYNAMICS OF HYPERVELOCITY IMPACT

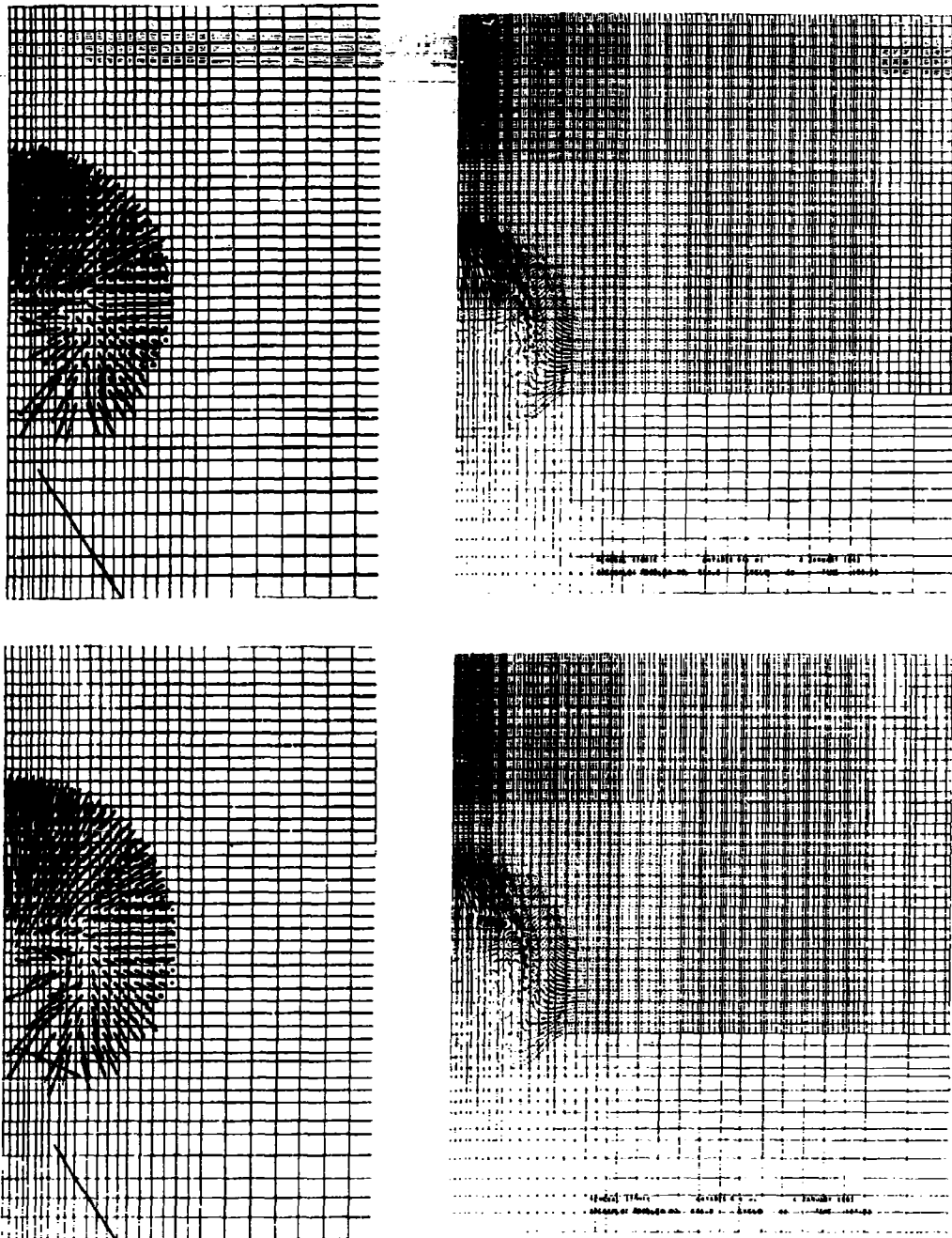


Fig. 7

# HYDRODYNAMICS OF HYPERVELOCITY IMPACT

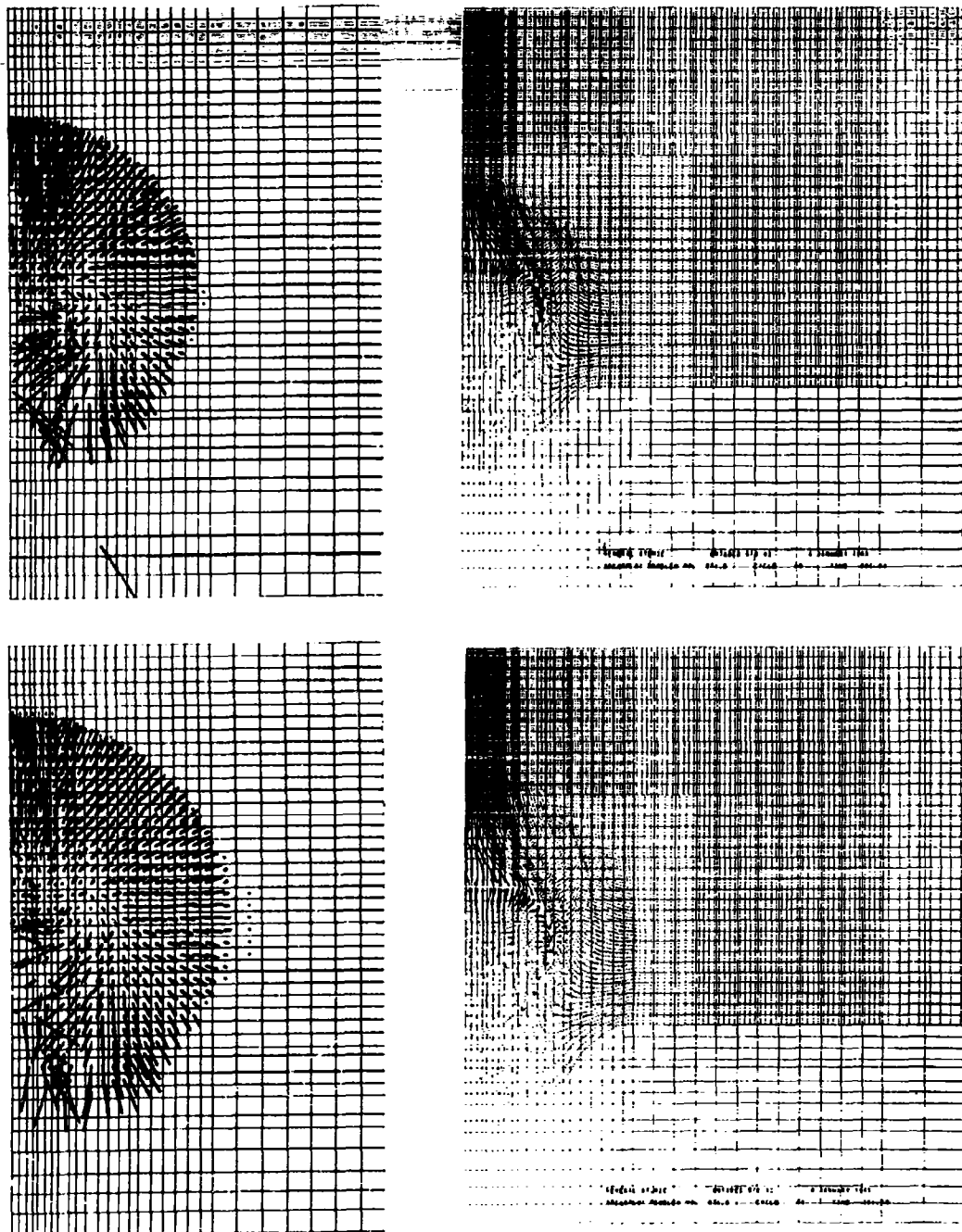


Fig. 8

# HYDRODYNAMICS OF HYPERVELOCITY IMPACT

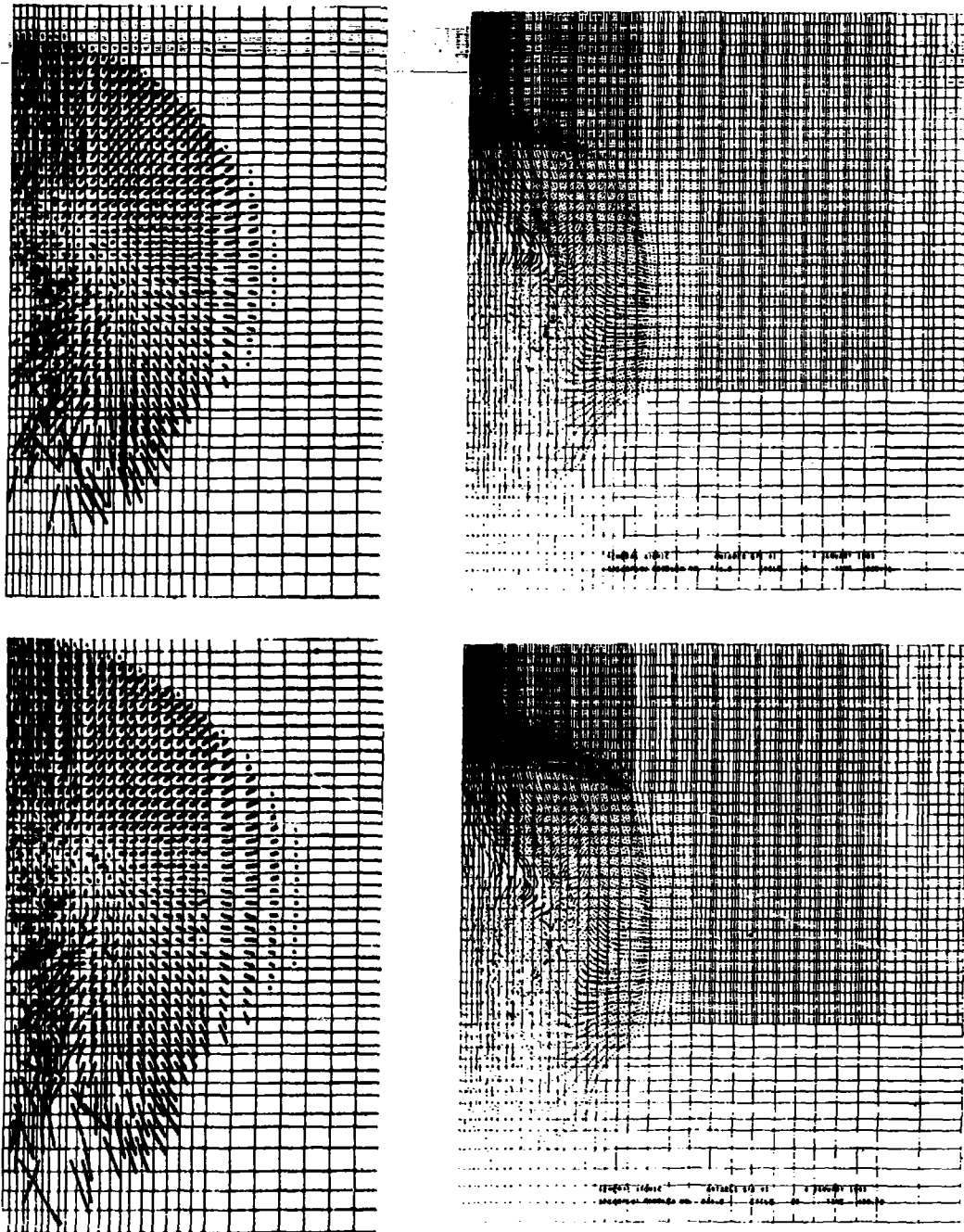


Fig. 9

# HYDRODYNAMICS OF HYPERVELOCITY IMPACT

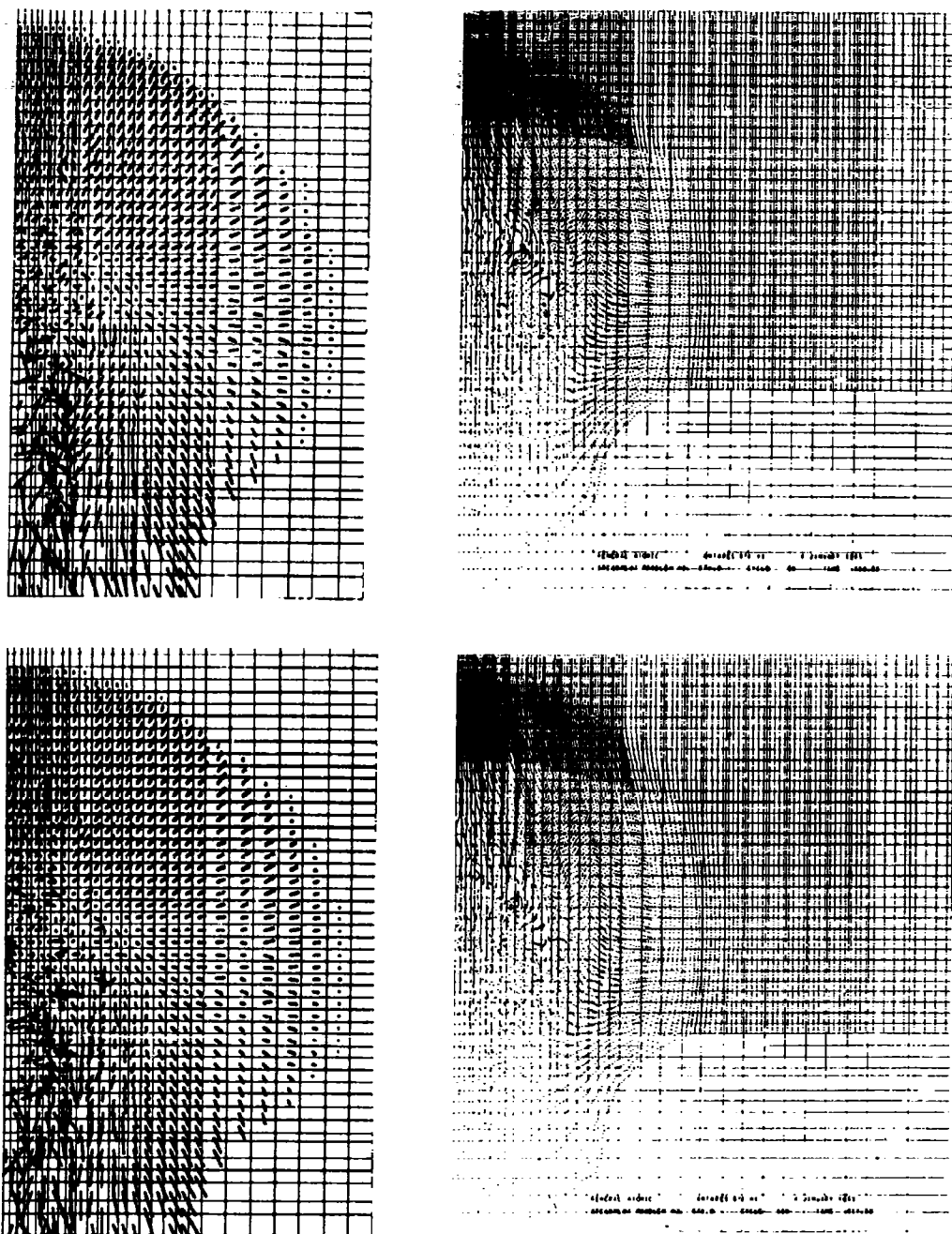


Fig. 10

## HYDRODYNAMICS OF HYPERVELOCITY IMPACT

from 4 to a maximum of 16 particles per cell. The 4-cm/ $\mu$ sec problem required only 1.75 hours on the IBM 7090 computer to reach the 7- $\mu$ sec time in the flow. At the state of maximum compression, the problem has a shock strength of 48 megabars and agrees to 5% with theoretical plane-wave predictions. The plane-wave theory, however, is relevant for comparison only so long as the flow is not influenced by rarefaction waves. As indicated by the velocity fields of Fig. 4, lateral rarefactions reach the center of the projectile at about 0.5  $\mu$ sec.

The maximum number of cells in the current version of SPEAR cannot exceed 2000, but cells can be of different sizes by zoning with variable  $\Delta r$  and  $\Delta z$  spacing. If variable zoning is required, the best results are obtained when the aspect ratio of adjacent cells varies by no more than a factor of two. One zoning technique, used successfully throughout the current investigation, is to zone the cells in the target on a nearly equal area basis within several pellet diameters of the impact center, thus providing uniform space resolution in the more important regions of the flow.

At the time of impact, shock waves are transmitted in both directions from the projectile-target interface. By the time the shock wave traverses the projectile, the projectile is completely embedded in the target, and (as suggested by simple plane-wave considerations) the energy at this time is approximately half kinetic and half internal and is distributed over a mass which is twice that of the initial projectile. This state of maximum compression is then relieved by means of rarefaction waves from the free surfaces and by spherical divergence within the target. The expanding shock wave can be seen in the figures as moving well ahead of the actual crater cavity and lip formation. The pressure profiles that define the shock front are shown for several times as Fig. 11. A more extensive plot of the shock wave attenuation is presented as Fig. 12, which shows the peak shock strength as a function of distance from the impact center.

The analysis in the following two sections makes frequent use of certain radial and axial momenta which are produced by the impact. The axial momentum is defined as the sum  $\sum m_i v_i$  over all cells  $i$  for which the axial component of velocity  $v_i$  is positive. This momentum is initially that of the projectile, and typically increases more than an order of magnitude during the hydrodynamic phase of the interaction. The radial



# HYDRODYNAMICS OF HYPERVELOCITY IMPACT

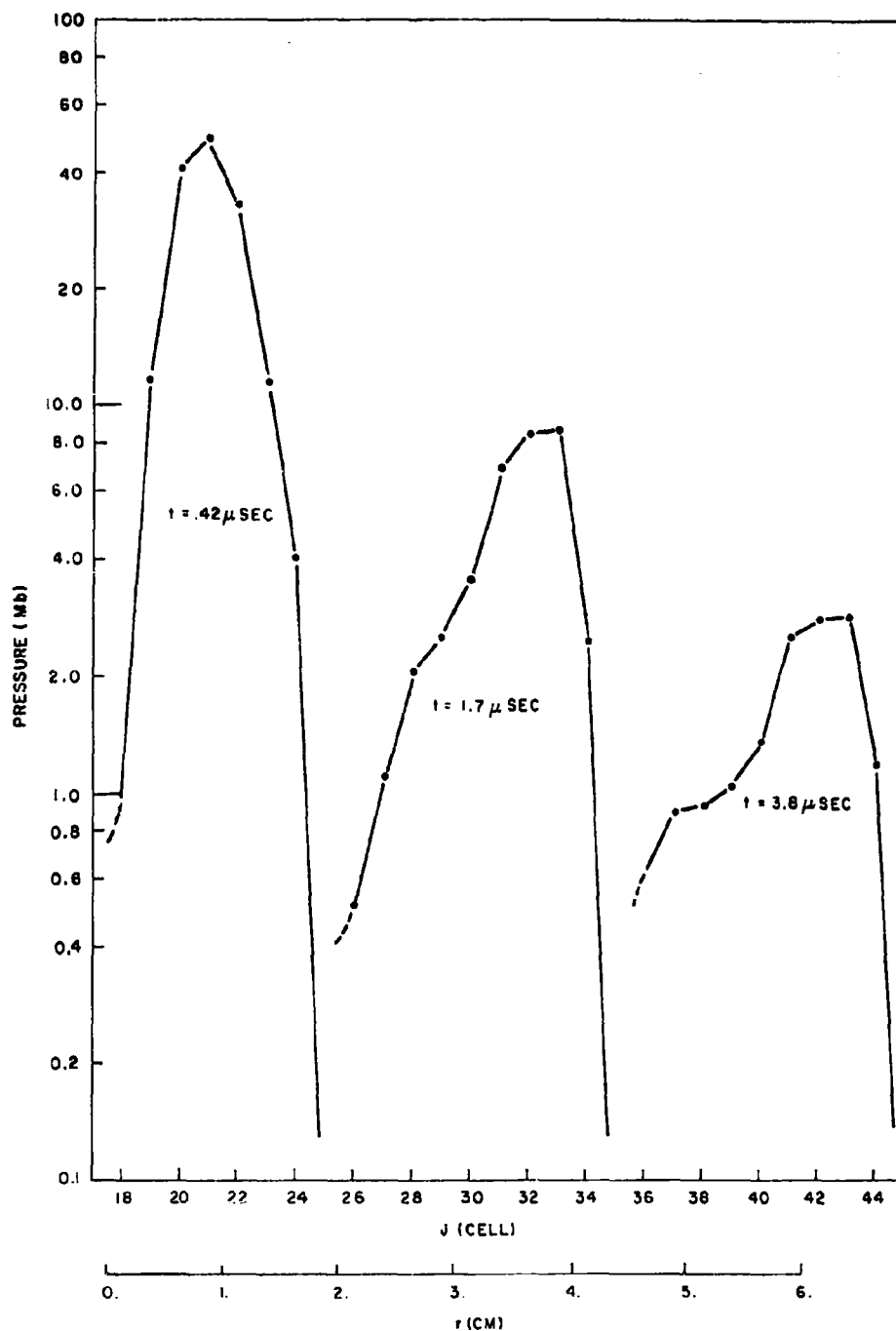


Fig. 11--Pressure versus distance along axis at three successive times in the 4 cm/ $\mu\text{sec}$  problem

# HYDRODYNAMICS OF HYPERVELOCITY IMPACT

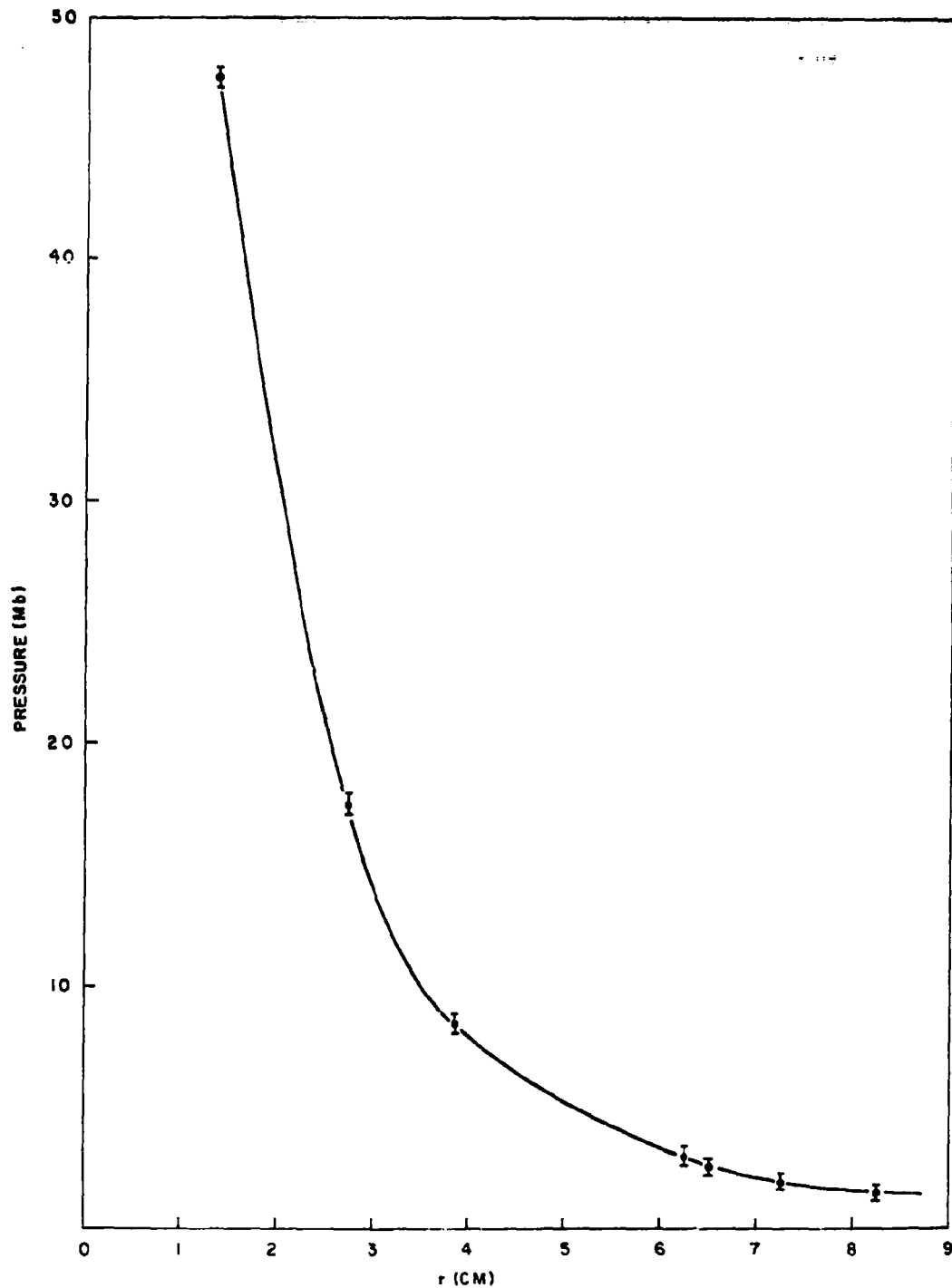


Fig. 12--Shock pressure as a function of distance along axis  
in the 4 cm/ $\mu$ sec problem

## HYDRODYNAMICS OF HYPERVELOCITY IMPACT

momentum is analogously defined as  $\sum m_1 u_1$  for cells in which  $u_1 > 0$ , the summation being further restricted to cells  $z > 0$  within the original front surface of the target. The radial and axial momenta for the 4 cm/ $\mu$ sec problem are plotted as Fig. 13. These integrated momenta provide precise measures of the magnitude of the impact disturbance and have been especially useful in the quantitative comparisons of interactions.

Many other properties of the interaction are provided by SPEAR in regular data printouts. The data presented in the present section are typical of the results which are obtainable from the several volumes of listings, which include individual cell quantities as a function of time.

### V. DIMENSIONAL ANALYSIS; SCALING RELATIONS FOR METALS

In order to avoid the necessity of treating each new material individually, it is desirable to establish (approximate) scaling relations by which the known solutions for one metal can be transformed to any other metal. The success of such an undertaking depends upon whether the individual equations of state can be expressed in a dimensionless form that is essentially the same for all metals. To this end, a natural choice of dimensionless variables is  $p = P/\rho_0 c_0^2$ ,  $\Phi = 1 - V/V_0$ , and  $e = E/c_0^2$ . Similarly, velocities of interest are made dimensionless by dividing by  $c_0$ , so that shock-wave velocity and shock-particle velocity, respectively, are  $D/c_0$  and  $v/c_0$ . Here,  $c_0$  is defined by  $c_0^2 = (\partial P/\partial \rho)_s$  evaluated at  $P = 0$ .

The consequent correlation of the Hugoniot curves of the various metals is seen as Fig. 14, where the dimensionless pressure  $p$  is plotted against shock-particle velocity  $v/c_0$ . For the nine metals, the curves agree with a mean curve (e.g., Fe or Ni) to about  $\pm 7\%$ . The same agreement would be obtained by plotting the shock-wave velocity  $D/c_0$  or the compression  $\Phi$  against  $v/c_0$ , since  $D/c_0 = p/(v/c_0)$  and  $\Phi = (v/c_0)^2/p$  from the Rankine-Hugoniot equations. A plot of  $\Phi$  versus  $p$  would show a  $\pm 10\%$  agreement with the  $\Phi$  indicated by a mean curve.

The above correlation is sufficiently accurate to be useful, and the present paragraph is devoted to a discussion of the associated physical similarity of impacts: The only properties identifying a specific metal in the correlation are  $\rho_0, c_0$ . Thus, for a family of geometrically similar

# HYDRODYNAMICS OF HYPERVELOCITY IMPACT

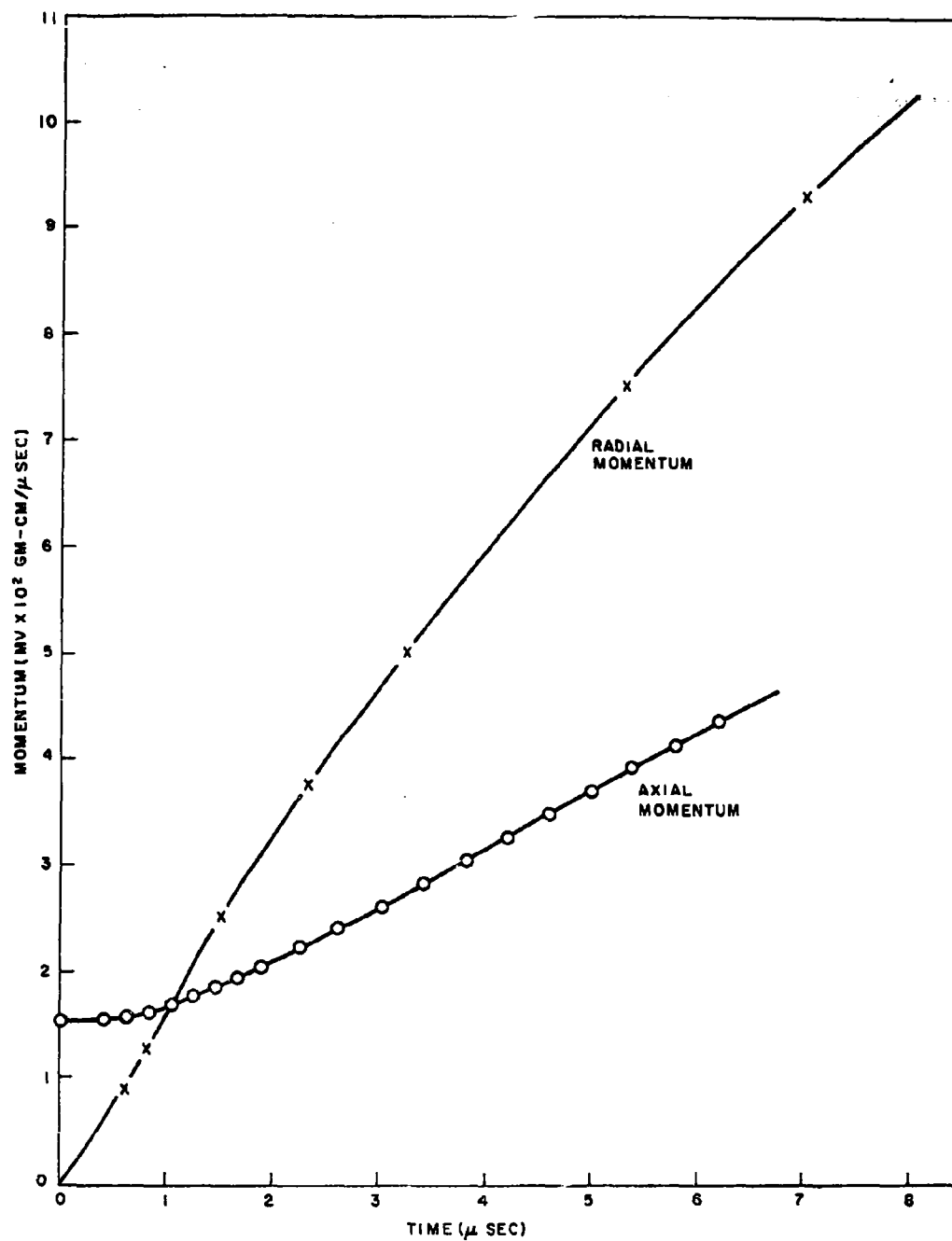


Fig. 13--Axial and radial momenta, 4 cm/ $\mu\text{sec}$  problem

# HYDRODYNAMICS OF HYPERVELOCITY IMPACT

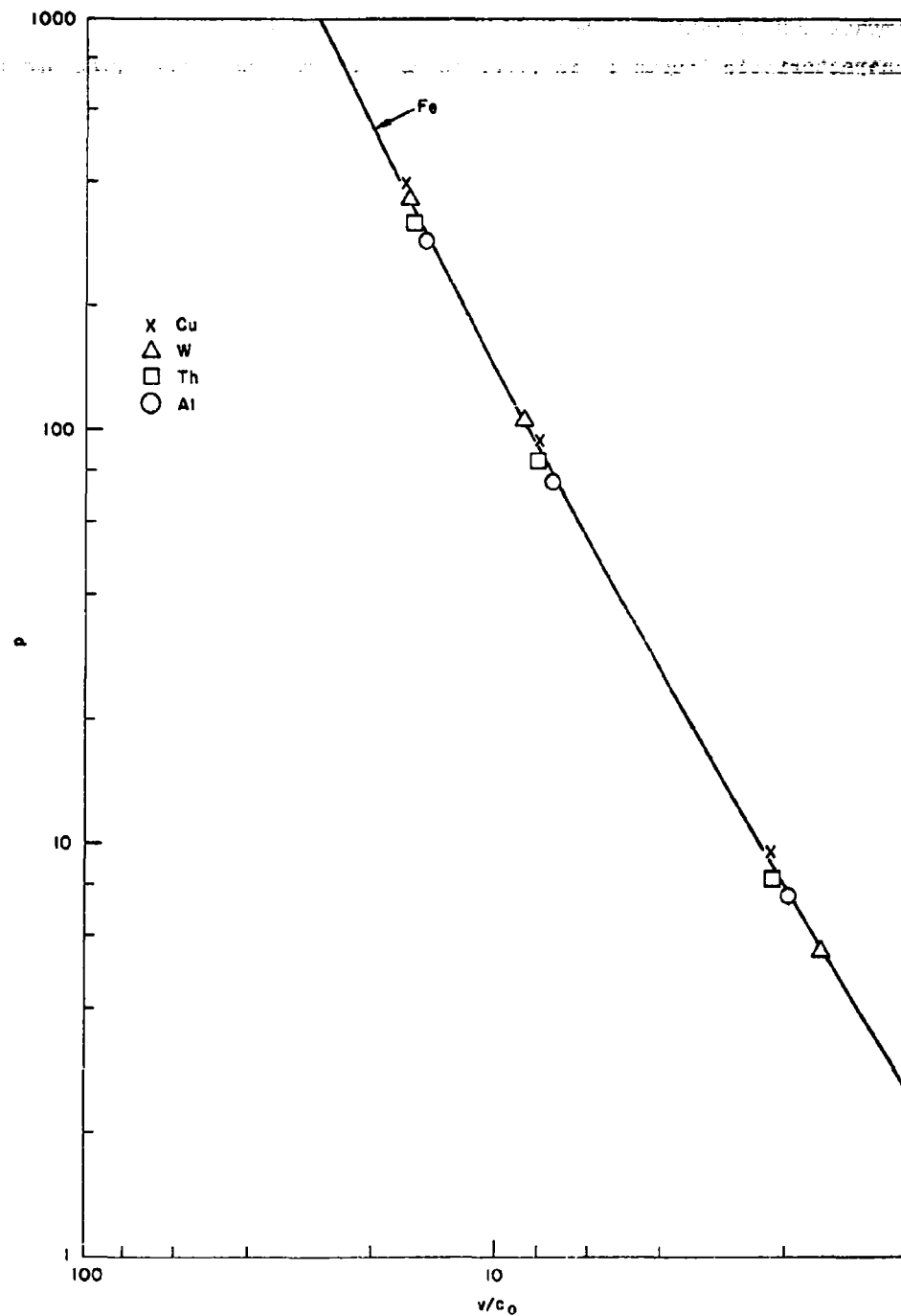


Fig. 14--Pressure versus shock-particle velocity in dimensionless variables; data for Be, Mo, Ni, and Ti are not plotted, but lie within extremes indicated by the Cu and Th points

## HYDRODYNAMICS OF HYPERVELOCITY IMPACT

impact configurations, one needs  $\rho_0$ ,  $c_0$ , the impact velocity  $v_0$ , and some characteristic length  $l_0$  in order to have a completely specified problem. The solution for a given dependent variable must then be some function of  $\rho_0$ ,  $c_0$ ,  $v_0$ ,  $l_0$  and the independent variables  $z$ ,  $h$ ,  $t$ . The condition that the solution be dimensionally correct restricts this functional dependence to the special forms:

$$P/\rho_0 c_0^2 = f_1 \left( \frac{v_0}{c_0}, \frac{z}{l_0}, \frac{r}{l_0}, \frac{tc_0}{l_0} \right),$$

$$u/c_0 = f_2 \left( \frac{v_0}{c_0}, \frac{z}{l_0}, \frac{r}{l_0}, \frac{tc_0}{l_0} \right),$$

$$v/c_0 = f_3 \left( \frac{v_0}{c_0}, \frac{z}{l_0}, \frac{r}{l_0}, \frac{tc_0}{l_0} \right),$$

$$\rho/\rho_0 = f_4 \left( \frac{v_0}{c_0}, \frac{z}{l_0}, \frac{r}{l_0}, \frac{tc_0}{l_0} \right).$$

Thus, impacts which are initially geometrically similar, and for which the projectile "Mach number"  $v_0/c_0$  are the same, have the same solution in dimensionless variables; i.e.,  $P/\rho_0 c_0^2$ ,  $u/c_0$ , etc., are the same in two such impacts for the same values of  $z/l_0$ ,  $r/l_0$ ,  $tc_0/l_0$ . It is therefore a straightforward matter to transform the known solution for one metal to the solution of an equivalent problem for another metal. Similarly, a complete determination (various geometries and all  $v_0/c_0$ ) of the impact hydrodynamics for one metal provides a basis for the general hydrodynamic description of like-material impact.

The above scaling relations are, of course, approximate insofar as the agreement among the individual equations of state is approximate. The task of evaluating the accuracy of the scaling relations by direct consideration of errors in the equation-of-state correlation is, however, quite tedious. Instead, several computations have been made for impact problems which should be the same under the proposed scaling. The comparison of computed results with those obtained by scaling then affords a direct test

## HYDRODYNAMICS OF HYPERVELOCITY IMPACT

of the accuracy of the scaling relations. The results of these comparisons are discussed in the following paragraphs.

Three problems were computed in which a 1-cm diameter by 1-cm long cylindrical projectile strikes a plate of 1-cm thickness. Materials in the three problems were W, Fe, and Al. Impact velocities for the interactions were  $10^7$ ,  $10^7$  and  $1.3 \times 10^7$  cm/sec, in proportion to the respective  $c_0$  of the materials. Several stages in the W-W interaction are shown as Fig. 15. Of particular interest in the present section, however, are tests of the scaling relations which are afforded by the problems: Initial shock pressures for the W, Fe, and Al are 662, 266, and 149 megabars, respectively. When divided by the  $\rho_0 c_0^2$  from the equation-of-state formulations, the corresponding reduced pressures 215, 208, and 199 agree to about 8%. Further, the flow configurations at corresponding times ( $= tc_0/l_0$ ) are reproduced as Fig. 16, where the interactions are seen to be almost identical. Finally, the total positive momenta, ( $\sum_i v_i$  summed over all cells for which  $v_i$  is positive) have been computed as a function of time. The curve for Fe is plotted in Fig. 17, where also the curves obtained by straightforward scaling of the Al and W data are plotted for comparison. The curves agree within about 5%.

An additional comparison was made for Fe and Al in which the plate thickness was 5 cm, other problem parameters being the same as in the above series. Comparisons of the flow configurations at corresponding times are given as Figs. 18 and 19. Momentum curves from the two problems are plotted as Fig. 20. Agreement is comparable to that indicated above for the thin-plate impacts.

In the present investigation, iron has been studied more extensively than any other metal. In general, the above tests of the scaling relations indicate that the results from the computations for iron can be transformed to other metals with an uncertainty of some 5% or less in most quantities of interest. This accuracy is sufficient for most applications, and the scaling relations will be used to generalize the computed results.

A final remark may be made in connection with a possible modification of the scaling relations. A choice of dimensionless variables based on the shock-wave velocity for some finite compression (e.g.,  $D$  for  $V/V_0 = 0.5$ ) in place of the sound speed  $c_0$  would lead to a better equation-of-state

# HYDRODYNAMICS OF HYPERVELOCITY IMPACT

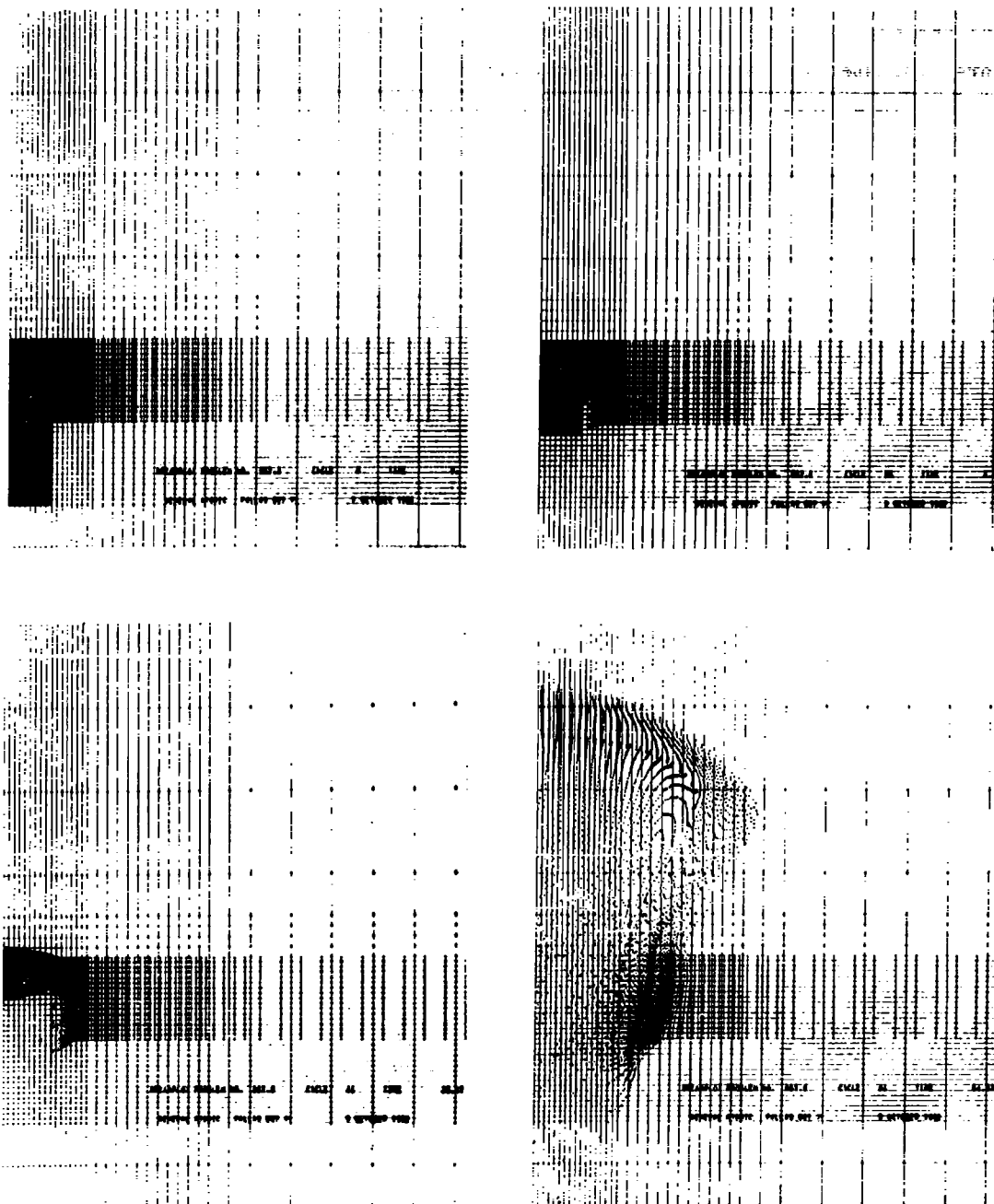


Fig. 15--Four stages at times 0.0, 0.09, 0.16, and 0.65  $\mu\text{sec}$  in the interaction of a 1-cm diameter tungsten pellet, having initial velocity of 10 cm/ $\mu\text{sec}$ , and a 1-cm thick tungsten target



[illegible]

89

# HYDRODYNAMICS OF HYPERVELOCITY IMPACT

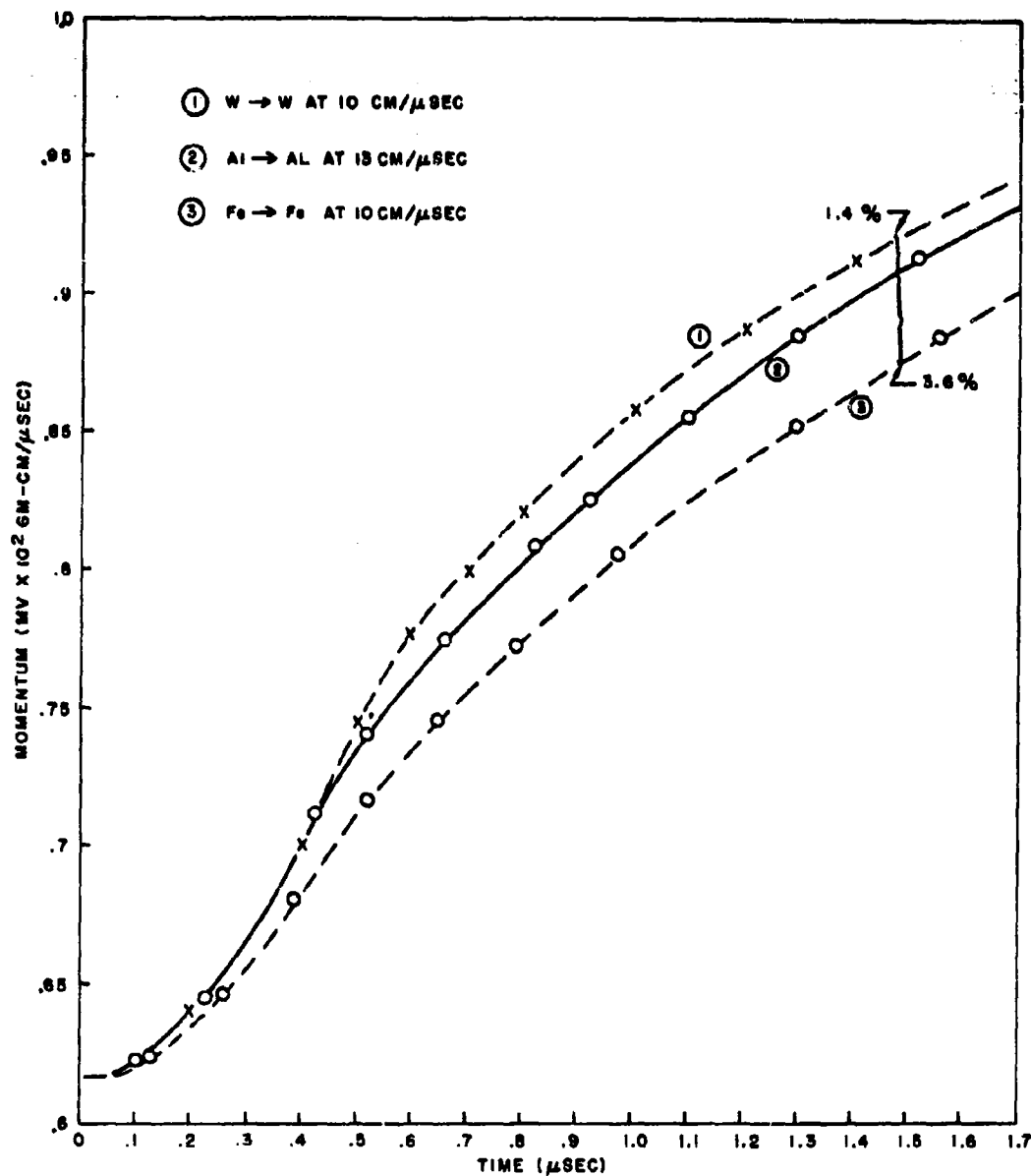


Fig. 17--Positive momenta versus time for the thin-plate impacts; for purposes of comparison with the iron curve, the Al and W data have been scaled; the curves would agree if the equation-of-state correlation were exact

## HYDRODYNAMICS OF HYPERVELOCITY IMPACT

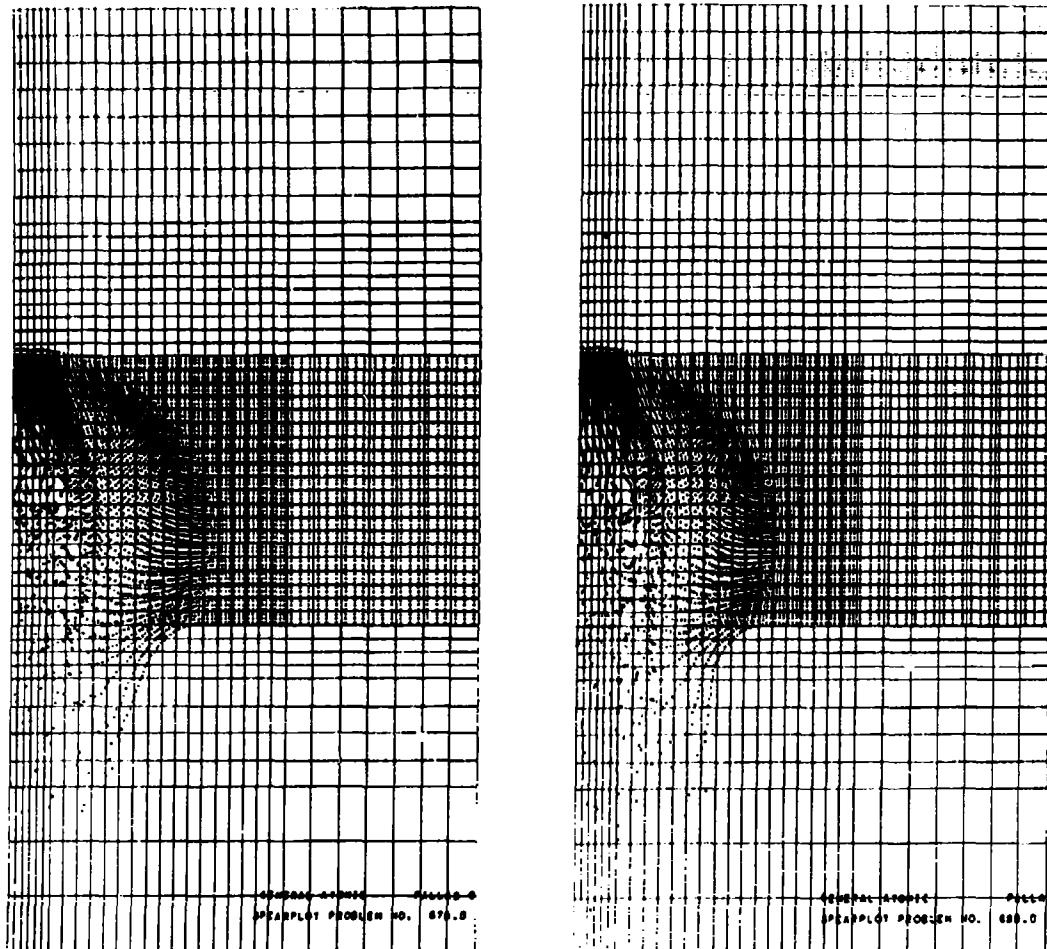


Fig. 18--Flow configuration at corresponding times in the Fe-Fe and Al-Al impacts with thick (five projectile lengths) plates

# HYDRODYNAMICS OF HYPERVELOCITY IMPACT

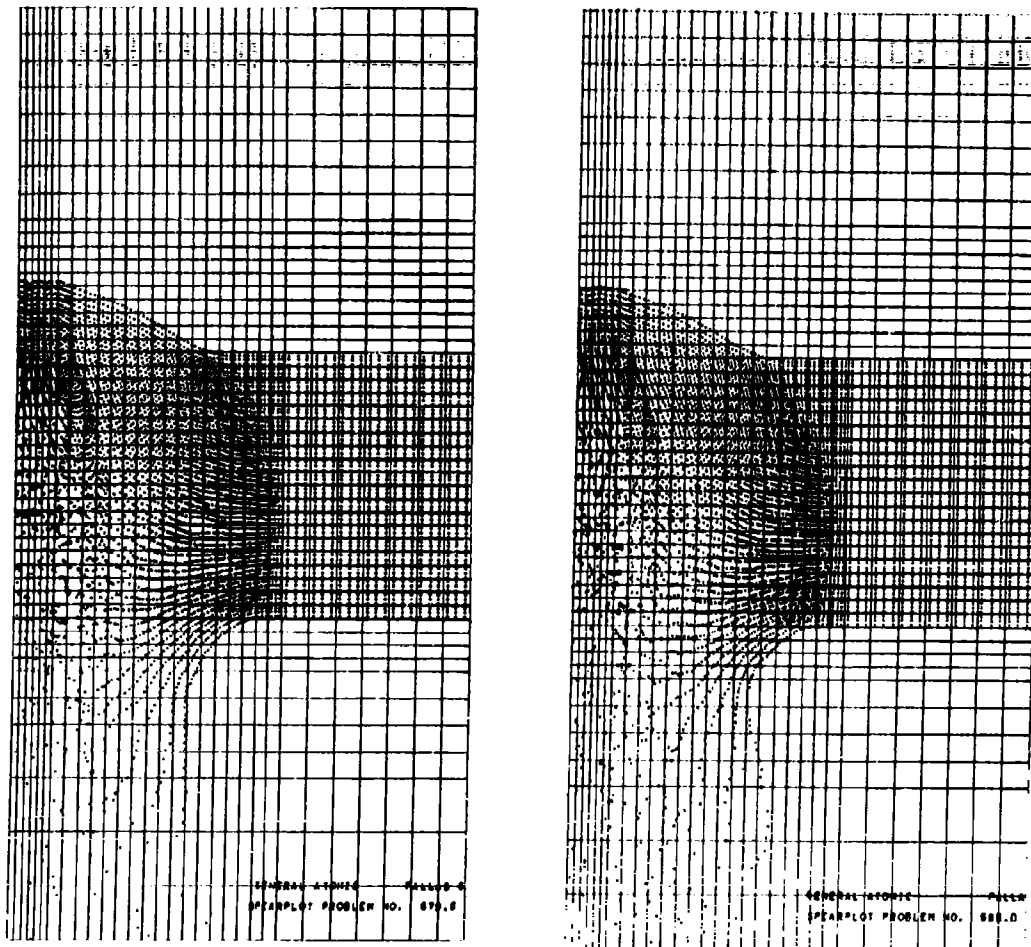


Fig. 19--Flow configuration at corresponding times in the Fe-Fe and Al-Al impacts with thick (five projectile lengths) plates

# HYDRODYNAMICS OF HYPERVELOCITY IMPACT

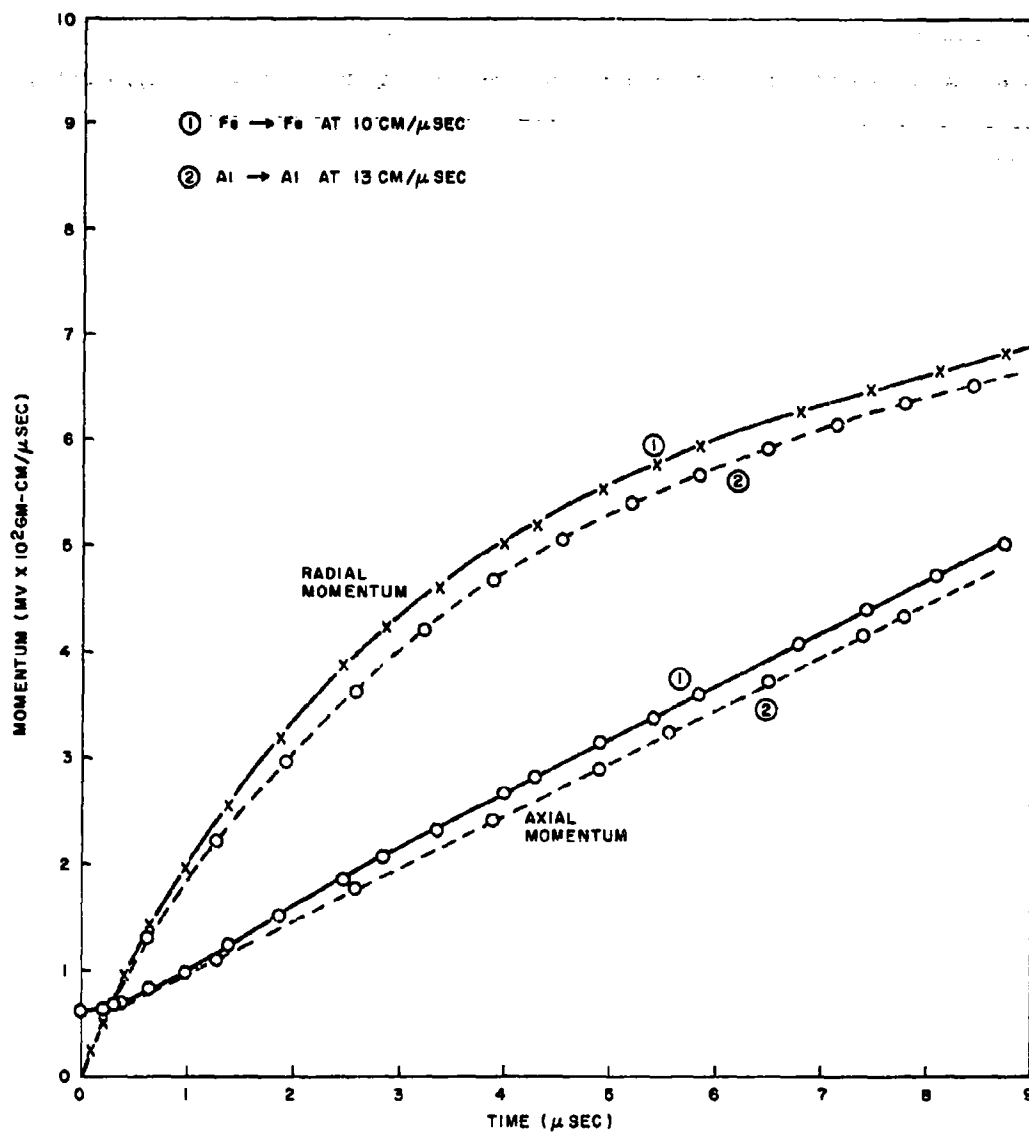


Fig. 20--Momenta versus time for the thick-plate problems; for purposes of comparison with the iron curve, the aluminum data has been scaled

## HYDRODYNAMICS OF HYPERVELOCITY IMPACT

correlation at pressures of interest and a consequent improvement in the scaling accuracy. Errors incurred by the scaling process would apparently be reduced by a factor of two or three. Such scaling relations may be used in future work where increased accuracy is desired, but it will be necessary first to verify the procedure by a series of comparisons such as those described above for the  $c_0$  correlation.

### VI. IMPACT ON THICK TARGETS; THE LATE-STAGE ASYMPTOTIC SOLUTION

A series of impacts have been studied in which an iron projectile interacts with a thick iron plate. The projectile, in all cases a right circular cylinder with equal length and diameter, impacts at velocities of  $5 \times 10^5$ ,  $10^6$ ,  $4 \times 10^6$ ,  $10^7$ , and  $2.5 \times 10^7$  cm/sec. The plate thickness was chosen sufficiently great that no disturbance reaches the back surface during times of concern in the present section.

For the purpose of comparing results from two computations, it is desirable to have comparable cell size and mass resolution. This objective was met by dividing the problems into two sets--one with velocities  $5 \times 10^5$ ,  $10^6$ , and  $4 \times 10^6$  cm/sec and the other with  $4 \times 10^6$ ,  $10^7$ , and  $2.5 \times 10^7$  cm/sec (the  $4 \times 10^6$  cm/sec problem being repeated). Within each set, the target space and mass resolutions were identical and the projectile mass was chosen to keep projectile kinetic energy constant. Initial shock strengths in the various problems range from 1.5 megabars in the  $5 \times 10^5$  cm/sec problem to 1580 megabars at  $2.5 \times 10^7$  cm/sec.

Although detailed descriptions of the individual impacts are excluded from the present discussion for the sake of brevity, it is of particular interest to inquire whether the impact disturbance retains, at late times, a qualitative dependence on the impact velocity. Specifically, do impacts at two different velocities have late-stage asymptotic solutions which are essentially the same except for a simple scale factor? The affirmative answer to this question makes it possible to use the established equivalence and simple scaling in order to extrapolate experimental impact data to the highest velocities of interest.

The most direct test of equivalence in late stages of the flow is made by comparing mass configurations, pressures, and velocities. Such a

## HYDRODYNAMICS OF HYPERVELOCITY IMPACT

comparison is seen as Figs. 21 and 22 for impacts at  $4 \times 10^6$  cm/sec and  $10^7$  cm/sec. The particular times in the two problems were selected on the basis that the shock pressures (radial direction) were equal (1.9 megabars). A comparison of the mass distribution and the velocity fields in the figures shows that the flows are essentially the same. Sizable differences are limited to a relatively small mass of debris in the vicinity of the collision point, for which the pressures are now substantially less than those carried by the shock wave.

More extensive comparisons of corresponding times in the above pair of problems indicate that the  $4 \times 10^6$  cm/sec flow is on a slightly larger scale, by a factor  $F = 1.04 \pm 0.05$ . (Since the mass ratio in the two problems was chosen to keep projectile energy constant, an  $F = 1$  would imply exact energy equivalence.) A more precise determination of  $F$ , however, is afforded by comparing integrated quantities for the two flows: In Fig. 23 are plotted the curves for the total positive momenta within the flows. The  $4 \times 10^6$  cm/sec flow is seen to have the larger momentum, although the ratio of momenta in the two problems at late times is substantially less than the initial ratio of 2.5. The failure of the two unscaled curves to agree at late times implies that the impacts are not exactly equivalent on an equal energy basis. Agreement at late times is, however, obtained by enlarging the  $10^7$  problem by a scale factor  $F = 1.05$ ; i.e., times in the  $10^7$  problem are increased by a factor 1.05 and momentum by a factor  $(1.05)^3$ . The consequent scaled curve is indicated as a dashed line in the figure. Also indicated for comparison is the  $10^7$  problem when scaled to have the same initial momentum as the  $4 \times 10^6$  problem.

A comparison similar to the above, but using instead the total momentum normal to a plane containing the axis of symmetry, indicates a value  $F = 1.04 \pm 0.03$ .

The results given above are assumed sufficient to show that the two interactions have the same late-stage asymptotic solution when the  $10^7$  cm/sec problem is scaled by a factor  $F = 1.05 \pm 0.02$ . Thus, the impacts are equivalent if the ratio of the two projectile masses is

$$\left( \frac{10^7}{4 \times 10^6} \right)^2 \frac{1}{(1.05)^3} = 5.4 \quad ,$$

# HYDRODYNAMICS OF HYPERVELOCITY IMPACT

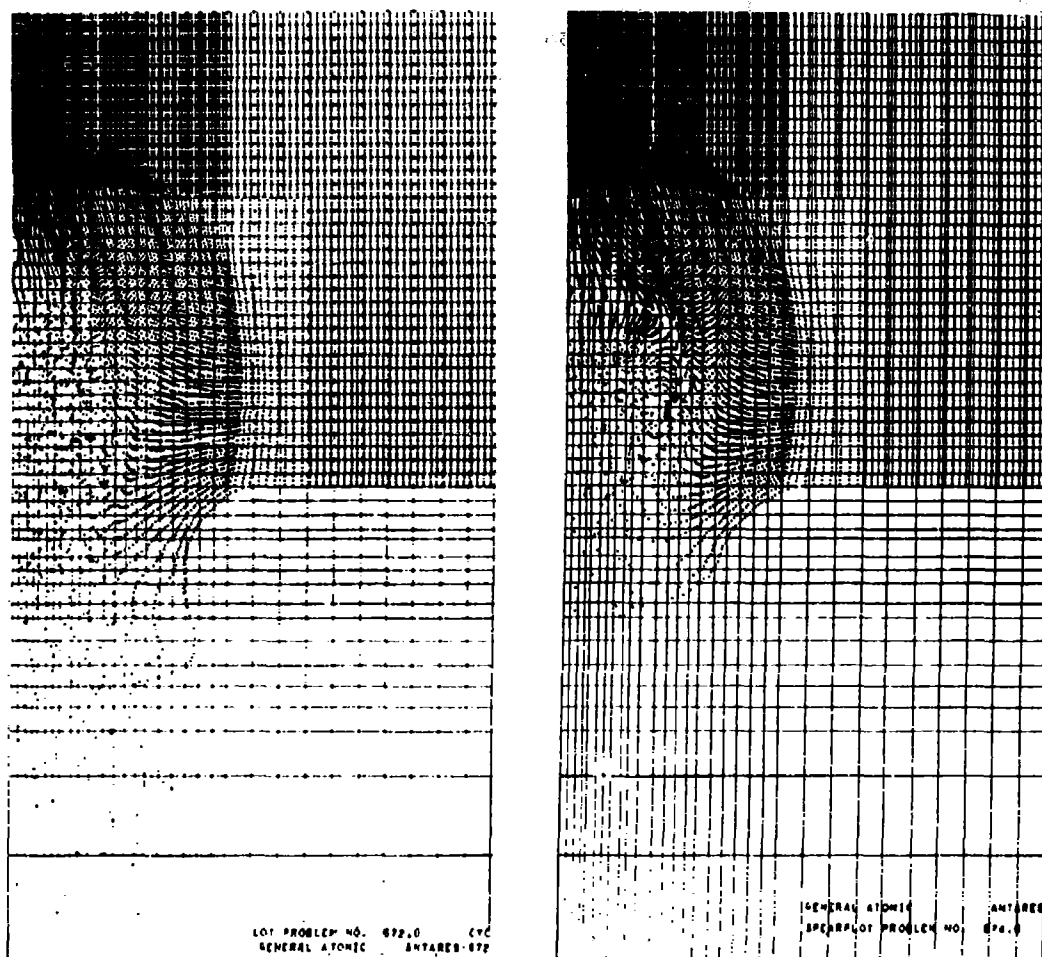


Fig. 21--Comparison of the late-time mass configurations for the  $10^7$  and the  $4 \times 10^6$  cm/sec iron problems



# HYDRODYNAMICS OF HYPERVELOCITY IMPACT

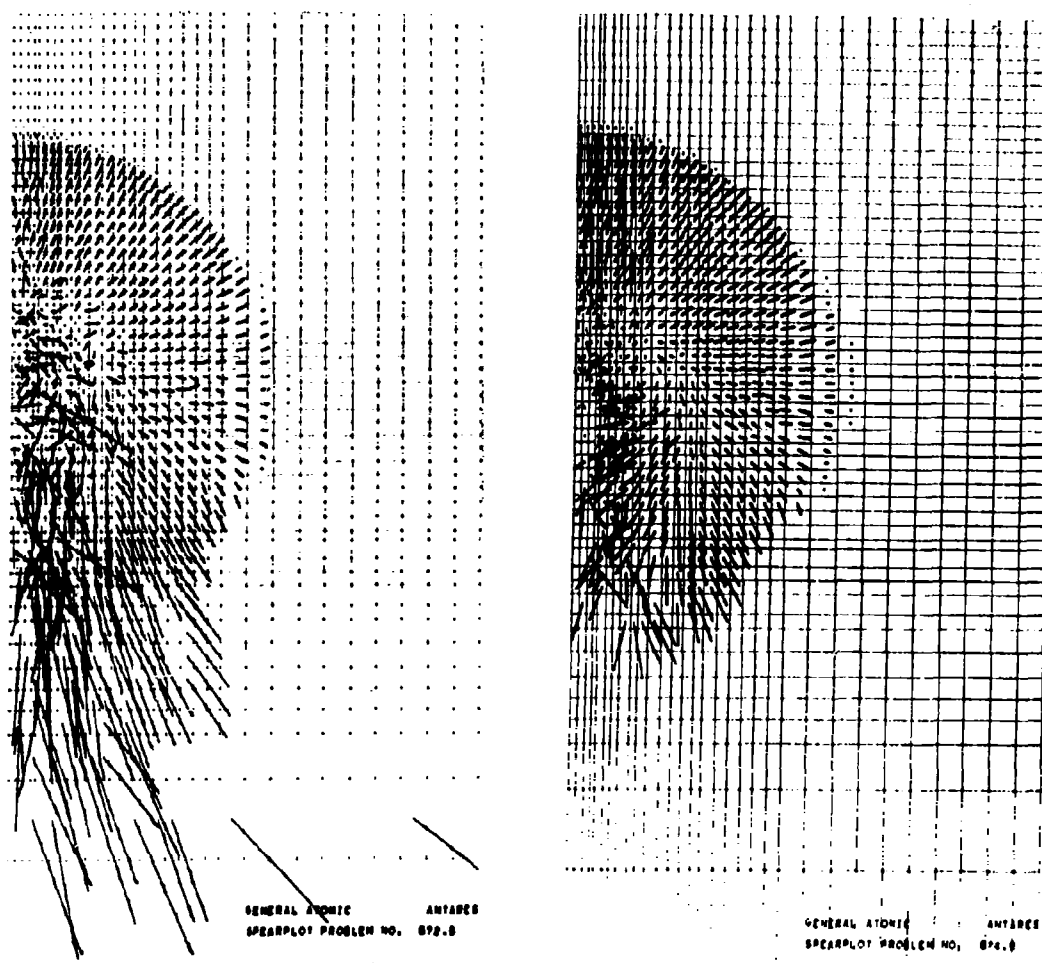


Fig. 22--Comparison of the late-time velocity distributions for the  $10^7$  and the  $4 \times 10^6$  cm/sec iron problems

# HYDRODYNAMICS OF HYPERVELOCITY IMPACT

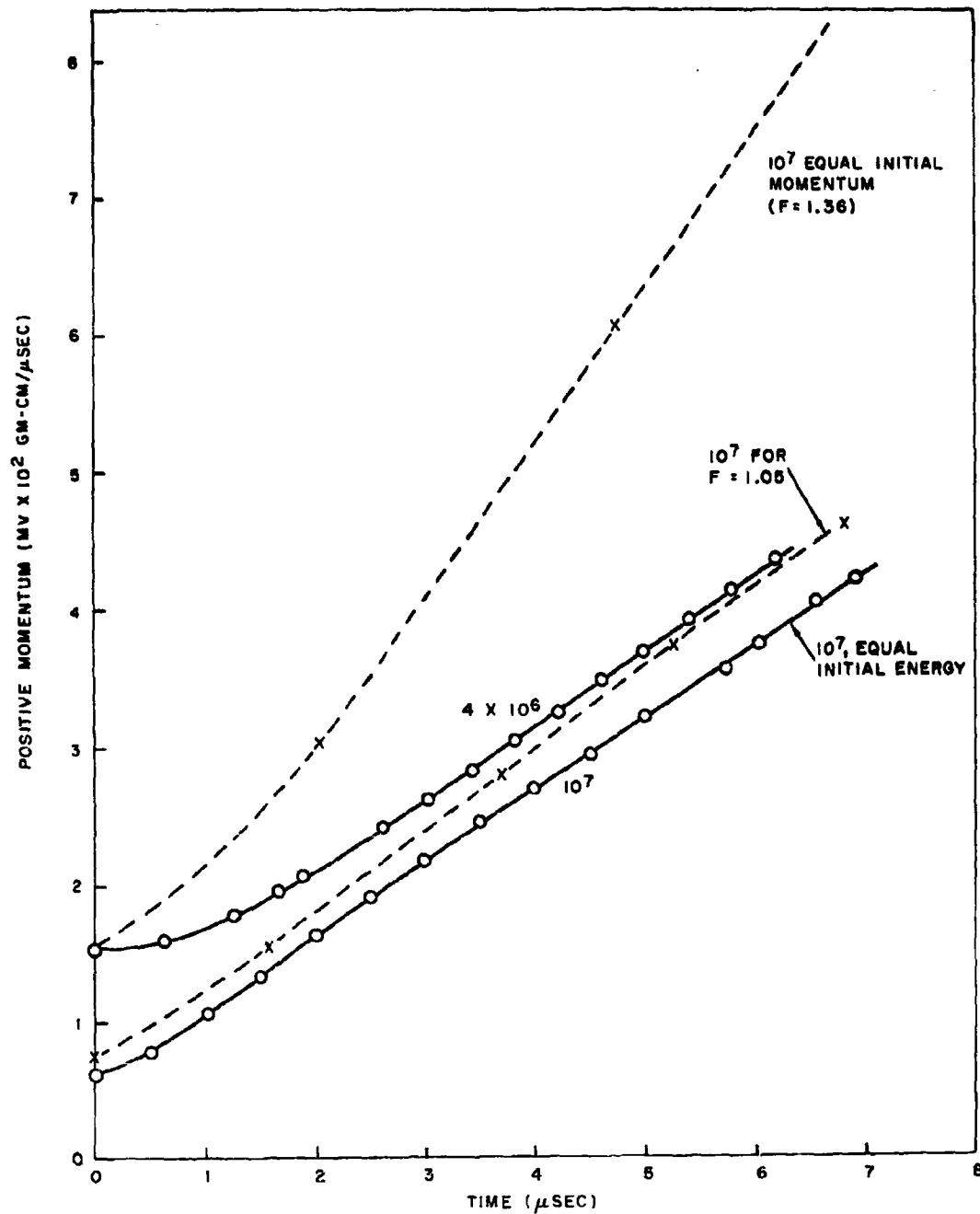


Fig. 23--Comparison of total positive momenta in the  $4 \times 10^6$  cm/sec problem, the  $10^7$  cm/sec problem, and two scaled versions of the  $10^7$  cm/sec problem

## HYDRODYNAMICS OF HYPERVELOCITY IMPACT

or for projectile linear dimensions in the ratio  $\sqrt[3]{5.4} = 1.75$ . The two impacts then lead to the same late-stage effects, such as the crater depth  $p$ . It is desirable to express this latter result in the more conventional form\*

$$p/d = k (v_o/c_o)^\alpha ,$$

where  $d$  is the projectile dimension,  $k$ ,  $c_o$  are constants, and  $v_o$  is the projectile velocity. Denoting the two impacts by subscripts 1 and 2 then gives

$$\frac{d_2}{d_1} = \left( \frac{v_1}{v_2} \right)^\alpha \quad \text{or} \quad \alpha = \frac{\log (2.5)}{\log (1.75)} = 0.61 .$$

Thus, for fixed projectile size, crater dimensions increase as the 0.61 power of impact velocity in the range  $4 \times 10^6$  cm/sec to  $10^7$  cm/sec. The uncertainty  $\pm 0.02$  in  $F$  corresponds to an uncertainty  $\pm 0.02$  in  $\alpha$ .

Considerations similar to the above have also been carried out for the other problems in the present series. Consequent values of  $\alpha$  are:

$$\alpha = 0.61 \pm 0.02 \text{ for the velocity range } 10^7 \text{ to } 2.5 \times 10^7 \text{ cm/sec;}$$

$$\alpha = 0.62 \pm 0.03 \text{ for the } 10^6 \text{ to } 4 \times 10^6 \text{ cm/sec velocity range;}$$

$$\alpha = 0.65 \pm 0.07 \text{ for the } 5 \times 10^5 \text{ to } 10^6 \text{ cm/sec range.}$$

The quoted error limits on  $\alpha$  are offered with some reservation because of possible undetected consistent errors within the computations. Tests have been made, however, with improved space and mass resolutions to explore the dependence of the momentum curves, and hence  $\alpha$ , on the finite difference approximations. Similarly, equation-of-state variations have been made to investigate a possible dependence of results on assumed material properties such as the simple representation of vaporization. The results of all checks have indicated a negligible effect on  $\alpha$ .

---

\*The most general dimensionally consistent form is  $p/d = f (v_o/c_o)$ . But  $f = k (v_o/c_o)^\alpha$  is suitable provided  $\alpha$  is only a weak function of  $v_o$ , as will be the case.

## HYDRODYNAMICS OF HYPERVELOCITY IMPACT

The success of the present approach depends on demonstrating hydrodynamic equivalence prior to the onset of material strength effects. It should be noted that the method will fail at sufficiently low velocities (probably around  $2$  to  $3 \times 10^5$  cm/sec for iron), when strength effects cannot be neglected throughout the early nonequivalent phases of the interactions. A second, less fundamental, limitation arises at low impact velocities in that increased mass resolution is required for the accurate computation of weak hydrodynamics. The above relatively large uncertainty in  $\alpha$  for the  $5 \times 10^5$  to  $10^6$  cm/sec range, in particular, can probably be reduced by using more particles to represent the material. The associated uncertainty in penetration (5%) is, however, not large within the indicated twofold change in velocity.

It is sufficiently accurate and very convenient to take  $\alpha$  to be a constant independent of impact velocity. Using the average value  $\bar{\alpha} = 0.62$  for the entire range, the general expression for penetration can then be written

$$p/d = k (v_0/c_0)^{0.62}$$

where  $p$ ,  $d$  are standard dimensions for the crater and projectile, respectively;  $c_0 \equiv (\partial p / \partial \rho)^{1/2}$  at  $P = 0$ ,  $\rho = \rho_0$ ;  $v_0$  is impact velocity, and the dimensionless constant  $k$  can be determined from a single experiment. It should be noted that the exponent 0.62 is independent of the metal under consideration by virtue of the dimensional analysis considerations of Section V. The constant  $k$ , however, depends on strength properties and must be determined separately for each material. Resulting extrapolations for the experimental data on iron and aluminum are seen as Figs. 24 and 25.

## VII. CONCLUSION

Numerical techniques have been applied to obtain a solution to the hydrodynamic equations which govern the early phase of the hypervelocity impact process. Late stages of the interaction, where deformation forces are no longer great compared to the yield strength, have not been treated. Within the hydrodynamic phase, however, it is found that the late time

# HYDRODYNAMICS OF HYPERVELOCITY IMPACT

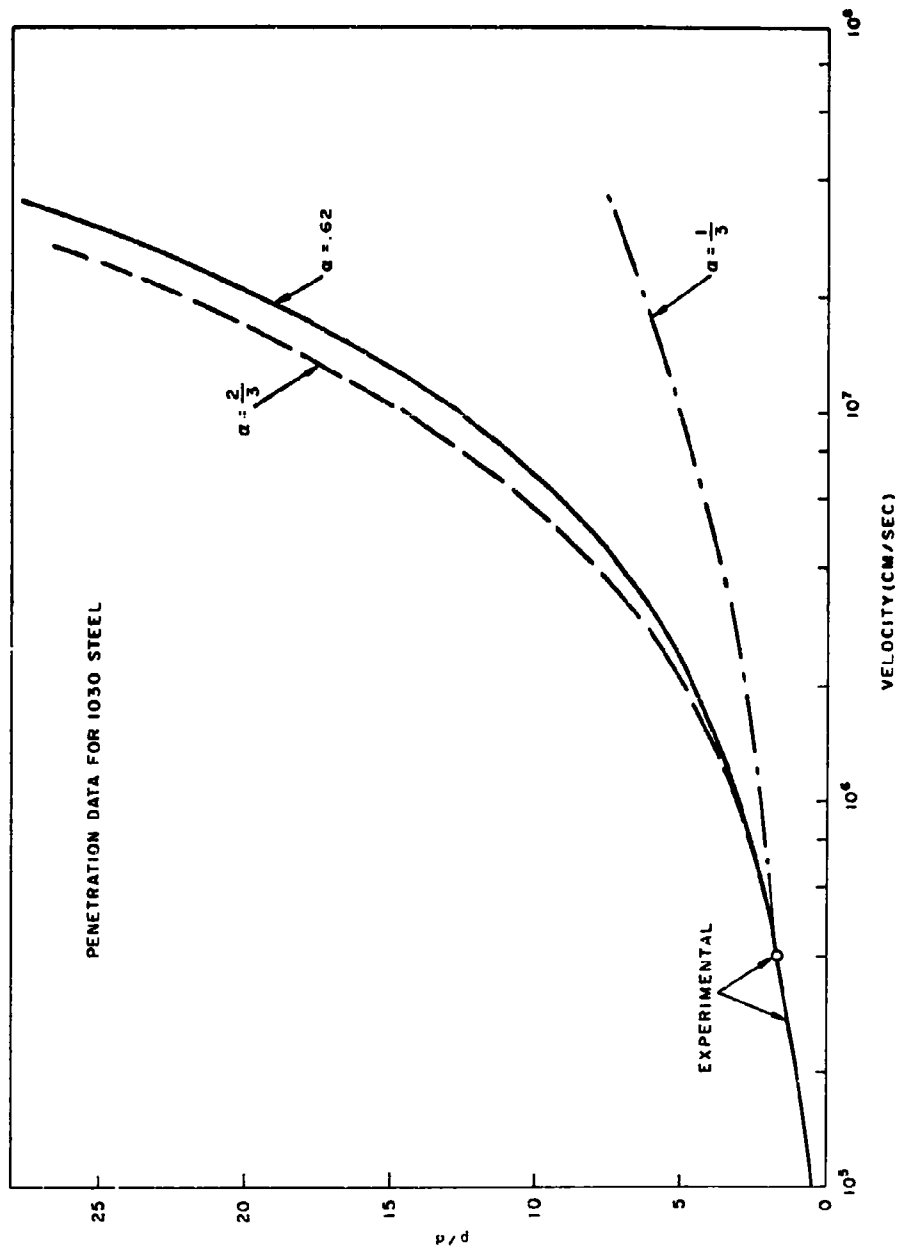


Fig. 24--Penetration data for 1030 steel. Experimental to  $p/d = 1.7$  and  $v_0 = 4 \times 10^5$  cm/sec. Extrapolated according to  $p/d = k(v_0/c_0)^\alpha$  with  $\alpha = 0.62$ . The  $\alpha = 2/3$ ,  $1/3$  curves are shown for comparison

# HYDRODYNAMICS OF HYPERVELOCITY IMPACT

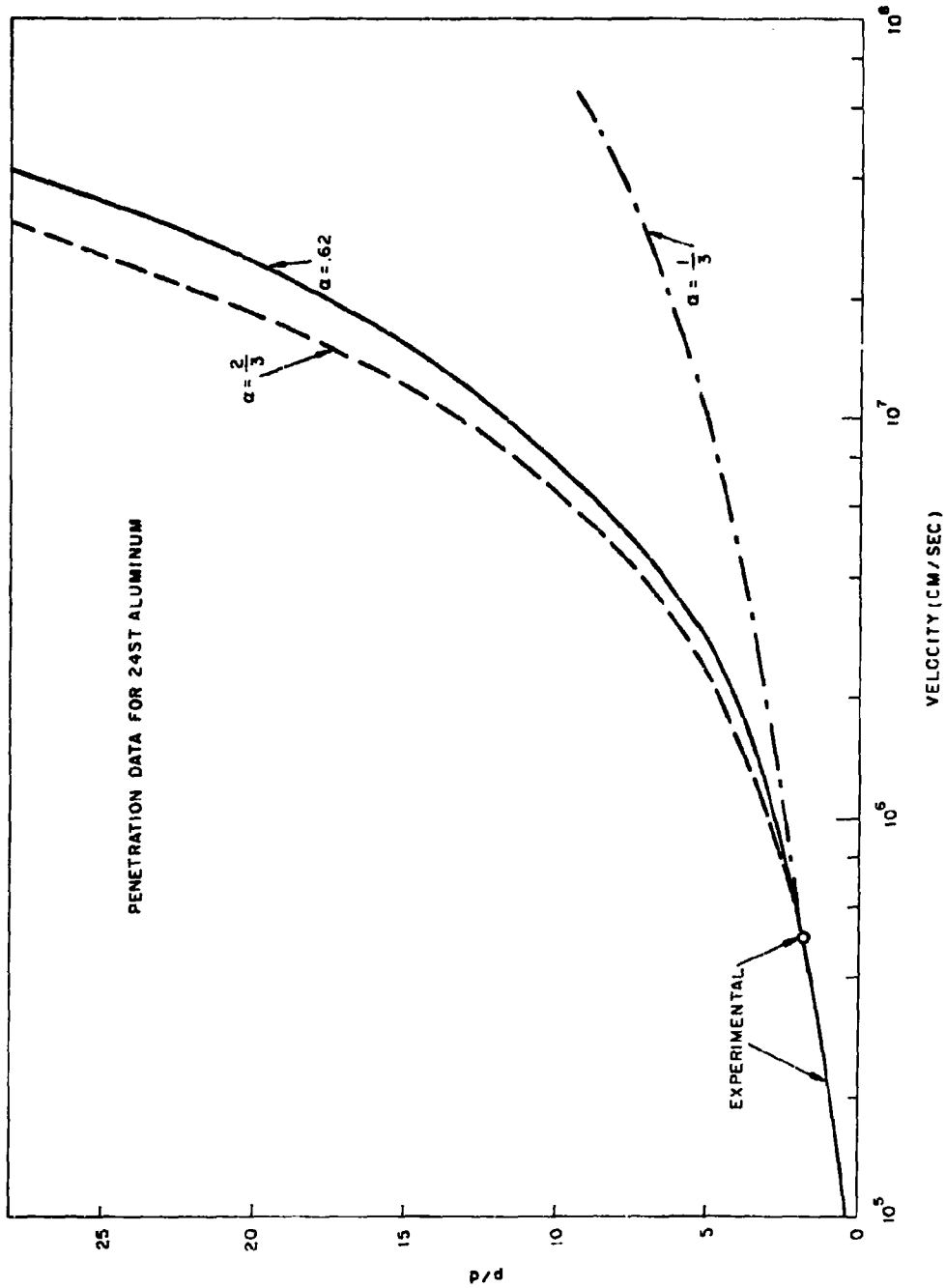


Fig. 25--Penetration data for 24 ST aluminum. Experimental to  $p/d = 1.8$  and  $v_0 = 5 \times 10^5$  cm/sec. Extrapolated according to  $p/d = k(v_0/c)^\alpha$  with  $\alpha = 0.62$ . The  $\alpha = 2/3, 1/3$  curves are shown for comparison

## HYDRODYNAMICS OF HYPERVELOCITY IMPACT

asymptotic solution is independent of the impact velocity except for a simple scale factor. This means, in particular, that the (untreated) late-stage deformation problem is the same for all impact velocities. The determination of scale factors from the computations and the data from a single hypervelocity impact experiment for the material then permits one to completely specify the crater dimensions as a function of impact velocity. The result is that the early stages of the impact process are completely determined by the hydrodynamic theory, and over-all effects, such as the final crater, are determined by a combination of experimental and theoretical results.

It is fortuitous that these considerations have led to a determination of cratering effects. The asymptotic solution within the hydrodynamic phase will not occur at low impact velocities, where strength effects become important in early stages of the interaction. In order to extrapolate the experimental cratering data, on the other hand, one must have at least one impact experiment for which the velocity is sufficiently high that the asymptotic solution can be assumed. For most materials of interest the necessary impact velocities have been exceeded by a factor of two or more and the results are available from data tabulations.<sup>(3)</sup>

The alternative to the present approach would appear to involve the explicit treatment of the late-stage strength-dependent deformation. As noted in the Introduction, such an undertaking requires a substantially more elaborate computation than the hydrodynamic problem, and also non-trivial uncertainties must be expected in connection with material strength properties for high strain rates. It therefore seems probable that the most reliable predictions of cratering phenomena, for velocities greater than those attainable in controlled experiments, are to be made by the hydrodynamic approach which has been used in the present study.

A number of important aspects of impact have not been considered. Among these are the collision of unlike materials, the effects of projectile shape and the impact behavior of nonmetallic solids. It is expected that continuing work along lines indicated in the present report will make it possible to understand and predict the effects of these variations.

## HYDRODYNAMICS OF HYPERVELOCITY IMPACT

### REFERENCES

1. Evans, M. W., and F. H. Harlow, "The Particle-in-Cell Method for Hydrodynamic Calculations," Los Alamos Scientific Laboratory LA-2139, November, 1957; and F. H. Harlow, "Two Dimensional Hydrodynamic Calculations," Los Alamos Scientific Laboratory, LA-2301, September, 1959.
2. Bjork, R. L., "Effects of Meteoroid Impact on Steel and Aluminum in Space," Tenth International Astronautical Congress, London, 1959, p. 505.
3. Hermann, W., and O. F. Jones, "Survey of Hypervelocity Impact Information," Massachusetts Institute of Technology, ASRL 99-1, October, 1961.
4. Eichelberger, R. J., and J. W. Gehring, "Effects of Meteoroid Impacts on Space Vehicles," Ballistics Research Laboratory, BRL-1155, December, 1961.
5. Tillotson, J. H., "Metallic Equations of State for Hypervelocity Impact," General Atomic, GA-3216, July, 1962.



**VISCO-PLASTIC SOLUTION OF HYPERVELOCITY  
IMPACT CRATERING PHENOMENON**

by

**T. D. Riney**

**Space Sciences Laboratory  
General Electric Missile and Space Division  
King of Prussia, Pennsylvania**

## VISCO-PLASTIC SOLUTION OF CRATERING

### ABSTRACT

A computer program (PICWICK) has been developed for the solution of the equations governing the visco-plastic model for hyper-velocity impact. The program is capable of comparing various equations of state, flow-resistance coefficients, and fracture criteria. Some choices for these relations are briefly discussed and the computational method, on which the computer program is based, is described.

A series of calculated flow-fields depicting iron-iron impact illustrate the bounded instability of the basic numerical scheme. That this problem may be overcome is then demonstrated by two series of flow-fields calculated for lead-lead impact situations. The results show the rapidity with which the shock intensity decreases due to geometrical divergence and, consequently, lead to the conclusion that consideration of the pressures generated at impact cannot serve as a valid basis for neglecting target strength.

# VISCO-PLASTIC SOLUTION OF CRATERING

## INTRODUCTION

The response of metallic materials when subjected to hyper-velocity impact is assumed to be governed by the visco-plastic model presented previously<sup>(1)</sup>. The model describes the behavior of metals under impulsive loading so intense that the elastic and strain-hardening effects may be assumed to be negligible. On the other hand, it meets the physical requirement that the inertial (compressibility), viscous, and strength effects be included<sup>(2)</sup>. Thus, the stress tensor,  $\tau_{ij}$ , and the strain-rate tensor,  $D_{ij}$ , are assumed related according to

$$\tau_{ij} = -p \delta_{ij} + \mu \left( D_{ij} - \frac{2}{3} \text{div } \vec{u} \delta_{ij} \right), \quad (1)$$

where  $\delta_{ij}$  is the Kronicker delta,  $p$  the thermodynamic pressure,  $\mu$  the flow-resistance coefficient, and  $\vec{u} = (u, v, w)$  is the velocity vector. Here  $p$  depends only on thermodynamic state but  $\mu$  depends as well on the invariants of the strain-rate deviator. Both relations must be specified if (1) is to provide a constitutive equation for a material.

Given the required relations for  $p$  and  $\mu$ , (1) may be incorporated into the partial differential equations expressing the conservation of momentum and energy. The resulting equations together with the continuity equation then govern the behavior of the medium subjected to intense impulsive loading providing it remains continuous. In the case of axially symmetric impact (see Fig. 1), the equations in Eulerian form, reduce to

$$\text{(Mass)} \quad \frac{\partial \rho}{\partial t} + u \frac{\partial \rho}{\partial r} + v \frac{\partial \rho}{\partial z} + \rho \text{div } \vec{u} = 0 \quad (2)$$

$$\begin{aligned} &\text{(Radial} \\ &\text{Momentum)} \quad \rho \left( \frac{\partial u}{\partial t} + u \frac{\partial u}{\partial r} + v \frac{\partial u}{\partial z} \right) = \frac{\partial}{\partial r} \left( P + S_{rr} \right) + \frac{S_{rr} - S_{\theta\theta}}{r} + \frac{\partial S_{rz}}{\partial z} \end{aligned} \quad (3)$$

# VISCO-PLASTIC SOLUTION OF CRATERING

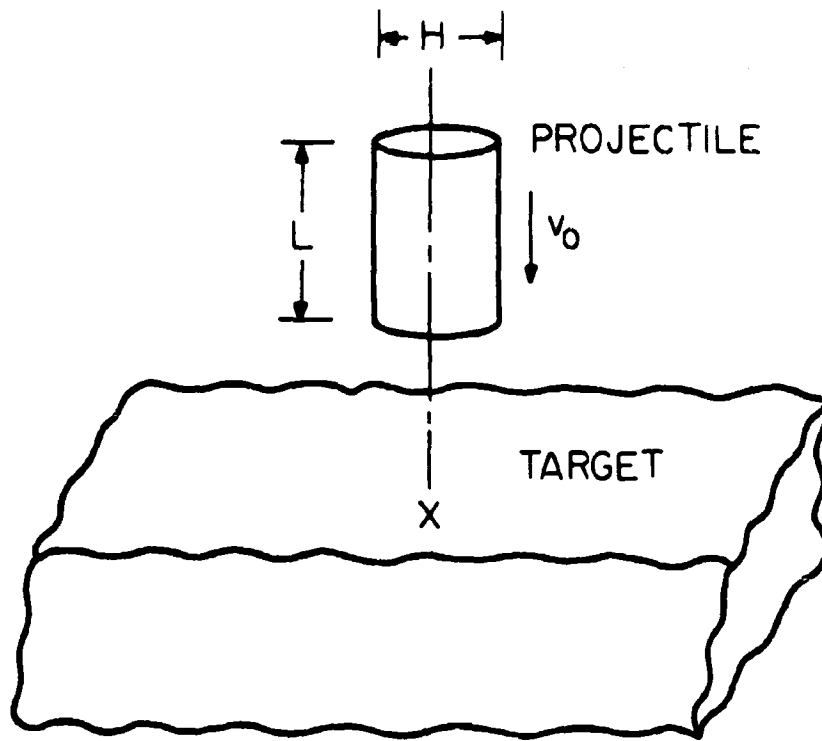


Figure 1.

Illustration of projectile-target configuration just before impact.

## VISCO-PLASTIC SOLUTION OF CRATERING

$$\begin{aligned} & \text{(Axial Momentum)} \quad \rho \left( \frac{\partial v}{\partial t} + u \frac{\partial v}{\partial r} + v \frac{\partial v}{\partial z} \right) = \frac{\partial}{\partial z} (P + S_{zz}) + \frac{1}{r} \frac{\partial}{\partial r} (r S_{rz}) \\ & \hspace{15em} (4) \end{aligned}$$

$$\text{(Energy)} \quad \rho \left( \frac{\partial I}{\partial t} + u \frac{\partial I}{\partial r} + v \frac{\partial I}{\partial z} \right) + p \operatorname{div} \vec{u} = \mu D^2. \quad (5)$$

Here  $\rho$  is the density,  $I$  the specific internal energy, and the following notations have been introduced:

$$\left. \begin{aligned} P &= -p - \frac{2}{3} \mu \operatorname{div} \vec{u} & \operatorname{div} \vec{u} &= \frac{1}{r} \frac{\partial (ru)}{\partial r} + \frac{\partial v}{\partial z} \\ S_{zz} &= \mu D_{zz} = 2\mu \frac{\partial v}{\partial z} & S_{rr} &= \mu D_{rr} = 2\mu \frac{\partial u}{\partial r} \\ S_{rz} &= \mu D_{rz} = \mu \left( \frac{\partial u}{\partial z} + \frac{\partial v}{\partial r} \right) & S_{\theta\theta} &= \mu D_{\theta\theta} = 2\mu \frac{u}{r} \\ D^2 &= D_{rz}^2 + \frac{1}{2} (D_{rr}^2 + D_{\theta\theta}^2 + D_{zz}^2) - \frac{2}{3} (\operatorname{div} \vec{u})^2 \end{aligned} \right\} \quad (6)$$

In writing (6) we have assumed that the flow is strictly adiabatic.

Since equations (2) through (6) do not apply to a discontinuous medium provisions must also be made for material fracture. The rupture of the material and its subsequent ejection from the crater during the cavitation process accounts for a large percentage of the final crater volume.

### CONSTITUTIVE RELATIONS

For each material requiring calculations the equation of state, the flow-resistance coefficient, and the fracture criteria for a dynamic tri-axial stress condition must be specified. Actually, none of these have been firmly established by experiments under the severe conditions of pressure, strain-rate, and temperature which occur during hypervelocity impact. At the present state of knowledge it is necessary to extrapolate boldly from data observed under far less severe

## VISCO-PLASTIC SOLUTION OF CRATERING

conditions. In a recent paper<sup>(3)</sup> some of the available experimental data were brought together within a framework general enough to permit the construction of tentative constitutive relations for the plastic - hydrodynamic regime that are sufficiently realistic for engineering and physical calculations. Rather than repeat the discussion given there we will concern ourselves principally with those choices for the constitutive relations for which calculations are currently being carried out.

It should be emphasized, however, that the method of solution that has been developed, to be described later, is capable of handling various choices for the equation of state, the flow-resistance coefficient, and the fracture criterion. Several choices have indeed been written into the computer program as sub-routines so that they may be readily changed.

In the compressive regime the most reliable equation of state available has been determined by the Los Alamos group from velocity measurements of shock waves induced by high explosives. The pressure is expressed as a function of density and specific internal energy:

$$p = f(\rho, I).$$

It is also necessary to provide an equation of state for the tensile regime since rarefaction regions occur near the edge of the projectile-target interface during the early stages of the process, and near the lip of the forming crater during the later stages. Apparently no experimental data are available under these extreme conditions. It seems reasonable and expedient to use the tangent line of  $f(\rho, I)$  to extend the equation of state into the tensile regime (Fig. 2):

$$h(\rho, I) = \zeta \left[ \frac{\partial f}{\partial \zeta} \right]_{\zeta=0} + [f]_{\zeta=0}$$

# VISCO-PLASTIC SOLUTION OF CRATERING

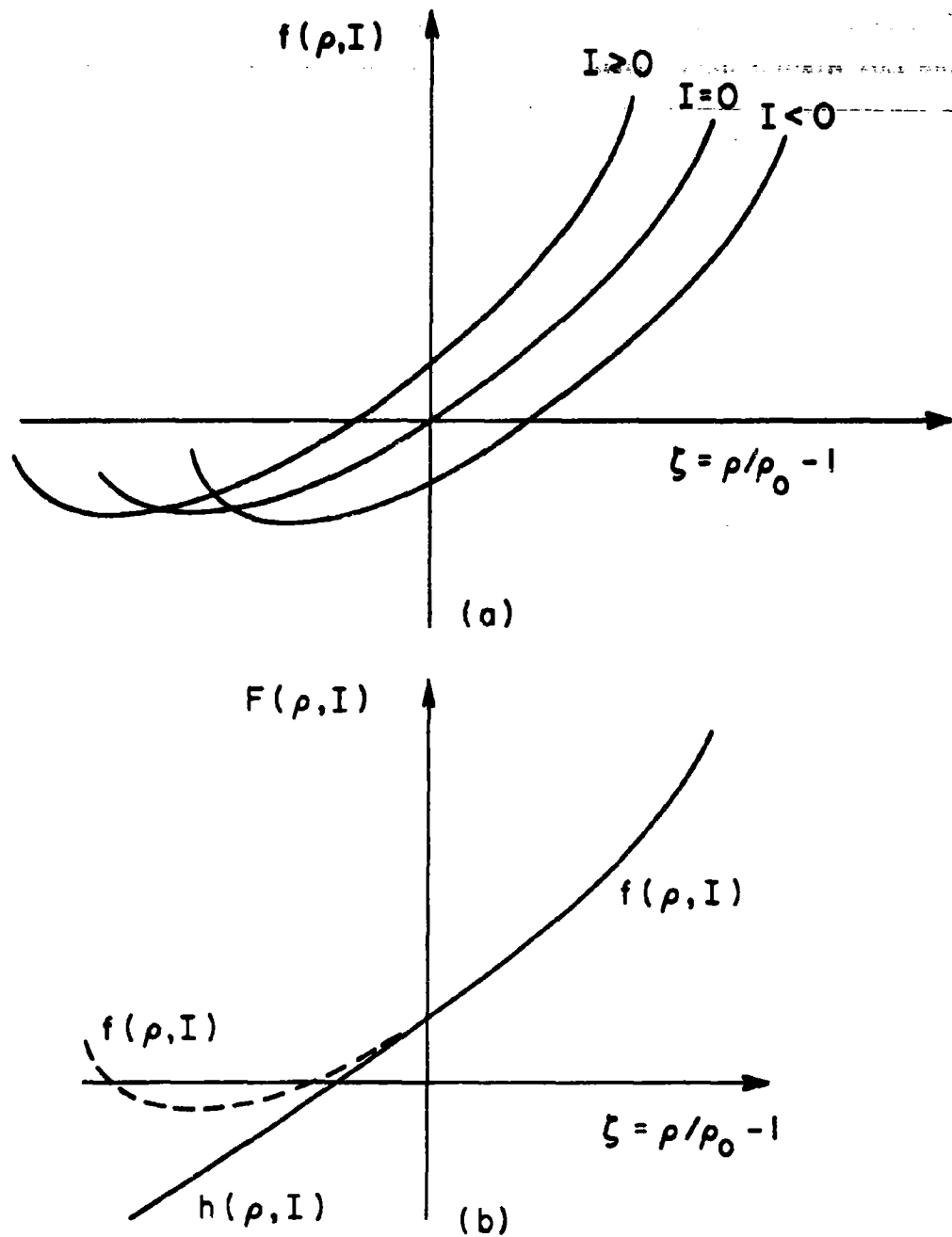


Figure 2. Schematic of equation of state:  
 (a) Function equal to pressure in compressive region.  
 (b) Extrapolation into tensile region.

## VISCO-PLASTIC SOLUTION OF CRATERING

The statically determined pressure-compression data of Bridgman fits the Los Alamos data. Hence, when  $I = 0$  the above extrapolation is equivalent to assuming that in the neighborhood of  $p = 0$ , the bulk modulus of the metal in tension is the same as its value in compression. Explicit expressions for  $f(\rho, I)$  and  $h(\rho, I)$  have been given elsewhere. <sup>(3, 8)</sup>

In our original formulation of the visco-plastic model the flow-resistance coefficient was assumed to be simply

$$\begin{aligned} \mu(D) &= \eta_0 + \frac{S_0}{|D|} & (|\tau| \geq S_0) \\ &= \infty & (|\tau| < S_0) \end{aligned} \quad (7)$$

where  $S_0$  denotes the static yield shear stress of the material,  $\eta_0$  denotes the viscosity factor, and the second invariant of the stress deviator,  $\tau^2 = \mu^2 D^2$ , is a measure of the deformation experienced by the medium. Thus, the material was considered rigid if stressed below its yield strength, whereas above this value it was assumed to behave as a Newtonian viscous liquid.

Actually both  $\eta_0$  and  $S_0$  are not constant but depend on the thermodynamic state of the medium:

$$\eta_0 \rightarrow \eta(I, p) \quad S_0 \rightarrow S(I, p).$$

Both decrease in value if the specific internal energy (essentially the temperature) is increased while holding the pressure constant,

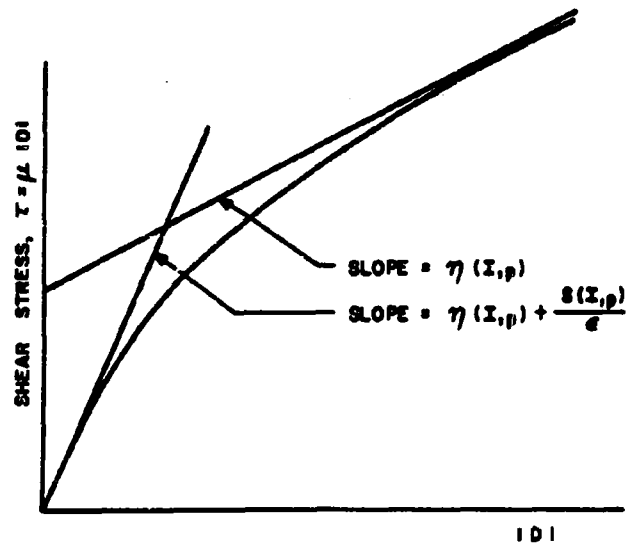
$$\left( \frac{\partial \eta}{\partial I} \right)_{p_0} < 0 \quad \left( \frac{\partial S}{\partial I} \right)_{p_0} < 0;$$

both increase in value if the pressure is increased while the internal energy is held constant,

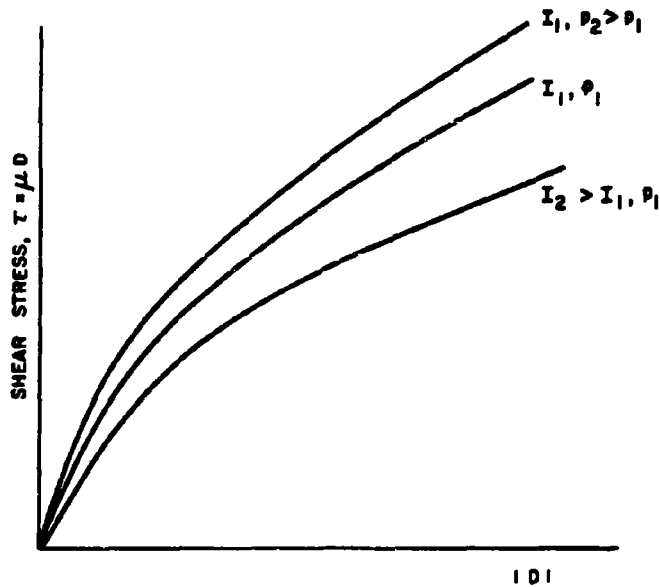
$$\left( \frac{\partial \eta}{\partial p} \right)_{I_0} > 0 \quad \left( \frac{\partial S}{\partial p} \right)_{I_0} > 0.$$



# VISCO-PLASTIC SOLUTION OF CRATERING



(a)



(b)

Figure 3.

Schematic representing the dependence of the shearing stress on the rate of deformation: (a) Effect of  $\epsilon$ , (b) Effect of internal energy (or temperature) and pressure.

# VISCO-PLASTIC SOLUTION OF CRATERING

In order to explicitly account for these effects, the definition of the flow-resistance coefficients may be written as follows:

$$\mu \equiv \mu(I, p, D) \\ \equiv \frac{S(I, p)}{|D| + \epsilon} \left[ 1 + \frac{\eta(I, p)}{S(I, p)} (|D| + \epsilon) \right] \quad (8)$$

The internal energy pressure, and strain-rate dependence of  $\mu$  are depicted schematically in Fig. 3. The quantity  $\epsilon > 0$  is introduced chiefly to remove the moving surface of separation between the rigid and fluid regions of the medium. This not only simplifies the calculations, however, but is also more realistic because the stresses now depend upon the strain-rate in a continuous manner. Under prolonged loading this model permits deformation to occur even for  $|\tau| < S$ , but the impact mechanism is completed long before such creep effects can occur.

Alternate forms that are being considered for the flow-resistance coefficient include the following

$$\mu = \frac{S(I, p)}{|D| + \epsilon} \left[ 1 + \left\{ \frac{\eta(I, p)}{S(I, p)} (|D| + \epsilon) \right\}^{1/\delta} \right] \quad (9)$$

$$\mu = \frac{S(I, p)}{|D| + \epsilon} \left[ 1 + \ln \left\{ 1 + \frac{\eta(I, p)}{S(I, p)} (|D| + \epsilon) \right\} \right] \quad (10)$$

$$\mu = \frac{1}{\omega_1 \max(D_0, |D|)} \left[ \lambda_1 + T \ln \left\{ \frac{\max(D_0, |D|)}{\nu_0} \right\} \right] \quad (11)$$

In the above relations  $T$  is the absolute temperature and  $\delta$ ,  $\omega_1$ ,  $\lambda_1$ ,  $\nu_0$  are experimentally determined material constants;  $D_0$  is given by

$$D_0 = \frac{\nu_0}{\sqrt{3}} \exp(-\lambda_1/T).$$

Approximate values for these constants and the bases for proposing the relations (8) through (11) have been presented elsewhere.<sup>(3)</sup>

## VISCO-PLASTIC SOLUTION OF CRATERING

One criterion for material rupture may be reduced under the assumption that the fracture occurs whenever both the pressure is negative (i. e. hydrostatic tension exists) and the second invariant of the stress deviator exceeds a critical value:

$$p < 0 \text{ and } |\tau| \geq \sigma_{cr}. \quad (12)$$

The critical value of  $\sigma_{cr}$  will depend upon the temperature and the length of time during which the stress is applied.

A rational assumption is that the damage suffered by a segment of the medium is cumulative; that is, in each small time increment the fracture will proceed at a rate appropriate to the stress distribution and temperature occurring during that time increment. In the numerical scheme, however, the stress field is expressed in Eulerian coordinates, and excessive bookkeeping would be required to account for the cumulative damage suffered by the material particles. It is therefore assumed that damage is accumulated only for the time interval,  $\delta t$ , corresponding to one time cycle of the numerical scheme.

Under these assumptions the fracture criterion for which there is apparently the most experimental data for uniaxial dynamic conditions generalizes to give<sup>(3)</sup>

$$\int_{t_1}^{t_2} \exp \left[ - \frac{\lambda^* - \omega^* |\tau|}{T} \right] \delta t = t_0,$$

where  $t_0$ ,  $\lambda^*$  and  $\omega^*$  are material constants. To determine the point at which fracture occurs, replace  $|\tau|$  by its critical value,  $\sigma_{cr}$ , and accumulate only for time  $\delta t$  to get

$$\sigma_{cr} = \frac{1}{\omega^*} \left[ \lambda^* - T \ln (\delta t / t_0) \right].$$

In terms of the specific internal energy, the relation is approximated by

## VISCO-PLASTIC SOLUTION OF CRATERING

$$\sigma_{cr} = \frac{1}{\omega^*} \left[ \lambda^* - \left( \frac{1}{c} - 300 \right) \ln \frac{\delta t}{t_o} \right], \quad (13)$$

where  $c$  is a mean value of the specific heat.

From experimental results over a wide range of stresses and temperatures Zhurkov<sup>(4)</sup> has deduced empirical values for these constants for a number of metals. These values as well as an alternate fracture criterion have been presented elsewhere<sup>(3)</sup>.

### METHOD OF SOLUTION

In developing a finite difference formulation of the equations governing the axisymmetric impact problem, the extension of an existing scheme devised for two-dimensional hydrodynamics is a natural approach. Several methods of treatment have been used for those problems dependent upon two or more space coordinates. These variations usually employ (a) Langrangian coordinates in which the mesh of cells is imbedded in the medium and moves with it, (b) Eulerian coordinates which are not fixed in the medium but are usually stationary in the laboratory frame of reference, or (c) a mixed Euler-Lagrange system which attempts to take advantage of the better features of both fixed and moveable coordinates.

The chief difficulty with schemes employing Langrangian coordinates is the large distortion which is involved in the present problem. The Eulerian systems have the disadvantage that to account for the projectile-target interface and the free surfaces of the projectile and target is extremely difficult. These are the basic reasons for the decision to adopt the particle-in-cell method which has been developed at Los Alamos<sup>(5, 6, 7)</sup> and to extend it to account for the resistance to flow and fracture. A step-by-step prescription for carrying out the numerical calculations for the visco-plastic equations has been presented previously<sup>(8)</sup>; here the scheme will only be described in general terms.

## VISCO-PLASTIC SOLUTION OF CRATERING

An axial section of the projectile-target configuration is superposed by the fixed space mesh used to describe the subsequent motion of the configuration. On this plane of symmetry the cells of the space mesh appear as rectangles with sides of length  $\delta r = h$  by  $\delta z = k$ ; each cell is actually a toroid of revolution, Fig. 4. The projectile-target material is represented on this axial plane by discrete mass points called "particles"; each particle is actually a circle about the axis of symmetry. Each particle is assigned a fixed mass whose value is proportional to the radius of the cell within which it lies originally, i.e., at  $t = 0$ . The  $r$  and  $z$  coordinates of each particle are stored in the computing-machine memory. These are changed in time in accordance with the subsequent motion of the material through the fixed mesh of computational cells. The conservation of mass is therefore automatic.

At the end of the  $n^{\text{th}}$  time cycle the mass (equal to the sum of the masses of the particles located in that cell) velocity, pressure, and specific internal energy are associated with each cell. To obtain the corresponding data at the end of the  $(n + 1)^{\text{th}}$  time cycle one makes a three-phase calculation. In Phase I the cellwise field functions are changed neglecting the motion of the medium. Thus, the transport terms are dropped from the momentum and energy equations and (3), (4) and (5) are replaced by difference formulas for computing tentative new cellwise velocity components and specific internal energy. In Phase II the mass particles are moved according to the velocity of the cell in which it is located and the velocities of the neighboring cells. In moving, the particles carry their share of the cellwise energy and momentum with them; the field functions are then recalculated to account for the motion. In Phase III various functionals are computed which furnish checks on the accuracy of the calculations. For example,

# VISCO-PLASTIC SOLUTION OF CRATERING

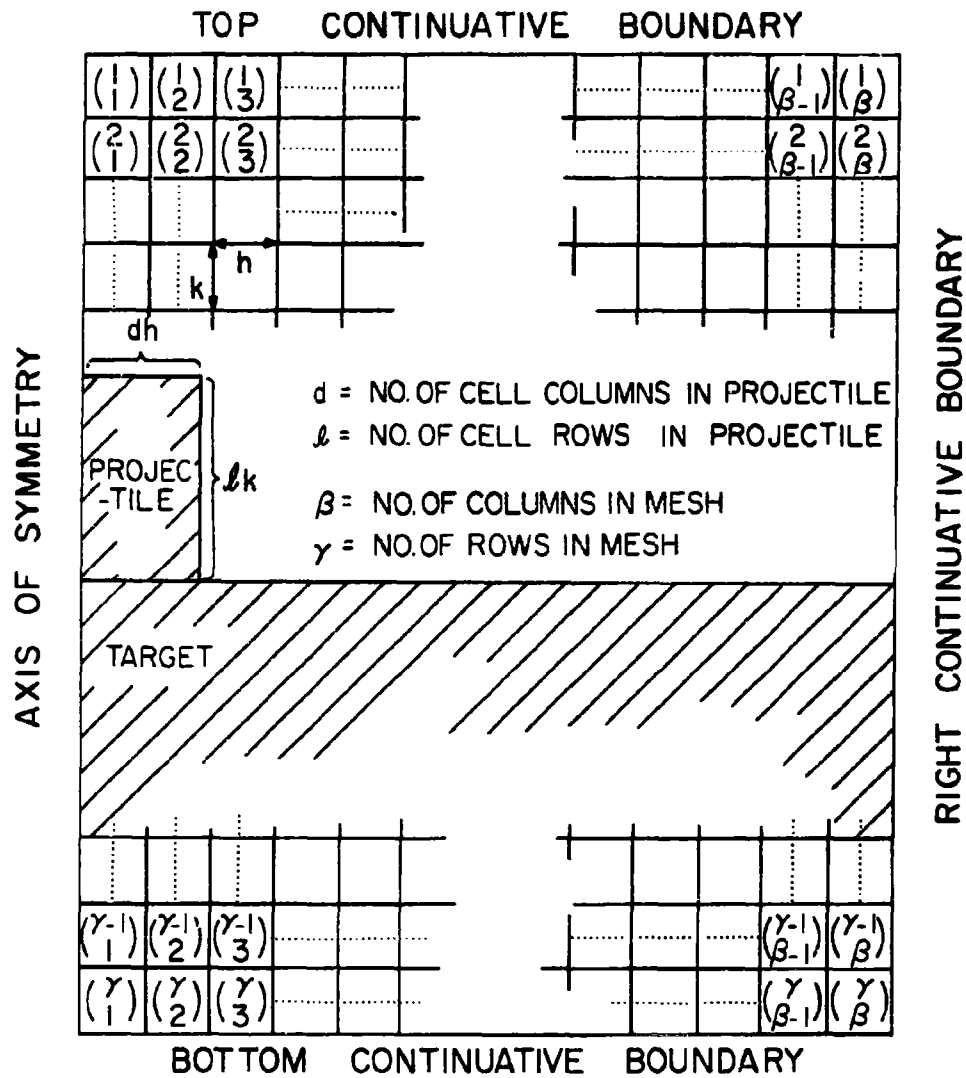


Figure 4. Rectangular mesh superimposed on the projectile-target configuration at instant of impact ( $t = 0$ ).

## VISCO-PLASTIC SOLUTION OF CRATERING

books are kept on the total axial momentum and total energy of the system. These quantities are rigorously conserved during the calculations of both Phases I and II (no truncation error).

No mass particles are permitted to cross the left boundary of the mesh (axis of symmetry) as this would violate the assumption of rotational symmetry. No such restriction applies at the top, bottom, and right boundaries of the mesh; these are treated as "continuative boundaries". Accordingly, the boundary cells along these three sides are treated as interior, being bounded on the outside by cells with identically the same properties in any instant as their adjacent interior neighbors.

Special considerations are required when computing in a cell adjacent to an empty cell (if the cell itself is empty no calculations are made). The velocity of the empty cell is then assumed to be equal to that of the cell being computed; the pressure and the viscosity stresses are assumed to vanish on the boundary of an empty cell.

At the end of Phase II of each time cycle, a tentative value for the pressure to be used in the next time cycle is first computed for each cell  $(\overset{j}{i})$ ,

$$\begin{aligned} \tilde{p}_i^j &= f(\rho_i^j, I_i^j) & \text{if } \xi_i^j = \frac{\rho_i^j}{\rho_0} - 1 \geq 0 \\ &= h(\rho_i^j, I_i^j) & \text{if } \xi_i^j = \frac{\rho_i^j}{\rho_0} - 1 < 0 \end{aligned} \quad (14)$$

Then the hypothesized fracture criterion is applied to the cell and if satisfied one sets  $p_i^j = 0$ . If the criterion is not satisfied the metal remains a continuous medium in cell  $(\overset{j}{i})$  and one sets  $p_i^j = \tilde{p}_i^j$ .

For example, if the fracture criterion of (12) and (13) is being applied one sets

# VISCO-PLASTIC SOLUTION OF CRATERING

$$\begin{aligned}
 p_i^j &= 0 \text{ if } \tilde{p}_i^j < 0 \\
 &\text{and } (|\pi|)_i^j \geq \frac{1}{\omega^*} \left\{ \lambda * - \left[ \frac{1}{c} I_i^j - 300 \right] \ln \delta t / t_0 \right\} \\
 &= \tilde{p}_i^j \text{ otherwise}
 \end{aligned} \tag{15}$$

If the material in a cell does satisfy the fracture criteria then that cell is tagged and given special consideration in the subsequent Phase I calculations since the material within it is no longer part of the continuous medium. In calculating neighboring cells it is treated in the same manner as if it were empty; the field variables in the cell itself are left unchanged. The tag is removed at the end of the Phase I calculations.

As time goes on, the size of the crater increases and the stress wave propagates further into the target. More target material must then be covered by the calculation mesh than is necessary at earlier times. As the dimensions of the disturbances increase, however, sufficient resolution may be obtained by using a larger net size, in both time and space, than was permissible during the initial stages of the process. It is therefore advantageous to repartition the system during the course of a computational run.

The method of repartitioning used is to double the linear dimensions of the cells, i. e., four of the original cells are combined to form a single enlarged cell in the new mesh. The area covered by the mesh is thus increased fourfold without increasing the number of cells in the mesh. To assure that the storage capacity of the computer is not exceeded, it is also required that the total number of mass particles in the new mesh is no greater than in the original mesh. The method provides for this if the original number of particles per cell,  $N$ , is a perfect square. The procedure is illustrated in Fig. 5 for the case of  $N = 4$ .



# VISCO-PLASTIC SOLUTION OF CRATERING

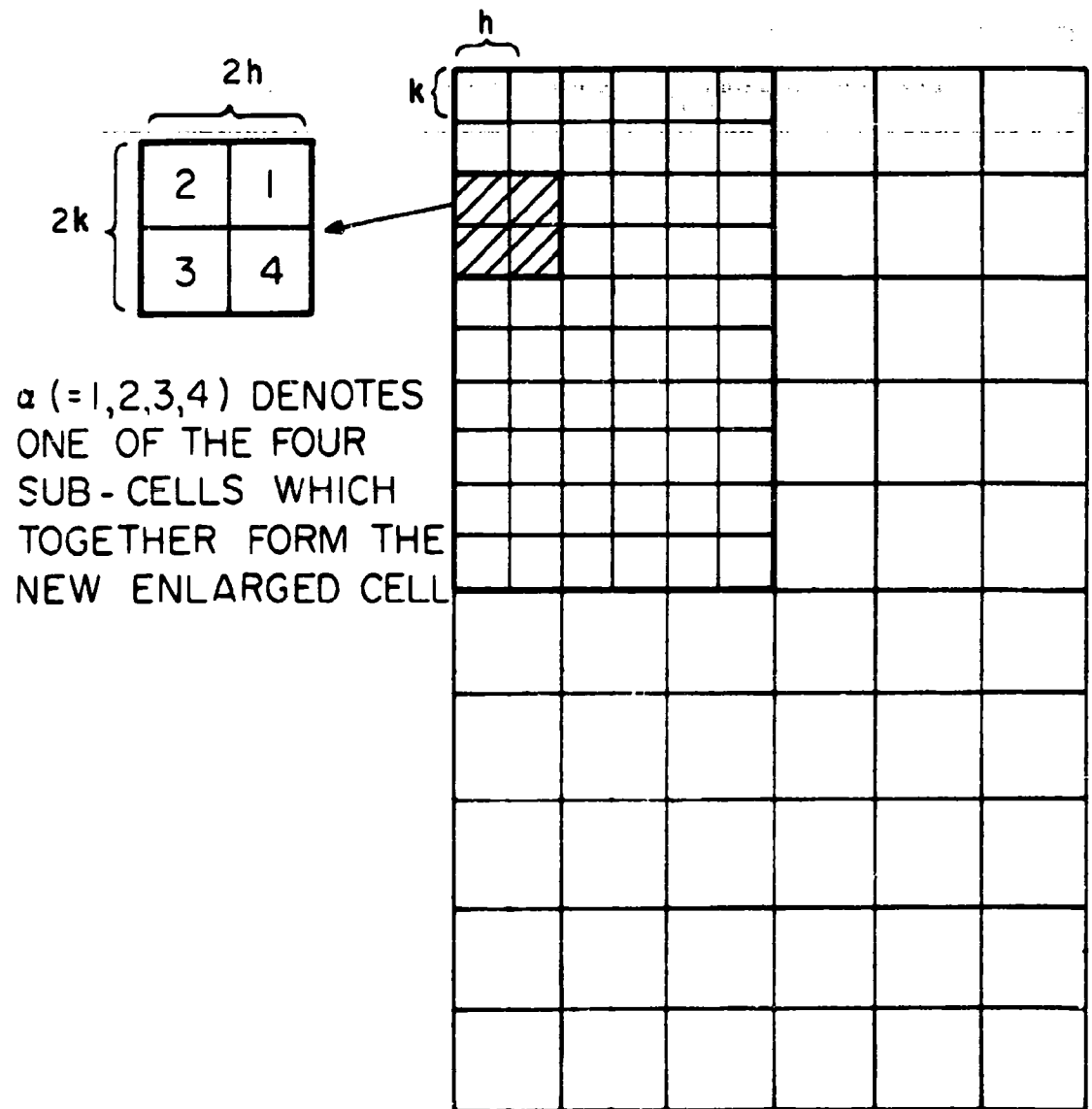


Figure 5.

Schematic representation of the repartitioning in which the mesh area is increased four-fold.

## VISCO-PLASTIC SOLUTION OF CRATERING COMPUTER PROGRAM (PICWICK)

The computational procedure taxes both the memory capacity and the speed of most computers. The optimum programming logic depends upon the trade-off between computation time and storage capacity of the particular computer used. In developing PICWICK, a computer program for the IBM 7094 that uses only internal storage, careful use was made of movable storage. This was found to be very important because the nearly optimum resolution thus obtained is apparently just sufficient to make useful calculations possible without resorting to super computers, such as Stretch, or time consuming external memory.

Mass, energy, and axial momentum are conserved during the repartitioning process, but losses from the mesh prior to repartitioning, either by particle motion or by diffusion across the mesh boundaries, cannot be recovered. If the repartitioning is delayed too long the loss of mass, energy and momentum across the continuative mesh boundaries will introduce large errors. To avoid this PICWICK has been written to automatically repartition whenever the pressure in a given number of cells adjacent to the continuative boundaries exceeds a specified value.

The basic particle-in-cell method of computation is inherently unconditionally unstable, but the amplitude of the oscillations about the true solution is bounded. Moreover, the amplitude may be made as small as desired by taking the time increment of each computational cycle,  $\delta t$ , small enough<sup>(9)</sup>. The stability limit on  $\delta t$  is often more restrictive than the accuracy requirement on  $\delta t$ . In some cases the preferred method of merely choosing  $\delta t$  very small may require too much computer time.

## VISCO-PLASTIC SOLUTION OF CRATERING

In order to allow for adding stability to the difference equations used in Phase I, an "artificial viscosity" of the form<sup>(7)</sup>

$$\vec{q} = \frac{1}{2} \rho (a u_0) \delta x \frac{\partial \vec{u}}{\partial x}$$

has also been included. Here  $a$  and  $u_0$  are constants to be determined by numerical experiment. This device is more often necessary when using PICWICK for the special case that the flow-resistance coefficient is set equal to zero,  $\mu = 0$ , i.e., when considering the perfect fluid model. With  $\mu > 0$  the required stability may be produced by the components  $S_{rr}$  and  $S_{zz}$  of the tensor  $S_{ij}$ , provided  $\mu > 0.25 (a u_0) \rho \delta x$ . The presence of the real viscosity has other and more "real" effects. Its presence affects not only the other components of  $S_{ij}$  but also contributes to  $P$  in a significant fashion. Both real and artificial viscosities were also included in the earlier one-dimensional calculations with the visco-plastic model<sup>(1,2)</sup>.

The stability problem is illustrated by the first series of computer results presented in the next section.

### CALCULATED FLOW FIELDS

Calculations using PICWICK are currently in progress. In the present paper computed flow-fields are presented for the following four impact situations:

- (i) Iron projectile of height 0.8 cm and diameter 1.6 cm impacting a thick iron target at  $v_0 = 0.863$  cm/ $\mu$ -sec.
- (ii) Lead projectile of height 0.8 cm and diameter 1.6 cm. impacting a thick lead target at  $v_0 = 0.526$  cm/ $\mu$ -sec.
- (iii) Lead projectile of height 0.8 cm and diameter 1.6 cm impacting a thick lead target at  $v_0 = 2.21$  cm/ $\mu$ -sec.
- (iv) Iron projectile of height 0.8 cm and diameter 2.0 cm impacting a thick iron target at  $v_0 = 0.863$  cm/ $\mu$ -sec.

## VISCO-PLASTIC SOLUTION OF CRATERING

In cases (i), (ii), and (iii) the iron and lead are treated as a perfect fluid, i. e., the special case  $\mu = 0$  and  $\sigma_{cr} = 0$  is treated. In case (iv) iron is treated as a simple viscous fluid with  $\mu = 0.8$  megapoise and  $\sigma_{cr} = 0$ .

In all of the calculations presented nine particles per cell were used and, initially, the dimensions of each computational cell were  $h = k = 0.1$  cm. No artificial viscosity was used, i. e.,  $\bar{q} = 0$ . The computer results depicting the flow fields at various stages of the cratering processes are presented in Figs. 6 through 17. An arrow in the figures represents the velocity vector for the material particle located at its tail at the indicated instant of time after impact. In each figure the initial impact velocity vector, denoted by  $v_0$ , and the original projectile dimensions are also shown for scaling purposes. Isobars are superposed on the flow fields.

It takes a finite time for the rarefaction wave to propagate to the axis of symmetry from the edge of projectile-target interface where it is generated. Until the rarefaction region arrives the flow remains one dimensional. From symmetry it is clear that where one dimensional flow persists, the interface will be located a distance of  $v_0 t/2$  below the original interface position.

The calculations for iron-iron impact at  $0.863$  cm/ $\mu$  sec ( $\mu = 0$ ), case (i), are depicted in Figs. 6 through 9. This sequence of results is presented to illustrate one of the pitfalls of the basic particle-in-cell method of numerical solution. In Fig. 6 the flow-field is behaving correctly and in Fig. 7 an instability is just becoming apparent. In Fig. 8 the instability has caused the separation of the compressed behind the shock front into two sub-regions even at the axis of symmetry. There is no physical mechanism for this effect as no rarefaction wave has yet progressed to the compressed region.

# VISCO-PLASTIC SOLUTION OF CRATERING

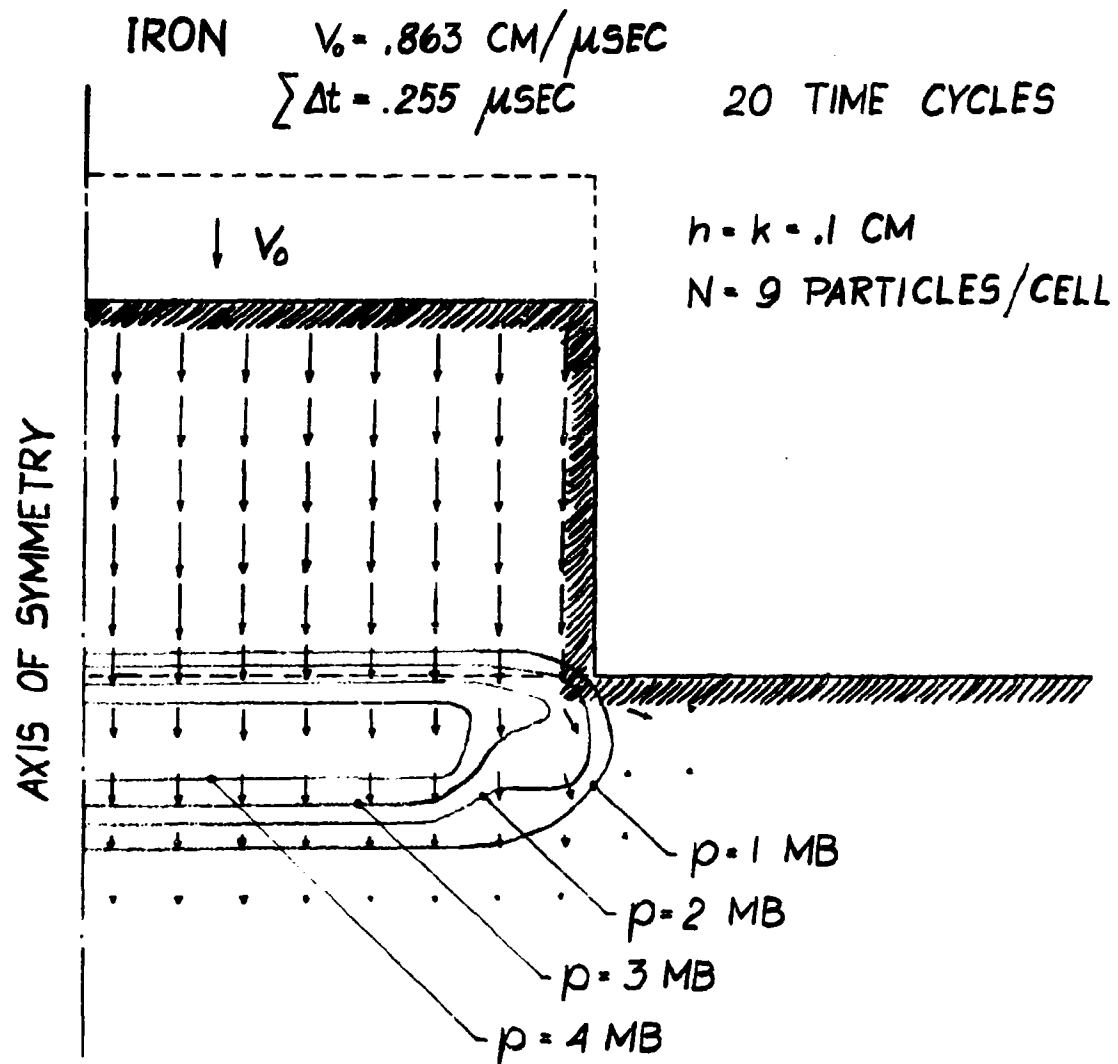


Figure 6.

Flow field when iron is considered a perfect fluid ( $\mu = 0$ ),  $0.255 \mu\text{sec}$  after impact at  $0.863 \text{ cm}/\mu\text{sec}$ .

# VISCO-PLASTIC SOLUTION OF CRATERING

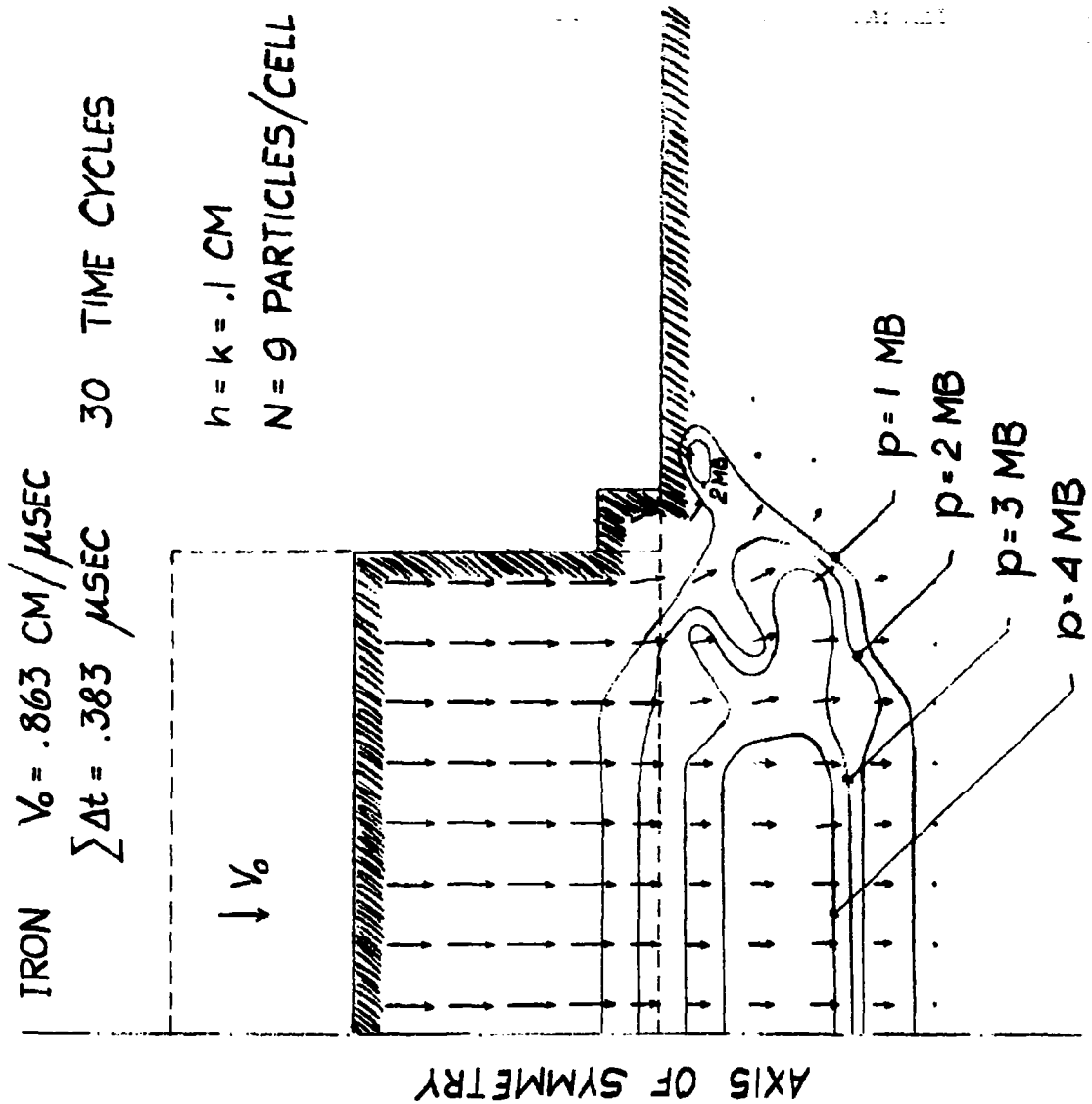


Figure 7. Flow field when iron is considered a perfect fluid ( $\mu = 0$ ),  $0.383 \mu \text{ sec.}$  after impact at  $0.863 \text{ cm}/\mu \text{ sec.}$

# VISCO-PLASTIC SOLUTION OF CRATERING

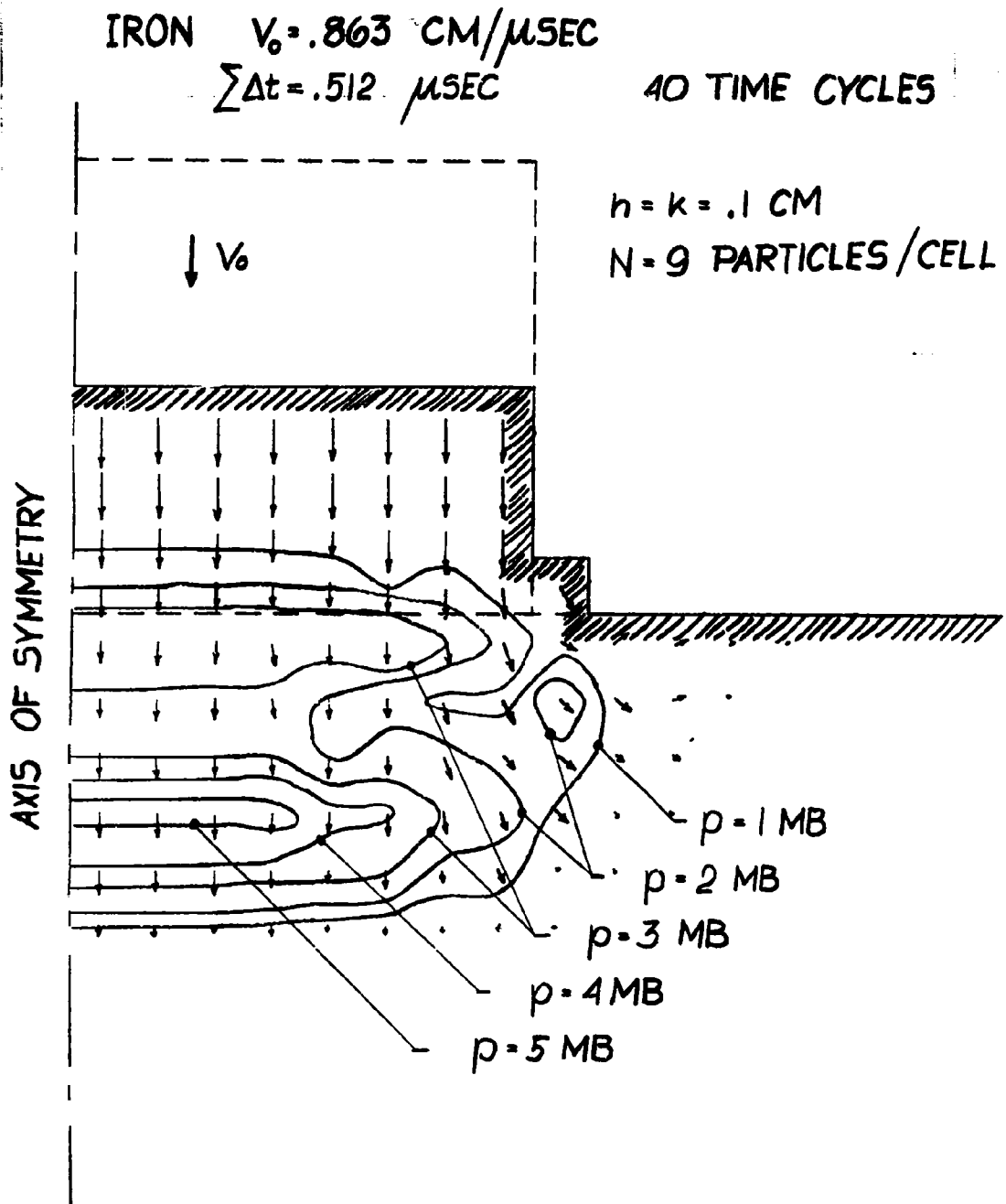


Figure 8. Flow field when iron is considered a perfect fluid ( $\mu = 0$ ),  $0.512 \mu \text{ sec.}$  after impact at  $0.863 \text{ cm}/\mu \text{ sec.}$  Note the separation of compressed region behind shock wave into two subregions.

# VISCO-PLASTIC SOLUTION OF CRATERING

IRON  $V_0 = .863 \text{ CM}/\mu\text{SEC}$   
 $\sum \Delta t = .769 \mu\text{SEC}$

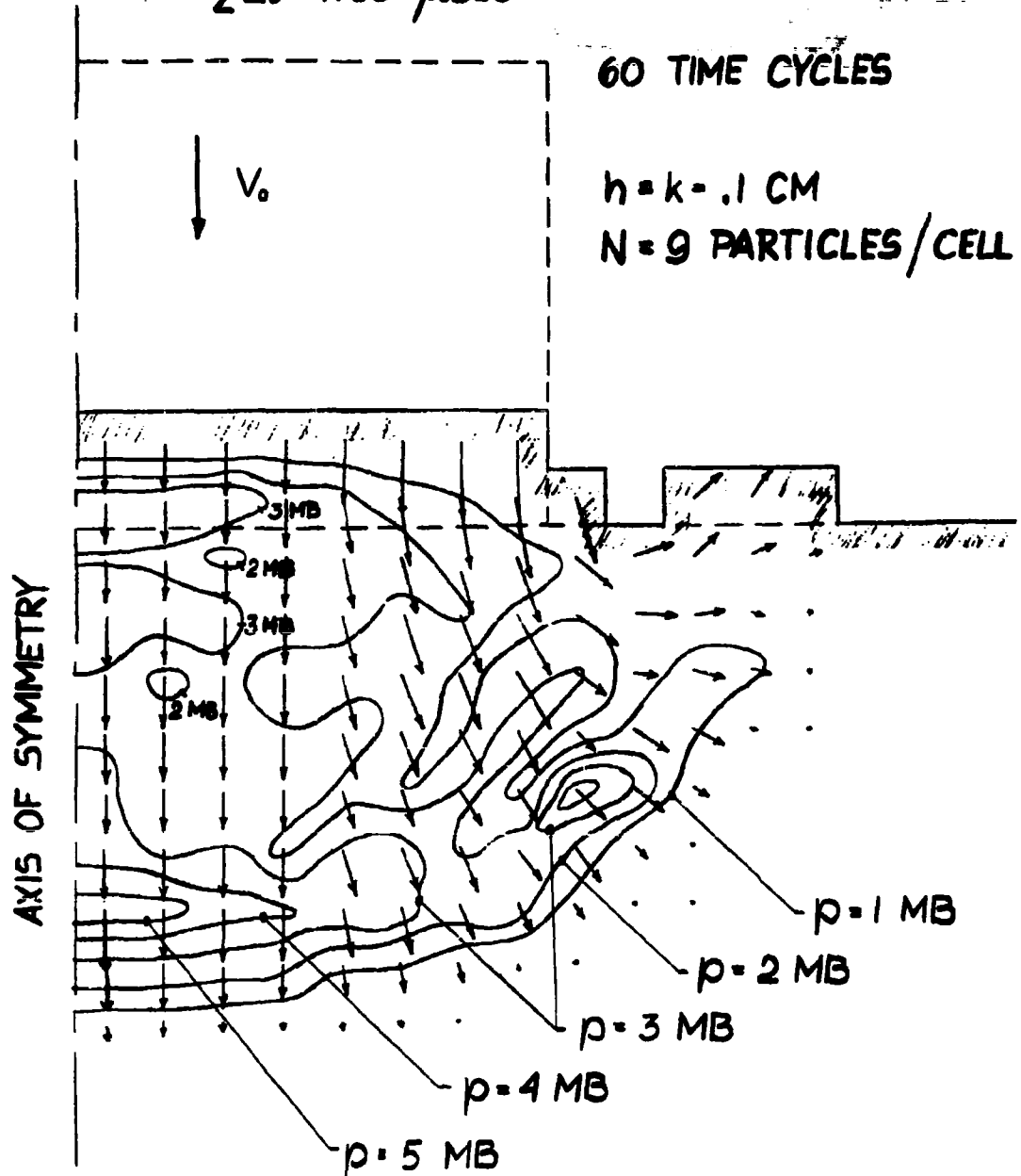


Figure 9. Flow field when iron is considered a perfect fluid ( $\mu = 0$ ),  $0.769 \mu\text{ sec.}$  after impact at  $0.863 \text{ cm}/\mu\text{ sec.}$  The instability persists but remains bounded. It is apparent that the instability would not be detected if only the flow field were studied without observing the pressure field.



## VISCO-PLASTIC SOLUTION OF CRATERING

The choice of  $\delta t = 0.0128 \mu\text{sec}$  is therefore too large for sufficient accuracy. The instability persists in Fig. 9, but has not become significantly worse; this indicates that the instability is bounded.

The calculations for lead-lead impact at  $0.526 \text{ cm}/\mu\text{sec}$ , case (ii), are depicted in Figs. 10 through 13. Lead is more compressible and has a lower sound speed than iron. The choice of  $\delta t = 0.021 \mu\text{sec}$  was found to be sufficiently small for accurate results to be obtained in this case. The sequence of figures illustrate the transition from one-dimension flow near the projectile-target interface to axisymmetric flow in which lateral flow and the ejection of material from the crater by backward flow are the predominant features. Figure 12 is of special interest as it shows the shock front just after it has reached the bottom continuative boundary (denoted by the short dashed line at the bottom of the figure). Five time cycles later the mesh was automatically repartitioned. Subsequently the time step is also doubled. In Fig. 13 the flow-field is depicted  $5.39 \mu\text{sec}$  after impact.

The calculations for lead-lead impact at  $2.21 \text{ cm}/\mu\text{sec}$ , case (iii), are depicted in Figs. 14 through 16. The choice of  $\delta t = 0.005$ , dictated by our stability and accuracy requirements, was found satisfactory. After only  $1 \mu\text{sec}$  from the instant of impact the top of the projectile has already penetrated below the original target surface and the backward flow of the material from the rear of the projectile and from the edge of the forming crater are well under way.

Figure 17 is included to demonstrate the ability of PICWICK to handle physical models other than perfect fluids, case (iv). At this time no long runs have been made with  $\mu > 0$ , but they are planned.

# VISCO-PLASTIC SOLUTION OF CRATERING

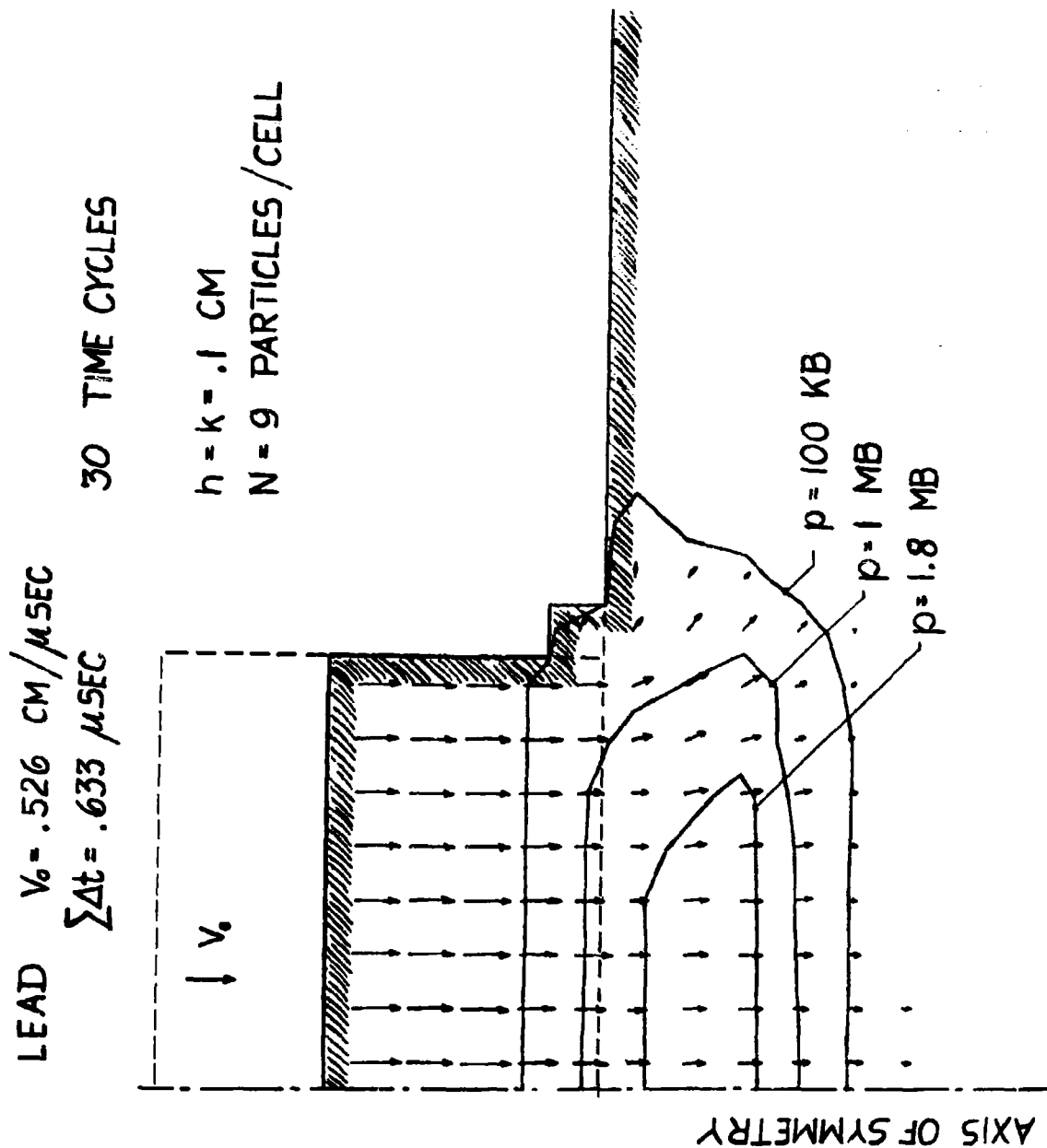


Figure 10.

Flow field when lead is considered a perfect fluid ( $\mu = 0$ ),  $0.633 \mu\text{sec.}$  after impact at  $0.526 \text{ cm}/\mu\text{sec.}$

# VISCO-PLASTIC SOLUTION OF CRATERING

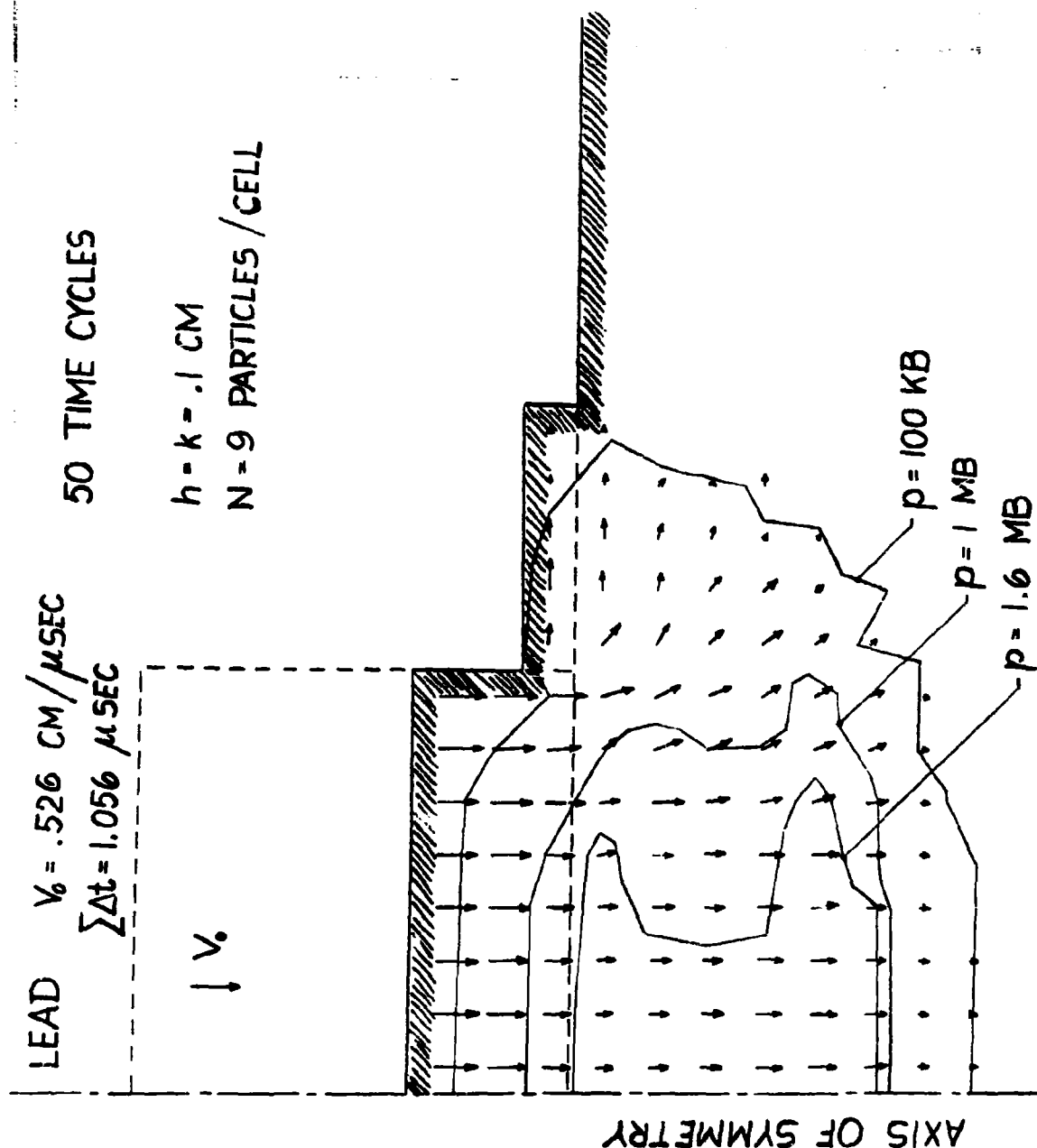


Figure 11.

Flow field when lead is considered a perfect fluid ( $\mu = 0$ ), 1.056  $\mu\text{sec}$ . after impact at 0.526  $\text{cm}/\mu\text{sec}$ .

# VISCO-PLASTIC SOLUTION OF CRATERING

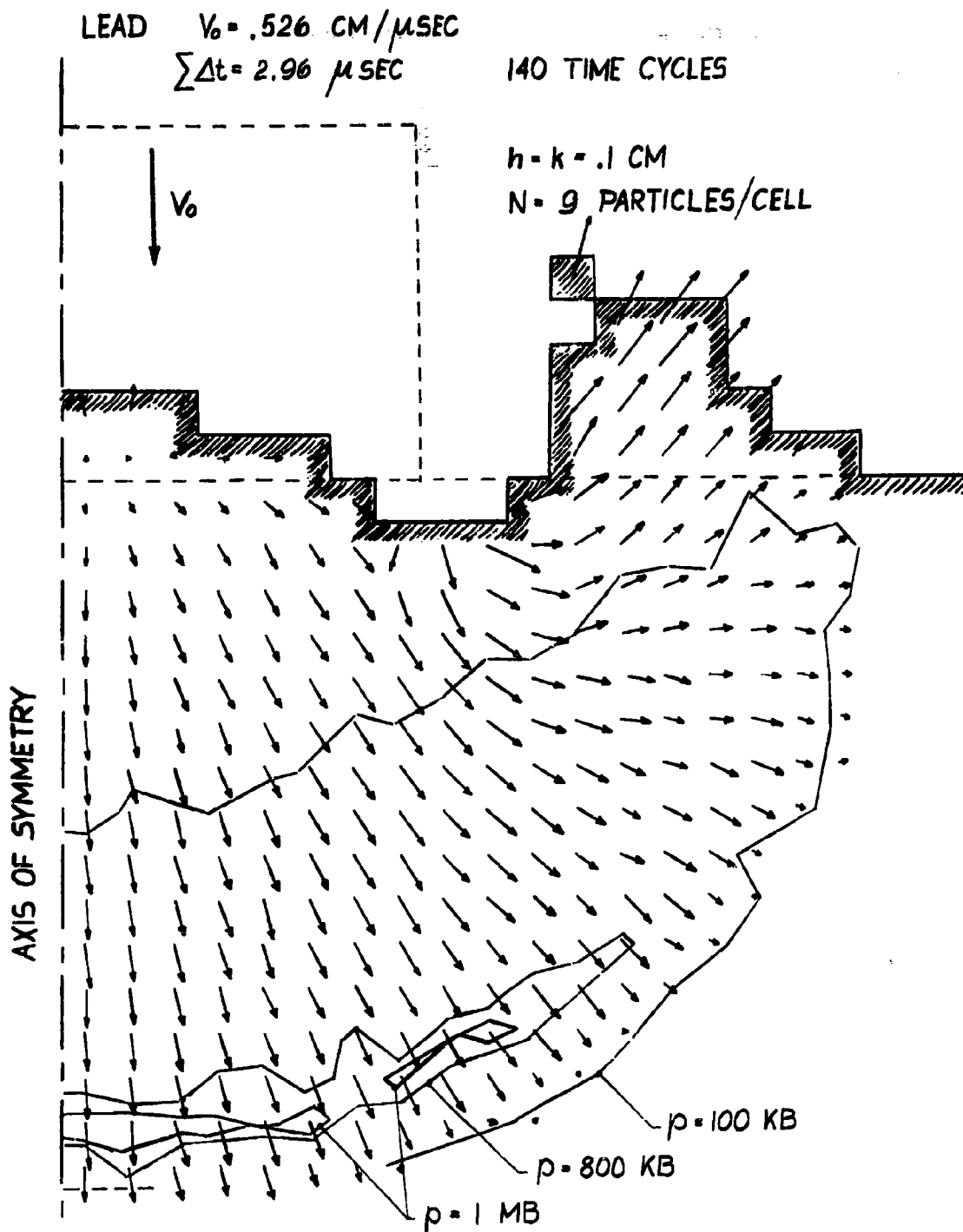


Figure 12. Flow field when lead is considered a perfect fluid ( $\mu = 0$ ),  $2.96 \mu\text{sec}$ . after impact at  $0.526 \text{ cm}/\mu\text{sec}$ . The shock front has reached the bottom continuable boundary which is denoted by the short dashed line in the lower part of the figure.

# VISCO-PLASTIC SOLUTION OF CRATERING

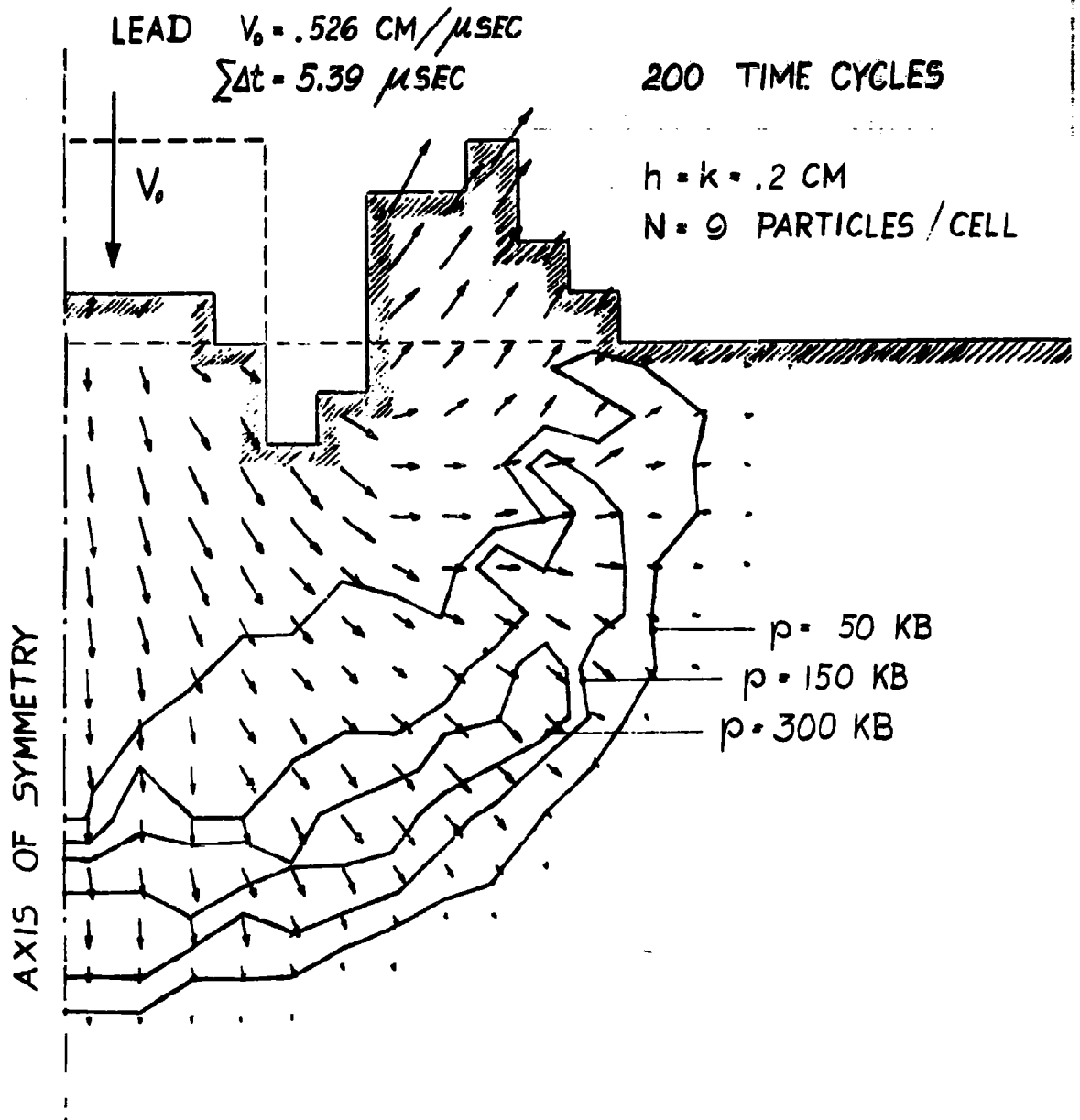


Figure 13. Flow field when lead is considered a perfect fluid ( $\mu = 0$ ),  $5.39 \mu \text{ sec.}$  after impact at  $0.526 \text{ cm}/\mu \text{ sec.}$  The computational mesh has been repartitioned.

# VISCO-PLASTIC SOLUTION OF CRATERING

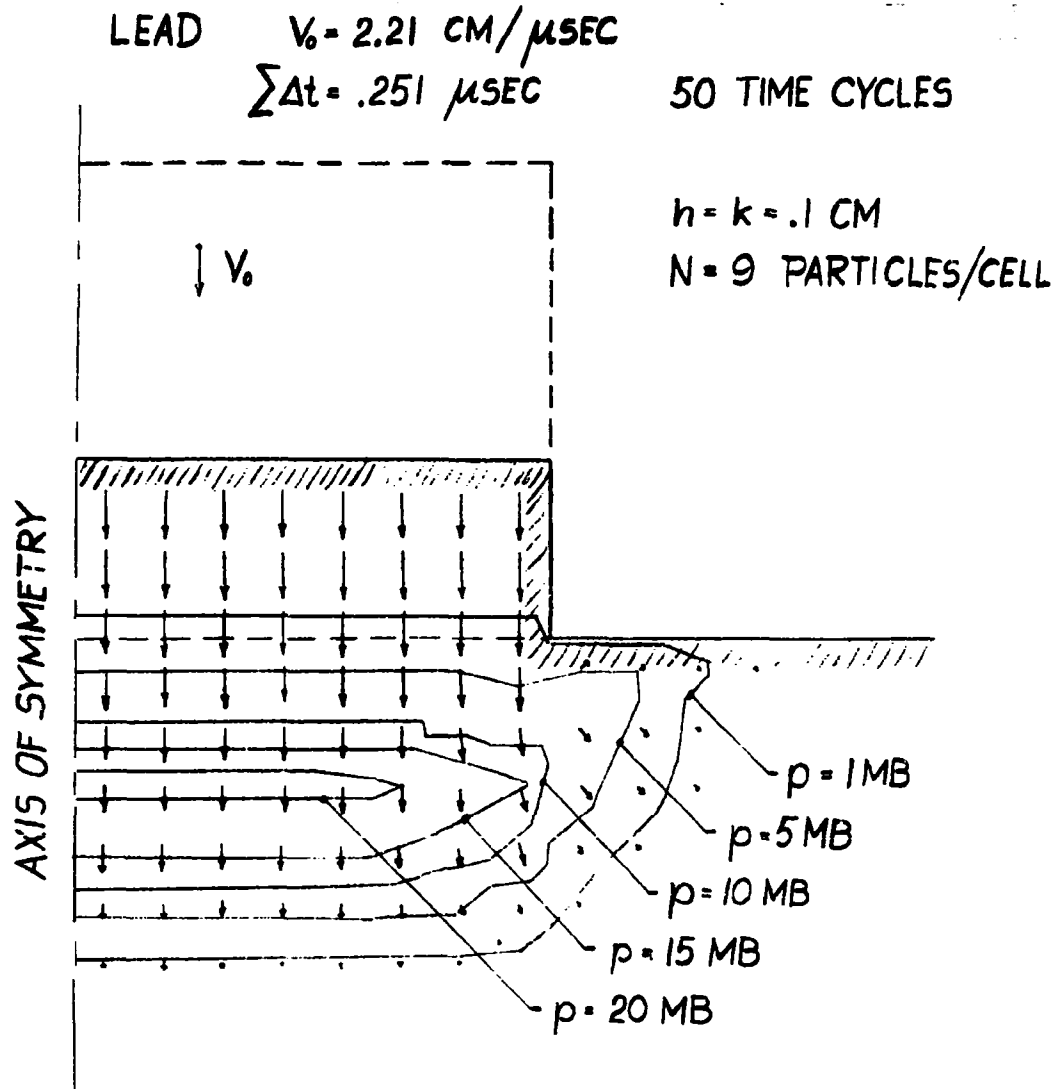


Figure 14.

Flow field when lead is considered a perfect fluid ( $\mu = 0$ ),  $0.251 \mu \text{ sec.}$  after impact at  $2.21 \text{ cm}/\mu \text{ sec.}$

# VISCO-PLASTIC SOLUTION OF CRATERING

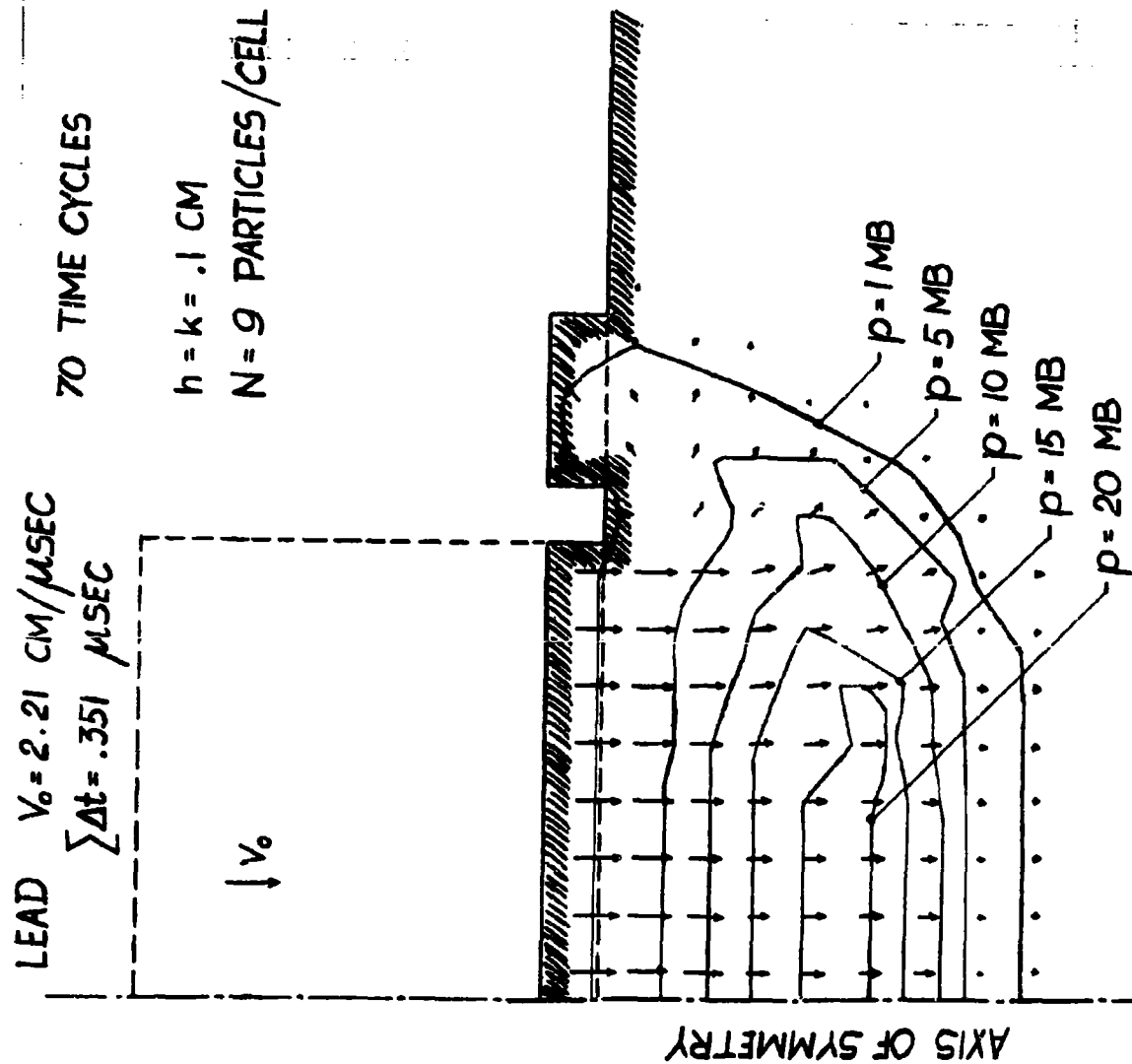


Figure 15.

Flow field when lead is considered a perfect fluid ( $\mu=0$ ),  $0.351 \mu \text{ sec.}$  after impact at  $2.21 \text{ cm}/\mu \text{ sec.}$

# VISCO-PLASTIC SOLUTION OF CRATERING

LEAD  $V_0 = 2.21 \text{ CM}/\mu\text{SEC}$   
 $\sum \Delta t = 1.004 \mu\text{SEC}$

200 TIME CYCLES

$h = k = .1 \text{ CM}$

$N = 9 \text{ PARTICLES/CELL}$

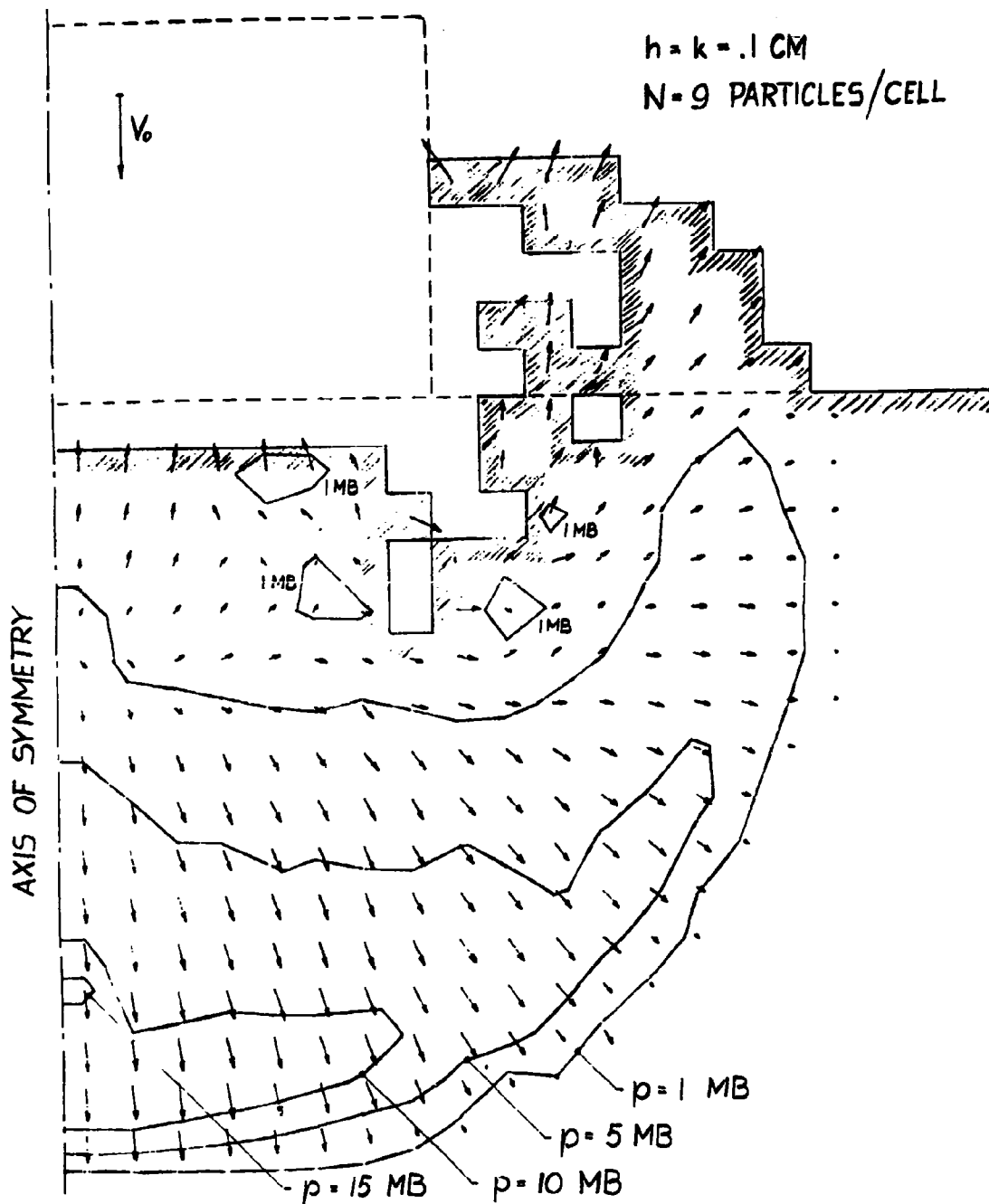


Figure 16.

Flow field when lead is considered a perfect fluid ( $\mu = 0$ ),  $1.004 \mu\text{sec.}$   
 after impact at  $2.21 \text{ cm}/\mu\text{sec.}$



# VISCO-PLASTIC SOLUTION OF CRATERING

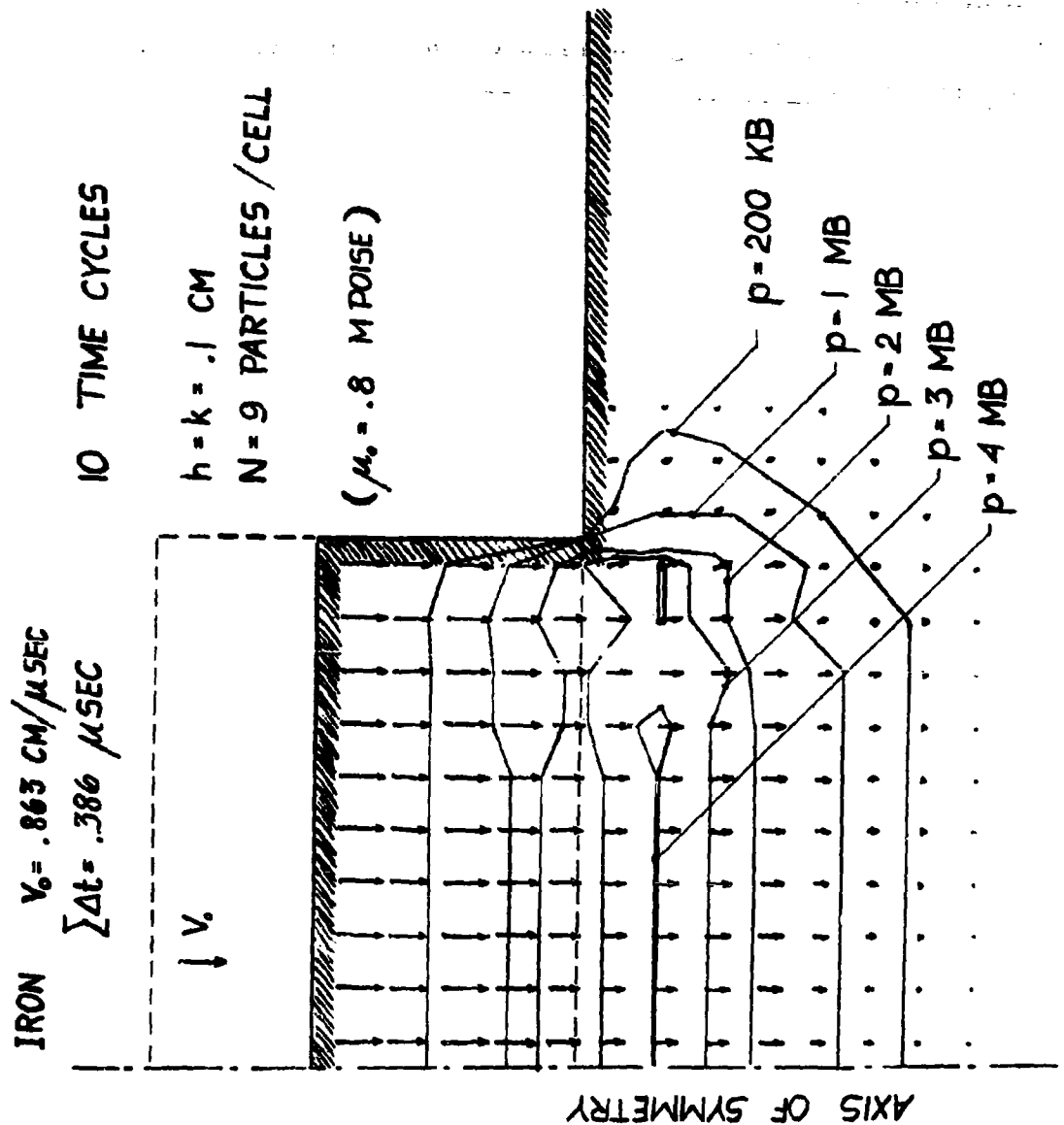


Figure 17. Flow field when iron is considered a viscous fluid ( $\mu = 0.8$ ),  $0.386 \mu\text{sec.}$  after impact at  $0.863 \text{ cm}/\mu\text{sec.}$

## VISCO-PLASTIC SOLUTION OF CRATERING

### CONCLUSIONS

A computer program (PICWICK) has been developed which is capable of comparing various proposed equations of state, flow-resistance coefficients, and fracture criteria. Some choices for these relations have been briefly discussed and the computational method on which the computer program is based has been described. Up to the present time, however, the calculations have been made principally for the special case in which the impacting bodies are treated as a perfect fluid, i.e.  $\mu = 0$  and  $\sigma_{cr} = 0$ .

Some important observations can already be made from the flow-fields plotted from these early results. It was demonstrated that unless care is taken significant errors can result from a bounded instability which is inherent in the basic numerical method. In Fig. 8 this manifested itself by a separation of the compressed region behind the shock front. It is of interest that this same type of behavior is apparent in the flow-field depicted in Fig. 7 of Bjork's paper<sup>(10)</sup>.

It is also important to notice the rapidity with which the intensity of the shock is decreased by the geometrical divergence of the problem. Comparison of Figs. 10 and 13, for example, shows that the shock strength decreased from 1.8 mb to 0.3 mb in only  $5.39 \mu\text{sec}$ . The cratering process is really just getting started; it will continue for well over a hundred microseconds with ever decreasing shock strength. Pressures operative immediately after impact are clearly not representative for the greater part of the cratering process and cannot serve as a valid basis for neglecting the strength of the target.

The calculations for the cases (ii) and (iii) are continuing. Cases (i) and (iv) are also being run with smaller values of  $\delta t$ . A series of calculations in which the resistance to flow and the fracture are also included is planned.

## VISCO-PLASTIC SOLUTION OF CRATERING

### ACKNOWLEDGEMENTS

The author is grateful to Dr. F. W. Wendt for his encouragement and for reading the manuscript, and to Mr. A. B. Sinopoli for assistance in obtaining the numerical results. He is also indebted to his colleagues for their help in reducing the computer data in order to meet the paper deadline. This work was supported in part by contract AF 08(635)-1713, Eglin Air Force Base, Florida, under Project 9860 funded by the Office of Aerospace Research.

## VISCO-PLASTIC SOLUTION OF CRATERING

### REFERENCES

1. Riney, T.D., "Theory of High Speed Impact", Summary Report, November 3, 1960 - November 2, 1961 (APGC-TDR-62-20).
2. Riney, T.D., and Chernoff, P.R., "Inertial, Viscous and Plastic Effects in High Speed Impact", Proc. of Fifth Symposium on Hypervelocity Impact, Vol. 1, Part 2, (April, 1962).
3. Riney, T.D., "Behavior of Metals During Hypervelocity Impact Cratering", Presented at Eighth Midwestern Mechanics Conference in Cleveland, Ohio, April 3, 1963. To be published in the Conference Proceedings.
4. Zhurkov, S.N., and Sanfirova, T.P., "Relation Between Strength and Creep of Metals and Alloys", Journal of Technical Physics, USSR, Vol. 28, p. 1719, 1958.
5. Evans, M. W., and Harlow, F. H., "The Particle-in-Cell Method for Hydrodynamic Calculations", Los Alamos Scientific Laboratory, LA-2139, November, 1957.
6. Harlow, F. H., "Two-Dimensional Hydrodynamic Calculations", Los Alamos Scientific Laboratory, LA-2301, September, 1959.
7. Harlow, F. H., "PIC Method for Fluid Dynamics Calculations" (To be published).
8. Riney, T.D., "Solution of Visco-Plastic Equations for Axisymmetric Hypervelocity Impact", Summary Report, November 3, 1961 - November 2, 1962 (APGC-TDR-62-74).
9. Daly, B.J., "The Bounding of Instabilities of the PIC Difference Equations", LA-2414, March, 1963.
10. Bjork, R.L., "Effects of a Meteoroid Impact on Steel and Aluminum in Space", Technical Report P-1662, Rand Corporation, Eng. Division, Dec. 16, 1958.

UNIVERSITY OF CALIFORNIA  
Lawrence Radiation Laboratory  
Livermore, California

Contract No. W-7405-eng-48

THE CALCULATION OF STRESS WAVES IN SOLIDS

Mark L. Wilkins  
Richard Giroux

# THE CALCULATION OF STRESS WAVES IN SOLIDS

Mark L. Wilkins and Richard Giroux

Lawrence Radiation Laboratory, University of California  
Livermore, California

March 11, 1963

## ABSTRACT

Finite difference techniques are used to solve the continuum equations in two dimensions with axial symmetry. The Tresca yield assumption is used in an equation of state that describes elastic, elastic-plastic, and hydrodynamic flow. Problems are presented where stress waves are induced in solids from the detonation of high explosives, and from the impact of two materials. The effect of strength of materials on wave shapes and on exterior boundaries is shown as a function of time.

# THE CALCULATION OF STRESS WAVES IN SOLIDS

Mark L. Wilkins and Richard Giroux

Lawrence Radiation Laboratory, University of California  
Livermore, California

March 11, 1963

## INTRODUCTION

In recent years experiments on impact loading of metals have demonstrated the existence of elastic-plastic effects in the hundreds of kilobars range (Ref. 1). The implication is that the hydrodynamic model is not sufficient to describe the stress behavior of metals at these pressures. To study the effects of anisotropic stresses in a material, a computer program, HEMP code, has been developed to solve the continuum equations in two dimensions with axial symmetry.

While experiments have demonstrated the existence of a departure from hydrodynamic theory at relatively high pressures, the rheological equation of state at these pressures is not well defined. The equation of state used here will provide a theoretical description applicable to a wide class of practical problems, but uses simple idealizations of the outstanding features of the real phenomena. It is felt that experiments in conjunction with calculations will be an effective way of determining properties of materials at high pressures.

This article is arranged in three parts:

- Part I      Description of the HEMP Code
- Part II     Discussion of the Equation of State Used
- Part III    Application to Stress Wave Problems

## PART I. HEMP CODE

The equations listed below are solved in Lagrange coordinates by finite difference techniques. Sliding interfaces are allowed between an elastic and a hydrodynamic region, but not between two elastic regions. However, an elastic region may slide along a fixed boundary.

## STRESS WAVES IN SOLIDS

The stresses are decomposed into a hydrostatic component  $P$  (all three stress components equal) and an anisotropic component,  $\sigma$  (stress deviator) which describes the resistance of the material to shear distortion. The stress deviators are calculated in terms of an incremental stress resulting from an incremental strain. The time derivative of the stress-strain relations [Eqs. (4)] gives the desired ordered sequence and provides the integrating factor when the material element changes from an elastic to an elastic-plastic state (Ref. 2). It should be noted that the time derivative does not mean that the stresses are rate dependent.

The stresses are incremented in the X-Y coordinate system and must be corrected for any rotation in this plane that may have occurred during the interval from  $n$  to  $n + 1$  (Ref. 3). This comes about because, if an element rotates through an angle  $\omega$  in the interval from  $n$  to  $n + 1$ , the stresses at  $n$  will no longer be referred to the X-Y coordinate system in their new position. Therefore, the stresses at  $n$  must be transformed to the X-Y coordinate system by a rotation through the angle  $\omega$  (see page 94, Ref. 4). The transformation equations result in a correction  $\delta$  that is added to the stresses of Eq. (4). The angle  $\omega$  is given by:  $\sin \omega = 1/2 [\partial \dot{Y} / \partial X - \partial \dot{X} / \partial Y]$ .

### Basic Equations of the HEMP Code

(1) Equations of motion in X-Y coordinates with cylindrical symmetry about the X = axis:

$$\frac{\partial \Sigma_{xx}}{\partial X} + \frac{\partial T_{xy}}{\partial Y} + \frac{T_{xy}}{Y} = \rho \ddot{X}$$

$$\frac{\partial T_{xy}}{\partial X} + \frac{\partial \Sigma_{yy}}{\partial Y} + \frac{\Sigma_{yy} - \Sigma_{\theta\theta}}{Y} = \rho \ddot{Y}$$

$$\Sigma_{xx} = {}^{de}\sigma_{xx} - (P + q)$$

$$\Sigma_{yy} = {}^{de}\sigma_{yy} - (P + q)$$

$$\Sigma_{\theta\theta} = {}^{de}\sigma_{\theta\theta} - (P + q).$$



## STRESS WAVES IN SOLIDS

(2) Equation of continuity:

$$\frac{\dot{V}}{V} = \frac{\partial \dot{X}}{\partial X} + \frac{\partial \dot{Y}}{\partial Y} + \frac{\dot{Y}}{Y}$$

(3) Energy equation:

$$\dot{E} = -(P + q) \dot{V} + V \left[ de_{\sigma_{xx}} \dot{\epsilon}_{xx} + de_{\sigma_{yy}} \dot{\epsilon}_{yy} + de_{\sigma_{\theta\theta}} \dot{\epsilon}_{\theta\theta} + T_{xy} \dot{\epsilon}_{xy} \right].$$

(4) Artificial viscosity:

$$q = C_0^2 \rho^0 (\dot{V}/V)^2 A/V$$

where

$$C_0^0 = \text{constant}$$

A = zone area

$$\rho^0 = \text{reference density.}$$

(5) Equation of state:

$$\text{Stress components} \quad \begin{cases} de_{\sigma_{xx}} = 2\mu \left[ \dot{\epsilon}_{xx} - \frac{1}{3} \frac{\dot{V}}{V} \right] + \delta_{xx} \\ de_{\sigma_{yy}} = 2\mu \left[ \dot{\epsilon}_{yy} - \frac{1}{3} \frac{\dot{V}}{V} \right] + \delta_{yy} \\ de_{\sigma_{\theta\theta}} = 2\mu \left[ \dot{\epsilon}_{\theta\theta} - \frac{1}{3} \frac{\dot{V}}{V} \right] \\ \dot{T}_{xy} = \mu \left[ \dot{\epsilon}_{xy} \right] + \delta_{xy} \end{cases}$$

where

$\mu$  = shear modulus

$\delta$  = correction for rotation (see text)

$$\text{Velocity strains} \quad \begin{cases} \dot{\epsilon}_{xx} = \frac{\partial \dot{X}}{\partial X} & \dot{\epsilon}_{\theta\theta} = \frac{\dot{Y}}{Y} \\ \dot{\epsilon}_{yy} = \frac{\partial \dot{Y}}{\partial Y} & \dot{\epsilon}_{xy} = \frac{\partial \dot{Y}}{\partial X} + \frac{\partial \dot{X}}{\partial Y} \end{cases}$$

$$\text{Hydrostatic pressure} \quad \begin{cases} P = a(\eta - 1) + b(\eta - 1)^2 + c(\eta - 1)^3 + d\eta E \\ \eta = 1/V = \rho/\rho^0 \end{cases}$$

## STRESS WAVES IN SOLIDS

Tresca yield condition

$$|de_{\sigma_{\max}} - de_{\sigma_{\min}}| - 2\tau^0 \leq 0$$

where

$\tau^0$  = shear strength.

$de_{\sigma_{\max}}$  and  $de_{\sigma_{\min}}$  are the maximum and minimum of the three principal stress deviators  $de_{\sigma_1}$ ,  $de_{\sigma_2}$ , and  $de_{\sigma_3}$ .

Notation:

$X, Y$	space coordinates
$\dot{X}$	velocity in X direction
$\dot{Y}$	velocity in Y direction
$\Sigma_{xx}, \Sigma_{yy}, \Sigma_{\theta\theta}, T_{xy}$	total stresses
$de_{\sigma_{xx}}, de_{\sigma_{yy}}, de_{\sigma_{\theta\theta}}$	stress deviators
$\epsilon_{xx}, \epsilon_{yy}, \epsilon_{\theta\theta}, \epsilon_{xy}$	strains
$P$	hydrostatic pressure
$V$	relative volume
$E$	internal energy per original volume density.

The dot over a parameter signifies a time derivative along the particle path.

### PART II. EQUATION OF STATE

This discussion refers to Eqs. (5) of Part I.

The elastic range is described by Hooke's law written in terms of natural stress-strain. At the elastic limit, the yield condition of H. Tresca (1868) is used since it has been very successful in describing the flow of ductile metals. This assumption states that the plastic flow begins when the maximum shear reaches the resistance of the material to shear  $\tau^0$ . The yield conditions must be independent of the coordinate system. In each cycle, therefore, the three stress deviators  $de_{\sigma_{xx}}$ ,  $de_{\sigma_{yy}}$ , and  $de_{\sigma_{\theta\theta}}$  are transformed to the principal stress coordinate system, giving the three principal stress deviators  $de_{\sigma_1}$ ,  $de_{\sigma_2}$ , and  $de_{\sigma_3}$ . The maximum shear is given by  $\tau = (\sigma_{\max} - \sigma_{\min})/2$  (Ref. 4), where  $\sigma_{\max}$  and  $\sigma_{\min}$  are the maximum and the minimum of the three principal stresses. The projections of the radius vector in the principal stress coordinate system are adjusted such that  $\tau \leq \tau^0$ . The stresses in the X-Y coordinate system will then be adjusted in the same way by the transformation equations.

## STRESS WAVES IN SOLIDS

The hydrostatic pressure  $P$  is obtained from Hugoniot data.

For the purpose of the calculations presented in the next section, it is assumed that one-dimensional Hugoniot data measure the hydrostatic pressure plus the shear distortion stress. Using the shear strength at the elastic limit for aluminum,  $\tau^0 = 0.00149$  mb calculated from C. D. Lundergan data (Ref. 5) and the Hugoniot data of J. M. Walsh (Ref. 6), the equation of state for aluminum becomes:

$$\tau^0 = 0.00149 \text{ mb}$$

$$\mu = 0.248 \text{ mb}$$

$$P = 0.73 (\eta - 1) + 1.72 (\eta - 1)^2 + 0.4 (\eta - 1)^3$$

$$\rho^0 = 2.7$$

$$\eta = \rho / \rho^0.$$

We are considering that the only motion is in the X direction. The constants in the pressure relation have been chosen such that the total stress  $\Sigma_{xx} = -P + \text{de}\sigma_{xx}$  reproduces the elastic data up to the Hugoniot elastic limit. In terms of the Lamé constants,  $\lambda + \mu$ , the equations give:  $-\Sigma_{xx} = (\lambda + 2\mu) \Delta V$ . Beyond the elastic limit the equations reduce for the one-dimensional case to:  $-\Sigma_{xx} = +P + 4/3 \tau^0$  and  $-\Sigma_{xx}$  reproduces the Hugoniot data. The equations [Eqs. (4)] will give as an unloading path  $-\Sigma_{xx} = +P - 4/3 \tau^0$ .

The above description allows the material to unload first elastically and then plastically along a curve offset below the hydrodynamic pressure. Calculations show that even though  $\tau^0$  is small compared to a given total stress  $-\Sigma_{xx}$ , the effect on the wave structure is very pronounced. This is because rarefactions behind a shock wave can travel faster than they would with an all-hydrodynamic material (see Fig. 1).

The value of  $\tau^0$  can be made a function of pressure to describe the fact that some materials can support more shear with increasing pressures. If  $\tau^0$  is set to  $\infty$ , the program will describe a completely elastic case. If  $\tau^0$  is set to zero, the stress deviator will automatically be set to zero and a hydrodynamic description will result. This would be the case when distortion is taking place at low pressure and enough work has been done to melt the material.

In resumé, it is seen that the one-dimensional Hugoniot measurements, together with a shear modulus  $\mu$  and a shear strength  $\tau^0$ , have been extended to describe a three-dimensional stress system by means of Eqs. (4). The yield

# Flying Plate

## STRESS WAVES IN SOLIDS

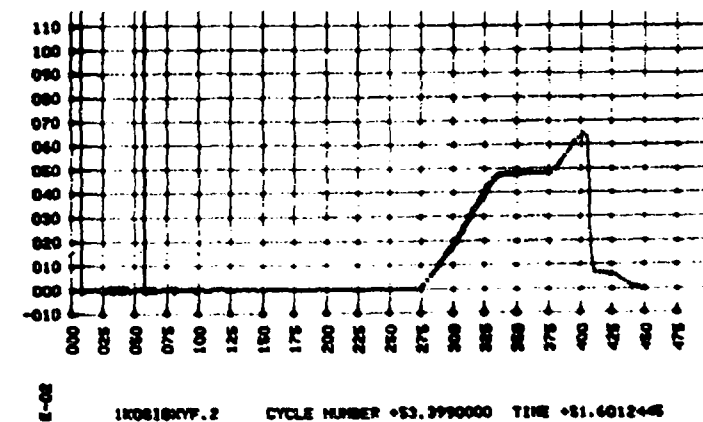
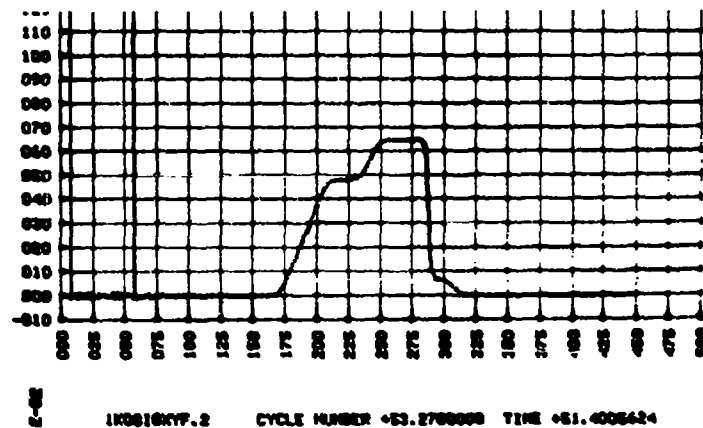
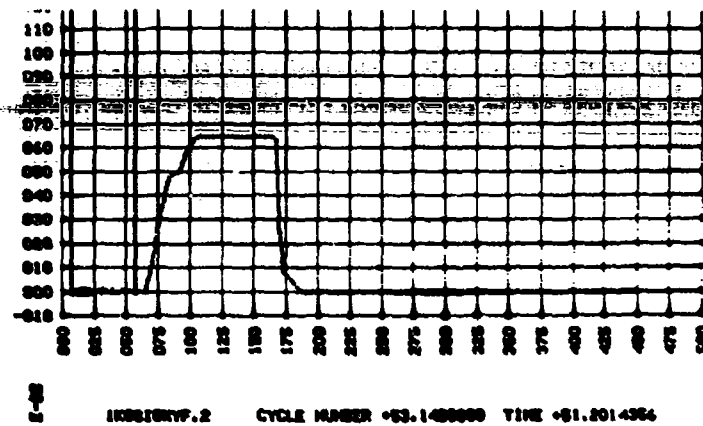


FIGURE I

Stress vs position in Al resulting from the impact of  
a flying Al plate with velocity  $\dot{x} = 0.08 \frac{\text{cm}}{\mu\text{s}}$

## STRESS WAVES IN SOLIDS

point from elastic to elastic-plastic flow is determined by the value of  $\tau^0$  chosen. The yield point from elastic-plastic to hydrodynamic flow occurs when  $\tau^0$  is set to zero. The latter yield criterion could be based on the internal energy in a mass element.

### PART III. APPLICATION TO STRESS WAVE PROBLEMS

Figure 1 shows the stress,  $-\Sigma_{xx}$ , as a function of position  $X$  in an aluminum target plate for different times. The stress was a result of a flying aluminum plate with a velocity  $X = 0.08$  cm/ $\mu$ sec striking the target plate. The elastic precursor can be seen travelling in front of the plastic wave. The step behind the plastic wave is a result of the elastic relief wave travelling faster than the plastic relief wave. The relief waves result when the reflected impact shock reaches the rear surfaces of the flying plate. The calculation was made using the constants given for aluminum in Part II ( $\tau^0 = 0.00149$  mb) and the equation of state of Part I [Eqs. (5)].

Figure 2 shows the result of a cylindrical charge of high explosive detonated in contact with an aluminum plate. The point of detonation was the upper right-hand corner on the line of cylindrical symmetry (upper horizontal line). The high explosive was PBX 94/04 and the aluminum equation of state used  $\tau^0 = 0.00149$  mb.

Figure 3 shows the same problem as above, but with an arbitrary shear strength  $\tau^0 = 0.010$  mb.

Figure 4 shows the stress waves in an all-elastic medium resulting from a spherical detonation. The explosive (Comp B) was originally in a 1-cm-radius sphere and was detonated from the center. The elastic material extends from 1 to 5 cm and has the elastic parameters for copper. The figure shows stresses versus radius. To the left of the interface, shown by the dotted vertical line, is the hydrodynamic pressure of the high explosive. To the right are the radial and tangential stresses plotted positive in compression. The stress connecting to the high-explosive pressure is the radial stress. An additional shock originating from the hydrodynamic spherical cavity can also be seen. The point of interest here is that the radial stress goes into tension behind the spherically expanding front. The head-on interaction of two spherically expanding shocks (for example if Figs. 2 and 3 had high-explosive charges on both sides of the aluminum) could result in a fracture when the two tension tails met. This geometry has been studied experimentally by C. R. Cassity (Ref. 7).

# STRESS WAVES IN SOLIDS

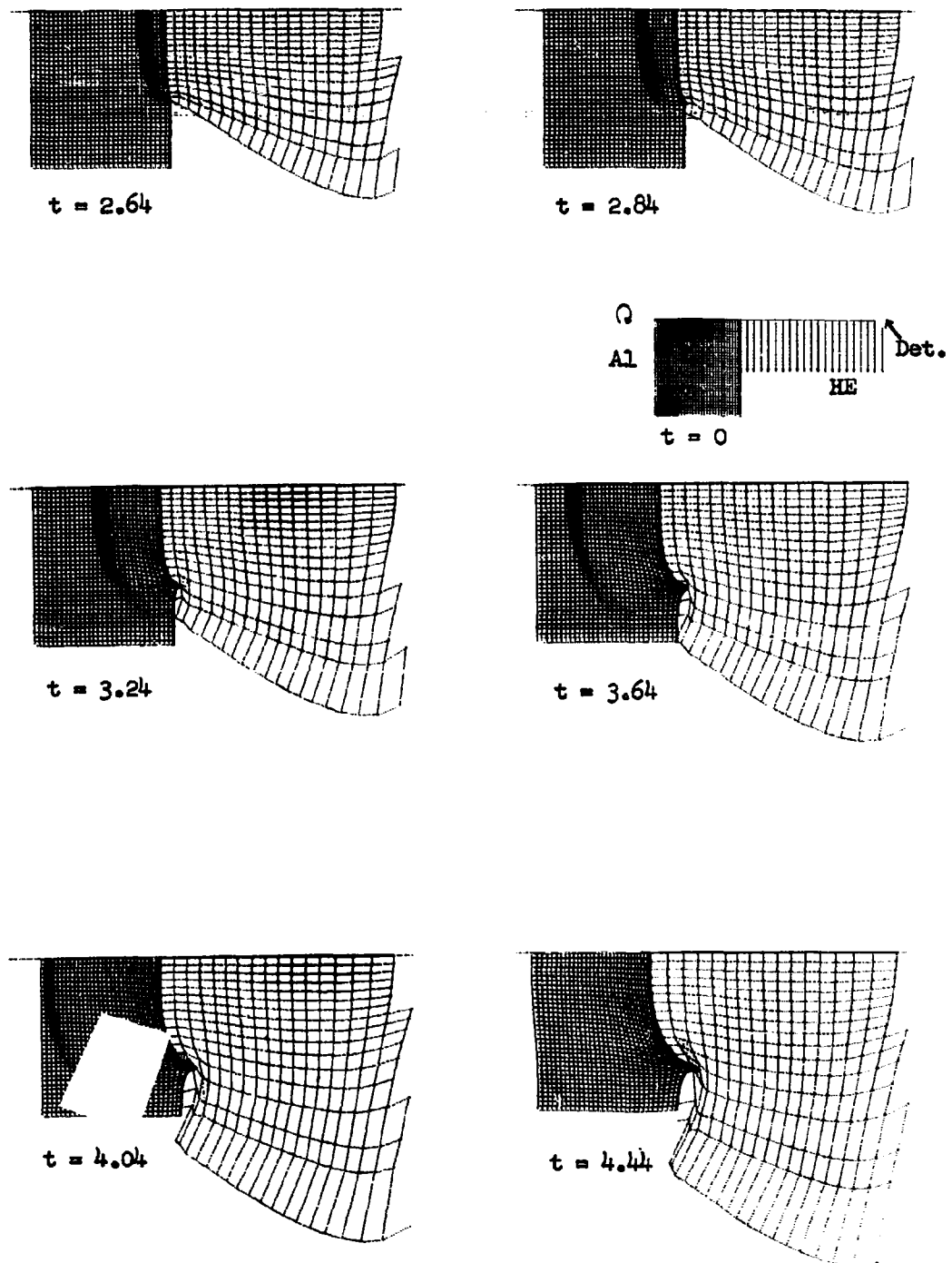


Figure II

Time sequence (in microseconds) of a cylindrical HE charge detonated against Al with shear strength  $\tau^0 = 0.00149$  mb. The shaded zones give the position of the stress front.

# STRESS WAVES IN SOLIDS

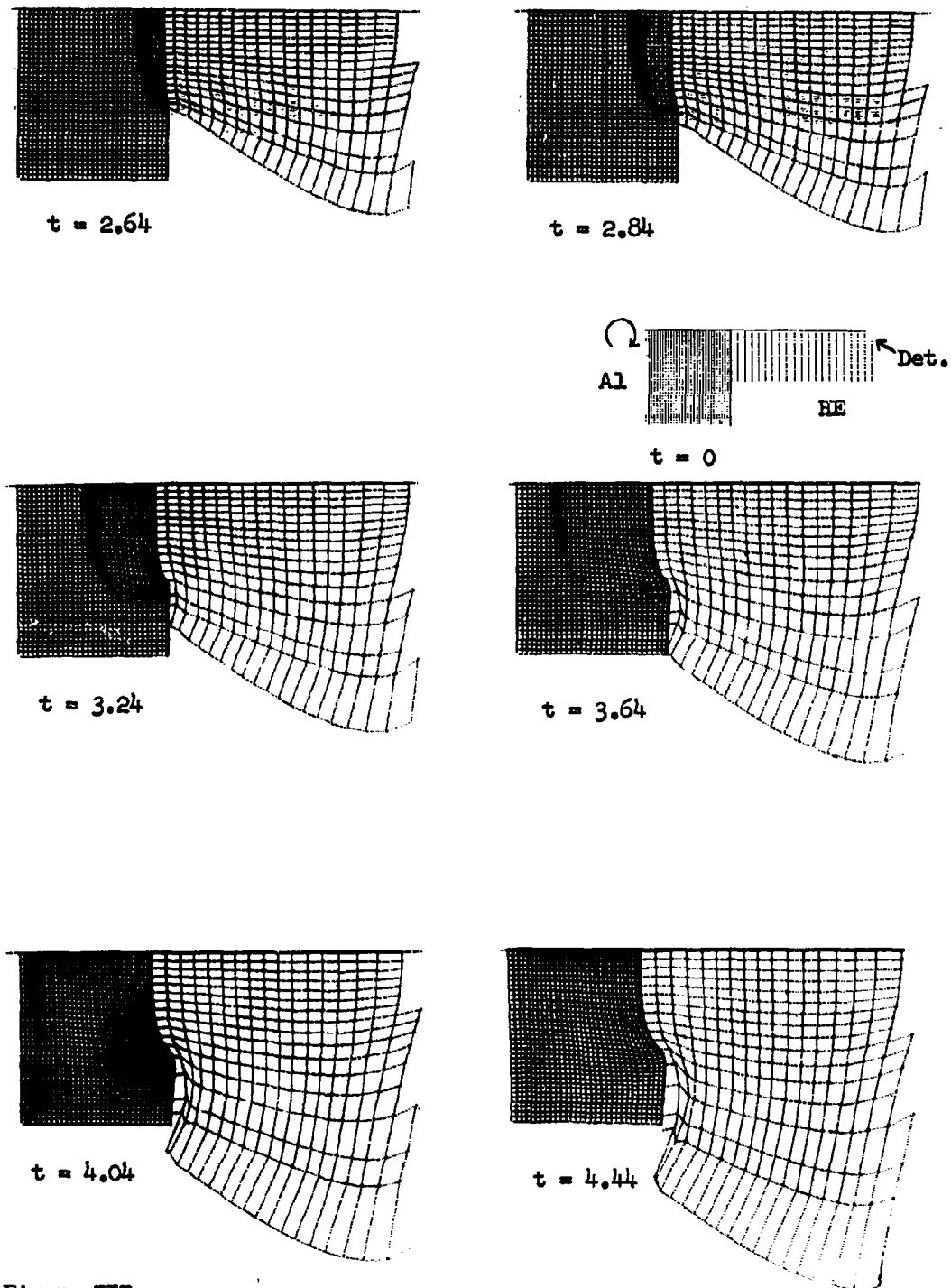


Figure III

Time sequence (in microseconds) of a cylindrical HE charge detonated against Al with shear strength  $\tau^0 = 0.010$  mb.

# STRESS WAVES IN SOLIDS

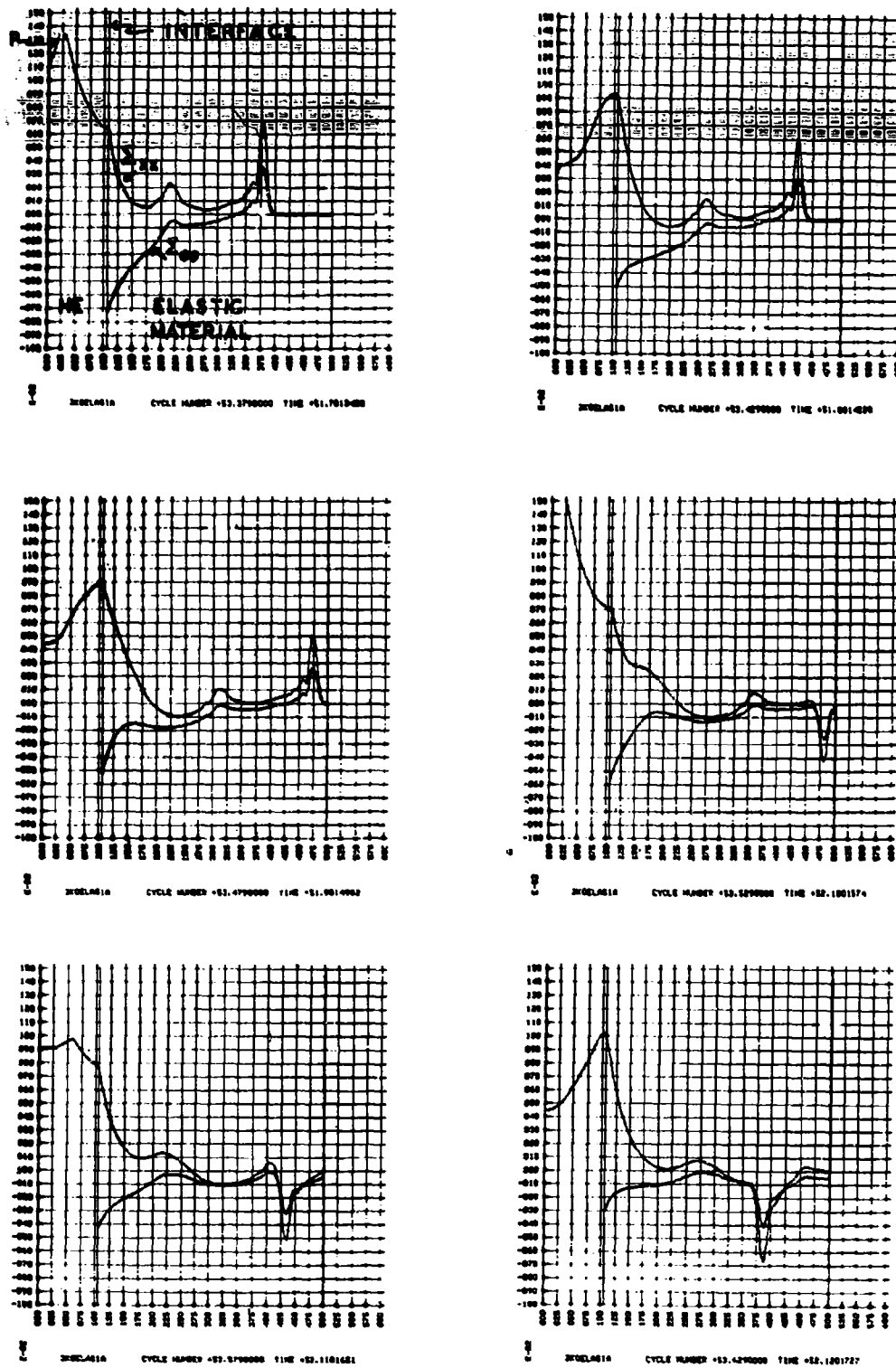


Figure IV

Stress vs radius for spherically diverging elastic waves.



## STRESS WAVES IN SOLIDS

Figure 5 shows the impact of a flying iron cylindrical disk striking an aluminum target. The aluminum shear strength  $\tau^0 = 0.00149$  mb. The upper horizontal line is the axis of cylindrical symmetry.

# STRESS WAVES IN SOLIDS

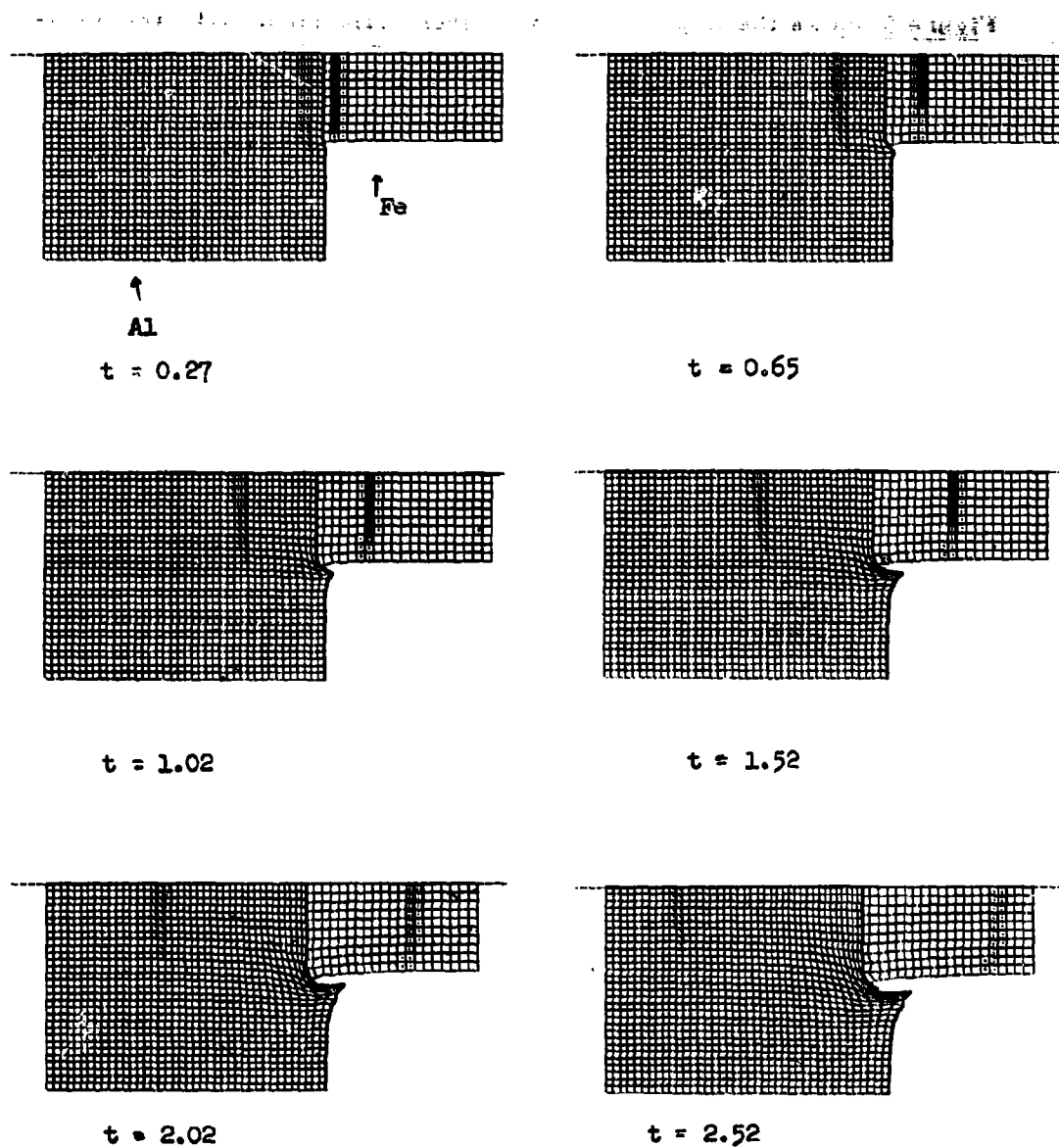


**Figure V**  
 Iron cylindrical pellet with velocity  $\dot{x} = -.1\text{cm}/\mu\text{s}$  striking an  
 Al plate with  $\tau^0 = 0.00149$ .

## STRESS WAVES IN SOLIDS

### REFERENCES

\* Work performed under the auspices of the U. S. Atomic Energy Commission.

1. L. V. Al'tshuler, S. B. Kormer, M. I. Brazhnik, L. A. Vladimirov, M. P. Speranskaya, and A. I. Funtikov, "The Isentropic Compressibility of Aluminum, Copper, Lead, and Iron at High Pressures," Soviet Physics JETP, 11, (No. 4), 766-775, (1960).

2. L. W. Morland, "The Propagation of Plane Irrotational Waves through an Elastoplastic Medium," Phil. Trans. Roy. Soc., A251, 341-383, (1959).

3. G. Maenchen and J. Nuckolls, "Calculations of Underground Explosions," UCRL-6438, Part II, Paper J, (1961).

4. A. Nadai, Theory of Flow and Fracture of Solids, McGraw-Hill Book Company, Inc., New York, (1950).

5. C. D. Lundergan, "The Hugoniot Equation of State of 6061-T6 Aluminum at Low Pressures," SC-4637 (RR), (1961).

6. John M. Walsh, Melvin H. Rice, Robert G. McQueen, and Frederick L. Yarger, "Shock-Wave Compressions of Twenty-Seven Metals," Phys. Rev. 108, (No. 2), 196-216, (1957).

7. C. R. Cassity, "Stress Waves in Solids," J. Appl. Phys., 31, (No. 8), 1377-1381, (1960).

A Hypervelocity Impact Model  
for Completely Deforming Projectiles

Prepared by:

J. L. Luttrell

U. S. NAVAL ORDNANCE LABORATORY  
White Oak, Silver Spring, Maryland

## A HYPERVELOCITY IMPACT MODEL

### ABSTRACT

A simple mathematical model of crater formation by a hypervelocity impact has been developed. The model predicts the depth and duration of penetration into thick ductile targets by compact deforming projectiles which are small compared to the final crater volume.

## A HYPERVELOCITY IMPACT MODEL

The craters formed in thick targets by compact projectiles, at velocities high enough to destroy the projectiles, are frequently observed to be approximately hemispherical. Based on this observation and the assumptions that the particle velocity field about a growing crater is similar to that of a translating spherical boundary, and that crater growth is resisted by a similar stress distribution to that of infinite solid exposed to hydrostatic pressure on a spherical internal boundary, a mathematical model of the penetration,  $P$ , into a material of density,  $\rho$ , and strength,  $S$ , formed by a projectile of mass,  $m$ , and velocity,  $v$ , has been developed.

A sphere of radius,  $r$ , moving in a fluid at rest at infinity, has an additional apparent mass equal to  $\rho 2/3 \pi r^3$ , due to the kinetic energy supplied to the flow about the sphere.

An infinite solid loaded internally on a spherical surface by a normal pressure,  $p$ , develops a tangential tensile stress on the loaded surface. If  $p = 2S$  plastic flow occurs. If the target is semi-infinite with a hemispherical cavity forming on the surface the projected area of the cavity being  $\pi r^2$ , the force normal to the plate is  $p \pi r^2 = 2 \pi r^2 S$ . The work done in plastically forming a hemispherical crater would then be the flow pressure  $p$  integrated over the crater surface  $2 \pi r^2$  and integrated again along  $r$

$$W = \int 2S(2 \pi r^2) dr = 4/3 \pi r^3 S. \quad (1)$$

Assuming impact has occurred the momentum of the system is  $(m + \rho 2/3 \pi r^3) \dot{P}$  and the mechanical resistance to penetration is the tension on the yielding crater surface  $2 \pi r^2 S$ . Since there are no external forces

$$\frac{d}{dt} [(m + \rho 2/3 \pi r^3) \dot{P}] + S 2 \pi r^2 = 0. \quad (2)$$

The case being considered is that of  $P = r$  and  $\dot{P} = \dot{r}$

$$(m + \rho 2/3 \pi r^3) \ddot{r} + \rho 2 \pi r^2 \dot{r}^2 + S 2 \pi r^2 = 0. \quad (3)$$

$$(\frac{m}{\rho} + 2/3 \pi r^3) \dot{r} d\dot{r} + (\dot{r}^2 + \frac{S}{\rho}) 2 \pi r^2 dr = 0. \quad (4)$$

$$(\frac{m}{\rho} + 2/3 \pi r^3) (\dot{r}^2 + \frac{S}{\rho})^{1/2} = K. \quad (5)$$

The constant of integration,  $K$ , is evaluated by equating the initial projectile kinetic energy,  $E$ , to the sum of the

# A HYPERVELOCITY IMPACT MODEL

kinetic energy and the work of deformation of projectile and target when  $r = a$ . The parameter,  $a$ , is defined as the radius of a sphere of target material having the same mass as the projectile. Since equal though opposite forces are acting on the projectile and target, the work of initial deformation is assumed to be equal.

$$E = \frac{m}{2} v^2 = \frac{m}{2} \dot{r}^2 + 1/2 \rho^{2/3} \pi a^3 \dot{r}^2 + 2(4/3 \pi a^3 S) \quad (6)$$

but by the definition of  $a$ ,  $\rho^{2/3} \pi a^3 = \frac{m}{2}$

so that at  $r = a$

$$\dot{r}^2 = 2/3(v^2 - 4\frac{S}{\rho}) \quad (7)$$

$$\text{and } K = 3/2 \frac{m}{\rho} (2/3 v^2 - 5/3 \frac{S}{\rho})^{1/2} \quad (8)$$

The maximum value of  $r$  occurs when  $\dot{r} = 0$ ; therefore since the final penetration is  $P = r_{\text{max}}$  and combining equations (5) and (8) with  $\dot{r} = 0$

$$P = \left\{ \frac{9}{4\pi} \frac{m}{\rho} \left[ \frac{\rho}{S} 2/3 v^2 - 5/3 \right]^{1/2} - \frac{3}{2\pi} \frac{m}{\rho} \right\}^{1/3} \quad (9)$$

For a spherical projectile, and a target of the same density the penetration in calibers

$$\frac{P}{d} = .674 \left[ \left( \frac{v^2}{S/\rho} - 2.5 \right)^{1/2} - .82 \right]^{1/3} \quad (10)$$

Some representative predictions of this model are tabulated below.

	$S$ dynes/cm <sup>2</sup>	$\sqrt{S/\rho}$ KM/sec	Velocity in KM/sec for		
			$P/d=1.4$	$P/d=1.8$	$P/d=2.3$
Low alloy steel	$7 \times 10^9$	.3	3.0	6.0	12.0
Mild steel	$3 \times 10^9$	.2	2.0	4.0	8.0
Aluminum 24ST	$3 \times 10^9$	.33	3.3	6.6	13.2
Aluminum, soft	$5 \times 10^8$	.13	1.3	2.6	5.2
Lead	$10^8$	.03	.3	.6	1.2

# A HYPERVELOCITY IMPACT MODEL

If  $P$  is known the duration,  $T$ , of the cratering process can be computed using equation (5) and the condition that  $\dot{r} = 0$  when  $r = P$ .

$$\left(\dot{r}^2 + \frac{S}{\rho}\right)^{1/2} = \frac{(\frac{m}{\rho} + 2/3 \pi P^3)}{(\frac{m}{\rho} + 2/3 \pi r^3)} \sqrt{\frac{S}{\rho}} \quad (11)$$

Separating variables:

$$T = \sqrt{\frac{\rho}{S}} \int_a^P \frac{dr}{\sqrt{\frac{(2a^3 + P^3)^2}{(2a^3 + r^3)^2} - 1}} \quad (12)$$

If the projectile volume is small compared to the final crater volume, i.e.  $P^3 \gg a^3$ , (12) approaches

$$\begin{aligned} T &\approx P \sqrt{\frac{\rho}{S}} \int_0^1 \frac{(r/P)^3 d(r/P)}{\sqrt{1 - (r/P)^6}} = \frac{P}{6} \sqrt{\frac{\rho}{S}} \frac{(-1/2)!(-1/3)!}{(-1/6)!} \\ &= .354 P \sqrt{\frac{\rho}{S}} \end{aligned} \quad (13)$$

As an illustration equation (13) predicts that hypervelocity cratering of lead will persist for about 120 microseconds per cm. of final depth while the duration in a hard aluminum alloy such as 24ST will be about 11 microseconds per cm.

This model is considered applicable where the initial inertial pressure  $1/2 \rho v^2$  is an order of magnitude greater than the mechanical strength of the materials of both projectile and target. There are additional limitations in that the crater shape was initially specified rather than derived and some phenomena which would be especially significant for brittle targets have been neglected.



Reproduction of this report is authorized for unlimited distribution.

# A BLAST-WAVE THEORY OF CRATER FORMATION IN SEMI-INFINITE TARGETS\*

by

William J. Rae\*\* and Henry P. Kirchner\*\*\*

Cornell Aeronautical Laboratory, Inc.  
Buffalo 21, New York

\*This research was sponsored by the National Aeronautics and Space Administration under Contract No. NAS 3-2121

\*\*Research Aerodynamicist, Aerodynamic Research Department

\*\*\*Staff Scientist, Computer Research Department

## BLAST-WAVE THEORY OF CRATER FORMATION

### ABSTRACT

An analytic formulation of the problem of crater formation is presented, using the methods of blast-wave theory. The approximations on which this approach is based are chiefly concerned with the self-similar, or progressing-wave nature of the solution, with the type of state equation used, and with the extent to which the conservation of energy and momentum can be fulfilled. These approximations and the limitations which they impose are reviewed, particularly as applied to the problem of shock propagation in solids. Neglect of momentum conservation is shown to be a good approximation, but use of the Mie-Grüneisen equation of state is found to be largely incompatible with the assumption of similarity. An approximate nonsimilar solution for impact-generated shock propagation is derived, and displays excellent agreement with observed shock-wave trajectories.

To derive a penetration law from any solution, some point in the trajectory must be chosen as the crater radius. The strong influence of this choice on the penetration law is discussed, and it is argued that the target strength should play a role in its determination. A simple choice of the crater-formation criterion, related to the intrinsic shear strength of the target, is utilized in conjunction with the nonsimilar solution, to derive a penetration law which correlates a large amount of data.

# BLAST-WAVE THEORY OF CRATER FORMATION

## TABLE OF CONTENTS

ABSTRACT	164
INTRODUCTION	166
1. Basic Equations	170
2. Similarity Assumption and its Implications	175
3. The Equation of State	179
4. Conservation of Energy and Momentum	182
5. Taylor Solution for Shock Propagation	197
6. Quasi-Steady Solution for Shock Propagation	201
7. Methods of Crater-Size Prediction	209
CONCLUDING REMARKS	215
REFERENCES	217
APPENDIX: Simulation of Meteoroid Impact by Energy Release	220
ACKNOWLEDGEMENT	225
LIST OF SYMBOLS	226

# BLAST-WAVE THEORY OF CRATER FORMATION

## INTRODUCTION

The fluid-mechanical approximation pioneered by Bjork<sup>1</sup> is commonly accepted as a proper description of the early phases of target deformation due to hypervelocity impact. In such a model, the motion of any small mass element is assumed to be governed by the pressures acting on its faces, while resistance to shear deformation is neglected. The differential equations that govern such inviscid motion are the usual Euler equations expressing the conservation of mass, momentum, and energy, together with the equation of state of the compressible medium. These differential equations contain two spatial variables, as well as the time, and the problem of solving them is extremely difficult. To date, the only solutions that have been reported are the numerical results of Bjork.<sup>1, 2</sup>

The purpose of this paper is to present an approximate analytic solution of the same set of equations. The solution is achieved by adapting the techniques of blast-wave theory, which has produced such rich dividends in the study of various high-energy fluid-flow problems.<sup>3, 4, 5</sup> The spirit of the approach is to simplify the analysis wherever possible by making certain approximations to the true physical situation. We seek generality and simplicity in the results. Some exactness in specifying details of the problem must, of course, be sacrificed.

The blast-wave theory has been developed, over the years, as a means of describing various high-energy gas flows. In order to apply such a theory to the problem of cratering by high-speed projectiles, each of its approximations must be carefully examined in this new context.

The most important approximations can be grouped into three main

## BLAST-WAVE THEORY OF CRATER FORMATION

categories; first, those concerned with the assumption of a self-similar form of solution, second, those associated with the equation of state of the medium, and third, those dealing with the extent to which global energy- and momentum-conservation conditions can be satisfied. After a brief review of the basic fluid-mechanical equations in Section 1, these three categories are discussed in detail in Sections 2, 3, and 4. Following this, Sections 5 and 6 present two different approximate solutions for the time-history of the shock as it penetrates the target. Finally, Section 7 takes up the question of crater-size prediction.

The assumption of similarity discussed in Section 2 supposes that the flow pattern behind the shock that advances into the target is always the same, if viewed on a scale given by the depth to which the shock has penetrated at that instant. This approximation has the effect of suppressing time as an independent variable, and constitutes a key mathematical simplification. At the same time, it imposes certain restrictions, the most important of which is that only certain forms of the state equation are permitted. Section 3 discusses the extent to which the Mie-Grüneisen equation approximates the permitted form. It is found that only the extremely high-pressure states of a Mie-Grüneisen material fulfill the required form, and in that range, the true equation of state can be replaced by a perfect gas of constant specific-heat ratio. In every impact, the shock ultimately degenerates to a stress wave, so that the high pressures required for the perfect-gas approximation are only achieved during a small portion of the process. Thus, a realistic description of shock propagation in solids requires a solution which accounts for the nonsimilar nature of the problem.

## BLAST-WAVE THEORY OF CRATER FORMATION

To conserve the total energy and momentum of the impacting particle, the solution must allow for spatial variations in two dimensions, and consequently a set of partial differential equations must be solved. Section 4 describes approximate solutions of these equations along the axis of symmetry, and compares these results with those obtained using only one spatial variable, the distance from the impact point. Solutions with only one spatial coordinate can conserve only the total energy of the system, and are found to be practically identical with the more complicated two-dimensional solutions. A corollary of this finding is that the energy of the projectile is the more important parameter, its momentum playing only a secondary role. In Section 4, the physical reasons for this behavior are described, and its implications on simulation of hypervelocity impact are discussed.

Sections 5 and 6 are devoted to a description of the trajectory traced out by the shock as it propagates through the target. The classical Taylor solution for self-similar motion of a shock through a perfect gas is reviewed in Section 5. With this as a background, we then present in Section 6 an approximate solution which allows for the nonsimilar nature of shock propagation in solids. In this solution, the shock speed tends naturally to the stress-wave limit at large time. Comparisons with experimental observations in transparent targets, and with Bjork's calculated shock trajectories, reveal an excellent correlation over a wide range of conditions. This correlation uses only the energy of the projectile, and the density and stress-wave velocity of the target. The fact that data up to an impact speed of 30 Km/sec are all correlated suggests that impact-generated shock propagation follows essentially the same mechanism over the entire speed range.

## BLAST-WAVE THEORY OF CRATER FORMATION

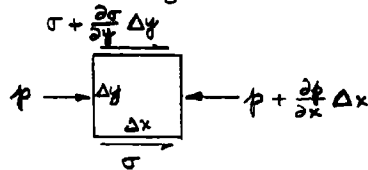
To predict crater size, the solution for shock position as a function of time is not enough. Section 7 points out that an auxiliary criterion is needed, to identify the point at which the crater will form. The correlation presented here indicates that the choice of this criterion is the most important factor in determining the ultimate penetration law. In Section 7, the question of choosing a proper crater-formation criterion is not settled, but several choices are discussed. One of these is shown to be capable of correlating a large amount of data, through proper selection of a certain constant.

The net effect of these studies has been to reveal the potentialities and the limitations of blast wave theory, as applied to crater formation in semi-infinite targets. Considerable progress has been made, notably in establishing the relative unimportance of momentum conservation, and in identifying the nonsimilar nature of the problem, and its connection with the Mie-Grüneisen state equation. At the same time, a great deal of work remains to be done in certain other areas, especially in regard to the formulation of a suitable criterion for crater formation.

# BLAST-WAVE THEORY OF CRATER FORMATION

## 1. BASIC EQUATIONS

When a particle strikes a target surface at high speed, large amounts of energy and momentum are quickly transferred to a very small portion of the surface. Consequently, a strong shock wave is driven into the target, generating extremely large pressures, typically measured in megabars. Because these pressures are so large compared with the material strength, one is led to the approximation that the impacted medium behaves like an inviscid, compressible fluid. In fact, the justification for such an approximation is not provided by the magnitude of the pressure themselves, but must come from a consideration of their gradients. Consider a small mass element



The net force acting in the  $x$ -direction is proportional to  $\frac{\partial \sigma}{\partial y} - \frac{\partial p}{\partial x}$ ; thus the neglect of resistance to shear deformation requires  $\frac{\partial p}{\partial x} \gg \frac{\partial \sigma}{\partial y}$ . To replace this comparison of gradients by a simple comparison of pressure with strength, is to assume that rates of change in the two perpendicular directions are of the same order, and that the proper orders of magnitude to use for  $p$  and  $\sigma$  are the impact pressure and material strength at high strain rates. There appears to be no reason for doubting either of these assumptions in the early stages of the impact process. Thus the problem of determining the response of the target material becomes essentially that of solving the fluid-mechanical equations (conservation of mass, momentum and energy) together with the equation state of the medium



# BLAST-WAVE THEORY OF CRATER FORMATION

Mass: (1)

$$\frac{D\rho}{Dt} + \rho \operatorname{div} \vec{q} = 0$$

Momentum: (2)

$$\rho \frac{D\vec{q}}{Dt} + \operatorname{grad} p = 0$$

Energy: (3)

$$\frac{De}{Dt} + p \frac{D(1/\rho)}{Dt} = 0 \quad \text{or} \quad \frac{Ds}{Dt} = 0$$

Equation of State: (4)

$$e = F(p, \rho)$$

Here,  $\rho$  denotes the density,  $p$  the pressure,  $e$  the internal energy per unit mass,  $s$  the entropy per unit mass, and  $\vec{q}$  the velocity vector. The symbol  $\frac{D}{Dt}$  is the convective derivative

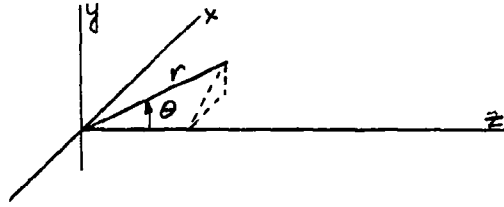
$$\frac{D}{Dt} = \frac{\partial}{\partial t} + \vec{q} \cdot \nabla \quad (5)$$

in which  $t$  is the time and  $\nabla$  the gradient operator. It should be noted that the assumption of an inviscid fluid has been made by setting the right-hand side of Eq. (2) equal to zero. If shearing forces were to affect the motion, they would appear in this equation. Consistent with this approximation, energy changes arising from viscous dissipation and heat conduction are omitted from the energy equation. In addition, energy changes due to radiation and chemical change are neglected. Thus the conservation of energy simply states that for each element of mass, changes of internal energy  $de$  are balanced by changes in the flow-work term  $p d(1/\rho)$ . Alternatively, this condition may be expressed by stating that the entropy of a given mass element does not change after it has been processed by the shock.

## BLAST-WAVE THEORY OF CRATER FORMATION

Finally, it should be noted that the use of an equation of state implies the assumption of thermodynamic equilibrium.

It is assumed that the target motion is symmetric about an axis normal to the original target surface. For such an axisymmetric flow, the scalar forms of the equations of motion in spherical coordinates are



( x, y plane is the target surface)

$$\frac{\partial p}{\partial t} + u \frac{\partial p}{\partial r} + \frac{w}{r} \frac{\partial p}{\partial \theta} + \rho \left( \frac{\partial u}{\partial r} + \frac{1}{r} \frac{\partial w}{\partial \theta} + \frac{2u}{r} + \frac{w}{r} \cot \theta \right) = 0 \quad (6)$$

$$\frac{\partial u}{\partial t} + u \frac{\partial u}{\partial r} + \frac{w}{r} \frac{\partial u}{\partial \theta} - \frac{w^2}{r} + \frac{1}{\rho} \frac{\partial p}{\partial r} = 0 \quad (7)$$

$$\frac{\partial w}{\partial t} + u \frac{\partial w}{\partial r} + \frac{w}{r} \frac{\partial w}{\partial \theta} + \frac{uw}{r} + \frac{1}{\rho r} \frac{\partial p}{\partial \theta} = 0 \quad (8)$$

$$\frac{\partial e}{\partial t} + u \frac{\partial e}{\partial r} + \frac{w}{r} \frac{\partial e}{\partial \theta} - \frac{1}{\rho^2} \left( \frac{\partial p}{\partial t} + u \frac{\partial p}{\partial r} + \frac{w}{r} \frac{\partial p}{\partial \theta} \right) = 0 \quad (9)$$

$$e = F(p, \rho) \quad (10)$$

Here  $u$  and  $w$  denote the velocity components in the  $r$ - and  $\theta$ - directions respectively. Equations (6) to (10) constitute five relations for the quantities  $p$ ,  $\rho$ ,  $u$ ,  $w$  and  $e$ . One can also work with the entropy, rather than the internal energy, in which case the last two equations are replaced by

# BLAST-WAVE THEORY OF CRATER FORMATION

$$\frac{\partial A}{\partial t} + u \frac{\partial A}{\partial r} + \frac{w}{r} \frac{\partial A}{\partial \theta} = 0 \quad (11)$$

$$A = A(p, \rho) \quad (12)$$

The boundary conditions that apply at the shock wave, i.e. at  $r = R_s(\theta, t)$ , state that the discontinuities in velocity, pressure, density, etc. across the wave are given by the Rankine-Hugoniot relations. For a shock advancing into a medium at rest these are

$$\begin{array}{c|c} \begin{array}{c} u_1 \\ \rightarrow \\ \rho_1, p_1, e_1 \end{array} & \begin{array}{c} u_s \\ \rightarrow \\ \rho_0, p_0, e_0 \end{array} \end{array} \quad \begin{array}{l} u_0 = 0 \\ \rho_0, p_0, e_0 \end{array}$$

$$\rho_0 u_s = \rho_1 (u_s - u_1) \quad (13)$$

$$p_1 - p_0 = \rho_0 u_s u_1 \quad (14)$$

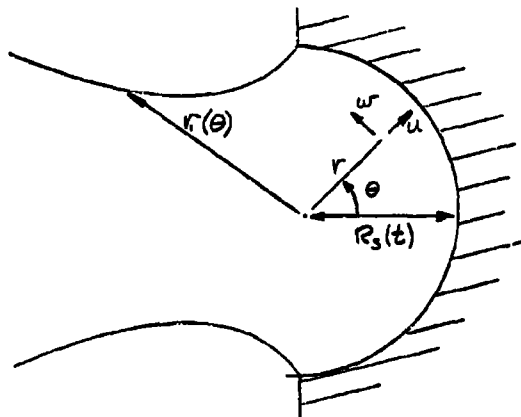
$$e_1 - e_0 = \frac{1}{2} (p_0 + p_1) \left( \frac{1}{\rho_0} - \frac{1}{\rho_1} \right) \quad (15)$$

In the analysis of this paper, it is assumed that the shock wave is always hemispherical in shape as it advances into the target. This assumption is based on observations of shock shape in lucite<sup>6,7</sup> and in wax<sup>8,9</sup> under hyper-velocity impact conditions. Further verification comes from the nearly

## BLAST-WAVE THEORY OF CRATER FORMATION

hemispherical shape of the craters formed at high impact speed.

At this point, then, the fluid-mechanical problem posed is the solution of Eqs. (6) to (10), which describe the motion of an inviscid, compressible fluid, behind a hemispherical shock wave advancing into a semi-infinite target.



The motion must be such that the boundary conditions (13) to (15) are satisfied at the shock, while along the surface  $r=r_1(\theta)$  (whose location is unknown) the pressure and material density must vanish.

The solution of such a boundary-value problem is an extremely difficult task. To date only numerical solutions have been presented.<sup>1</sup> The object of the present paper is to review the approximations of blast-wave theory and then to apply them in an effort to derive an analytic solution.

## BLAST-WAVE THEORY OF CRATER FORMATION

### 2. SIMILARITY ASSUMPTION AND ITS IMPLICATIONS

Mathematically speaking, the most important approximation made in the blast-wave theory is the assumption that the flow is self-similar, i. e. the distributions of the various physical quantities (such as pressure, density, etc.) at each instant are taken to be the same when viewed on a scale defined by the shock radius at that instant. Thus each quantity, instead of depending separately on the time and on the distance  $r$  from the impact point, is assumed to be a function only of the combination  $r/R_s(t)$ . This reduction of the number of independent variables constitutes a significant simplification in the differential equations that must be solved. The essence of the similarity assumption is to suppress time as an independent variable. This is done by introducing the similarity coordinate

$$\eta = \frac{r}{R_s(t)} \quad (16)$$

and by redefining the velocity components, pressure, density, and internal energy by the dimensionless functions

$$\begin{aligned} u(r, \theta, t) &= \dot{R}_s \phi(\eta, \theta) & p(r, \theta, t) &= \rho_0 \dot{R}_s^2 f(\eta, \theta) \\ w(r, \theta, t) &= \dot{R}_s \omega(\eta, \theta) & \rho(r, \theta, t) &= \rho_0 \psi(\eta, \theta) \\ & & e(r, \theta, t) &= \dot{R}_s^2 g(\eta, \theta) \end{aligned} \quad (17)$$

When these relations are substituted into Eqs. (6) to (9) and derivatives with respect to  $r$  and  $t$  are replaced in terms of derivatives with respect to  $\eta$ , one finds that all explicit time dependence can be suppressed from the differential equations if one chooses

$$R_s = At^N \quad (18)$$

# BLAST-WAVE THEORY OF CRATER FORMATION

Thus, out of the whole set of solutions of the basic equations, the similarity assumption restricts us to that subset for which the shock radius is proportional to a power of the time. When this is done the basic equations become

$$(\phi - \eta) \frac{\partial \psi}{\partial \eta} + \frac{\omega}{\eta} \frac{\partial \psi}{\partial \theta} + \psi \left( \frac{\partial \phi}{\partial \eta} + \frac{1}{\eta} \frac{\partial \omega}{\partial \theta} + 2 \frac{\phi}{\eta} + \frac{\omega}{\eta} \cot \theta \right) = 0 \quad (19)$$

$$- \frac{1-N}{N} \phi + (\phi - \eta) \frac{\partial \phi}{\partial \eta} + \frac{\omega}{\eta} \frac{\partial \phi}{\partial \theta} - \frac{\omega^2}{\eta} + \frac{1}{\psi} \frac{\partial f}{\partial \eta} = 0 \quad (20)$$

$$- \frac{1-N}{N} \omega + (\phi - \eta) \frac{\partial \omega}{\partial \eta} + \frac{\omega}{\eta} \frac{\partial \omega}{\partial \theta} + \frac{\phi \omega}{\eta} + \frac{1}{\eta \psi} \frac{\partial f}{\partial \theta} = 0 \quad (21)$$

$$- 2 \frac{1-N}{N} g + (\phi - \eta) \frac{\partial g}{\partial \eta} + \frac{\omega}{\eta} \frac{\partial g}{\partial \theta} - \frac{f}{\psi^2} \left\{ (\phi - \eta) \frac{\partial \psi}{\partial \eta} + \frac{\omega}{\eta} \frac{\partial \psi}{\partial \theta} \right\} = 0 \quad (22)$$

The parameter  $N$  which appears here is for the moment unspecified.

After elimination of time as an explicit variable in the differential equations, the next step is to see if the boundary conditions are compatible with the similarity assumption. At the shock  $(\eta = 1, -\pi/2 \leq \theta \leq +\pi/2)$  equations (13), (14), (15) and (10) become

$$\psi(1, \theta) [1 - \phi(1, \theta)] = 1 \quad (23)$$

$$f(1, \theta) = \phi(1, \theta) + \frac{p_0}{\rho_0 \dot{R}_s^2} \quad (24)$$

$$g(1, \theta) = \frac{1}{2} \left[ \frac{p_0}{\rho_0 \dot{R}_s^2} + f(1, \theta) \right] \left[ 1 - \frac{1}{\psi(1, \theta)} \right] \quad (25)$$

$$\dot{R}_s^2 g(1, \theta) = F \left[ \rho_0 \dot{R}_s^2 f(1, \theta), \rho_0 \psi(1, \theta) \right] \quad (26)$$

## BLAST-WAVE THEORY OF CRATER FORMATION

The first three of these are independent of the time if the initial pressure in the undisturbed medium  $p_0$  is small compared with  $\rho_0 \dot{R}_s^2$ , which is of the order of the pressure being generated at the shock. This condition will certainly be met whenever the fluid-mechanical model is appropriate. Thus the question of whether a similarity solution is compatible with the boundary conditions depends solely on whether the form of the internal energy function  $F$  is such as to permit the time dependence to be eliminated from Eq. (26). Sedov<sup>10</sup> has pointed out that this can be done whenever the internal energy is of the form

$$e = p \psi(\rho) \quad (27)$$

where  $\psi(\rho)$  is any function of the density. For such a case, Eq. (26) becomes

$$g(i, \theta) = \rho_0 f(i, \theta) \psi[\rho_0 \psi(i, \theta)] \quad (28)$$

and all explicit time dependence is eliminated. Thus a self-similar solution is possible whenever the medium obeys the equation of state (27). In this case, the boundary values at the shock can be conveniently found by solving Eqs. (23)-(25) for  $\phi$ ,  $f$ , and  $g$  in terms of  $\psi$

$$\phi(i, \theta) = f(i, \theta) = 1 - \frac{1}{\psi(i, \theta)} \quad (29)$$

$$g(i, \theta) = \frac{1}{2} \left[ 1 - \frac{1}{\psi(i, \theta)} \right]^2 \quad (30)$$

When these relations are substituted in Eq. (28), the result is an expression which can be solved for the density ratio at the shock

## BLAST-WAVE THEORY OF CRATER FORMATION

$$\frac{1}{2} \left[ 1 - \frac{1}{\psi(1, \theta)} \right] = \rho_0 \varphi \left[ \rho_0 \psi(1, \theta) \right] \quad (31)$$

The fact that the density ratio is constant is the fundamental prerequisite for similarity. The other quantities at the shock are found from Eqs. (29) and (30).

From the point of view of application to shock propagation in solids, the most important implication of the similarity assumption is its restriction to state equations of a special kind. In the next Section we indicate the extent to which real materials are described by such a special family of state equations.



## BLAST-WAVE THEORY OF CRATER FORMATION

### 3. THE EQUATION OF STATE

For most solids, the equation of state appropriate in the range of pressures generated during hypervelocity impact is the Mie-Grüneisen relation<sup>11</sup>

$$e(p, \rho) - e_c(\rho) = \frac{p - p_c(\rho)}{\rho \Gamma(\rho)} \quad (32)$$

where the subscript  $c$  denotes the cohesive contribution and where  $\Gamma$  is the Grüneisen constant, which depends weakly on  $\rho$ . The cohesive contributions can be found from measured shock wave data. Along the Hugoniot, Eq. (32) takes the form

$$e_H(\rho) - e_c(\rho) = \frac{p_H(\rho) - p_c(\rho)}{\rho \Gamma(\rho)} \quad (33)$$

Subtracting this from Eq. (32) then gives

$$e - e_H(\rho) = \frac{p - p_H(\rho)}{\rho \Gamma(\rho)} \quad (34)$$

The Mie-Grüneisen equation can be rearranged as

$$e = \frac{p}{\rho \Gamma(\rho)} - \Delta(\rho) \quad (35)$$

where

$$\Delta(\rho) = \frac{p_c(\rho)}{\rho \Gamma(\rho)} - e_c(\rho) = \frac{p_H(\rho)}{\rho \Gamma(\rho)} - e_H(\rho) \quad (36)$$

By comparison with Eq. (27), it can be seen that only the leading term of Eq. (35) can be accommodated in a self-similar solution. Such a solution will therefore be valid only when the pressure is sufficiently high that  $\Delta(\rho)$

## BLAST-WAVE THEORY OF CRATER FORMATION

is small in comparison with the leading term. In fact, every impact will span a time interval during which this approximation fails. Furthermore, the pressures at which  $\Delta(\rho)$  is too large to be neglected are nevertheless sufficiently high that the compressible-fluid approximation is still well justified. Thus the similarity solution can describe only the early phases of the fluid-dynamic process. A proper description at later times requires a nonsimilar solution which accounts for the presence of the term  $\Delta(\rho)$ . For the moment we defer this somewhat more difficult problem, and examine what can be done with the similarity solution itself, keeping in mind that it will apply only to the earlier stages.

Some of the theoretical analyses of shock waves in solid media<sup>12</sup> use the approximation that the state equation can be represented by that of a perfect gas with constant specific-heat ratio  $\gamma$ , namely

$$e = \frac{p}{(\gamma-1)\rho}, \quad \text{i. e.,} \quad \psi(\rho) = \frac{1}{(\gamma-1)\rho} \quad (37)$$

For this case, Eq. (31) reveals that the density ratio at the shock has the constant value

$$\psi(1, \theta) = \frac{\rho_1}{\rho_0} = \frac{\gamma+1}{\gamma-1}$$

The use of a perfect gas may be viewed as an approximation to the leading term of the Mie-Grüneisen equation, if the Grüneisen factor  $\Gamma(\rho)$  is replaced by the constant value  $\gamma-1$ . This approximation, with  $\gamma$  chosen in the range from 2 to 4, amounts to a high-pressure approximation to the Mie-Grüneisen relation, and it makes available all the results of the extensive

## BLAST-WAVE THEORY OF CRATER FORMATION

literature dealing with blast waves in perfect gases. It should be borne in mind, of course, that the similarity solution is not limited to the predictions made with a perfect gas model. The variation of  $\Gamma$  could be accounted for, but is neglected as a matter of convenience. When the perfect-gas approximation is made, the energy equation becomes

$$\frac{\partial p}{\partial t} + u \frac{\partial p}{\partial r} + \frac{w}{r} \frac{\partial p}{\partial \theta} + \frac{\gamma p}{\rho} \left( \frac{\partial \rho}{\partial t} + u \frac{\partial \rho}{\partial r} + \frac{w}{r} \frac{\partial \rho}{\partial \theta} \right) = 0 \quad (38)$$

In terms of the similar functions, this is

$$-2 \frac{1-N}{N} f + (\phi - \eta) \left( \frac{\partial f}{\partial \eta} - \frac{\gamma f}{\psi} \frac{\partial \psi}{\partial \eta} \right) + \frac{w}{\eta} \left( \frac{\partial f}{\partial \theta} - \frac{\gamma f}{\psi} \frac{\partial \psi}{\partial \theta} \right) = 0 \quad (39)$$

In addition to this identification with the Mie-Grüneisen equation, a perfect-gas approximation may also be examined by seeing how accurately it represents the isentropes of a given material. This is done in Reference 13 for the case of iron, where it is shown that the approximation of a constant  $\gamma$  is satisfactory for describing the high-pressure states of iron as long as the function  $\Delta(\rho)$  does not become significant.

Section 5 below gives a description of shock propagation due to hyper-velocity impact, based on the perfect-gas approximation throughout. In Section 6, we present a solution which accounts for the influence of the non-similar term  $\Delta(\rho)$  in an approximate way. In addition, Section 6 indicates work currently in progress, which properly accounts for the nonsimilar effect.

## BLAST-WAVE THEORY OF CRATER FORMATION

### 4. CONSERVATION OF ENERGY AND MOMENTUM

The total energy and momentum of the system must be conserved, as may be confirmed by forming the proper volume integral of the vector equations of motion, Eqs. (1) to (3). The actual integrals, whose values must be constant, may be derived as follows: Consider as the mass element a ring of volume  $r dr d\theta \cdot 2\pi r \sin\theta$ . The total energy  $E$  and momentum  $P$  are

$$\begin{aligned} E &= \int_0^\pi \int_0^{r_1(\theta)} \left[ e + \frac{1}{2} (u^2 + w^2) \right] \cdot \rho \cdot 2\pi r^2 \sin\theta \, dr d\theta \\ &= 2\pi \rho_0 \dot{R}_s^2 R_s^3 \int_0^\pi \sin\theta \int_0^{\eta_1(\theta)} \left[ q + \frac{1}{2} (\phi^2 + \omega^2) \right] \psi \eta^2 \, d\eta d\theta \end{aligned} \quad (40)$$

$$\begin{aligned} P &= \int_0^\pi \int_0^{r_1(\theta)} (u \cos\theta - w \sin\theta) \cdot \rho \cdot 2\pi r^2 \sin\theta \, dr d\theta \\ &= 2\pi \rho_0 \dot{R}_s^2 R_s^3 \int_0^\pi \sin\theta \int_0^{\eta_1(\theta)} (\phi \cos\theta - \omega \sin\theta) \psi \eta^2 \, d\eta d\theta \end{aligned} \quad (41)$$

Here we encounter a fundamental difficulty. If we are to have a self-similar solution, the differential equations require  $R_s = A t^N$ . However, a single value of  $N$  will not permit both of the relations above to be independent of time. Constancy of energy can be achieved only with  $N = 2/5$ , while momentum conservation requires  $N = 1/4$ , and in either case the parameter  $A$  is used to match the quantity being conserved. Thus it appears at first glance that a satisfactory solution cannot be achieved under the assumption of similarity. Reference 13 describes one method for overcoming this difficulty. The essence of the idea is that  $N$  is determined by a totally different consideration, and a second free parameter is introduced in such a way that both conservation conditions may be satisfied simultaneously.

## BLAST-WAVE THEORY OF CRATER FORMATION

It is clear, of course, that any solution which hopes to satisfy both conservation conditions simultaneously must make provision for mass ejection from the expanding crater. Consequently, a solution which supposes that the flow is one-half of a spherically symmetric disturbance (ignoring variations in the  $\theta$  - direction) cannot satisfy momentum conservation. On the other hand, such solutions are considerably simpler than those which permit variations in the  $\theta$  direction. In the remainder of this Section, we first describe the symmetric solution, and then take up the question of approximate solutions in which provision is made for mass ejection. An important conclusion emerges from the comparison of these two, namely, that the vastly simpler spherically-symmetric solution is for practical purposes identical with the more complicated solution which allows for mass ejection.

When the flow is spherically symmetric,  $\omega$  and all derivatives with respect to  $\theta$  vanish, and the similarity equations become ordinary differential equations. Denoting the ordinary derivative with respect to  $\eta$  by a prime, these are

$$(\phi - \eta)\psi' + \psi\left(\phi' + 2\frac{\phi}{\eta}\right) = 0 \quad (42)$$

$$-\frac{1-N}{N}\phi + (\phi - \eta)\phi' + \frac{f'}{\psi} = 0 \quad (43)$$

$$-2\frac{1-N}{N}f + (\phi - \eta)\left(f' - \frac{\gamma f}{\psi}\psi'\right) = 0 \quad (44)$$

The parameter  $\gamma$  may be thought of as related to the Grüneisen constant, as mentioned earlier. These equations may be solved explicitly for the derivatives in the form

# BLAST-WAVE THEORY OF CRATER FORMATION

$$\psi' = \frac{-(\phi-\eta)^2 \frac{2\psi\phi}{\eta} + 2\frac{1-N}{N} f - \frac{1-N}{N} \psi\phi(\phi-\eta)}{(\phi-\eta)[(\phi-\eta)^2 - \gamma f/\psi]} \quad (45)$$

$$\phi' = \frac{\frac{1-N}{N} \phi(\phi-\eta) + \frac{\gamma f}{\psi} \frac{2\phi}{\eta} - 2\frac{1-N}{N} \frac{f}{\psi}}{(\phi-\eta)^2 - \frac{\gamma f}{\psi}} \quad (46)$$

$$f' = \frac{f \left\{ (\phi-\eta) \left[ 2\frac{1-N}{N} - \frac{2\gamma\phi}{\eta} \right] - \gamma \frac{1-N}{N} \phi \right\}}{(\phi-\eta)^2 - \frac{\gamma f}{\psi}} \quad (47)$$

From Eqs.(37), (23)-(26), the boundary conditions at the shock can be found as

$$\phi(1) = f(1) = \frac{2}{\gamma+1} ; \quad \psi(1) = \frac{\gamma+1}{\gamma-1} \quad (48)$$

Equations (45) to (48) (with  $N = 2/5$ ) were first presented by G. I. Taylor<sup>14</sup> who worked out a few numerical and approximate analytical solutions for  $\gamma$  ranging from 1.2 to 1.67, the range appropriate for gases. Subsequently, an analytic solution (also with  $N = 2/5$ ) was published independently by J. L. Taylor<sup>15</sup>, Latter<sup>16</sup>, and Sakurai<sup>17</sup>. Simultaneously with G. I. Taylor's work, Sedov<sup>10</sup> had also found this analytic solution.

The parameter  $N$  must be specified before solutions of these equations can be found. It appears that physically acceptable solutions exist only when  $N = 2/5$ , a value which conserves the total energy, as noted above. When  $N$

## BLAST-WAVE THEORY OF CRATER FORMATION

is taken to be different from  $2/5$ , the solution exhibits infinite slopes.

Reference 13 presents results typical of those found in the range  $.25 < \gamma < .4$  when a solution of this sort is attempted. This nonexistence of symmetric solutions apparently explains the difficulty encountered by Davids et al<sup>18</sup> in attempting to find a spherically symmetric solution for constant momentum.

In what follows,  $\gamma$  is chosen as  $2/5$ , and the terms "constant-energy" and "spherically symmetric" are used interchangeably in referring to the solution.

Solutions of these equations for  $\gamma$  in the range from 2 to 20 are presented in Reference 13. Figures 1 and 2 show typical results, for the cases  $\gamma = 3$  and  $\gamma = 16$ . These figures display the usual feature that the density drops off rather sharply behind the shock, indicating that most of the mass processed is concentrated near the shock. For  $\gamma > 7$ , a cavity begins to form at small values of  $\eta$ , as pointed out by Sedov<sup>10</sup>, and the particle velocities show a marked increase near the edge of the cavity.

The problem of obtaining solutions when  $\theta$  is included as an independent variable is considerably more difficult. The basic equations are partial differential equations and, as pointed out in Reference 13, they are of mixed character, containing both elliptic and hyperbolic regions. Furthermore, they must meet a zero-pressure boundary condition along a line whose location is unknown in advance. To make matters worse, the differential equations contain a parameter  $\gamma$  whose value is unspecified. No attempt has been made to solve these equations; instead, partial solutions are sought by restricting attention to conditions along the axis of symmetry. In this way we can learn a great deal about the solution with relatively little effort. Along the axis of

# BLAST-WAVE THEORY OF CRATER FORMATION

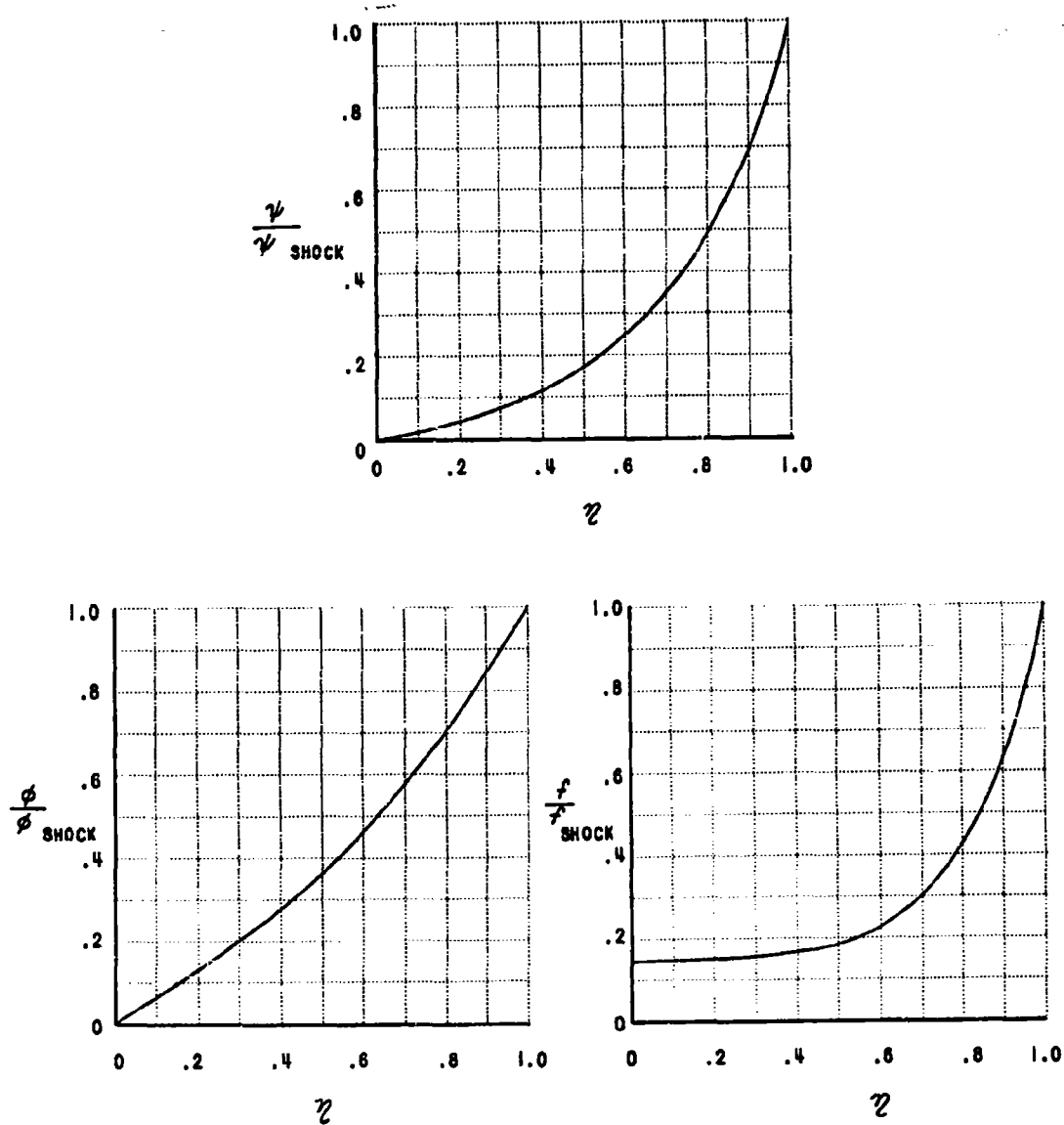


Figure 1 DISTRIBUTION OF DENSITY, PARTICLE VELOCITY, AND PRESSURE  
CONSTANT-ENERGY, SPHERICALLY-SYMMETRIC BLAST WAVES  
 $\gamma = 3$



# BLAST-WAVE THEORY OF CRATER FORMATION

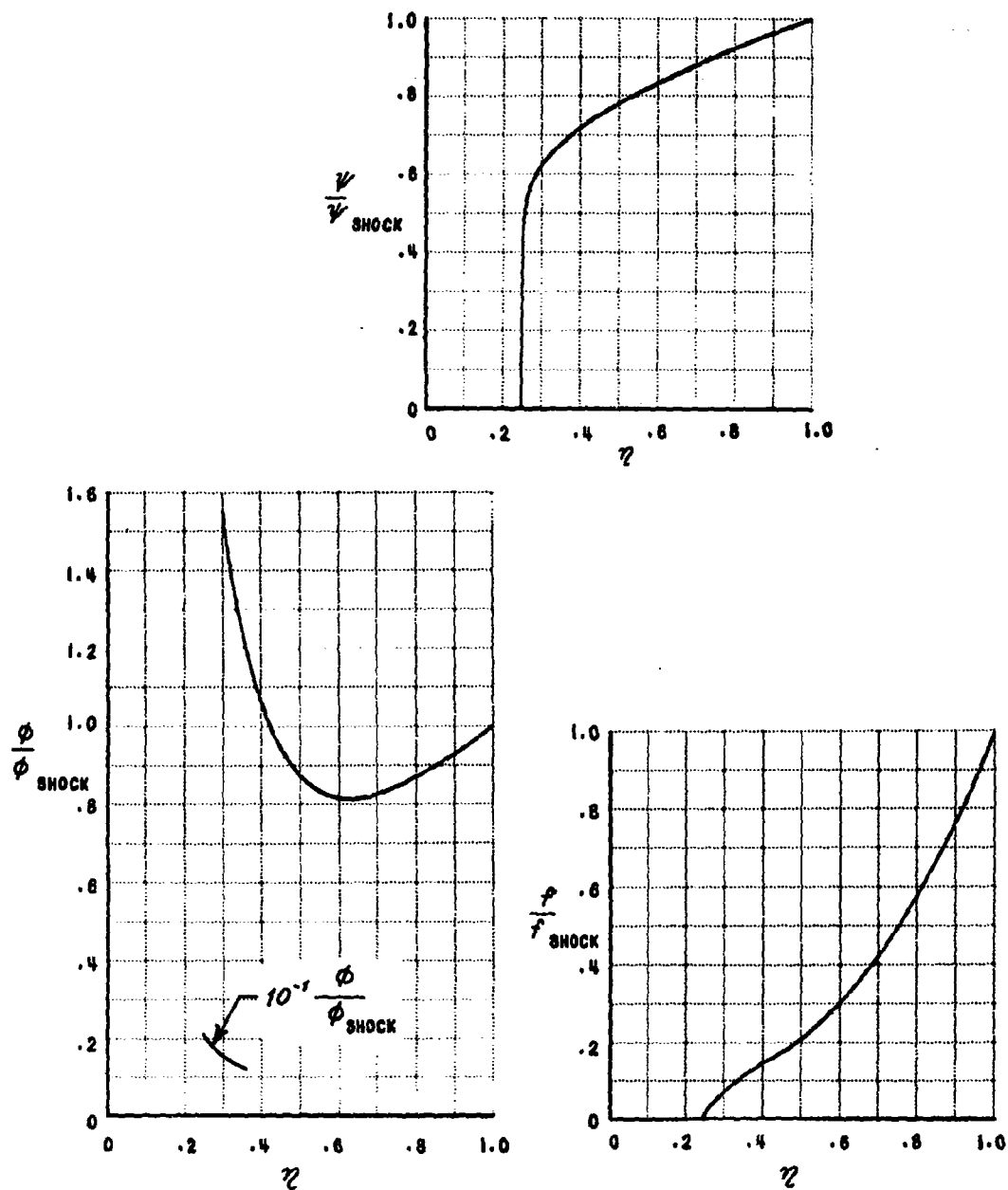


Figure 2 DISTRIBUTION OF DENSITY, PARTICLE VELOCITY, AND PRESSURE  
CONSTANT-ENERGY, SPHERICALLY-SYMMETRIC BLAST WAVES  
 $\gamma = 16$

# BLAST-WAVE THEORY OF CRATER FORMATION

symmetry

$$\theta = 0, \quad 0 \leq \eta \leq 1 \quad ; \quad \theta = \pi, \quad 0 \leq \eta \leq \infty$$

the similarity equations take the form

$$(\phi - \eta) \psi' + \psi \left( \phi' + \frac{\tau}{\eta} + 2 \frac{\phi}{\eta} \right) = 0 \quad (49)$$

$$- \frac{1-N}{N} \phi + (\phi - \eta) \phi' + \frac{f'}{\psi} = 0 \quad (50)$$

$$- 2 \frac{1-N}{N} f + (\phi - \eta) \left( f' - \frac{\gamma f}{\psi} \psi' \right) = 0 \quad (51)$$

where primes indicate ordinary derivatives with respect to  $\eta$ , and where the quantity  $\tau(\eta)$  is given by

$$\tau(\eta) = 2 \frac{\partial \omega}{\partial \theta} (\eta, 0) \quad (52)$$

(The factor 2 originates from the contribution of the term  $\omega \cot \theta$ .)

Except for the presence of  $\tau$  in Eq. (49), these are identical with the Taylor equations for a spherically symmetric disturbance, discussed above. The function  $\tau(\eta)$  represents the influence of off-axis conditions, as must be expected whenever a partial differential equation is specialized to a single line in the plane of its independent variables. The boundary conditions at the shock are

$$\phi(1) = f(1) = \frac{2}{\gamma+1} \quad ; \quad \psi(1) = \frac{\gamma+1}{\gamma-1} \quad ; \quad \tau(1) = 0 \quad (53)$$

Equations (49) to (51) may be solved explicitly for the derivatives in

the form

$$\psi' = \frac{-(\phi - \eta)^2 \left( \frac{2\psi\phi}{\eta} + \frac{\psi\tau}{\eta} \right) + 2 \frac{1-N}{N} f - \frac{1-N}{N} \psi\phi(\phi - \eta)}{(\phi - \eta) \left[ (\phi - \eta)^2 - \gamma f / \psi \right]} \quad (54)$$

# BLAST-WAVE THEORY OF CRATER FORMATION

$$\phi' = \frac{\frac{1-N}{N} \phi(\phi-\eta) + \frac{\gamma f}{\psi} \left( \frac{2\phi}{\eta} + \frac{\tau}{\eta} \right) - 2 \frac{1-N}{N} \frac{f}{\psi}}{(\phi-\eta)^2 - \gamma f/\psi} \quad (55)$$

$$f' = \frac{f \left\{ (\phi-\eta) \left[ 2 \frac{1-N}{N} - \gamma \left( \frac{2\phi}{\eta} + \frac{\tau}{\eta} \right) \right] - \gamma \frac{1-N}{N} \phi \right\}}{(\phi-\eta)^2 - \frac{\gamma f}{\psi}} \quad (56)$$

These obviously have a singularity at the point where the denominator vanishes. This quantity is the special case, for  $\omega = 0$ , of the function discussed in Reference 13, whose sign determines whether the partial differential equations (19), (21), (39), have elliptic or hyperbolic character. The point on the axis of symmetry where the denominator changes sign corresponds to the intersection of this line with the axis. In order that the solution may pass smoothly through this point, the numerators in Eqs. (54) to (56) must also vanish there. Reference 13 points out that such a condition is achieved if the function

$$H(\eta) = (\phi - \eta) \left\{ \frac{2}{\gamma} \frac{1-N}{N} - \frac{2\phi}{\eta} - \frac{\tau}{\eta} \right\} - \frac{1-N}{N} \phi$$

vanishes at the same point.

The function  $\tau(\eta)$  cannot be chosen arbitrarily. Thus the only parameter that can be used to guarantee a smooth crossing of the sonic point is  $N$ , and this consideration forms the criterion for the choice of  $N$ . For each  $\gamma$ , and a specification of  $\tau(\eta)$ ,  $N$  is chosen so as to provide a continuous transition through the singularity. Thus  $N$  will in general be a function of  $\gamma$ . It should be noted in passing that this problem never comes up in the spherically-symmetric, constant-energy case. There the vanishing

## BLAST-WAVE THEORY OF CRATER FORMATION

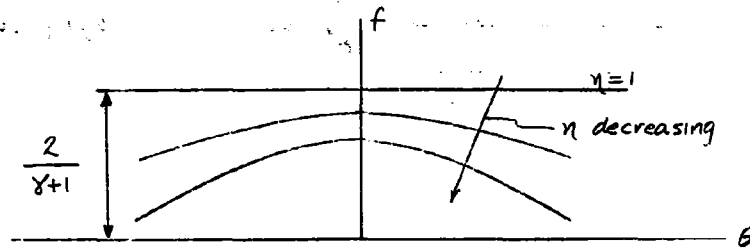
of the denominator always coincides with either the origin (for  $\gamma < 7$ ), or with the edge of the cavity (for  $\gamma > 7$ ), and the entire flow field is elliptic in that solution.

In order to actually obtain a smooth crossing of the singularity, Eqs. (54) to (56) must be solved for various values of  $N$  (and given  $\gamma$ ) until such a crossing is found. Before such an integration can be done,  $\tau(\eta)$  must be specified. However, no rigorous determination of  $\tau(\eta)$  and with it  $N(\gamma)$ , can be made without solving the full partial differential equations. Approximations to  $N$  may be found by approximating  $\tau$  and then integrating Eqs. (54) to (56). Instead of approximating  $\tau$  itself, one may instead relate  $\tau$  to other physical quantities which may be approximated more easily. In particular, by differentiating Eq. (21) with respect to  $\theta$ , and then specializing for the axis of symmetry, one finds

$$-\frac{1}{2} \frac{1-N}{N} \tau + \frac{1}{2} (\phi - \eta) \tau' + \frac{\tau^2}{4\eta} + \frac{\phi\tau}{2\eta} + \frac{1}{\eta\psi} \frac{\partial^2 f}{\partial \theta^2}(\eta, 0) = 0 \quad (59)$$

from which it is seen that approximations to the pressure distribution can be used to generate corresponding approximations to  $\tau$ . This process can be continued, of course, by taking higher-order derivatives, with respect to  $\theta$ , of any of the equations of motion. Each of the resulting expressions will contain at least one unknown function, so the utility of the procedure is dictated by one's ability to approximate the unknown function. For this purpose, Eq. (57) is especially useful. At the shock, the pressure is uniform, while behind the shock it begins to decrease. The rate of decrease is faster near  $\theta = \pm \frac{\pi}{2}$ , as the influence of the vacuum outside the developing crater makes itself felt. Qualitatively, the pressure distribution would be expected to have the appearance

# BLAST-WAVE THEORY OF CRATER FORMATION



The quantity  $\frac{\partial^2 f}{\partial \theta^2}(\eta, 0)$ , which is essentially the curvature of these lines at  $\theta = 0$ , will be zero at the shock and will become negative with increasing magnitude as  $\eta$  falls below one. Such considerations suggest the approximation

$$\frac{\partial^2 f}{\partial \theta^2}(\eta, 0) = -K(1-\eta)^a f(\eta, 0) \quad (58)$$

where  $K$  and  $a$  are constants. Crudely, one may think of this approximation as fitting a cosine variation to the curves above, with a multiplicative function of  $\eta$  introduced in such a way as to guarantee zero curvature at the shock.

The constants  $a$  and  $K$  must be chosen so as to yield values of  $\tau$  which are at most of the same order as that of  $\phi$ .

Figure 3 shows results which have been found for the case  $a = 1$ , and  $K = 10$ . For a given value of  $\gamma$ , and selected values of  $\eta$ , the equations are integrated by a Runge-Kutta procedure, starting from the shock values given in Eq. (53). A smooth crossing of the singularity is achieved with the value  $\eta = .375$ , and the distributions of density, particle velocity, pressure and the function  $\tau$  are shown in the figure. The results given here are typical of those which occur for other values of  $\gamma$ . In addition, some calculations have been made with  $K = 1$ , and the results are not far different from those

# BLAST-WAVE THEORY OF CRATER FORMATION

$$\gamma = 3 \quad \tau \text{ FOUND FROM } \frac{\partial^2 f}{\partial \theta^2}(\eta, 0) = -10(1-\eta)f(\eta, 0)$$

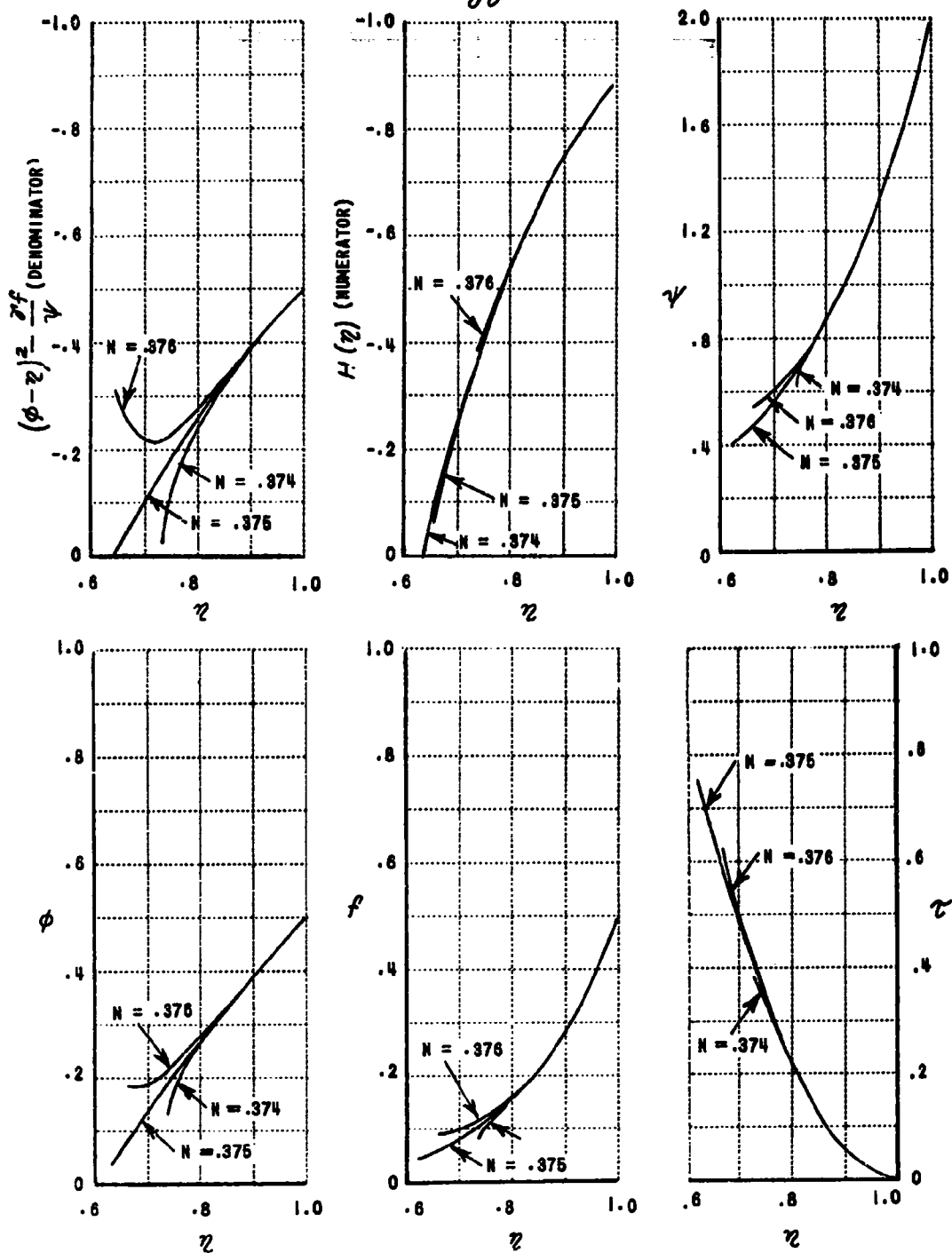


Figure 3 CENTERLINE DISTRIBUTIONS OF DENSITY, PRESSURE, AND VELOCITY

## BLAST-WAVE THEORY OF CRATER FORMATION

shown here.

In general, it is found that values of  $\gamma$  corresponding to a smooth crossing of the singularity are quite close to the value  $2/5$  that applies for the symmetric, constant-energy solution. Furthermore, the quantity  $\tau$  does not attain an appreciable value until some distance away from  $\gamma = 1$ , where the density has fallen to a low value. Thus we might expect that, near the shock at least, these solutions will not differ greatly from the constant-energy solution. This is indeed the case. Figure 4 compares the two types of solution for  $\gamma = 3$  and shows that, along the centerline at least, the motion of most of the mass involved is well approximated by the solution for  $\gamma = 2/5$ . One may expect this trend to persist even for  $\theta > 0$ , suggesting that the Taylor solution will in general be an excellent approximation to the considerably-more-complicated-asymmetric solution. The comparison shown in this figure is typical of the results found at other values of  $\gamma$ .

So far as blast-wave theory is concerned, then, the energy of the projectile plays the dominant role, its momentum being of only secondary importance. In assessing the significance of this finding, it is well to bear in mind three different flow models that might be considered. In addition to the two described above, it is also possible, in principle, to find a solution in which provision is made for mass ejection, but which has zero net momentum:



Our conclusion about the relative unimportance of momentum conservation requires only that the first two of these models give nearly identical predictions. The fact is that we find close similarity to the correct flow pattern

# BLAST-WAVE THEORY OF CRATER FORMATION

$\gamma' = 3$  SOLUTION FOR  $N = 0.375$  BASED ON THE APPROXIMATION

$$\frac{\partial^2 f}{\partial \theta^2}(\eta, 0) = -10(1-\eta)f(\eta, 0)$$

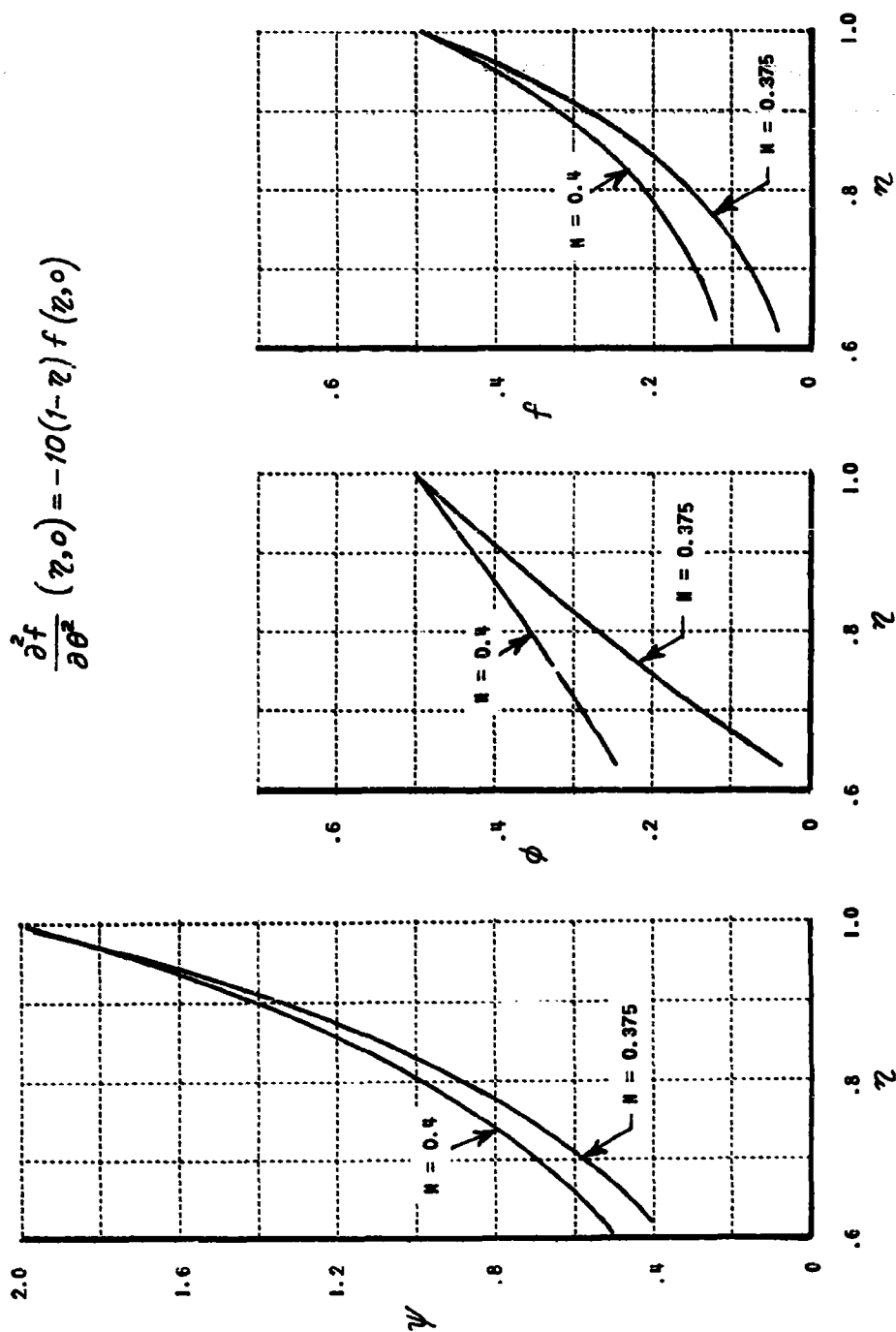


Figure 4 CONSTANT-ENERGY, SPHERICALLY-SYMMETRIC SOLUTION ( $N = 0.4$ ) COMPARED WITH "CENTERLINE" SOLUTION ( $N = 0.375$ )



## BLAST-WAVE THEORY OF CRATER FORMATION

even for the Taylor solution, in which the momentum varies as a function of time.

One plausible physical explanation is based on the experimental observation<sup>19</sup> that targets struck by hypervelocity projectiles often acquire momenta many times that of the projectile, implying that the material ejected from the target must also carry several times the projectile momentum. Thus it appears that the momentum of the projectile itself makes only a minor contribution to the over-all conservation process.

A corollary of this conclusion is that the conditions of hypervelocity impact can be simulated by any experiment which duplicates the energy of the incident particle, irrespective of whether its momentum is correctly matched. In particular, any intense source of short-pulse electromagnetic radiation, such as the output of some currently available lasers, should be capable of providing such a simulation. Such an experimental technique appears to hold promise, and the basis for it is discussed in some detail in the Appendix.

It is important to keep in mind that the predominant importance of energy, as revealed by these solutions, does not necessarily imply that crater volume will be scaled by the projectile energy. Actually, energy scaling is a feature which applies only to the rate of propagation of the shock wave itself. A description of the variation of crater size with various parameters of the impact process requires that the solution for shock radius be converted into a prediction of crater size. Whether the final result of such a process (which presumably will call material strength into play) will still be scaled by the energy of the process, is a question that is unresolved at this point.

As a final word of caution, it must be emphasized that our present data

## BLAST-WAVE THEORY OF CRATER FORMATION

concerning the unimportance of momentum conservation are restricted to the similarity, or strong-shock limit. It remains to be determined whether the same results will be found at lower pressures, where the nonsimilar nature of the problem must be considered.

In the next two Sections, we restrict our attention to solutions in which only the energy is conserved. Thus, the solutions are spherically symmetric. These solutions are used to develop an expression for the rate of shock propagation as a function of the kinetic energy of the impacting particle.

## BLAST-WAVE THEORY OF CRATER FORMATION

### 5. TAYLOR SOLUTION FOR SHOCK PROPAGATION

This Section reviews the well-known solution for a spherical blast wave in a perfect gas, in order to provide a background for the quasi-steady solution presented in the next section. By using the constant-energy distributions of pressure, density, and particle velocity described in the Section above, an explicit description of the shock propagation can now be given if the total energy  $E$  of the system is specified. The sum of the internal and kinetic energy of the fluid set into motion is given by the integral over a hemisphere

$$\begin{aligned} \int_0^{R_s} \left( e + \frac{1}{2} u^2 \right) 2\pi \rho r^2 dr &= \int_0^{R_s} \left( \frac{1}{\gamma-1} \frac{p}{\rho} + \frac{1}{2} u^2 \right) 2\pi \rho r^2 dr \\ &= 2\pi \rho_0 R_s^3 \dot{R}_s^2 I_1(\gamma) \end{aligned} \quad (59)$$

where

$$I_1(\gamma) = \int_0^1 \left( \frac{1}{\gamma-1} \frac{f}{\psi} + \frac{1}{2} \phi^2 \right) \psi \eta^2 d\eta \quad (60)$$

This integral has been evaluated for the values of  $\gamma$  mentioned above, by substituting in Eq. (60) the analytical solution. The results are shown in Figure 5.

If the total energy  $E$  is now specified, a simple differential equation for  $R_s(t)$  results

$$E = 2\pi \rho_0 R_s^3 \dot{R}_s^2 I_1(\gamma) \quad (61)$$

The term  $2\pi \rho_0 R_s^3$  is three times the target mass processed up to the time  $t$ . Thus,  $3 I_1(\gamma)$  may be thought of as a dimensionless coefficient giving the ratio of the mass-averaged value of  $e + \frac{1}{2} u^2$  to the quantity  $\dot{R}_s^2$ ,

# BLAST-WAVE THEORY OF CRATER FORMATION

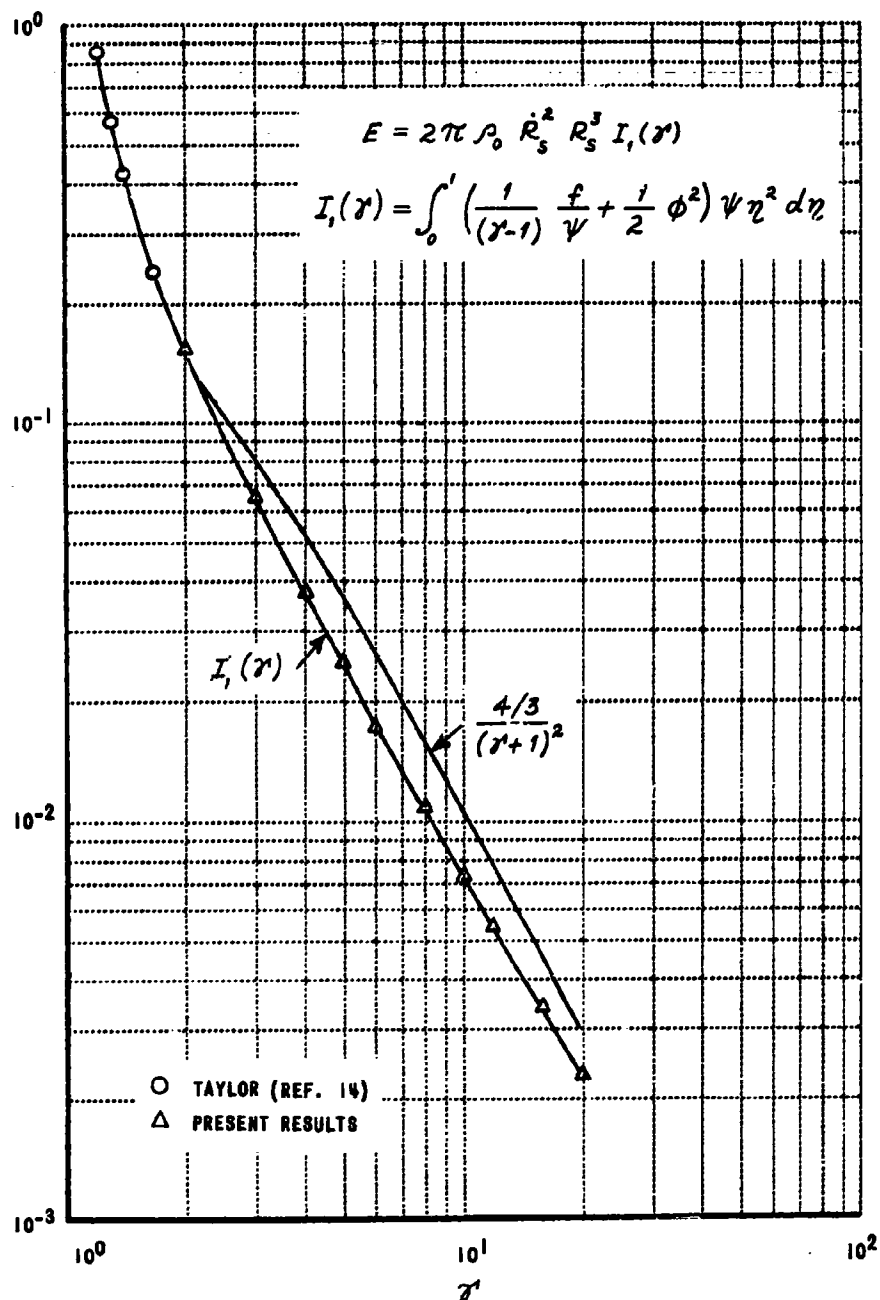


Figure 5 THE FUNCTION  $I_1(r)$  FOR SPHERICALLY-SYMMETRIC BLAST WAVES

# BLAST-WAVE THEORY OF CRATER FORMATION

i. e.

$$3I_1(\gamma) = \frac{E/\frac{2}{3}\pi\rho_0 R_s^3}{\dot{R}_s^2} = \frac{(e + \frac{1}{2}u^2)_{\text{avg.}}}{\dot{R}_s^2} \quad (62)$$

Since  $\dot{R}_s^2$  is proportional to the energy at the shock

$$\dot{R}_s^2 = \frac{(\gamma+1)^2}{4} (e + \frac{1}{2}u^2)_{\text{sh}} \quad (63)$$

we obtain

$$I_1(\gamma) = \frac{4}{3(\gamma+1)^2} \frac{(e + \frac{1}{2}u^2)_{\text{avg.}}}{(e + \frac{1}{2}u^2)_{\text{sh}}} \quad (64)$$

Because most of the mass is concentrated near the shock, the mass-averaged value of any quantity is very nearly its value at the shock. Thus the factor

$4/3(\gamma+1)^2$  is a good approximation to  $I_1$ , as shown in Figure 5. This factor originates from Eq. (63), which states that, the larger the value of  $\gamma$ , the larger must be the shock speed if a given energy per unit mass is to be achieved behind the shock. We may attach the same significance to  $I_1(\gamma)$ : if a given energy is to be distributed in two materials for which the  $\gamma$ 's differ, the shock speed will have to be greater in the material having the larger  $\gamma$ .

The solution of Eq. (61) is the classical Taylor solution for a strong blast wave

$$R_s(t) = \left( \frac{25}{8\pi I_1(\gamma)} \frac{Et^2}{\rho_0} \right)^{1/5} \quad (65)$$

Here the influence of  $\gamma$  is shown more clearly. For a given  $E$  and  $\rho_0$ , the shock radius will grow more rapidly for large values of  $\gamma$ .

## BLAST-WAVE THEORY OF CRATER FORMATION

To apply Eq. (65) to a given case, the total energy  $E$  and the value of the parameter  $\gamma$  must be specified. In all the applications made below, this energy is taken to be the kinetic energy of the impacting particle. The value of  $\gamma$  is associated with the magnitude of the Grüneisen factor,  $\Gamma$ , and hence it would be expected to lie in the range from, say, 2 to 3. Values even larger than this might be considered, especially in the range where the function  $\Delta(\rho)$  is too large to be neglected. Reference 13 makes application to problems in which  $\gamma$  is chosen to be as large as 20, in an effort to match the full Mie-Grüneisen equation.

## BLAST-WAVE THEORY OF CRATER FORMATION

### 6. QUASI-STEADY SOLUTION FOR SHOCK PROPAGATION

The similarity solution described above will be valid only in the limit of extremely high pressure, where the density ratio across the shock is constant. In an actual impact, however, such a condition is not met, especially during the later stages of the cratering process, when the shock strength begins to decay toward that of a stress wave.

Thus a proper description of shock propagation in real materials calls for an analysis in which the nonsimilar features of the problem are correctly accounted for. Analyses of this sort have been done for gases, with varying degrees of approximation. Notable among these is the perturbation method, explored by Sakurai<sup>20</sup>, among others. Applied to the present problem, the perturbation analysis would seek the first-order departure from similarity, for the case where  $\Delta(\rho)$  is small, but not negligible, compared with  $\rho/\rho_0(\rho)$ . A more powerful approach, valid over a wider range of pressure, has been developed by Oshima<sup>21</sup>, who calls it the "Quasi-Similarity" solution. The essence of his method is to solve the problem for a range of values of the shock Mach number  $M$ , defined as  $k_s/c$ , where  $c$  denotes the target sound speed. For each value of  $M$ , the correct boundary values are used at the shock, and certain terms are included in the differential equations to approximate the nonsimilar effect. The analysis leads to a solution for the shock Mach number as a function of time, starting from the blast-wave limit ( $M = \infty$ ) and tending toward the acoustic limit ( $M = 1$ ) at large time. At each instant, the distributions of pressure, density, etc., are given, once the shock Mach number is known. For air, Oshima's solution agrees well with experimental observation and with machine solutions, both in regard to the

## BLAST-WAVE THEORY OF CRATER FORMATION

shock propagation, and to the distributions behind the shock.

Oshima's method is being applied to the propagation of shock waves in solid media, but the results are incomplete. As an interim solution, we have worked out an analogous, but more approximate description of the shock propagation, which we shall identify by the term "Quasi-Steady." We assume that the distributions of pressure, density, etc., at any shock speed are the same as the self-similar, perfect-gas distributions which would have the same values at the shock. Thus, at the instant when the shock speed is such as to create a density ratio at the shock of 1.5, the solution is assumed to be the self-similar solution for  $\gamma = \frac{1.5+1}{1.5-1} = 5$ ; when  $P/\rho_0 = 1.4$ , the solution is assumed to be that for  $\gamma = 6$ , etc. Thus the right values at the shock are always used (as is the case in Oshima's work), but the distributions behind the shock are not correct. However, the quasi-similar distributions for air<sup>22</sup> at moderate shock Mach numbers show a qualitative resemblance to the present results<sup>13</sup> for  $\gamma$  in the range from 2 to 20. Thus, because most of the mass is concentrated near the shock, we may expect the quasi-steady solution to be a useful approximation.

The starting point for the analysis is the energy-balance integral

$$E = 2\pi\rho_0 R_s^3 \dot{R}_s^2 I_1(\gamma) \quad (66)$$

In a similarity solution,  $\gamma$  is taken to be a constant, related to the Grüneisen factor. We now propose to allow  $\gamma$  to vary, so as to match conditions at the shock at each instant. This is very simple for a large number of materials, whose Hugoniot are well approximated over a wide range<sup>11</sup> by

$$u_s = c + Su_1 \quad (67)$$



## BLAST-WAVE THEORY OF CRATER FORMATION

For such a material,  $\gamma$  is related to the shock speed by

$$\gamma = \frac{P_1/P_0 + 1}{P_1/P_0 - 1} = \frac{(2S-1)\frac{\dot{R}_s}{c} + 1}{\frac{\dot{R}_s}{c} - 1} \quad (68)$$

Use of this in Eq. (66) leads to a simple relation between shock speed and shock radius. Defining a length scale  $R_0$  by

$$R_0 = \left( \frac{E}{2\pi\rho_0 c^2} \right)^{1/3} \quad (69)$$

equation (66) can be rewritten in the dimensionless form

$$\frac{R_s}{R_0} = \left\{ \frac{1}{\left( \frac{\dot{R}_s}{c} \right)^2 \mathcal{I}_1 \left[ \gamma \left( \frac{\dot{R}_s}{c}; S \right) \right]} \right\}^{1/3} \quad (70)$$

Figure 6 shows this relation for  $S = 1.2, 1.5$ , and  $2.0$ . It is important to note that the shock speed approaches  $c$  when  $R_s$  becomes large, because as  $\dot{R}_s \rightarrow c$ ,  $\gamma \rightarrow \infty$ , and  $\mathcal{I}_1 \rightarrow 0$ . Thus the quasi-steady solution tends toward the acoustic, or stress-wave limit, at large time. Figure 7 shows a comparison of Eq. (70) with the experiments of Fraiser and Karpov<sup>8</sup>. The exact value of  $S$  for the target is probably somewhere in the range from 1.2 to 2, and theoretical predictions for both values are shown. The data, which lie quite close to the stress-wave velocity, are well predicted by the quasi-steady theory.

By using Eq. (70) to give  $\dot{R}_s$  as a function of  $R_s$ , a simple solution for the shock trajectory can be found from the identity

$$\frac{ct}{R_0} = \int_0^{R_s/R_0} \frac{c}{\dot{R}_s} d \left( \frac{R_s}{R_0} \right) \quad (71)$$

# BLAST-WAVE THEORY OF CRATER FORMATION

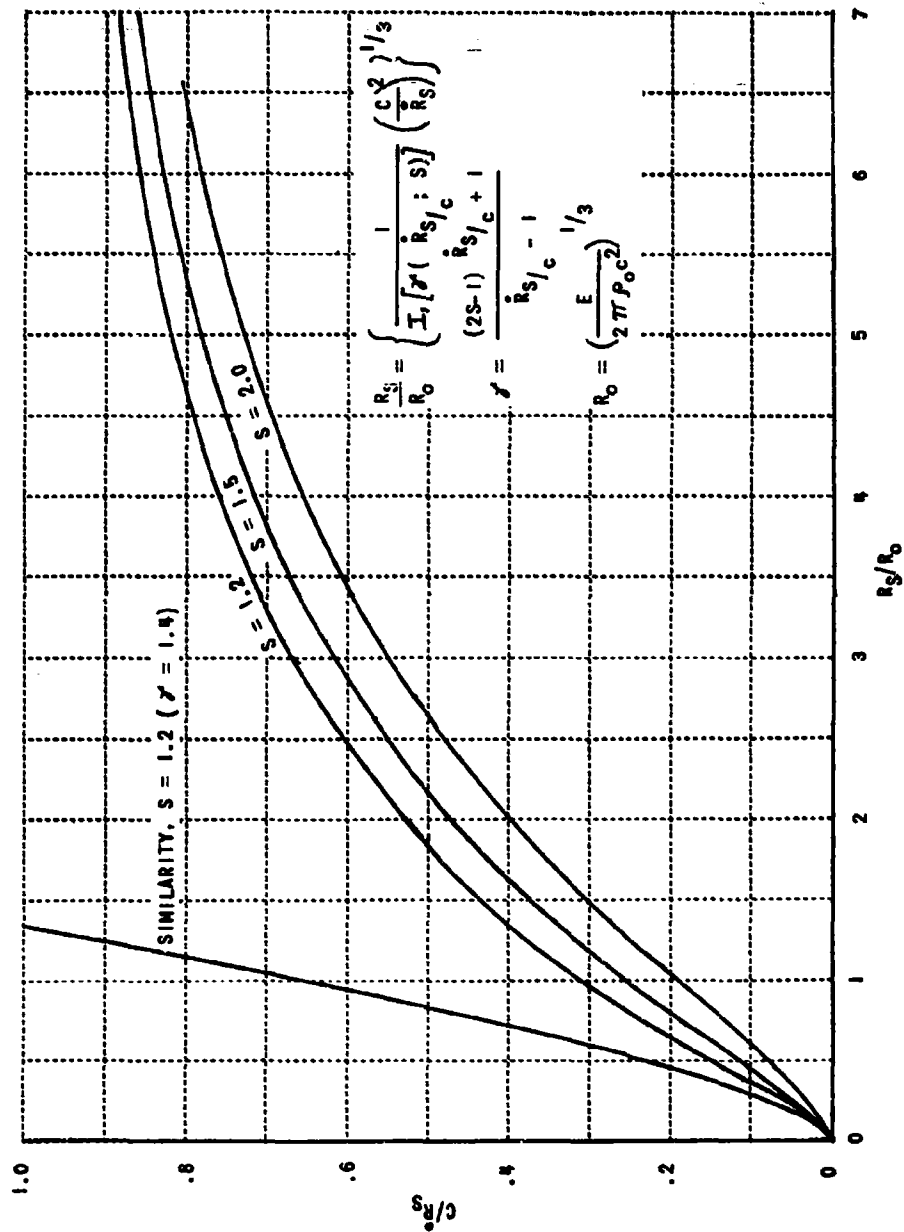


Figure 6 SHOCK SPEED - SHOCK RADIUS RELATION FOR "QUASI-STEADY" SOLUTION

# BLAST-WAVE THEORY OF CRATER FORMATION

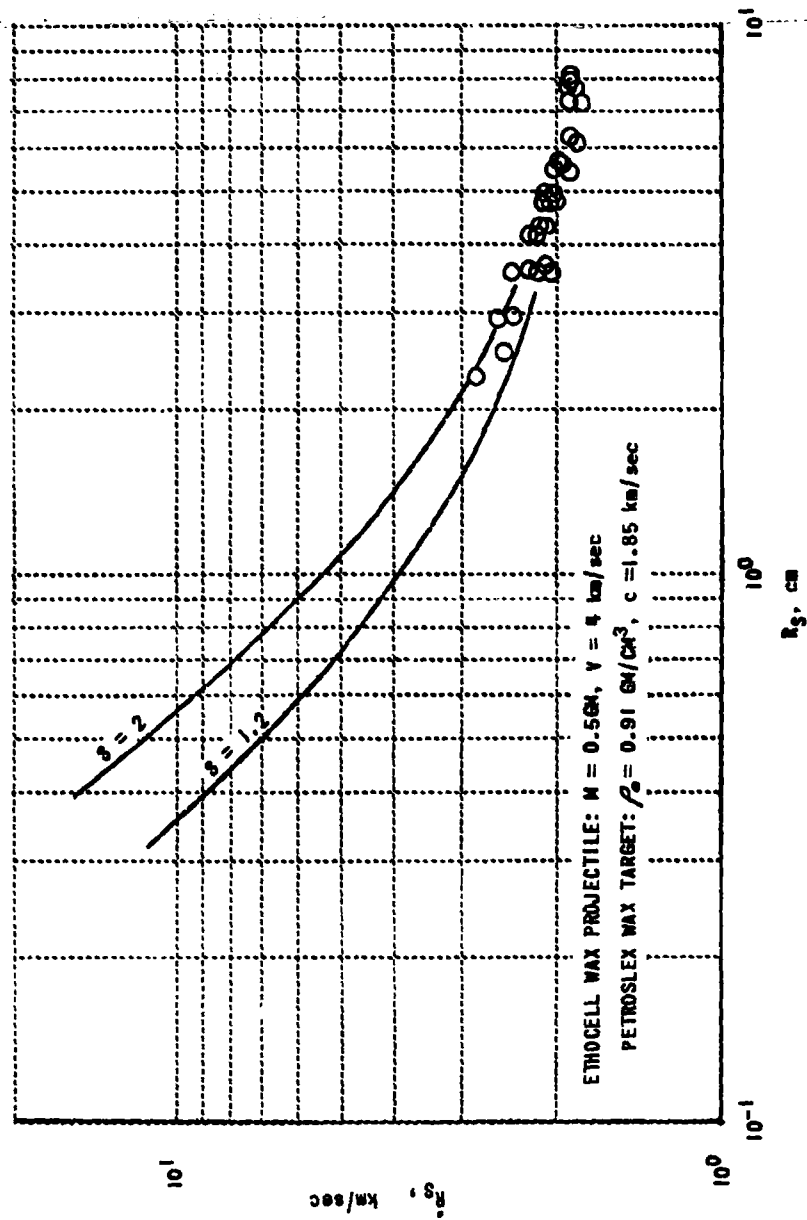


Figure 7 QUASI-STEADY PREDICTION OF SHOCK SPEED - SHOCK RADIUS  
 RELATION COMPARED WITH DATA OF FRASIER & KARPOV

## BLAST-WAVE THEORY OF CRATER FORMATION

Figure 8 shows this relation for the three values of  $S$  mentioned before. Larger values of  $S$  are associated with faster shock propagation, a manifestation of the same phenomenon as that due to  $\gamma$  in the perfect-gas approximation. Also shown on this figure are the experimental data of Eichelberger and Gehring<sup>6</sup> and of Halperson and Hall<sup>7</sup> for a Lucite target, as well as the shock histories calculated by Bjork for iron striking Tuff<sup>2</sup>, and for iron striking iron<sup>1</sup>. The agreement found here, over such a wide range of impact conditions, indicates that the quasi-steady theory is a useful approximation, especially at times greater than  $R_0/c$ . Of course, in the early stages of the impact process before the projectile has been destroyed, the shock propagates at a constant speed. It is only after this early phase that our approximation of an instantaneous point-release of energy becomes valid. We may in general expect the measured trajectories to begin with a constant-speed phase ( $R_s \propto t$ ), followed by a transition to a power-law behavior ( $R_s \propto t^N$ ), with  $N$  between .40 and 1.0, depending on the duration of the impact phase. This exponent increases toward 1.0 again at large time, as the (constant) stress-wave speed is approached. For  $c t / R_0$  greater than about 1.0, the correlation of Fig. 8 is quite good, although some scatter is still present. There is not enough data, at present, to determine whether this remaining scatter represents an additional impact-speed dependence, or whether it is simply an effect of  $S$  not properly accounted for by the quasi-steady theory. The application of Oshima's method, currently in progress, will shed considerable light on this question by properly accounting for the influence of the state equation, but there is obviously a great need for further measurements of shock-wave trajectories,

# BLAST-WAVE THEORY OF CRATER FORMATION

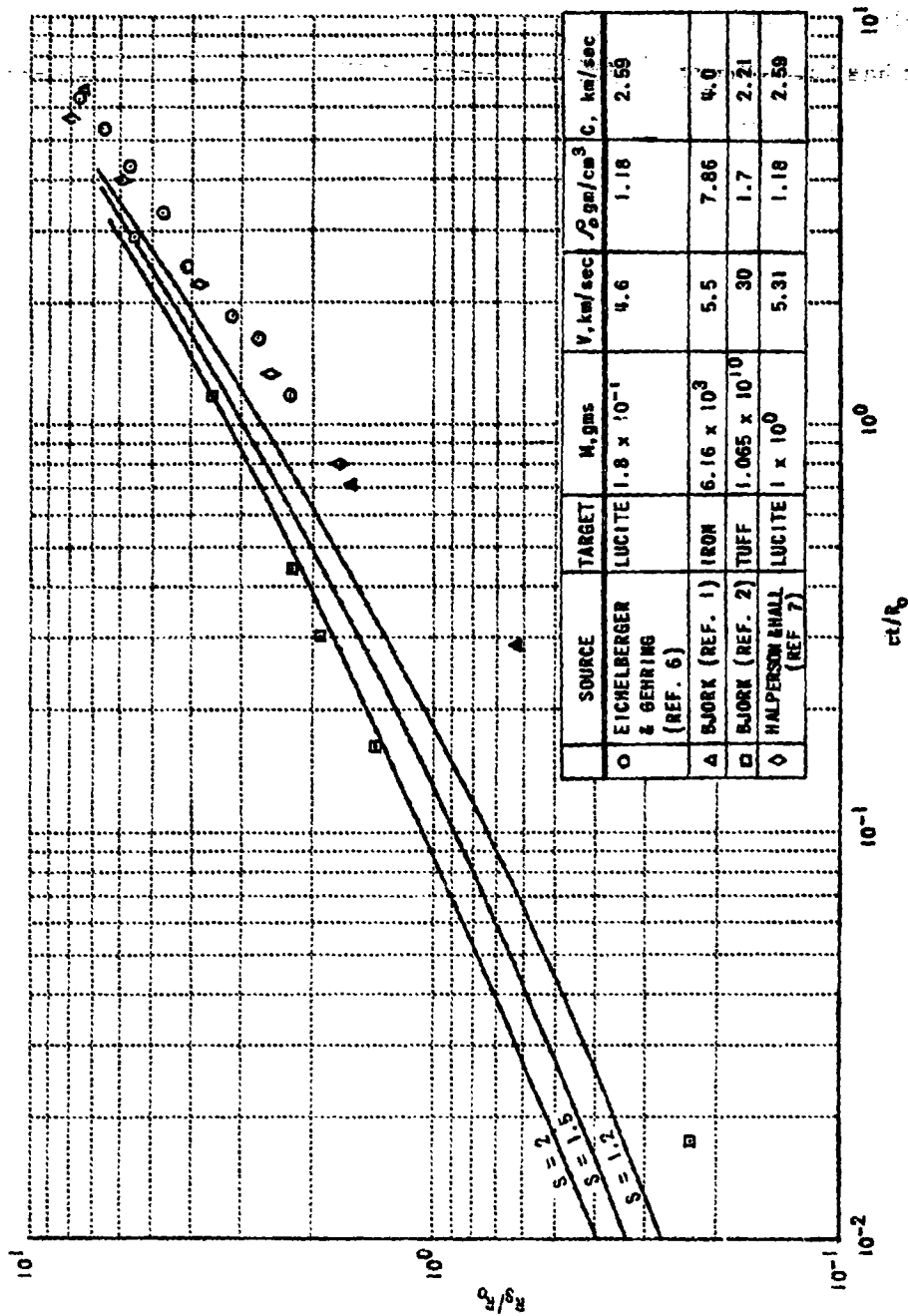


Figure 8 QUASI-STEADY SOLUTION FOR SHOCK TRAJECTORY

## BLAST-WAVE THEORY OF CRATER FORMATION

especially in metals.

It has been observed<sup>6</sup> that the characteristic time for shock propagation in Lucite is considerably shorter than the time during which material is ejected from an aluminum or lead target, under identical impact conditions, and the difference is sometimes attributed to the dynamic strength of the plastic at high strain rate. In this regard, it is interesting to note in Fig. 8 the close correlation between Bjork's calculations in iron ( $S \approx 1.6$ ) and the experimental observations in Lucite ( $S \approx 1.5$ ), all at approximately 5 km/sec. This correlation indicates that in both substances the characteristic time for shock propagation is  $R_0/c$ , which is actually smaller for metals than for Lucite, due to their larger values of  $\rho c^2$ . Assuming that impact-generated shock waves propagate in essentially the same manner in all metals, this correlation would suggest that the duration of material ejection may be considerably longer than, say, the time required for the shock to degenerate down to some preassigned fraction of its initial strength. Again, measurements of shock propagation within the target are needed to resolve the question.

## BLAST-WAVE THEORY OF CRATER FORMATION

### 7. METHODS OF CRATER-SIZE PREDICTION

The success of the above analysis in predicting shock propagation is quite encouraging. However, from the viewpoint of spacecraft design, it does not solve the problem at hand, namely, to predict crater size. To accomplish such a task, additional analysis is needed. It is important to understand that every theory of crater formation contains two ingredients: first, a theory for predicting the shock-wave time history, and the flow of material behind it, and second, a criterion for choosing some point in the trajectory as the crater radius. Bjork<sup>1</sup>, for example, chooses the instant when a stationary region of zero pressure can be found, and identifies this region by the appearance of a distribution of small velocities, which are randomly oriented.\* Other authors, for example Davids and Huang<sup>12</sup>, have used different criteria, and we shall present below some considerations of still another.

Before doing so, however, we must emphasize the central importance of the crater-formation criterion. The correlation shown in Figure 8 may be taken as evidence that, so far as shock-wave propagation is concerned, no essentially new phenomena occur over the impact-speed range up to 30 km/sec. Thus, any change in the penetration law, compared to its low-speed behavior, must be accounted for largely by the criterion used in

---

\*Such a criterion cannot be applied in conjunction with the present solution, which never predicts a stationary region. Indeed, there is no mechanism, except for the influence of external forces, or for very special shock-wave interaction patterns, by which an inviscid fluid can be permanently brought to rest. Any analytic solution would predict that the pressure and particle velocity tend asymptotically toward zero at large time, of course, but their distributions are always nonzero, continuous, and never display a random orientation.

## BLAST-WAVE THEORY OF CRATER FORMATION

defining the crater radius.

This paper makes no effort to settle the question of how the crater-formation criterion should be chosen. We wish only to draw attention to the fact that its choice is a crucial element in determining the penetration law.

On the other hand, we do share with some other authors the impression that the material strength must play a role in the crater-formation criterion. The establishment of a crater of fixed size implies that material has been brought to rest, and as noted above there is no mechanism for accomplishing this feat within the framework of an inviscid theory. Thus it appears that at large time, a transition must be made to a theory which accounts for the strength of the target. Indeed, the entire hydrodynamic analysis begins with the approximation that the motion of any mass element is controlled by the pressures on its surfaces, while its resistance to shear deformation can be neglected. Whenever the inviscid theory itself predicts pressures comparable to or less than the shear strength of the target, the fundamental approximations are clearly in error. Thus we ought to assign, as a boundary for application of the hydrodynamic theory, some level of pressure comparable with the target strength.

Reference 13 not only adopts such a boundary for the fluid-dynamic theory, but actually employs it as a crater-formation criterion. In that work, the crater radius is assumed to be equal to the shock radius at the instant when the pressure behind the shock has decayed to the intrinsic strength  $G/2\tau$ ,  $G$  being the dynamic shear modulus. This criterion was used in conjunction with the similarity solution, to deduce a penetration law



## BLAST-WAVE THEORY OF CRATER FORMATION

which displayed reasonable agreement with experiment.

Now that a more realistic description of the shock propagation is available (from the quasi-steady theory outlined above), it is of interest to investigate the penetration law derived from the same criterion. If we require that the pressure generated at the shock be equal to a strength level designated for the moment as  $\mathcal{P}$ , we find from Eqs. (14) and (67) that the corresponding shock speed is given by

$$\frac{\dot{R}_s}{c} = \frac{1 + \sqrt{1 + 4s \mathcal{P}/\rho_0 c^2}}{2} \quad (72)$$

Figure 9 gives the corresponding value of the shock radius, which, by this criterion, would be taken as the radius of the crater that will ultimately develop. Thus, the crater radius also scales with  $R_0$ :

$$R_c = k R_0 = k \left( \frac{\pi/6 \rho_p d^3 v^2}{4\pi \rho_0 c^2} \right)^{1/3} \quad (73)$$

where  $v$  is the impact speed and  $k$  is shown in Figure 9. It is obvious that a large amount of experimental data could be correlated by this formula, by an empirical choice of the strength level  $\mathcal{P}$ . In fact, by choosing  $k = \left( \frac{12 \times 10^{-9} \rho_0 c^2}{B} \right)^{1/3}$ , (where  $\rho_0 c^2$  is in cgs units, and the Brinell hardness  $B$  is measured in the customary units of kilograms force per square millimeter), the penetration law recommended by Eichelberger and Gehring<sup>6</sup> is recovered. Figure 10 shows a typical correlation, for aluminum projectiles striking copper targets. The parameter  $k$  has been chosen by matching the data at 3.97 km/sec.

It is interesting to note that  $k = 4.85$ , which, according to Figure 6 (with  $S = 1.54$ ) means that the shock was traveling at approximately 1.3 times

# BLAST-WAVE THEORY OF CRATER FORMATION

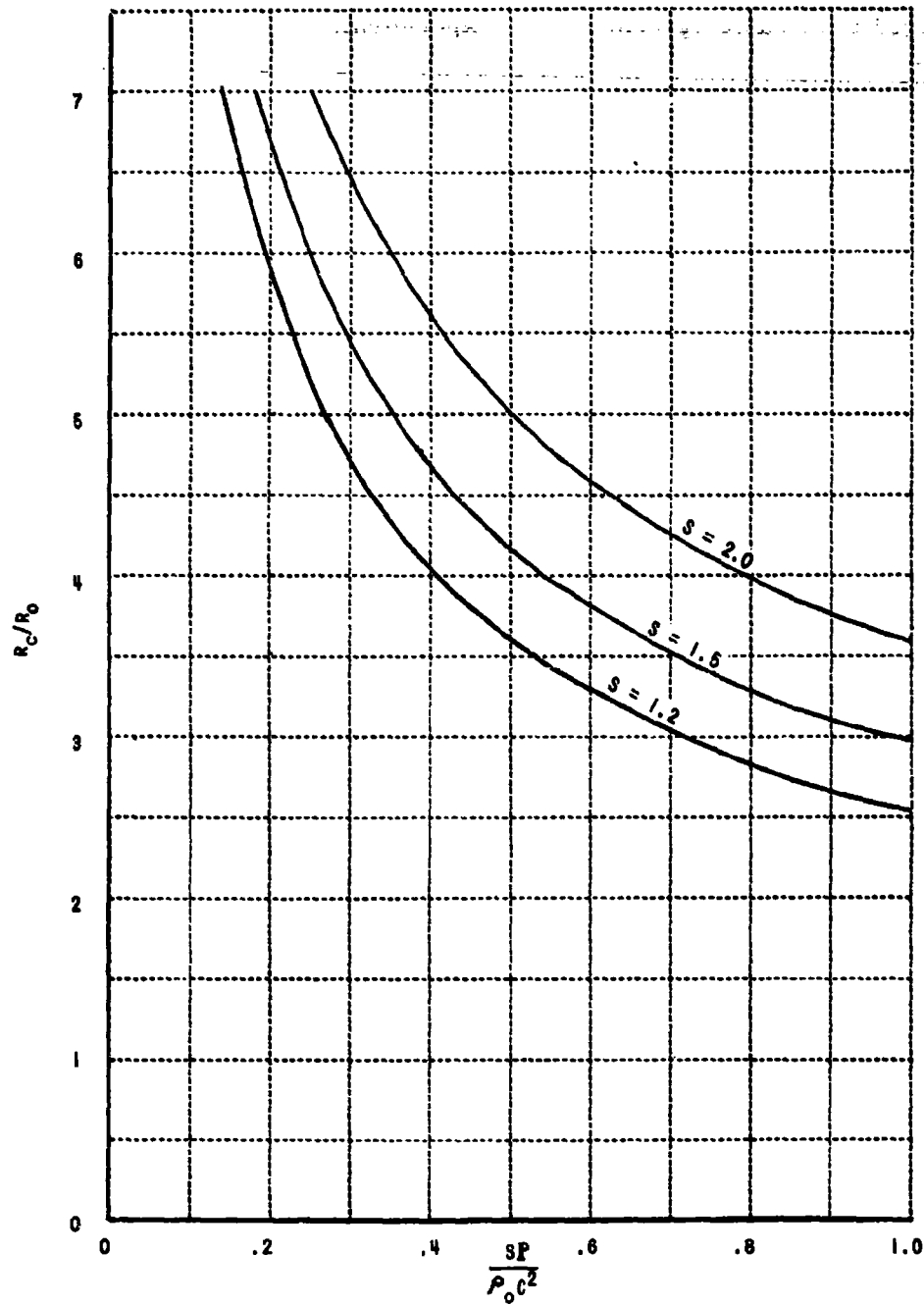


Figure 9 QUASI-STEADY PREDICTION OF SHOCK RADIUS FOR WHICH  $P_1 = P$

# BLAST-WAVE THEORY OF CRATER FORMATION

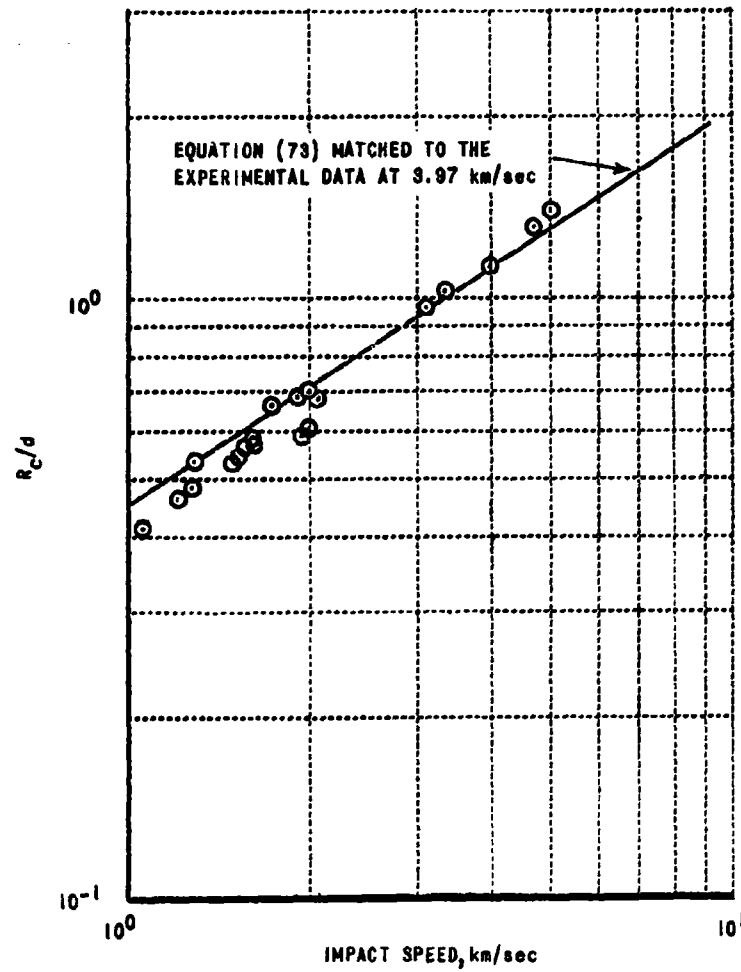


Figure 10 SEMI-EMPIRICAL CORRELATION OF CRATERS FORMED BY ALUMINUM STRIKING COPPER

## BLAST-WAVE THEORY OF CRATER FORMATION

the stress-wave speed when it passed the position corresponding to  $R_c$ .

While these results are encouraging, they nevertheless contain an empirical factor whose significance is not clearly defined at present. Thus, extrapolations to higher impact speed cannot be made with confidence. Our conclusion is that there is a need for an analytical crater-formation criterion whose accuracy is comparable with that of the present quasi-steady (and of the forthcoming quasi-similar) solution. We feel that the target strength will play a role in this criterion, but that considerable work remains to be done.

## BLAST-WAVE THEORY OF CRATER FORMATION

### CONCLUDING REMARKS

Our goal in this research has been an analytic description of hyper-velocity impact. To this end, the approximations of blast-wave theory have been reviewed to determine how well they apply to the problem of shock-wave propagation in solid targets. Most of the literature of blast-wave theory deals with the symmetric problem of a point release of energy in a gas. To adapt these analytical methods to the present problem, then, modifications are required in two areas: first, two spatial coordinates must be considered, and secondly, the equation of state appropriate to a solid must be used.

Solutions which allow for spatial variations in two directions have been found to be very close to the corresponding one-dimensional solutions in all important respects. Thus, the energy transferred by the impacting projectile is the dominant parameter, its momentum playing a minor role. Predictions of shock-wave trajectories based on this concept display excellent agreement with experiment.

The second area in which modifications of the classical blast-wave theory are needed is more significant. The nature of the state equation of solid materials, together with the fact that relatively weaker stages of shock propagation are of interest in this problem, make the assumption of similarity a weak one. Thus, shock propagation in solids is characteristically non-similar, in contrast to the situation normally encountered in gases. To account for this feature properly, analytical methods for treating nonsimilar problems must be used. Fortunately, the required methods are available, and are at present being adapted to this problem. As an interim solution, a crude approximation can be constructed from the similarity solutions themselves.

## BLAST-WAVE THEORY OF CRATER FORMATION

This solution, referred to here by the term "Quasi-Steady," shows remarkable agreement with the limited shock-wave trajectory data available at present. Data of this sort are the only kind that can serve as an unequivocal check on a hydrodynamical theory. Comparisons with final crater dimensions involve other aspects of the theory, especially the criterion used to define crater size, and are consequently not suitable as a check on the shock-propagation theory.

Ultimately, the practical goal of all research in this area is to establish the penetration law, especially in the high-speed regime which is experimentally inaccessible at the present time. From this point of view, the most important aspect of these studies has been to reveal the pivotal importance of the crater-formation criterion on the penetration law. The currently available evidence suggests that impact-generated shock propagation is essentially the same over the speed range from 4.6 to 30 km/sec. Thus, any difference in penetration law is felt to originate from the crater-formation criterion. The present work makes no effort to establish what this criterion should be, though it is felt that it should be related to the strength of the target. As an example of such a criterion, a simple choice related to the pressure being generated at the shock is shown to provide a basis for correlating a large amount of data. These results are encouraging, but still contain an element of arbitrariness, and their extension to the higher impact-speed range requires the development of a more satisfactory criterion.

## BLAST-WAVE THEORY OF CRATER FORMATION

### REFERENCES

1. Bjork, R. L., "Effects of a Meteoroid Impact on Steel and Aluminum in Space." Tenth International Astronautical Congress Proceedings, Vol. II, Springer Verlag (1960), pp. 505-514.
2. Bjork, R. L., "Analysis of the Formation of Meteor Crater, Arizona: A Preliminary Report." Journal of Geophysical Research 66 (1961), pp. 3379-3387.
3. Lees, L. and Kubota, T., "Inviscid Hypersonic Flow Over Blunt-Nosed Slender Bodies." Journal of the Aeronautical Sciences 24 (1957), pp. 195-202.
4. Cheng, H. K., Hall, J. G., Golian, T. C. and Hertzberg, A., "Boundary-Layer Displacement and Leading-Edge Bluntness Effects in High-Temperature Hypersonic Flow." Journal of the Aerospace Sciences 28 (1961), pp. 353-381.
5. Gibson, W. E. and Rudinger, G., "Analytical Study of the Dynamics of the Nuclear Bomb Cloud Rise." Cornell Aeronautical Laboratory Report No. AM-1342-A-2 (July 1960).
6. Eichelberger, R. J. and Gehring, J. W., "Effects of Meteoroid Impacts on Space Vehicles." American Rocket Society Journal 32 No. 10 (October 1962), pp. 1583-1591.
7. Halperson, S. M. and Hall, D. A., "Shock Studies in Transparent Plastic by High-Speed Photographic Techniques." Reports of NRL Progress (September 1961), pp. 37-39.
8. Frasier, J. T., and Karpov, B. G., "Impact Experiments on Wax." Proceedings of the Fifth Symposium on Hypervelocity Impact, Denver, October 30 - November 1, 1961, Vol. II, Part II (April 1962), pp. 371-388.

## BLAST-WAVE THEORY OF CRATER FORMATION

9. Frasier, J. T., "Hypervelocity Impact Studies in Wax." Ballistic Research Laboratories, Report No. 1124 (February 1961).
10. Sedov, L. I., "Similarity and Dimensional Methods in Mechanics." Academic Press (1959).
11. Rice, M. H., McQueen, R. G. and Walsh, J. M., "Compression of Solids by Strong Shock Waves." Solid State Physics, Advances in Research and Applications, Vol. 6, Academic Press (1958).
12. Davids, N. and Huang, Y. K., "Shock Waves in Solid Craters." Journal of the Aerospace Sciences 29 (1962), pp. 550-557.
13. Rae, W. J. and Kirchner, H. P., "Final Report on a Study of Meteoroid Impact Phenomena." Cornell Aeronautical Laboratory Report No. RM-1655-M-4 (February 1963).
14. Taylor, G. I., "The Formation of a Blast Wave by Very Intense Explosion, I, Theoretical Discussion." Proceedings of the Royal Society (A) 201 (1950), pp. 159-174.
15. Taylor, J. L., "An Exact Solution of the Spherical Blast-Wave Problem." Phil. Mag. 46 (1955), pp. 317-320.
16. Latter, R., "Similarity Solution for a Spherical Shock Wave." Journal of Applied Physics 26 (1955), pp. 954-960.
17. Sakurai, A., "On Exact Solution of the Blast-Wave Problem." J. Phys. Soc. Japan 10 (1955), pp. 827-828.
18. Davids, N., Huang, Y. K. and Juanzemis, W., "Some Theoretical Models of Hypervelocity Impact." Proceedings of the Fifth Symposium on Hypervelocity Impact, Denver, October 31 - November 1, 1961, Vol. I, Part I (April 1962), pp. 111-132.



## BLAST-WAVE THEORY OF CRATER FORMATION

19. Kineke, J. H., "Observations of Crater Formation in Ductile Materials." Proceedings of the Fifth Symposium on Hypervelocity Impact, Denver, October 30 - November 1, 1961, Vol. I, Part 2 (April 1962), pp. 339-370.
20. Sakurai, A., "On the Propagation and Structure of the Blast Wave, I." J. Phys. Soc. Japan 8 (1953), pp. 662-669.
21. Oshima, K., "Blast Waves Produced by Exploding Wire." Aeronautical Research Institute, Univ. of Tokyo, Report No. 358 (July 1960).
22. Lewis, C. H., "Plane, Cylindrical, and Spherical Blast Waves Based upon Oshima's Quasi-Similarity Model." AEDC TN 61-157 (December 1961).
23. Altshuler, L. V., Bakanova, A. A. and Trunin, R. F., "Shock Adiabats and Zero Isotherms of Seven Metals at High Pressures." Soviet Physics, JETP 15 No. 1 (July 1962), pp. 65-74.
24. Franken, P., "High Energy Lasers." International Science and Technology (October 1962), pp. 62-68.

## BLAST-WAVE THEORY OF CRATER FORMATION

### APPENDIX

#### SIMULATION OF METEOROID IMPACT BY ENERGY RELEASE\*

A major conclusion reached above is that crater formation is controlled chiefly by the energy of the impacting particle, its momentum playing only a secondary role. Thus we may expect to simulate hypervelocity impact by any experiment in which a strong shock wave is driven into a target by the deposition of energy in any form.

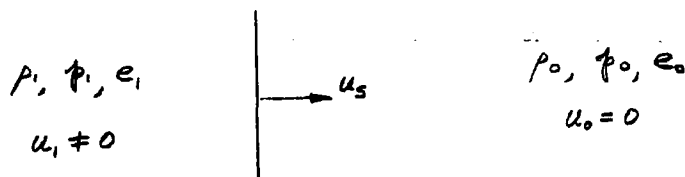
It is of central importance, in considering any simulation of this type, to be certain that the mode of energy deposition does in fact drive a strong shock wave into the target. We shall return to this question below, but for the moment we assume that this condition has been achieved, and present the results that follow as a consequence.

The severity of a high-speed particle impact may be judged by the strength of the shock wave driven into the target. Knowing the Hugoniot data for the target and projectile, it is possible to solve for the shock strength as a function of the impact speed. For the case of energy deposition by some other means, we must now identify the parameters which determine the initial shock strength. The quantity that does this is the power being absorbed by the target, per unit area in the plane of the shock. To see why this is so, consider a plane shock wave of unit area advancing at speed  $u_s$  into a medium of undisturbed density  $\rho_0$  :

---

\*The fact that such a simulation is possible was first pointed out to the authors by Dr. Franklin K. Moore.

# BLAST-WAVE THEORY OF CRATER FORMATION



In unit time, this shock processes an amount of mass given by  $\rho_0 u_s dt$ , per unit area, and raises it to the energy (per unit mass)

$$e_1 = \frac{p_1}{2\rho_0} \left(1 - \rho_0/\rho_1\right)$$

Thus the rate of energy acquisition by the material behind the shock, per unit time and area, is

$$\text{power/area} = \rho_0 u_s \frac{p_1}{2\rho_0} \left(1 - \rho_0/\rho_1\right) = \frac{1}{2} p_1 u_1$$

The strength of any shock wave may therefore be characterized by the amount of power per unit area which it delivers to the medium through which it travels. The Hugoniot curve for iron is interpreted in this light in Figure 11, where it is seen that weak shock waves ( $\rho_1/\rho_0 \approx 1.3$ ) impart about  $10^{10}$  watts/cm<sup>2</sup> while extremely strong shocks ( $\rho_1/\rho_0 \approx 3$ ) transfer to the medium some  $10^{13}$  watts/cm<sup>2</sup>. These orders of magnitude are typical of metals. It is interesting to note that the experiments reported by Altshuler et al<sup>23</sup> achieved shock waves of strength equivalent to  $4 \times 10^{11}$  watts/cm<sup>2</sup>.

For a given projectile-target combination, there is a one-to-one correspondence between impact speed and the power density at the impact point. Their relation is shown in Figure 12 for iron-on-iron. The point to be noted

# BLAST-WAVE THEORY OF CRATER FORMATION

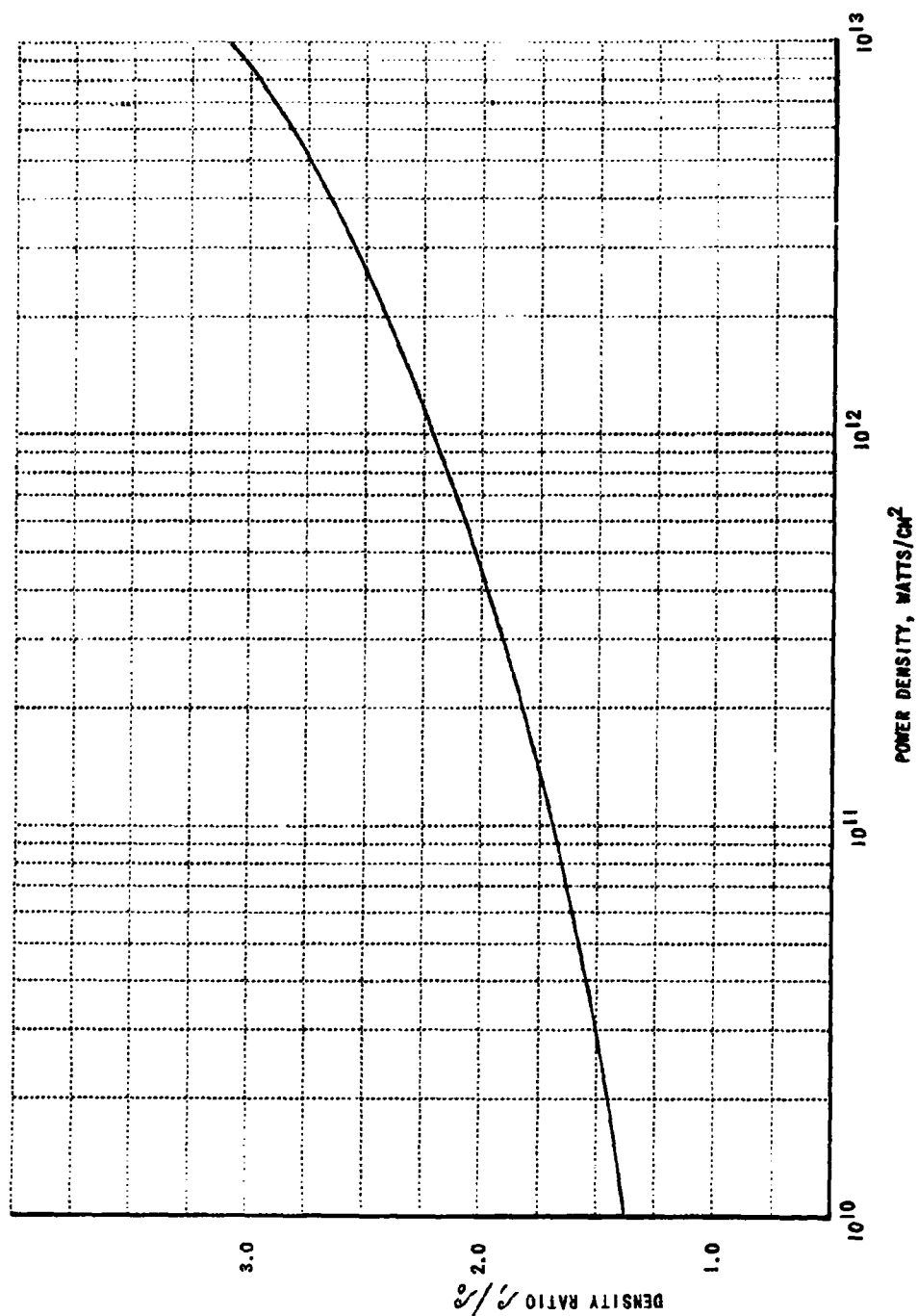


Figure 11 POWER-DENSITY RATING OF NORMAL SHOCK WAVES IN IRON

# BLAST-WAVE THEORY OF CRATER FORMATION

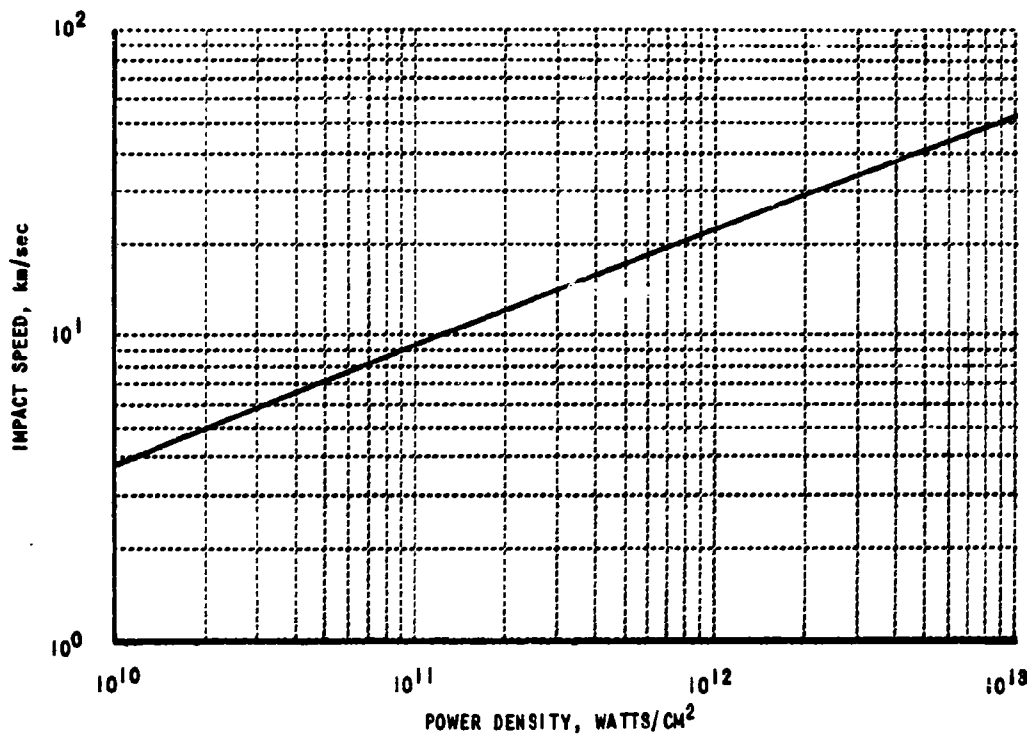


Figure 12 POWER-DENSITY RATING OF SHOCK WAVES DRIVEN INTO IRON TARGETS BY IRON PROJECTILES

## BLAST-WAVE THEORY OF CRATER FORMATION

is that any experimental technique capable of driving shock waves of strength greater than  $10^{11}$  watts/cm<sup>2</sup> can simulate impact conditions which are at present beyond the capability of conventional projection techniques. One energy source that appears to be suitable for such an application is the laser.\* By focusing the beam from such a device, power densities of  $10^{13}$  watts/cm<sup>2</sup>, delivered in less than a microsecond, can be delivered<sup>24</sup> with existing equipment. The fact that the maximum output of these devices is currently being improved at such a rapid rate indicates that, even in the presence of losses, simulation by a laser beam is a promising experimental technique.

The calculations presented in Figure 12 start from the hypothesis that the energy absorption takes place by means of a blast-wave mechanism. Particularly in the case of electromagnetic energy deposition, this assumption needs careful scrutiny. There would appear to be little doubt that this is the correct mechanism when the rate of energy input is sufficiently high. It is known that the mechanism of energy absorption in gases changes, at some point, from one of linear heat conduction to the nonlinear shock-wave mechanism. Exactly where such a transition will occur in the case of solid media is not at present known, although it is presumably amenable to theoretical analysis. The conclusions reached above are based on the assumption that a shock wave will be the correct mechanism whenever the incident power density exceeds  $10^{11}$  watts/cm<sup>2</sup>.

---

\*The use of such a device was suggested by Mr. A. Hertzberg.

## BLAST-WAVE THEORY OF CRATER FORMATION

### ACKNOWLEDGEMENT

The application of blast-wave theory to this problem was originally suggested to the authors by Dr. Franklin K. Moore. We are also indebted to Dr. Walter E. Gibson, Mr. A. Hertzberg, and Dr. Norman S. Eiss, Jr., for many valuable discussions.

Technical monitoring of this program was provided by Mr. James J. Kramer and Mr. Robert J. Denington of the Lewis Research Center. The authors are very grateful to these gentlemen for many helpful suggestions.

# BLAST-WAVE THEORY OF CRATER FORMATION

## LIST OF SYMBOLS

$C$	Velocity appearing in the relation $u_s = C + Su_1$
$e$	Internal energy per unit mass
$E$	Total energy
$f$	Dimensionless pressure, $p/\rho_0 \dot{R}_s^2$
$g$	Dimensionless internal energy $e/\dot{R}_s^2$
$I_1(r)$	Integral defined by Equation (60)
$N$	Exponent defining rate of shock propagation: $R_s \propto t^N$
$p$	Pressure
$P$	Total momentum
$P$	Strength level at which inviscid solution is terminated
$R_s$	Shock Radius
$R_0$	Length scale for shock propagation, $(E/2\pi\rho_0 c^2)^{1/3}$
$r, \theta$	Spherical coordinates
$s$	Entropy per unit mass
$S$	Dimensionless parameter in the relation $u_s = C + Su_1$
$t$	Time after impact
$u, w$	Velocity components in the $r$ - and $\theta$ -directions, respectively
$\Delta(p)$	Function appearing in Mie-Grüneisen state equation
$\Gamma(p)$	Grüneisen factor
$\gamma$	Specific-heat ratio in perfect-gas model
$\eta$	Similarity coordinate, $r/R_s(t)$
$\phi$	Dimensionless velocity, $u/\dot{R}_s$ , positive in the direction of increasing $\eta$



# BLAST-WAVE THEORY OF CRATER FORMATION

$\psi(p)$	Density function in state equation which allows similarity solution
$\psi$	Dimensionless density, $\rho/\rho_0$
$\rho$	Mass density
$\sigma$	Shear Stress
$\tau(\eta)$	$= 2 \frac{\partial \omega}{\partial \theta}(\eta, 0)$
$\omega$	Dimensionless velocity, $w/R_s$ , positive in the direction of increasing $\theta$
$( )_{s, sh}$	Evaluated at the shock
$( )_{o, i}$	Evaluated before, after, the shock
$( )_c$	Denotes cohesive contribution
$( )_H$	Evaluated along the Hugoniot
$( )'$	Ordinary derivative, $d/d\eta$

SPHERICAL SHOCK WAVES  
AND  
CAVITY FORMATION IN METALS<sup>(1)</sup>

N. Davids<sup>(2)</sup>, H. H. Calvit<sup>(3)</sup>, O. T. Johnson<sup>(4)</sup>

<sup>1</sup>This research has been sponsored by the Ballistic Research Laboratory, Aberdeen Proving Grounds. Their support is gratefully acknowledged.

<sup>2</sup>Professor of Engineering Mechanics, The Pennsylvania State University.

<sup>3</sup>Research Assistant, Department of Engineering Mechanics, The Pennsylvania State University.

<sup>4</sup>Physicist, Ballistic Research Laboratory, Aberdeen Proving Grounds.

## SPHERICAL SHOCK WAVES AND CAVITY EXPANSION IN METALS

by

N. Davids, H. H. Calvit, and O. T. Johnson

A theory of crater formation by impact awaits better understanding of the process of shock-wave propagation in solids, especially waves with spherical symmetry. This paper studies theoretically and experimentally the non-steady motion of metallic spheres initiated by explosive blast in a spherical cavity. The method of progressing waves is applied to determine the radius vs. time diagram of the propagation of the wave into the material and leads to values for cavity sizes. The assumptions are made that the material in the vicinity of the cavity possesses a polytropic equation of state, that entropy is constant for an element of material, and that the total energy is constant in time. The original partial differential equations of the problem are then reducible to a succession of ordinary differential equations. Using the Rankine-Hugoniot relations as initial conditions at the shock front, these equations have been integrated using a numerical program developed for a number of metals and the construction of  $r, t$ -diagrams carried out with values for particle velocities and pressure variation on the inner surface. The solutions of the differential equation of progressing waves have been studied by constructing a solution diagram, which is similar to a hodograph plane. An analysis was made of this plane and the role played by the singularities of the differential equation. The appropriate solution curve starts very close to a positive node of the equation, then approaches very close to a saddle-type singularity in a corner of the plane which has been found to represent a meaningful physical boundary

## SHOCK WAVES AND CAVITY FORMATION

condition, namely that pressure and velocity tend asymptotically to zero with increasing time in the proper manner.

Using an equation of state for Aluminum (obtained from data from Los Alamos publications) there is obtained the expansion of a cavity of 1.7 cm radius in a thick Aluminum sphere, filled with 31.6 grams of Pentolite, to its final measured value of 3.0 cm. The initial pressure, which is of the order of 300 kilobars, drops to less than 100 kb in less than 2 microseconds. At this time the shock velocity drops to its acoustic or elastic value in the material. However, the cavity continues to expand to its final stage in a time of 80 microseconds. The simultaneous drop of pressure, velocity, and departure of the medium from the polytropic equation of state signals the termination of the shock regime. This appears as a triangular region on the  $r, t$ -diagram, bounded by the shock front, the inner cavity, and the line  $t = 2$  microseconds. Beyond this time the material of the zone continues to flow radially outwards essentially as an incompressible fluid.

The assumption that metals behave similar to gases as a result of an explosion or impact, is limited to this shock zone, which is shorter in duration than may have been expected. From the known outward displacements of the outer radius of the sphere  $\approx (.1 \text{ inch})$  the increase in cavity volume is accounted for geometrically.

A similar time scale of events may be expected to take place in an impact crater, that is, the shock wave regime should be terminated essentially before the flow of material both radial and tangential, has started.

## SHOCK WAVES AND CAVITY FORMATION

The Ballistic Research Laboratory, Aberdeen Proving Grounds, is conducting a parallel experimental program on thick aluminum spheres and have furnished data needed for this analysis.

In each test, a 32 gram spherical 50/50 Pentolite explosive charge is detonated in the center of a thick walled aluminum sphere with the explosive in contact with the spherical cavity surface. The sphere cavity is approximately 34 mm in diameter (each cavity was machined to assure snug acceptance of the explosive charge). The spheres are machined from cast aluminum blocks. Provisions for inserting the explosive charge are accomplished by machining a threaded well in the sphere that extends radially from the sphere central cavity to the surface. The explosive is inserted by attaching it to a threaded plug which can be screwed into the sphere well until the explosive is seated in the cavity. The plug extends beyond the sphere surface and is used as an attach point for rigid mounting of the entire assembly.

Testing included spheres of two sizes. The initial tests were conducted with spheres having a diameter of 178 mm; later tests were conducted with 254 mm diameter spheres.

Measurements of initial free surface velocity and maximum radial expansion are accomplished by the use of two capacitance type displacement gages. These gages merely indicate the change in capacitance resulting from the variation in separation distances of two condenser plates, the gage constitutes one plate and the sphere surface the other.

Cathode ray oscilloscopes were used to record the displacement-time histories of the sphere surface.

## SHOCK WAVES AND CAVITY FORMATION

The scope sweeps were triggered by an ionization probe inserted into the explosive detonator well; the sweep start also provided a time zero point.

Measurements of the inner cavity and outer surface diameters were made before and after each test. Caliper measurements of the outer surface diameter are in reasonable agreement with the oscillograph records.

### 1. INTRODUCTION - Description of the Problem

The Ballistic Research Laboratory (BRL), Aberdeen Proving Grounds, is engaged in conducting an experimental program of internal explosions in small cavities in metal spheres. This paper presents the results of both the experimental and an analytical study of the problem, with particular emphasis on the propagation of shock waves in the metal immediately after detonation of the explosive.

Figs. 1 and 2 show a 7 inch sphere of aluminum such as has been used to date in BRL experiments. The phenomena, and hence their analysis, which result from detonation of the explosive in the inner cavity, are complex because different effects predominate in different parts of the material. Thus, there is an innermost zone or spherical shell where very large radial displacements have occurred under temperatures and pressures far beyond the range of conventional mechanical behavior. The material is in some type of "fluid" state in this zone and shows relatively little tendency for cracks to initiate there. Next, there is an intermediate zone of the sphere where the material begins to exhibit more normal mechanical behavior, as evidenced by the many small tension and shear cracks which have formed there. A few of the stronger cracks which get started may penetrate

SHOCK WAVES AND CAVITY FORMATION

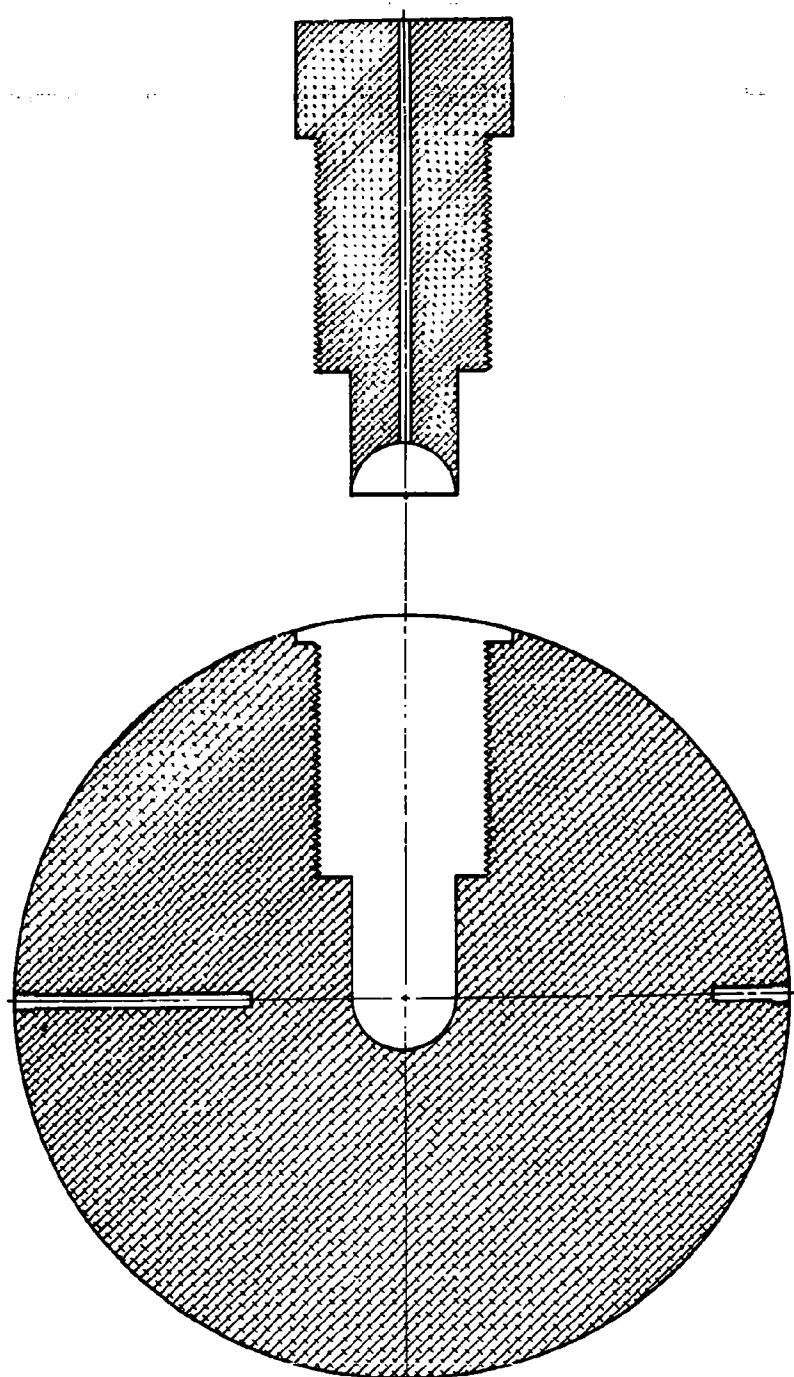
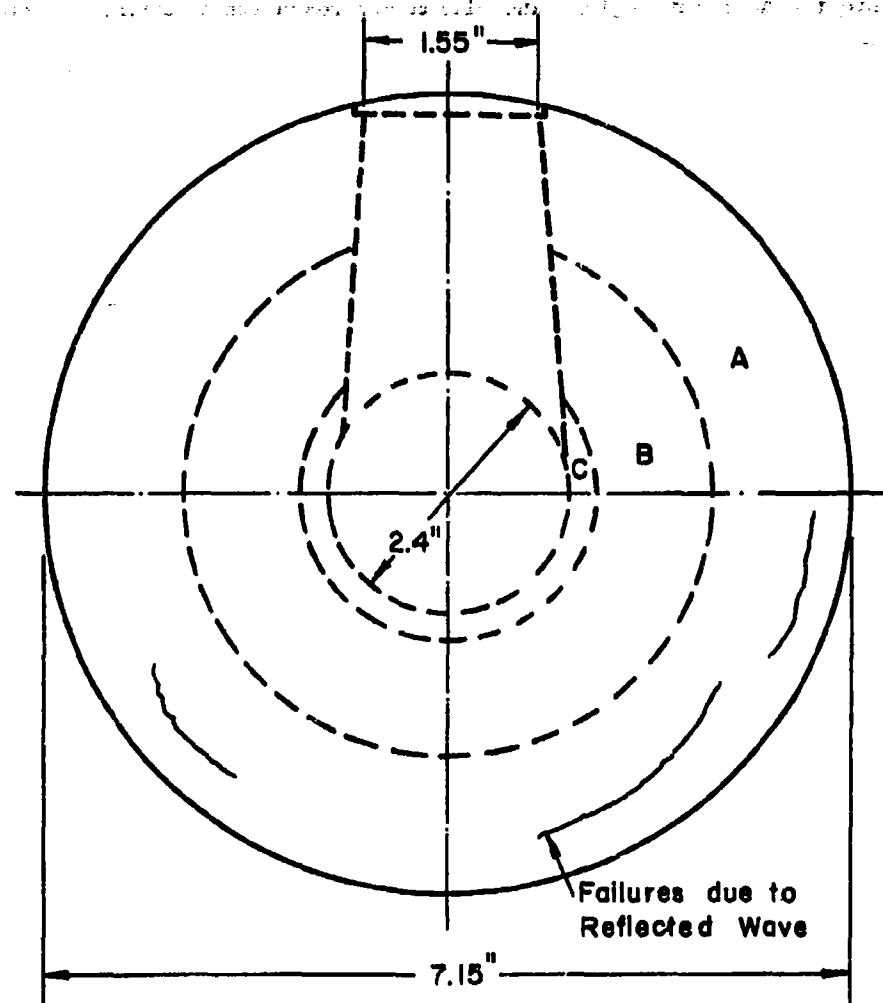


FIG. 1

ALUMINUM SPHERE AND PLUG

## SHOCK WAVES AND CAVITY FORMATION



Zone A - No damage, other than that of reflected wave

Zone B - Heavily damaged

Zone C - "Fluid" zone

Note - Dimensions are approximate

FIG. 2 - ALUMINUM SPHERE - POST SHOT.



## SHOCK WAVES AND CAVITY FORMATION

into the adjacent regions and ultimately reach the boundaries. Finally, there is an outermost zone dominated by the effect of the external boundary of the sphere. Here reflection effects such as scabbing cracks are often observed.

The transition between successive zones are not exact, but in some specimens, rather surprisingly enough, are fairly sharply delineated.

In this paper we shall make an analysis of the innermost shock zone. Its direct aim is to provide a description of the shock process in the metal. More specifically a useful theory must furnish a time for the duration of the process, the size of the zone influenced by the shock front, values for the displacements, and thermodynamic variables of pressure, density, and temperature in the material. A useful tool is the  $r, t$ -diagram which shows the path made by a set of concentric spherical shells. This diagram is possible because of the single space coordinate.

The problem of the shock expansion of spherical cavities is closely related to that of crater formation by hypervelocity projectiles. The features we have outlined above are present in the crater problem as well. The crater problem carries with it, however, the further complication of tangential flow, thus requiring two space coordinates. Except for the presence of the plug shown in Figs. 1 and 2, the arrangement for the blasts have spherical symmetry, and we may reasonably assert that radial motion occurs, so that all the physical quantities of the problem depend on only one space coordinate. There is however, a slight actual departure because of the plug or because of asymmetrical detonation, and which are not important to the problem.

## SHOCK WAVES AND CAVITY FORMATION

### 2. Spherical Shocks - Time Sequence of Effects

Just as the study of the problem has been conveniently divided up into spatial zones, we can divide up the sequence of events in the spherical blast process for detailed analysis as follows:

a) Initial Stage - Here the detonation wave of the exploding gas makes contact with the solid and then generates a shock wave in the solid. This stage might be considered as terminated when the density in the solid has dropped to its free space value, at the inner cavity.

b) Expansion Stage - The compressed solid expands radially outward and actually forms the cavity. This stage is dominated mostly by inertia forces.

c) Final Stage - Here the shock wave decays, permanent deformation of the cavity stops, and the material has undergone some permanent plastic strain.

The first stage lasts up to about 2.5 microseconds. The second turns out to be relatively long and can take up to about 100 microseconds or even longer. It must, of course, be understood that these phases need not be distinctly separated events in time, especially the terminating phase of the expansion.

### 3. Basic Mathematical Equations of Shock Waves

Because of spherical symmetry our problem is reducible to a radial and a time coordinate. Shock wave propagation in a solid is very closely related to that of a spherical wave in a gas. We may make the following assumptions about the medium:

1. Thermodynamic equilibrium holds (see [2], p. 3), i.e. that changes

## SHOCK WAVES AND CAVITY FORMATION

of state are adiabatic. By this we mean that entropy is constant along a "particle path", i.e., a fixed element of the medium.

2. The medium is a perfect fluid, i.e., any rigidity or shear effects are neglected.

3. The effects of entropy changes are negligible, i.e., that the pressure is a function of the density alone.

4. The total energy available for the motion is fixed.

If the medium were assumed to be polytropic with the adiabatic exponent  $\gamma$ , we would have,

$$f(p, \rho) = p\rho^{-\gamma} = \text{const.} = A \quad (3.1)$$

The conservation laws in Eulerian form, with subscripts denoting partial derivatives, become

$$\rho_t + u \rho_r + \rho u_r + 2u\rho/r = 0 \quad (\text{mass}) \quad (3.2)$$

$$u_t + uu_r + p_r/\rho = 0 \quad (\text{momentum}) \quad (3.3)$$

$$(p\rho^{-\gamma})_t + u(p\rho^{-\gamma})_r = 0 \quad (\text{state}) \quad (3.4)$$

The third of these equations is not quite equivalent to ( ), since it only expresses the fact that the entropy is constant along the path of an element, and does not imply its constancy throughout. This is a difference from the case of plane waves; another difference from the equations of one-dimensional flow is the additional term  $2u\rho/r$  occurring in (3.2) which stands essentially for the spherical attenuation of the wave. This term, of course, is very important to the problem.

## SHOCK WAVES AND CAVITY FORMATION

A complete geometrical description of the disturbance is afforded by the construction of an  $r, t$ -diagram, as shown in Fig. 3. Here the solid lines represent the motion of the points of a spherical surface, referred to as a "particle". The most prominent feature in this diagram is a discontinuity, or shock front which propagates through the material at the head of the disturbance. This curve, together with the cavity boundary, defines a region (shaded in the figure) in which the solution to the system of partial differential equations (3.2) to (3.4) applies. Certain boundary conditions, to be discussed later, must be satisfied. However, the difficulty of the problem is that, unlike the conventional boundary value problems, here the boundary curves are themselves unknown, and must be found as part of the problem. In fact, the determination of these two curves are the most important part of the problem.

### 4. The Method of Progressing Waves

The idea of this and similar mathematical methods is to reduce the partial differential equations to ordinary ones, by assuming the specific form for the shock front curve and imbedding it in a one-parameter family of curves. These curves are called "progressing waves". For general details of the method, see [2] p. 419-433. The method was used by R. G. Newton [4] to analyze blast shock problems, and a similar method is being used by Rae and Kirchner [18] in studying meteoroid impact phenomena.

Our "progressing wave" solutions are defined to be of the form,

$$u = t^{\beta} \xi U(\xi) \quad (4.1a)$$

$$\text{with } \xi = rt^{-\alpha}$$

$$\rho = t^{\delta} D(\xi) \quad (4.1b)$$

# SHOCK WAVES AND CAVITY FORMATION

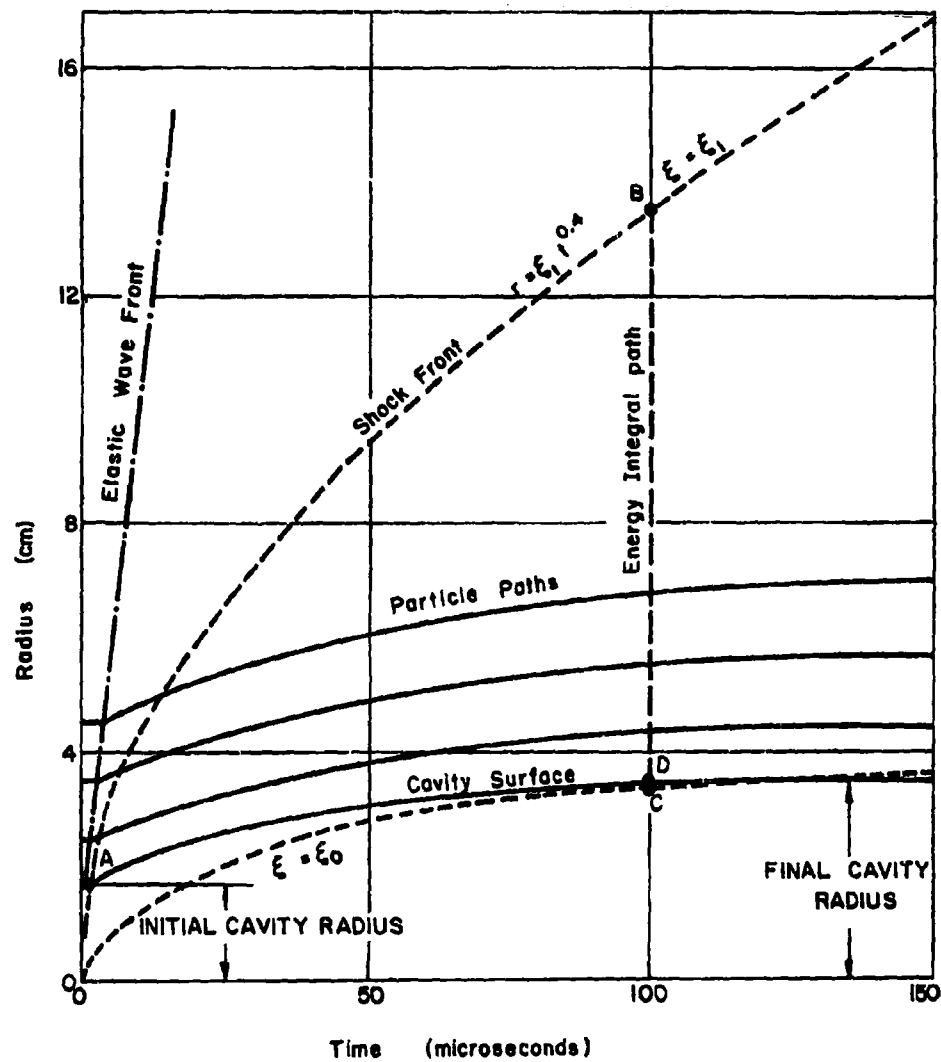


FIG 3 - CAVITY EXPANSION AND PARTICLE TRAJECTORIES

## SHOCK WAVES AND CAVITY FORMATION

$$p/\rho = t^\epsilon \xi^2 P(\xi) \quad (4.1c)$$

where  $\alpha$ ,  $\beta$ ,  $\delta$ ,  $\epsilon$  are parameters, and  $U$ ,  $D$ ,  $P$  functions to be determined. By introducing this variable  $\xi$  we have defined geometrically a family of surfaces  $\xi = \text{const.}$  in the  $r, t$ -plane, which will play an important role in the analysis. Although these are not the trajectories of the particles of the medium, we shall see that the shock front belongs to this family of surfaces.

We now substitute the expressions (4.1) into the equations of motion (3.2)-(3.4), enabling us to eliminate the explicit factor  $t$  by properly choosing the exponents, thereby leaving a system of functions of one independent variable  $\xi$ . This is accomplished by letting

$$\epsilon = 2\beta \quad ; \quad \beta = \alpha - 1 \quad (4.2)$$

See [17] for details.

This leads to the set of ordinary differential equations:

$$\xi D'/D = -(\delta + \xi U' + 3U)/(U - \alpha) \quad (4.3)$$

$$\xi U' = [-U(U - \alpha)(U - 1) + (\delta + 2\beta + 3U\gamma)P]/\Delta \quad (4.4)$$

$$dP/dU = \xi P'/\xi U' = P[N(U) + PQ(U)]/[R(U) + PS(U)] = F(U, P)/G(U, P) \quad (4.5)$$

where, after simplification

## SHOCK WAVES AND CAVITY FORMATION

$$N(U) = \gamma U(3\alpha - 1 - 2U) + (3 - \alpha)U - 2\alpha$$

$$Q(U) = [2\beta - (\gamma - 1)\delta]/(U - \alpha) + 2\gamma$$

$$R(U) = U(U - \alpha)(1 - U)$$

$$S(U) = \delta + 2\beta + 3U\gamma$$

The latter is the basic differential equation for progressing waves. After the appropriate solution has been found for  $P = P(U)$ , the function  $\xi = \xi(U)$  is found by a quadrature of (4.4) and the density function  $D(\xi)$ , from (4.3).

These progressing wave solutions, as we shall see, provide a sufficiently general mathematical description of an expanding cavity reasonably consistent with the given conditions of initiation of the process. There remains the problem of choosing the two parameters  $\alpha$  and  $\delta$ .

A condition of constant entropy is not in general satisfied by a spherical wave because of its attenuation. An alternate assumption is that the motion is adiabatic, i.e., has constant total energy. This is a reasonable one for the cavity expansion process, because of its short duration, provided certain secondary effects are neglected. With  $\xi = \xi_1$  representing the shock front at a time  $t$ , the total energy in the fluid shell (potential + kinetic) at time  $t$  is given by

$$E(t) = \int_{r_0}^{r_1} \left( \frac{P}{\gamma - 1} \right) 4\pi r^2 dr + \int_{r_0}^{r_1} \frac{1}{2} \rho u^2 4\pi r^2 dr \quad (4.6)$$

## SHOCK WAVES AND CAVITY FORMATION

where  $r_0 = \xi_0 t^\alpha$  is the inner radius of the shell (Fig. 1) and  $r_1 = \xi_1 t^\alpha$  is the location of the shock front.

Using the substitutions in (4.1) and assuming  $t$  is constant, we obtain

$$E(T) = 4\pi t^\delta + 5\alpha - 2 \int_{\xi_0}^{\xi_1} \left( \frac{P}{\gamma-1} + \frac{1}{2} u^2 \right) \xi^4 D(\xi) d\xi \quad (4.7)$$

Since the integral is independent of  $t$ , we make the energy independent of time by satisfying the relation

$$\delta + 5\alpha - 2 = 0 \quad \text{or} \quad \delta = 2 - 5\alpha \quad (4.8)$$

### 5. Boundary Conditions at Shock Front

We shall narrow down the number of parameters by requiring the compatibility of our solution with the basic Rankine-Hugoniot conditions across a shock front. If the undisturbed and disturbed medium parameters are  $u_0, \rho_0, p_0$  and  $u_1, \rho_1, p_1$  respectively and the shock wave velocity is  $C$ , then these relations are (see [2], p. 123-4), for a polytropic medium and when the undisturbed state is a medium at rest, with  $u_0 = 0$ , we obtain

$$\rho_1 (C - u_1) - \rho_0 C = 0 \quad (5.1a)$$

$$\rho_1 u_1 (C - u_1) - (p_1 - p_0) = 0 \quad (5.1b)$$

$$\rho_1 \left( \frac{1}{2} u_1^2 + \frac{1}{\gamma-1} \frac{p_1}{\rho_1} \right) (C - u_1) - p_1 u_1 = 0 \quad (E_0 = 0) \quad (5.1c)$$



# SHOCK WAVES AND CAVITY FORMATION

With  $\mu = \sqrt{(\gamma-1)/(\gamma+1)}$ , if  $p_0$  is negligible,

$$u_1 = c (1 - \mu^2) \quad (5.2a)$$

$$p_1 = \rho_0 u_1 c = \rho_0 c^2 (1 - \mu^2) \quad (5.2b)$$

$$\rho_1/\rho_0 = (\gamma + 1)/(\gamma - 1) = 1/\mu^2 \quad (5.2c)$$

$$c = \sqrt{dp/d\rho} = \sqrt{1 + \mu^2} c$$

The last quantity is conveniently referred to as the "sound speed" in shock wave analysis. These relations apply just as well to a spherical or curved surface as to a plane, since the effect of spherical divergence (the  $2u/r$  term) on a finite or sudden jump is of higher order. This may also be shown geometrically by considering an infinitesimal surface element of the shock front. Since  $\xi_1 = r t^{-\alpha}$  along the shock front,  $c = dr/dt = \alpha \xi_1 t^{\alpha-1}$ .

From (4.1) and the relations (4.3) the Rankine-Hugoniot equations become

$$t^{\delta+\beta} \xi_1 D(\alpha - U) - \rho_0 \alpha \xi_1 t^{\beta} = 0 \quad (5.3a)$$

$$t^{\delta+2\beta} \xi_1^2 DU (\alpha - U) - t^{\delta+2\beta} \xi_1^2 DP = 0 \quad (5.3b)$$

$$t^{\delta+3\beta} D\xi_1^2 \left( \frac{1}{2} U^2 + \frac{1}{\gamma-1} P \right) \xi_1 (\alpha - U) - t^{\delta+3\beta} \xi_1^3 DPU = 0 \quad (5.3c)$$

## SHOCK WAVES AND CAVITY FORMATION

We note that the time factor cancels in (5.3b) and (5.3c), so that they are automatically satisfied, but to secure independence of time in (5.3a), it is necessary to make

$$\delta = 0 \quad (5.3d)$$

With this condition, and the relations (4.2), the assumed form for the progressing wave solutions reduce to

$$u = r/t \, U(\xi) \quad p = (r/t)^2 \, D(\xi) \, P(\xi) \quad (5.4)$$

$$\rho = D(\xi) \quad p/\rho = (r/t)^2 \, P(\xi) \quad \text{with } \xi = r t^{-\alpha}$$

This solution shows that on the shock front or free surface, where  $\xi$  is constant, the physical quantities such as velocity, pressure, density, and wave velocity are constant on the rays  $r/t = \text{constant}$ . This also dimensionalizes the functions (5.4) correctly.

The complete set of exponents is now

$$\begin{aligned} \alpha &= 2/5 & \epsilon &= -6/5 \\ \beta &= -3/5 & \delta &= 0 \end{aligned} \quad (5.5)$$

### Initial Conditions

Since  $\xi = \xi_1$  on the shock front, we have, just behind it,

$$U(\xi_1) = \alpha(1 - \mu^2) = 2\alpha/(\gamma + 1) \quad (5.6a)$$

$$D(\xi_1) = \rho_0/\mu^2 \quad (5.6b)$$

## SHOCK WAVES AND CAVITY FORMATION

$$P(\xi_1) = \alpha^2 \mu^2 (1 - \mu^2) = 2\alpha^2 \mu^2 / (\gamma + 1) \quad (5.6c)$$

with  $\alpha = 2/5$ .

The right side of equations (5.6) give us, for a specified material, a definite initial point in the P-U plane, through which a single solution curve is determined in general. Note that the constant  $\xi_1$ , still undetermined, is not needed for this. We will discuss in Section 9 how this constant may be determined.

### 6. Equation of State of Aluminum

In Fig. 4 is shown a straight-line logarithmic fit of the relationship between pressure and relative density for 24ST aluminum in the range between 100 and 400 kilobars, the data being taken from [3]. This furnishes the polytropic-type relation

$$p \left( \frac{\rho}{\rho_0} \right)^{-7.60} = 52.7 \quad 100 \text{ kb} < p < 400 \text{ kb} \quad (6.1)$$

where  $p$  is in kilobars.

A few points are shown beyond the 400 kb range based on additional data taken from [3]. Here there is a slight but consistent departure from the equation of state (6.1). However under the conditions of our explosion the range of pressures does not exceed 400 kb.

Below about 100 kb we have a transition to elastic-plastic or elastic behavior. The nature of this transition is considerably uncertain. We may also note that, unlike gases, the value of  $\gamma$  is very high, i.e., relatively small density changes occur under very high pressures.

# SHOCK WAVES AND CAVITY FORMATION

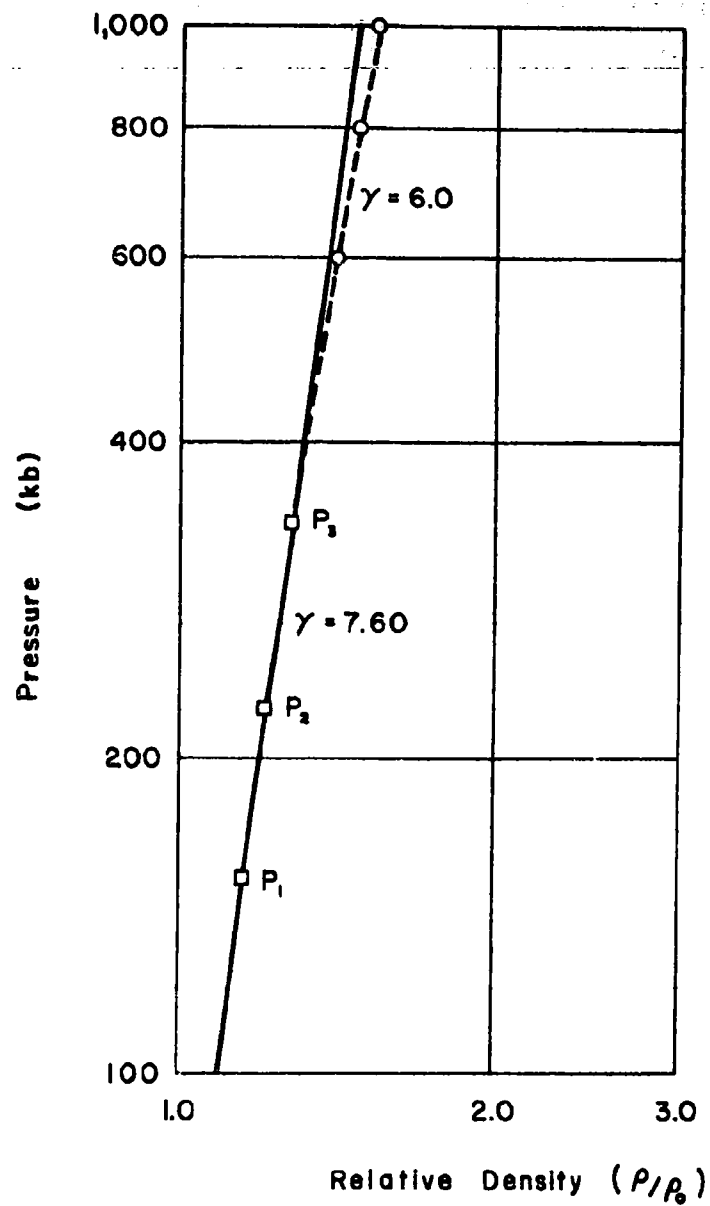


FIG. 4 - EQUATION OF STATE OF ALUMINUM

## SHOCK WAVES AND CAVITY FORMATION

The polytropic-type equation of state is a very convenient one to use for metals provided the pressure range is restricted, such as in (6.1). It has the advantage that the progressing wave procedure in Section 4 can be carried through. However, such an equation of state must always be modified at low pressures since the density of a solid does not tend to zero with the pressure. Other equations of state have been used, e.g. Sedov in [11], and Stanukovich [15], have used the formula

$$p = A [(\rho/\rho_0)^\gamma - 1] \quad (6.2)$$

For aluminum, the values  $A = 187$ ,  $\gamma = 4.27$ ,  $\rho_0 = 2.7$  provide a good fit to the data points of Fig. 4.

Further discussion of equations of state for solids is given by Huang [14].

### 7. The P, U-Diagram

Using the condition of constant energy, the 2/5-power law holds, and the differential equation (4.5) for progressing waves may be solved. This was done numerically by means of a FORTRAN program described in [17]. A family of integral curves in the diagram are shown in Fig. 5. All of them issue from the singular point A enclosed in a rectangle on the diagram, and which is located by equating  $F(U,P) = G(U,P) = 0$  in (4.5). For our set of constants this point is  $U_0 = 0.0916$ ,  $P_0 = 0.02884$ . A more detailed analysis of the singular points is given in [17]. It can be seen that all the curves come out of this "unstable nodal point" along a common tangent. The point  $U = 0$ ,  $P = 0$  is a stable nodal point, or "sink", and the point  $P_0 = 0$ ,  $U_0 = 0$  is a saddle point. The solution curve for

# SHOCK WAVES AND CAVITY FORMATION

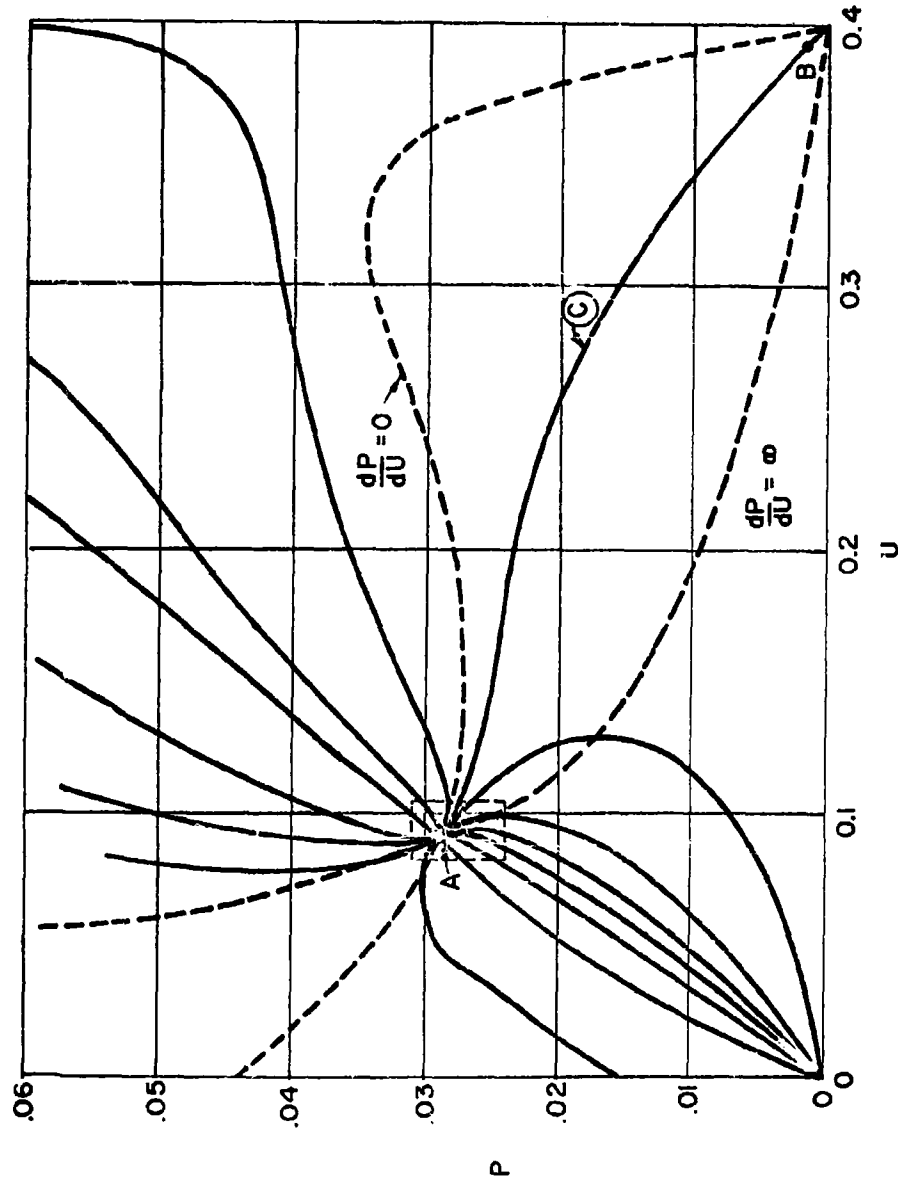


FIG 5 - P,U DIAGRAM, PROGRESSING WAVES : AL,  $\gamma = 7.6$

## SHOCK WAVES AND CAVITY FORMATION

the physical problem starts close to the source, then runs over very close to the saddle point. There is a unique curve (marked C in Fig. 5) which actually runs into the saddle. The accuracy of the computations is not sufficient to distinguish whether our solution actually coincides with C or not.

The "source" point itself represents a shock of infinite strength. Here the pressure and density just behind the shock front are infinite (with a finite total impulse, however) and the particle velocity is equal to the shock wave velocity. This type of condition arises in stress-wave propagation problems as well, in the form of a  $\delta$ -function at the wave-front. See [16]. It is a consequence of the assumed instantaneous (i.e. step) loading of the material. With such a loading we must start the propagation of either a zone of infinite pressure if the velocity is finite, or our front must start out with an infinite velocity.

The end-point of the solution curve C at  $U = \alpha$ ,  $P = 0$  provides a very reasonable physical condition of asymptotic character. For, if we consider any point A in the  $r, t$ -plane, Fig. 3, the "particles" must cross the family of curves

$$r = \xi t^\alpha \tag{7.1}$$

(shown dotted) from left to right, since we have compression shock. Thus the particle curve (solid) has a lower slope at A than that of the dotted curve:

$$u = \frac{r}{t} \quad U(\xi) < \frac{\delta r}{\delta t} = 0.4 \frac{r}{t}$$

## SHOCK WAVES AND CAVITY FORMATION

This condition is always satisfied since all the solution curves in the  $U, P$ -plane coming out of the unstable nodal point lie to the left of the vertical line  $U = 0.4$ . However, for the curve  $C$   $u \rightarrow 0.4 r/t$  as  $t \rightarrow \infty$ , i.e. the particle curve is asymptotic to (7.1). The  $P = P(U)$  curves which end in  $U = 0, P = 0$  give particle curves which cross all the curves of (7.1).

### 8. The Radius-Time $r, t$ -Diagram

Figs. 6 and 7 show an  $r, t$ -diagram plotted for an initial cavity radius of 1.698 cm. Pressures in kilobars are also shown on Fig. 6. This figure gives much more detail of the early phase of the expansion up to  $t = 2.5$  microsec. from its start at  $t = 0.9 \mu$  sec. In this elapsed time of  $1.6 \mu$  sec the inner cavity has only grown to 1.86 cm, which is only 13% of its ultimate change. However, the pressure has already fallen considerably. At the cavity surface it is down to 50 kb.

We also note that the shock velocity at point labelled  $P$  on the diagram is equal to the known elastic wave velocity of the material. Beyond this point the  $2/5$ -power law for the shock front starts to deviate from this velocity. Such a condition represents a discrepancy of the progressing wave method from this point on which is inevitable because of the equation of state used.

Figs. 8, 9, and 10 show how the pressure, particle velocity and density decay with time at the inner cavity surface. We note that  $\rho = \rho_0$  occurs for  $t = 2.5 \mu$  sec. Of course, we may not conclude that  $\rho$  becomes less than the free space density because the equation of state (6.1) no longer applies.



# SHOCK WAVES AND CAVITY FORMATION

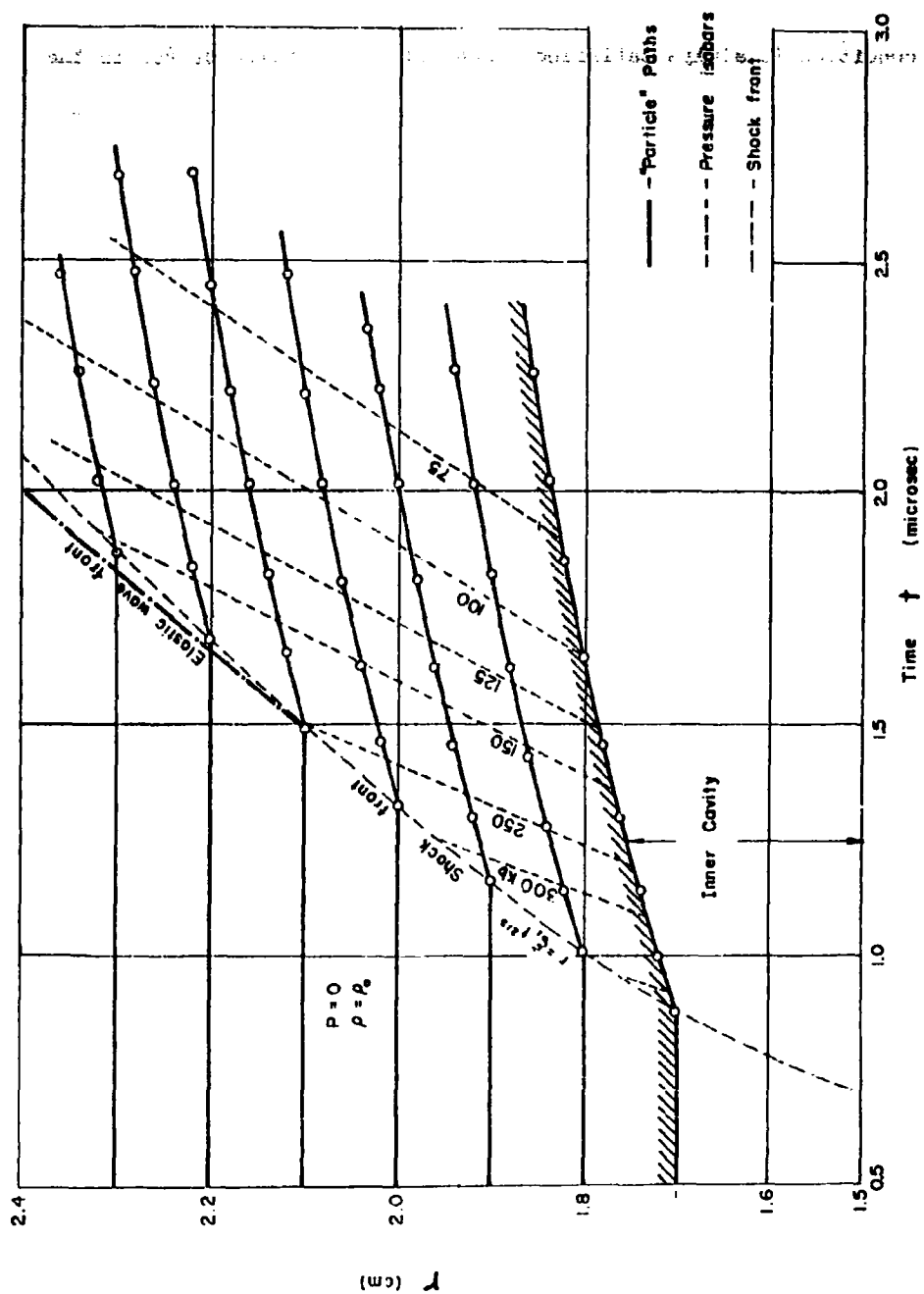


FIG 6 - r, t - DIAGRAM OF SHOCK REGION FOR ALUMINUM SPHERE

# SHOCK WAVES AND CAVITY FORMATION

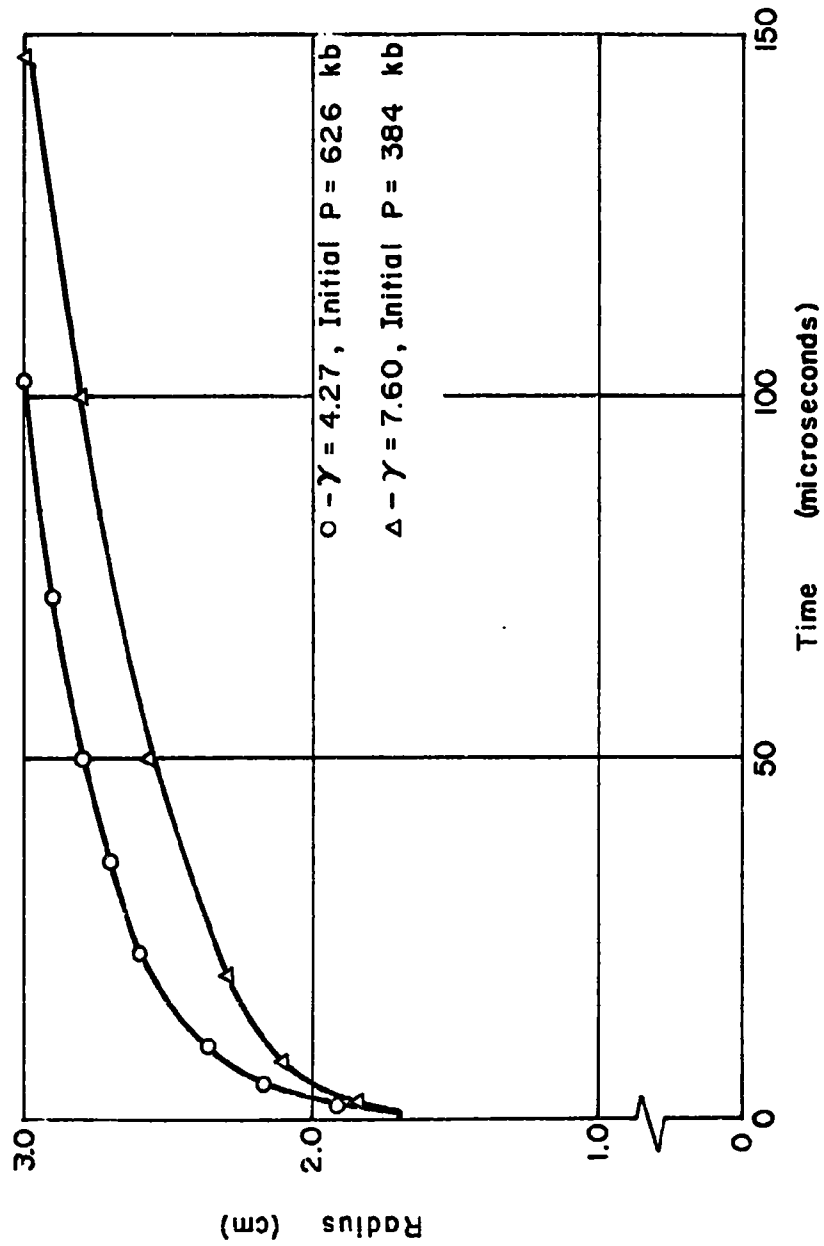


FIG. 7 - R-T DIAGRAM FOR CAVITY SURFACE FOR DIFFERENT  $\gamma$ 'S

# SHOCK WAVES AND CAVITY FORMATION

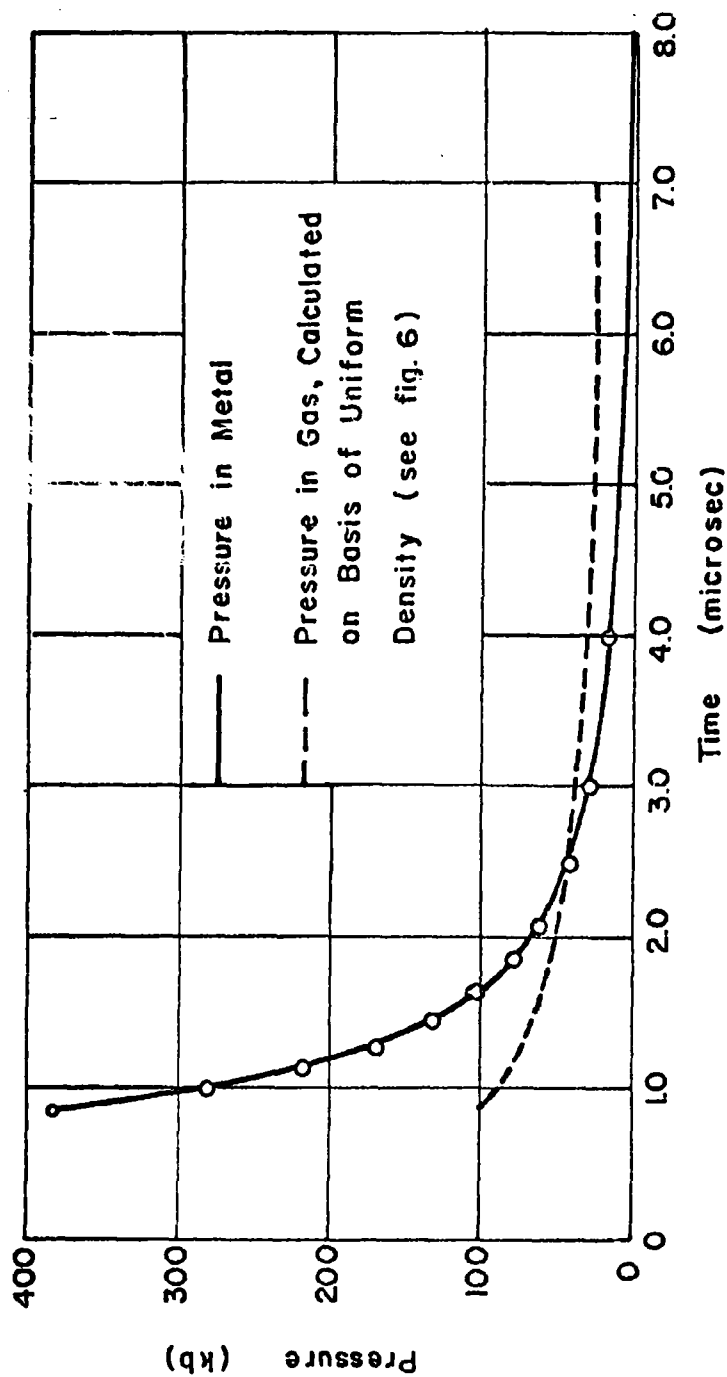


FIG. 8 - PRESSURE DECAY ON CAVITY SURFACE IN AL :

$$\gamma = 7.6, \quad \rho = 2.70 \text{ gm/cm}^3$$

# SHOCK WAVES AND CAVITY FORMATION

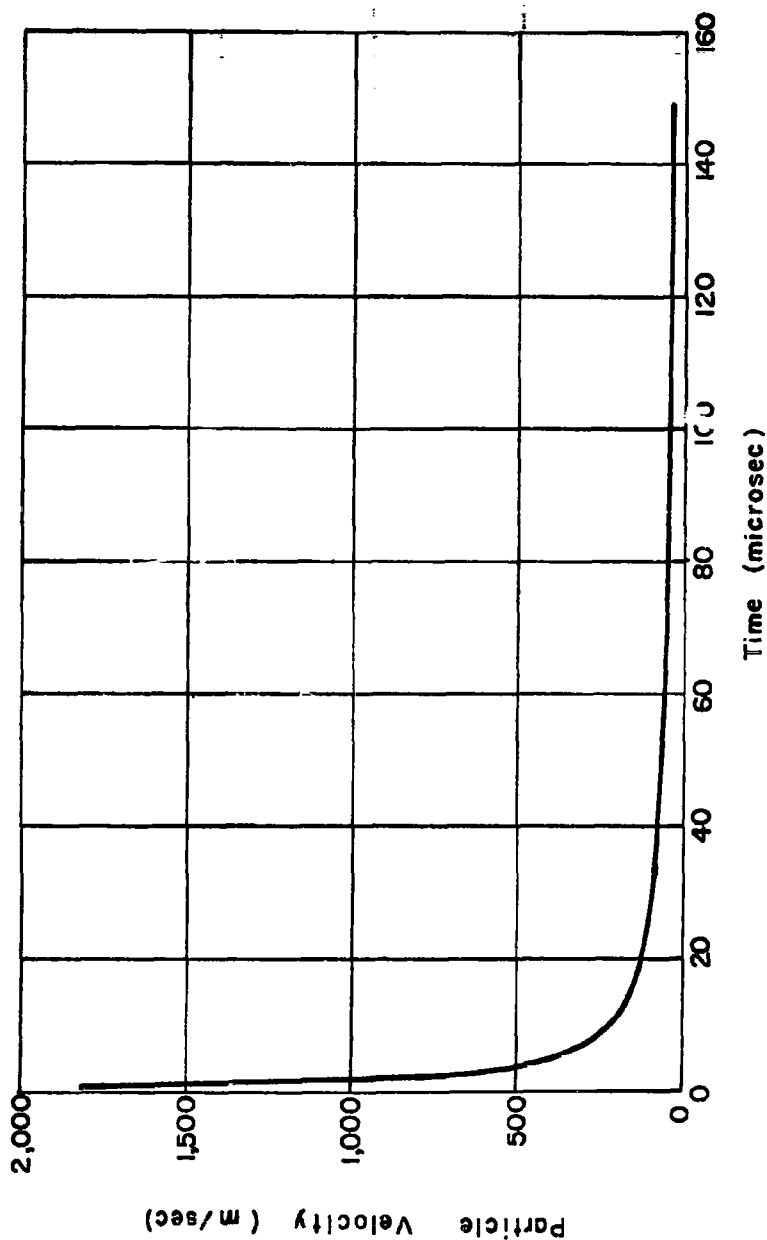


FIG 9 - PARTICLE VELOCITY ON CAVITY SURFACE

AL :  $\gamma = 7.6$  ,  $\rho_0 = 2.70 \text{ gm/cm}^3$

# SHOCK WAVES AND CAVITY FORMATION

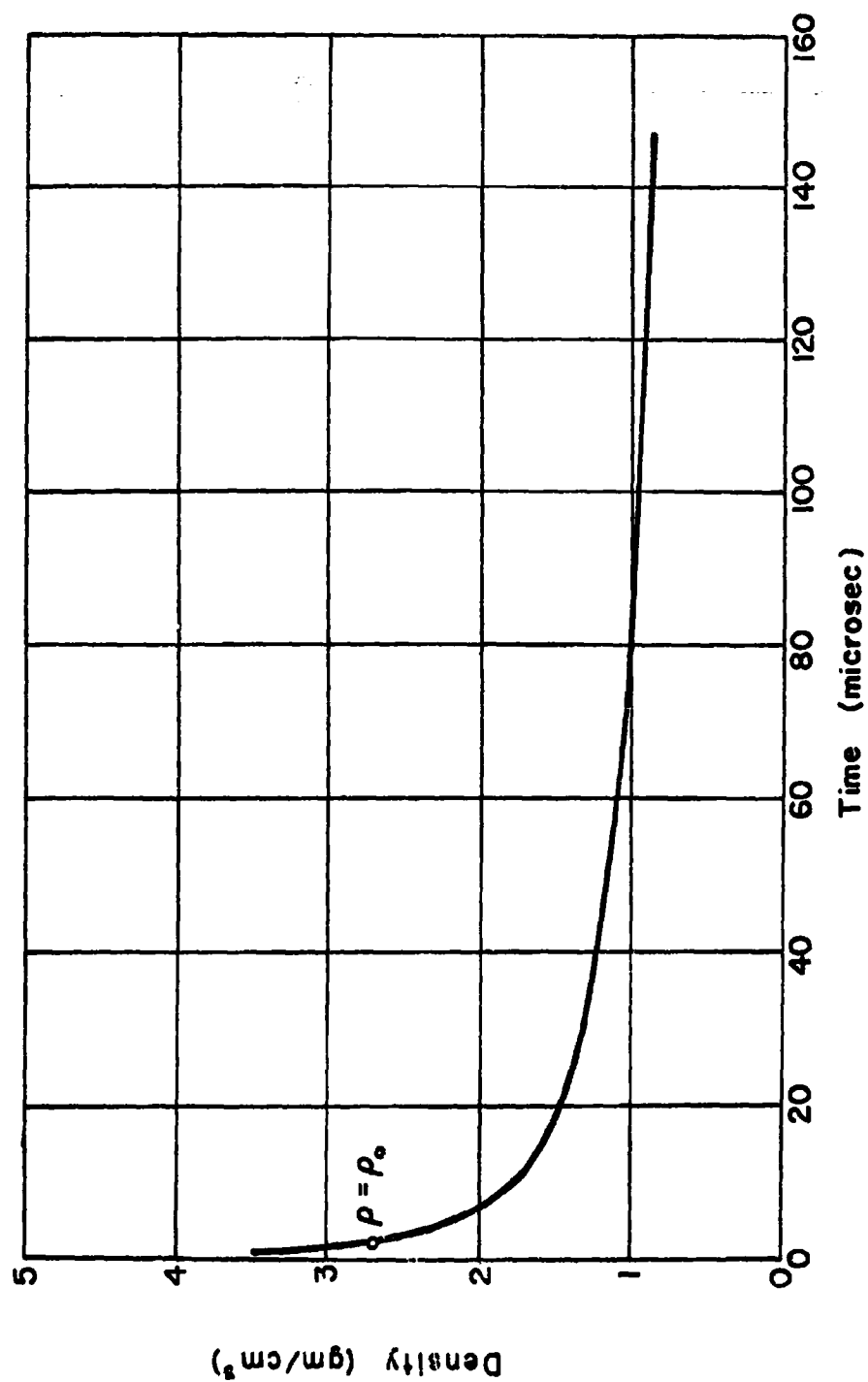


FIG 10 - VARIATION OF DENSITY AT CAVITY SURFACE ;

AL :  $\gamma = 7.6$   $\rho_0 = 2.70 \text{ gm/cm}^3$

# SHOCK WAVES AND CAVITY FORMATION

## 9. Results

TABLE 1  
Variation of physical quantities along  
solution curve and cavity surface

T	U	P	$\xi$	D	E	R <sup>(2)</sup>
sec x 10 <sup>-6</sup>				gm/cc	ergs x 10 <sup>12</sup>	cm
.8684	.09302	.02856	451.28 <sup>(1)</sup>	3.5182	-0.0	1.698
.9539	.09312	.02854	438.45	3.4282	-.188	1.713
1.062	.09324	.02852	424.25	3.3282	-.368	1.730
1.186	.09337	.02844	410.10	3.2282	-.520	1.748
1.329	.09352	.02846	396.02	3.1282	-.648	1.767
1.495	.09369	.02843	381.99	3.0282	-.755	1.786
1.688	.09389	.02840	368.02	2.9282	-.844	1.807
1.939	.09411	.02836	354.12	2.8282	-.918	1.828
2.181	.09436	.02832	340.29	2.7282(3)	-.979	1.851
2.496	.09466	.02827	326.52	2.6282	-1.029	1.874
2.872	.09500	.02821	312.83	2.5282	-1.069	1.900
3.323	.09539	.02815	299.2194	2.4282	-1.101	1.926
3.868	.09586	.02807	285.69	2.3282	-1.127	1.954
4.533	.09641	.02799	272.24	2.22818	-1.148	1.984
5.350	.09707	.02789	258.89	2.1282	-1.164	2.016
6.364	.09787	.02777	245.63	2.0282	-1.176	2.050
7.636	.09884	.02764	232.48	1.9282	-1.186	2.087
9.252	.10003	.02749	219.43	1.8282	-1.193	2.127
11.33	.10152	.02731	206.51	1.7282	-1.198	2.171
14.04	.10341	.02710	193.71	1.6282	-1.202	2.219
17.65	.10585	.02686	181.05	1.5282	-1.205	2.272
22.52	.10904	.02659	168.55	1.42818	-1.207	2.332
29.28	.11331	.02628	156.21	1.3282	-1.209	2.401
38.91	.11914	.02593	144.08	1.2282	-1.210	2.481
53.07	.12728	.02555	132.17	1.1282	-1.211	2.577
74.76	.13883	.02513	120.56	1.0282	-1.211	2.696
109.5	.15536	.02462	109.38	.9282	-1.212	2.849
168.3	.17866	.02384	98.85	.8282	-1.212	3.058
273.2	.21002	.02241	89.36	.7282	-1.212	3.355
470.8	.24867	.01974	81.30	.6282	-1.212	3.795
865.8	.29068	.01550	74.96	.5282	-1.212	4.465
1717	.32972	.01012	70.40	.4282	-1.212	5.514
3681	.35941	.00478	67.43	.3282	-1.212	6.968
7404	.37363	.00098	65.87	.2282	-1.212	9.257
8357	.36027	.00001	65.67	.1282	-1.212	9.687

(1) See below

(3) Free-space density  $\rho = \rho_0$

(2) Cavity radius

## SHOCK WAVES AND CAVITY FORMATION

From eq. (4.3), it can be seen that the  $\xi$ -function admits of an arbitrary multiplicative constant. This constant is determined from the known required density of the material behind the shock front given by the Rankine-Hugoniot conditions. This is given by (5.2c). From the equation of state (6.1),

$$\rho = 3.5182$$

$$p = 384 \text{ kb}$$

Then, from (5.6b) and (5.6c),

$$D = 3.5182, \quad P = .02856.$$

For an initial cavity radius of  $r = 1.698 \text{ cm}$ ,

$$t = r(DP/p)^{1/2} = 0.868 \text{ microseconds.}$$

This is the value which must be used as the starting time of the cavity motion in order to put the shock front at the given radius. We finally must have

$$\xi = \xi_1 = rt^{-\alpha} = (1.698) (.868 \times 10^{-6})^{-.4} = 451.28.$$

### 10. Energy Considerations

In the theory of progressing waves, an assumption of constant energy was made (see eq. (4.7) in order to provide the condition (4.8) for determining  $\alpha$  and with it, all the other exponents. The energy integral (4.7) is extended between two points, one of which is located on the shock front  $\xi = \text{const.} = \xi_1$  and a lower value  $\xi = \xi_0$ . The integral path, such as BC

## SHOCK WAVES AND CAVITY FORMATION

in Fig. 3, may be arbitrarily chosen, so long as it terminates on these two curves.

The energy in the disturbed part of the solid will, however, change with time because its lower boundary, the cavity surface, is not one of the family of  $\xi$ -curves. Thus the energy values in Table 1 represent an integration of the expression in (4.7) taken along the cavity surface curve. If we extend this integration far enough (say to 100 microsec) so that point D practically coincides with point C, the values in the table become asymptotically constant, and we have

$$E = \int_A^C = \int_A^B + \int_B^C = 0 + \int_B^D = - \int_{t_0}^{t_1}$$

From Table 1 we see that the energy does tend to a constant and we have just shown that this limit is the value of the energy integral (4.7).

$$E = 1.212 \times 10^{12} \text{ ergs} \quad (10.1)$$

If we now suppose that all (or any known fractional part) of the energy given up by the explosive is transmitted into the solid, then the shock process could be terminated when the energy reaches the amount available. It is not possible to determine a precise point of time because of the asymptotic way in which the energy increases. It is seen, however, that E reaches 90% of its ultimate value in 3 microseconds, which is a very short time compared with the expansion process.



## SHOCK WAVES AND CAVITY FORMATION

The post-shock expansion presumably must take place under constant energy conditions for a "long" period of time, until it is dissipated by viscosity of the flow, elastic waves, and other side effects.

For energy available in the explosive, Shear [6] gives the value

$$E_{\text{Total}} = 1.152 \text{ k cal/g}$$

which, for our explosive weight of 0.07 lb, gives

$$E_{\text{Total}} = 1.26 \times 10^{12} \text{ ergs}$$

Our calculated asymptotic value (10.1) from the progressing wave integration comes to 96% of this. Thus we have here an independent comparison to check the theory.

### 11. Experimental Details

The specimens used in the experimental portion of this study are thick walled aluminum spheres machined from blocks of 6061-T4 and 24ST. The spheres are of two sizes with nominal outside diameters of eighteen (18) and twenty-five (25) centimeters. Figure 1 illustrates the general sphere configuration. The inner cavity is machined to assure snug acceptance of a thirty-two (32) gram charge of Pentolite explosive. The threaded well is machined in the specimens in order to accept a threaded aluminum plug. The plug is fabricated with a hemispherical cup on the insert end, in order to seat the explosive. The small diameter hole drilled the length of the plug axis provides a means for running the firing line and ionization probe to the cavity. The portion of the plug extending beyond the threaded section is used for the purpose of mounting the entire assembly.

## SHOCK WAVES AND CAVITY FORMATION

Although the fundamental information required from this study consists of essentially determining the permanent deformation of the specimen the spheres are instrumented to determine initial free surface velocity, maximum radial expansion, and the shock velocity through the material. Instrumentation for the measurement of the free surface velocity, and maximum radial expansion consists of two condenser type micrometers. The grounded free surface of the specimen constitutes one plate of the condenser; the micrometer plate is spaced a few tenths of a centimeter from the free surface.

Quartz disc crystals affixed to aluminum rods of varying length are used to measure shock time of arrival. These rods are threaded into the sphere with the crystal surface normal to the sphere radii. (Figure 1).

The output from the condenser micrometers and the quartz crystals are recorded on cathode ray oscilloscopes. The scope sweeps are triggered by a simple ionization probe inserted through the plug into the explosive detonator cavity. Figure 11 illustrates the experimental arrangement.

Prior to assembly and testing measurements of the sphere outside surface and inner cavity diameters are made. After assembly the condenser micrometers are calibrated remotely, then the explosive is initiated. The scope traces are recorded with still cameras using polaroid films.

Table 2 contains a tabulation of the before and after physical measurements of each specimen. The inner cavity and outer surface diameters are averages of several measurements and do not reflect the asymmetrical distortion detected in the post shot observations. However, the

# SHOCK WAVES AND CAVITY FORMATION

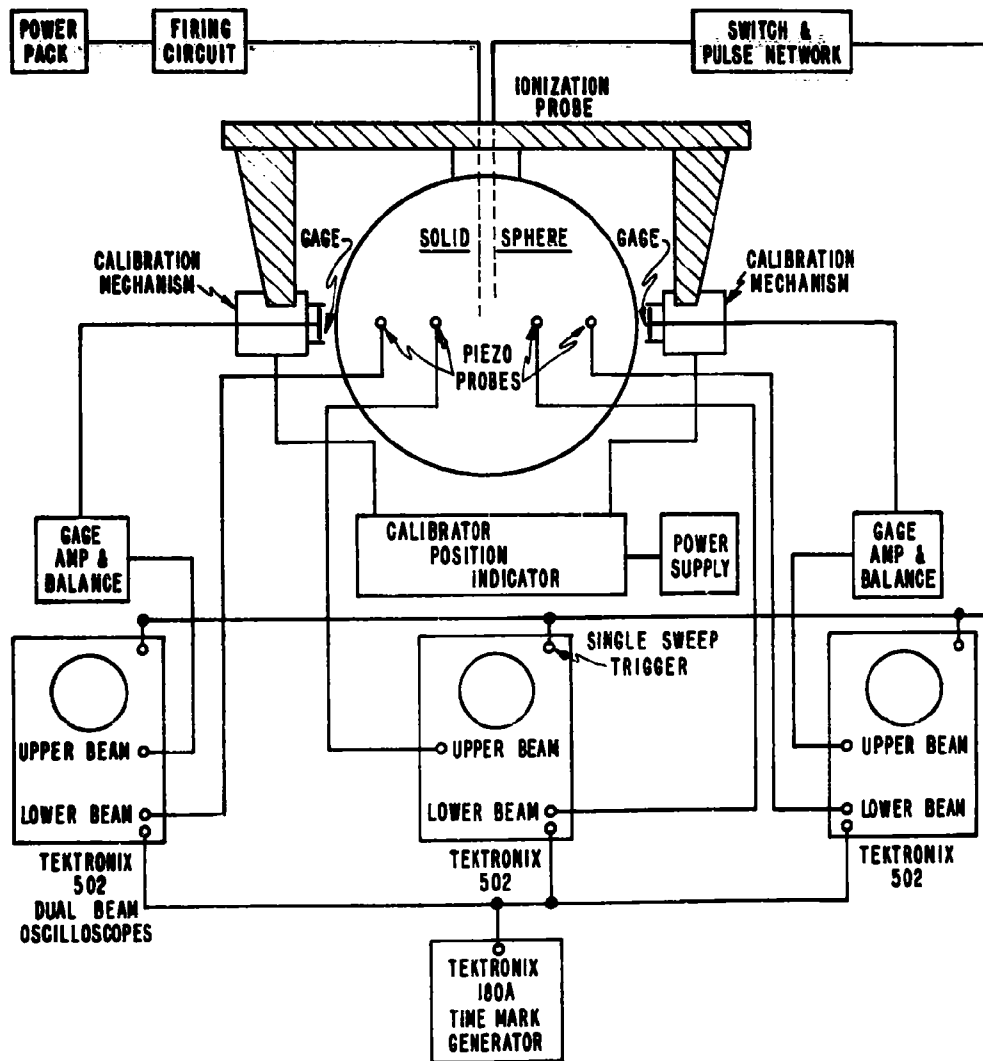


**FIG. II EXPERIMENTAL ARRANGEMENT**

## SHOCK WAVES AND CAVITY FORMATION

values determined from the recorded data presented in Table 3 do indicate this non-uniform distortion. The values in Table 2 indicate that the average increase in the specimen outside diameter is 2% for the small spheres and 1% for the larger one. For the inner cavity the post shot diameter indicates an increase of about 75% for the small specimens except for one with an increase better than 90%. The two large spheres display increases of better than 100%. In Table 3 the values derived from the oscilloscope records are presented. The average shock velocities through the material agree rather well. The difference in free surface velocity between the 6061-T6 and the 2024-T3 aluminum is quite apparent. The values determined for maximum radial expansion tend to indicate that there is non-uniform deformation occurring.

## SHOCK WAVES AND CAVITY FORMATION

TABLE 2  
Specimen Physical Measurements

Observations	Test Numbers							
	1	2	3	4	5	6*	7	8
Material	24ST	6061-T4	6061-T4	24ST	6061-T4	6061-T4	6061-T4	6061-T4
Explosive Weight, (gm)	32	32	32	32	32	32	32	32
Pre-Test Sphere Diam., (cm)	17.633	17.767	17.762	17.691	17.737	17.780	25.344	25.384
Post-Test Sphere Diam., (cm)	17.962	18.168	18.135	18.000	18.156	-	25.545	25.594
Pre-Test Cavity Diam., (cm)	3.396	3.396	3.396	3.396	3.396	3.396	3.356	3.396
Post-Test Cavity Diam., (cm)	5.946	5.956	5.842	5.890	6.678	-	7.511	7.249

\* Specimen failed

# SHOCK WAVES AND CAVITY FORMATION

TABLE 3  
Data as Determined from Capacitance Gages

	Test Number							
	1	2	3	4	5	6	7	8
Material	24ST	6061-T4	6061-T4	24ST	6061-T4	6061-T4	6061-T4	6061-T4
Average Shock Velocity, (cm/ $\mu$ s)	.59	.60	.48	-	.47	.60	.58	.62
Free Surface Velocity, (cm/ $\mu$ s)	No. 1 gage No. 2 gage	.57 -	.18 .18	.37 .26	.18 -	.29 .34	.15 .14	.11 -
Maximum Radial Expansion, (cm)	No. 1 gage No. 2 gage	8.960 -	9.107 -	9.063 9.082	9.003 9.074	9.075 -	12.839 12.829	12.808 12.195

## SHOCK WAVES AND CAVITY FORMATION

### 12. Summary and Conclusions

In this paper we have attempted to study the cavity formation process in the metal by determining how the important physical variables of cavity radius, velocity, pressure, and density vary with time and position near the cavity. The most prominent general feature of the whole process is the short time of the "shock" regime as compared with the total time of the expansion. One general criterion of the end of the shock is when the supersonic velocity of the shock front drops to sonic, i.e., at the point P of Fig. 6, where the slope attains the value for elastic disturbances in the material. The progressing wave curve cannot be used beyond this point since it would give a subsonic shock velocity. This situation has occurred after 0.5 microsec.

We note that the highest pressures and densities in the metal are located just behind the shock front, and trail off with decreasing radius to minimum values at the cavity boundary. We note that the equation of state (6.1) which has been used for the calculations has a lower limit of  $p = 100 \text{ kb}$ . This could also be used as a criterion for shock termination (point D, Fig. 6). It is reached in  $0.7 \mu \text{ sec}$ . These conditions thus determine a roughly parallelogram shaped region ODPE in the  $r, t$ -plane for the validity of the progressing wave region. Note that the cavity has only expanded 0.1 cm during this period, which is  $1/30$  of the total observed increase in radius. We are thus justified in referring to the shock process as impulsive, i.e., the later stages of the process are insensitive to many features of the shock part. Hence the progressing wave method of integration remains valid for the analysis of the shock zone.

## SHOCK WAVES AND CAVITY FORMATION

The asymptotic characteristics of the progressing waves are thus not of direct physical interest since they do not apply to the problem beyond the region described above. The expansion zone, headed by a wave traveling with the dilatational wave velocity goes on for at least 100  $\mu$  seconds, during most of which the metal continues to move by fluid or plastic flow.

The final cavity radius attained is of great interest to the general problem as this value is directly observable on the specimens after blast. In principle the prediction of this radius should afford a test of any theory, but the matter is not so direct as this, since several theories are involved. It is now evident that the cavity formation process is complicated. It starts under one theory (in which the state of the metal is fairly well established) but terminates in a different state of the material, about which information is almost completely lacking. Several mechanisms have been suggested for terminating the cavity expansion:

- (1) An energy-level criterion
- (2) A temperature criterion
- (3) A yield-point criterion

Criteria such as (2) or (3) are tempting because they tend to provide fairly definite marks as to when the material "freezes", either when a given temperature, or a given pressure is reached. However, knowledge of materials is still too incomplete to solve this problem. The total energy of the moving material stops increasing after the expansion phase has begun, so there is no change in energy. Furthermore, any quantitative use



## SHOCK WAVES AND CAVITY FORMATION

of energy balances would require careful accounting of all the energy losses as well. A discussion of some of these energy questions was given in the previous section.

### Summary

We summarize by noting that the following four phenomena are coincident in time:

1. The shock-wave becomes sonic.
2. The pressure at the cavity surface drops to less than 100 kb.
3. The total energy in the disturbed material reaches 90% of its maximum and then levels off asymptotically.
4. The average gas pressure in the cavity (uniform model) equals that in the metal.

All of these occur close to 2 microseconds after initiation of the explosion. This delineates a fairly definite time point of changeover of conditions. Up to this time ( $t = 2.5$  microsec. for the conditions of this report) we may say the effects of shock predominate. The progressing wave method furnishes an accurate theory for this regime. After this time a relatively long expansion period occurs at constant energy until ultimately terminated by degradation processes.

It is felt that more consistency among the measurements would be attained if rigid quality control on the specimens could be maintained. However, since these measurements are being made in regions of relatively low pressure, they are sensitive to inhomogeneity and anisotropy. Effort will be directed toward further refinement of the experiment.

## SHOCK WAVES AND CAVITY FORMATION

### 13. Acknowledgement

The work of this paper was sponsored by the Ballistic Research Laboratories, Aberdeen Proving Ground. Their support is gratefully acknowledged.

Acknowledgement is also due to R. L. Shear and A. Hoffman of the B.R.L. staff for many helpful discussions.

## SHOCK WAVES AND CAVITY FORMATION

### REFERENCES

1. Davids, N. and Huang, Y. K., "Shock Waves in Solid Craters", J. Aerospace Sci. 29-5, May 1962, pp. 550-557.
2. Courant, R. and Friedrichs, K., "Supersonic Flow and Shock Waves", Interscience Publishers, 1948.
3. Walsh, John M., Rice, Melvin H., McQueen, Robert G., Targer, Frederick L., "Shock-Wave Compressions of Twenty-Seven Metals," Phys. Review 108, No. 2, p. 196-216.
4. Newton, R. G., "A Progressing-Wave Approach to the Theory of Blast Shock", J. Appl. Mech., Sept. 1952, p. 257.
5. Shear, R. E. and McCane, P., "Normally-Reflected Shock Front Parameters", BRL Report 1273, 1960.
6. Shear, R. E., "Detonation Properties of Pentolite", BRL Report 1159, 1961.
7. Goodman, H. J., "Compiled Free-Air Blast Data on Bare Spherical Pentolite", BRL Report 1092, 1960.
8. Makino, R. C. and Shear, R. E., "Unsteady Spherical Flow Behind a Known Shock Line", BRL Report 1154, 1961.
9. Lawton, H. and Skidmore, I. C., "Hugoniot Curves for Inert Solids and Condensed Explosives"
10. Döring, W. and Burkhart, G., "Beiträge zur Theorie der Detonation", Berlin, 1939.
11. Sedov, L. I., "Similarity and Dimensional Methods in Mechanics", Translation by Morris Friedman from 4th Russian Ed., Academic Press, 1959.
12. Hopkins, H. G., "Dynamic Expansion of Spherical Cavities in Metals", Progress in Solid Mechanics I, Sneddon and Hill, North Holland, 1960.
13. Stoker, J. J., "Non-Linear Vibrations", Interscience, 1950.
14. Huang, Y. K., "Shock Waves in Hypervelocity Impact of Metals", September 1962, to be published.
15. Stanukovich, K. P., "Unsteady Motion of Continuous Media", London, Pergamon Press, 1960.

## SHOCK WAVES AND CAVITY FORMATION

16. Davids, N., "Transient Analysis of Stress Wave Penetration in Plates", J. Appl. Mech. 26E, No. 4, December 1959, pp. 651-660.
17. Davids, N. and Calvit, H. H., "Progressing Wave Analysis of Blast Waves in Spheres", Tech. Report I, BRL Project, Pennsylvania State Univ., Nov. 30, 1962.
18. Rae, W. J. and Kirchner, H. P., "Quarterly Progress Report on a Study of Meteoroid Impact Phenomena", September 1962, Cornell Aero. Labs., Buffalo, N.Y.

PROPERTIES OF SPHERICAL SHOCK WAVES  
PRODUCED BY HYPERVELOCITY IMPACT

By

Ray Kinslow

Chairman, Department of Engineering Science

Tennessee Polytechnic Institute

and

Consultant

von Kármán Gas Dynamics Facility

ARO, Inc.\*

---

\*The research reported in this paper was sponsored by the Arnold Engineering Development Center, Air Force Systems Command, under Contract No. AF40(600)-1000 with ARO, Inc. Further reproduction is authorized to satisfy needs of the U. S. Government.

## PROPERTIES OF SPHERICAL SHOCK WAVES

### ABSTRACT

A semi-empirical model is derived which will, it is hoped, contribute to the understanding of the nature of waves and fractures in solids caused by hypervelocity impact.

The distance within a solid at which the shock wave slows down to an elastic wave is considered as the radius of a "cavity" to the surface of which a forcing function can be applied to produce an elastic wave similar to that produced by the impact of a high velocity projectile.

By the use of a high-speed computer, the characteristics of the forcing function are found which will produce the same effects as those caused by a projectile. This forcing function can be described by a mathematical series, each term being of a form for which the general wave equation can be solved. This permits the computation of particle displacement, particle velocity, and principal stresses within the target.

# PROPERTIES OF SPHERICAL SHOCK WAVES

## CONTENTS

	<u>Page</u>
ABSTRACT . . . . .	274
NOMENCLATURE . . . . .	277
INTRODUCTION . . . . .	279
ASSUMPTIONS . . . . .	279
STRESS RELATIONS . . . . .	282
SOLUTION OF THE WAVE EQUATION . . . . .	286
CONDITIONS AT WAVE FRONT . . . . .	289
FRACTURES PRODUCED BY REFLECTED WAVES . . . . .	289
QUANTITATIVE RESULTS . . . . .	293
DISCUSSION . . . . .	315
REFERENCES . . . . .	319

## TABLE

1. Values of the Constants  $K_1, K_2, K_3, \dots K_n$   
and the Sum,  $K_1 + K_2/2 + K_3/3 + \dots K_n/n = \alpha C_1/p_1$  . . . . . 290

## ILLUSTRATIONS

1. Elastic Waves in Lucite Targets . . . . .	281
2. Observations of Hypervelocity Impact in Lucite Target . . . . .	283
3. Crater Depth for Various Projectiles and Targets as a Function of Impact Velocity . . . . .	284
4. Effect of Target Thickness upon Crater Depth . . . . .	285
5. Various Forcing Functions Having Same Momentum . . . . .	291
6. Types of Fractures Produced by Reflected Shock Waves . . . . .	292
7. Photographs Showing Deformation of Rear Surface of Aluminum Target . . . . .	294
8. Displacement of Rear Surface of Target as a Function of Time . . . . .	295
9. Peak Stress and Particle Velocity at Wave Front . . . . .	297
10. Dependence of Pulse Form upon Target Material . . . . .	298
11. Effect of Decay Constant upon Pulse Form . . . . .	299
12. Pulse Shapes for Various Values of $n, r$ , and $\alpha$ . . . . .	300

## PROPERTIES OF SPHERICAL SHOCK WAVES

13.	Multiple Fractures Near Rear Surface of Aluminum Target . . . . .	302
14.	Particle Displacement and Velocity as Functions of Radius and Time . . . . .	303
15.	Particle Displacement as a Function of Time . . . . .	305
16.	Principal Stresses in Target as Functions of Radius and Time . . . . .	307
17.	Mean and Shear Stresses in Target as Functions of Radius and Time . . . . .	308
18.	Development of Radial Tensile Stresses Caused by Reflected Shocks . . . . .	309
19.	Formation of Fractures Caused by Reflected Shock . . . . .	310
20.	Radial Stress as a Function of Shock Position for Various Impact Velocities . . . . .	312
21.	Spall Thickness as a Function of Target Thickness and Target Strength . . . . .	313
22.	Spall Thickness as a Function of Target Thickness, Target Strength, and Impact Velocity . . . . .	314
23.	Comparison of Shocks Caused by Various Impact Conditions . . . . .	316
24.	Comparison of Actual and Predicted Fracture Locations . . . . .	317



# PROPERTIES OF SPHERICAL SHOCK WAVES

## NOMENCLATURE

$C_1$	Momentum per unit area of forcing function
$C_2$	Ratio of forward momentum of forcing function to momentum of the impacting projectile
$C_3$	Attenuation constant
$c$	Velocity of propagation of a compressional elastic wave
$K_1, K_2, K_3, \dots K_n$	Constants
$M_p$	Projectile momentum
$M_s$	Momentum of forcing function
$N$	Number of equations to be solved simultaneously
$p$	Pressure (a function of time)
$p_1$	Pressure at $r_1$ when $t = 0$
$p_o$	Impact pressure
$r$	Radius vector
$r_1$	Crater depth
$r_o$	Projectile radius
$t$	Time
$u$	Particle displacement
$v$	Particle velocity
$\alpha$	Time decay constant
$\alpha_o$	See text
$\lambda$	Coefficient of dilation
$\mu$	Shear modulus
$\nu$	Poisson's ratio

} Lamé's constants

## PROPERTIES OF SPHERICAL SHOCK WAVES

$\rho$	Density of target material
$\sigma_m$	Mean stress
$\sigma_r$	Radial stress
$\sigma_s$	Shear stress
$\sigma_\theta$	Tangential stress
$\tau$	See text
$\phi$	Displacement potential function
$\omega_o$	See text
$\nabla^2$	Laplacian operator

## PROPERTIES OF SPHERICAL SHOCK WAVES

### INTRODUCTION

When a solid body is impacted by a hypervelocity projectile, the kinetic energy of the projectile is divided among several physical effects, such as permanent deformations; heat, light, and vaporization; ejection of most of the projectile and some of the target material; and shock waves. There is much disagreement among investigators as to the model or theory to use in describing these effects. A great deal of experimental data and considerable theoretical work has been published during the last few years. Many theories have been deduced with utmost rigor from rather arbitrary assumptions. Contradictory empirical relations have been formulated at various laboratories to fit their specific data. This paper dealing with the spherical pulse produced by hypervelocity impact will probably be no exception, but it is believed that the semi-empirical model described will contribute to the understanding of the nature of these waves and the effects produced by them.

A simplified description of the effect of hypervelocity impact is generally divided into the following stages: (a) The projectile is imbedded in the target material. (b) The crater expands very rapidly similar to an explosion. (c) The velocity of the crater surface decreases, thereby permitting a shock to become detached from its surface. Material flows along the wall of the crater and is ejected at a velocity up to eight or ten times the impacting velocity of the projectile. (d) Permanent deformation ceases, and the shock decays into a spherical elastic dilatation wave which continues to dissipate energy throughout the target. (e) As the wave reflects from the back or other free surface of the target, as tensile waves, secondary fractures and deformations occur if the tensile stress exceeds the fracture stress of the target material. This fracture stress is much greater than its static strength.

### ASSUMPTIONS

In this study, as in all other impact studies, it is necessary to make several assumptions concerning the phenomenon of hypervelocity impact. A few of these assumptions are rather arbitrary, others are based upon the work of previous investigators, and some are dependent upon the extrapolating of experimental data.

It is assumed that during the initial stage of impact the projectile is imbedded in the target material to a depth equal to the projectile radius. Gehring (1) gives the crater depth

## PROPERTIES OF SPHERICAL SHOCK WAVES

at this time as the length of the projectile multiplied by the ratio of the square roots of the densities of projectile and target material. For a Lexan projectile impacting an aluminum target (with which most of this study deals) this would give the crater depth as  $1.3 r_0$  instead of  $r_0$  as assumed. The effect of this assumption upon final results will be discussed later. The pressure at this time is very great, and the values used in this study are those given in the hypervelocity survey report by Hermann and Jones (2).

The shock front starts out at about the impact velocity. The strength of the shock rapidly attenuates, and its velocity slows down to the elastic wave velocity in a very short time. Davids (3) gives this time as one microsecond ( $\mu\text{sec}$ ) after impact for a 3/16-in. steel pellet striking a steel plate at 20,000 ft/sec. Kineke (4) gives the time as about  $3.5 \mu\text{sec}$  for a 0.18-g steel pellet striking a Lucite target at 4.6 km/sec. This is in agreement with the author's experiments at AEDC which indicate an average of about  $3.0 \mu\text{sec}$  for 0.3 x 0.3-in. Lexan cylinders (0.44 g) impacting Lucite targets at velocities ranging from 14,000 to 21,800 ft/sec.

The shock separates from the crater surface while the crater is still expanding, but generally slows down to the elastic wave velocity at a distance within the target about equal to the final crater depth. Theoretical studies by Davids (3) and Bjork (5) of steel projectiles (0.475-cm-diam sphere and 10 x 10-cm cylinder) impacting steel targets agree with this. Davids' study gives the crater depth as 1.2 cm with the wave becoming elastic at 1.3 cm. Bjork gives the crater depth as 19.5 cm, and a plot of distance-time relation seems to indicate that the wave becomes elastic at about 24 cm. The streak camera record by Kineke (4) of a steel pellet striking a Lucite target as well as the author's experiments are also in agreement with this (see Fig. 1). It is assumed in this study that the shock wave decays into an elastic wave at a distance within the target equivalent to the final crater depth ( $r_1$ ) and that the velocity of this wave is expressed by the relation

$$c = \left[ \frac{\lambda + 2\mu}{\rho} \right]^{\frac{1}{2}}$$

the velocity of irrotational waves of dilation.

# PROPERTIES OF SPHERICAL SHOCK WAVES

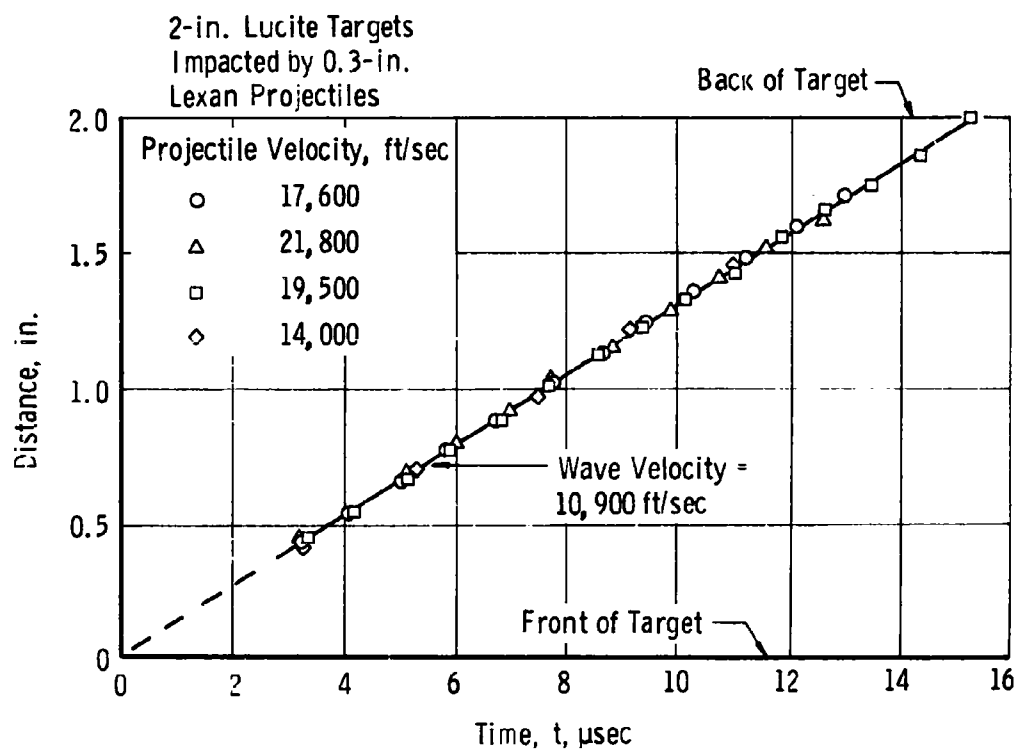


Fig. 1 Elastic Waves in Lucite Targets

## PROPERTIES OF SPHERICAL SHOCK WAVES

The material is considered to be homogeneous and isotropic. The waves are spherical, and their origin is on the target surface at the point of impact. This is verified by photographs of shock waves in Lucite produced by hypervelocity impact as shown in Fig. 2. Values of the crater depth are determined from Fig. 3, which gives crater depth as a function of velocity for various projectiles impacting copper and aluminum targets. It is assumed that target thickness has no effect on crater depth if the depth is less than one-half the target thickness, as shown in Fig. 4.

### STRESS RELATIONS

It has been shown (6) that spherical, longitudinal pulse propagation in a homogeneous, isotropic medium can be specified by the wave equation,

$$\frac{\partial^2 \phi}{\partial t^2} = c^2 \nabla^2 \phi$$

where  $\phi$  is a scalar displacement potential. The particle displacement and velocity are specified by the relations

$$u = \frac{\partial \phi}{\partial r} \text{ and } v = \frac{\partial u}{\partial t}$$

If  $r$  denotes the radius vector from the point of projectile impact, the principal stresses are given by the relations (7)

$$\begin{aligned} \sigma_r &= (\lambda + 2\mu) \frac{\partial u}{\partial r} + 2\lambda(u/r) \\ \sigma_\theta &= \lambda \left( \frac{\partial u}{\partial r} \right) + 2(\lambda + \mu)(u/r) \end{aligned}$$

From the principal stress, the maximum shear stress is found to be

$$\sigma_s = \frac{\sigma_r - \sigma_\theta}{2} = \mu \left( \frac{\partial u}{\partial r} - \frac{u}{r} \right)$$

and the mean pressure acting at a point is

$$\sigma_m = \frac{\sigma_r + 2\sigma_\theta}{3} = \left( \lambda + \frac{2}{3}\mu \right) \left( \frac{\partial u}{\partial r} + \frac{2u}{r} \right)$$

# PROPERTIES OF SPHERICAL SHOCK WAVES



## OBSERVATION OF HYPERVELOCITY IMPACT PHENOMENA

A test technique which enables the detailed observation of impact phenomena of a hypervelocity projectile has been developed in the von Kármán Gas Dynamics Facility. The above pictures show various stages of the projectile and back spall craters as follows: (1) plastic projectile approaching plexiglass target at 21,800 fps, (2) impact of projectile (3, 4, and 5) development of projectile's crater and transit of shock wave through the target, (6) reflection of shock wave and formation of back spall crater, and (7 and 8) latter stages of crater formations.

Fig. 2 Observations of Hypervelocity Impact in Lucite Target

# PROPERTIES OF SPHERICAL SHOCK WAVES

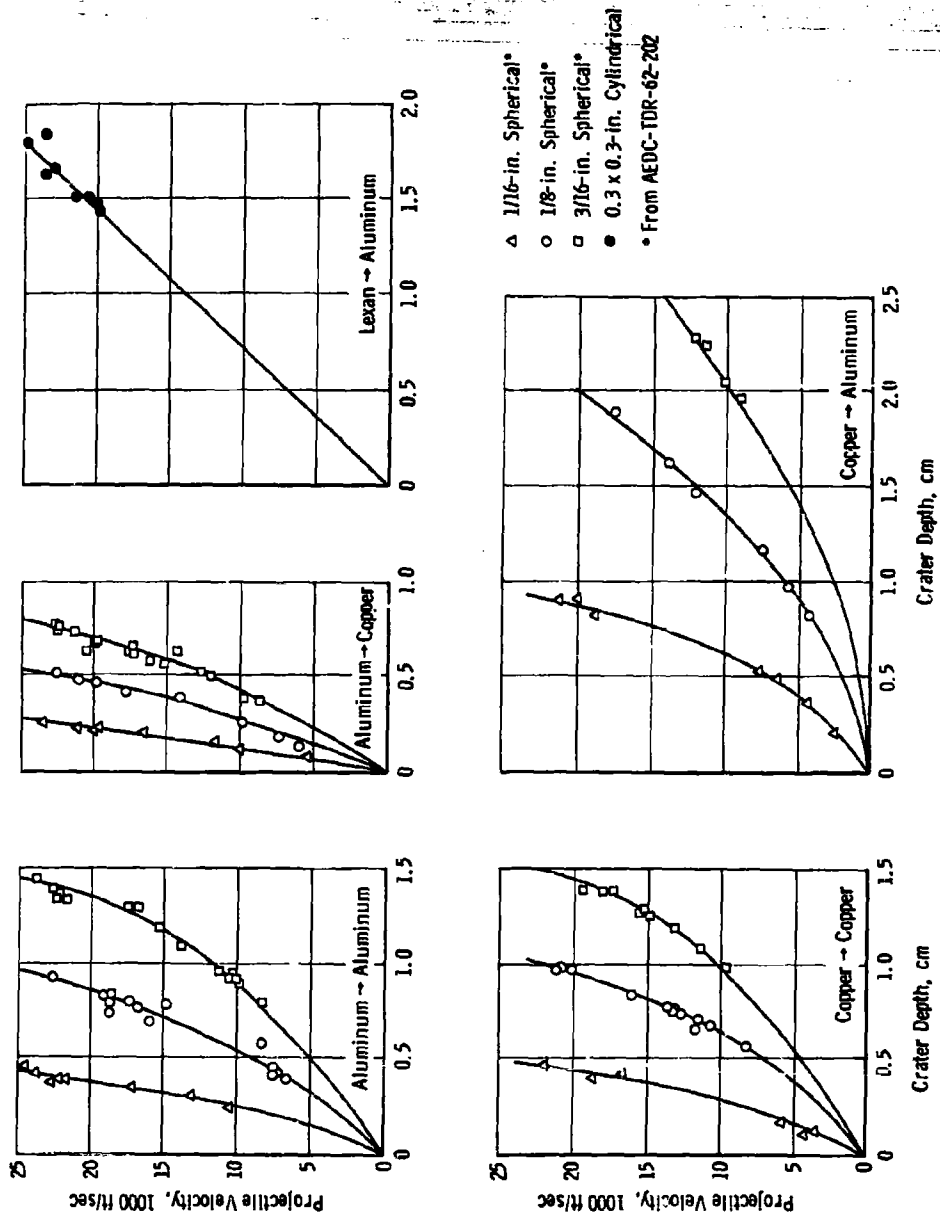


Fig. 3 Crater Depth for Various Projectiles and Targets as a Function of Impact Velocity



# PROPERTIES OF SPHERICAL SHOCK WAVES

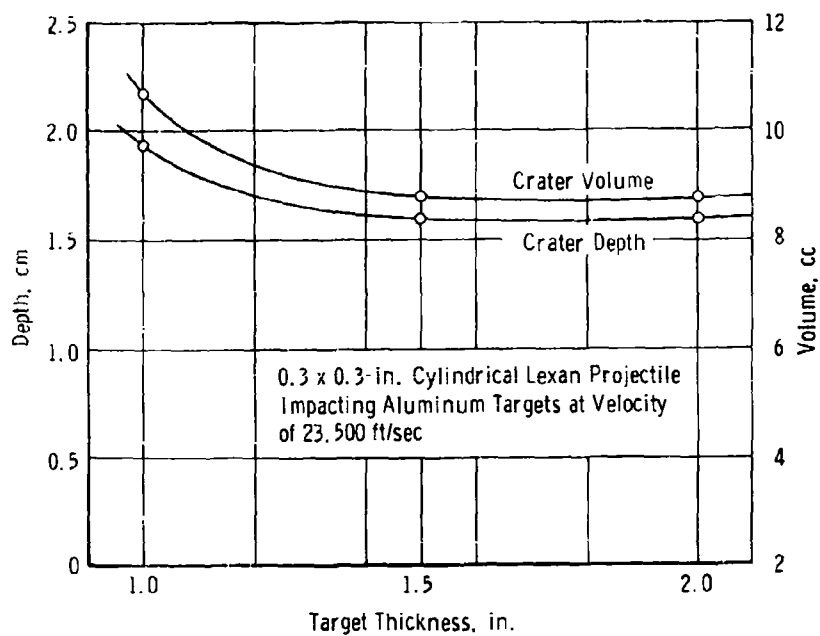
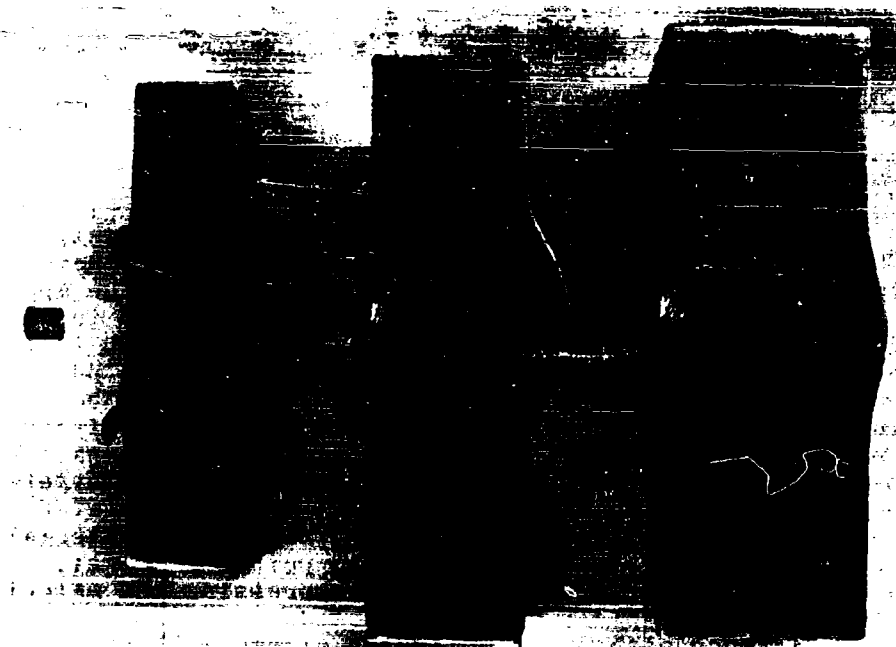


Fig. 4 Effect of Target Thickness upon Crater Volume and Depth

## PROPERTIES OF SPHERICAL SHOCK WAVES

The identity relating  $\sigma_r$ ,  $\sigma_m$ , and  $\sigma_s$  is

$$\sigma_r = \sigma_m + \frac{4}{3}\sigma_s$$

### SOLUTION OF THE WAVE EQUATION

The propagation of spherical waves in solid elastic media has been the object of much study, especially among seismologists (8) (9) and acousticians (10). In general, the approach has been to consider an infinite homogeneous medium in which there exists a hollow spherical cavity, within which there is generated a uniform, time-varying pressure,  $p$ . The problem has been to determine the resulting wave motion in the solid medium. There has also existed the problem of justifying the use of linear elasticity for these nonlinear phenomena. When a charge is fired within a hollow cavity, or when a hypervelocity projectile impacts a solid, a wave is generated in which the stress is much greater than that of the material strength. This wave diverges from the point of impact, or site of the explosion, crushing and compressing the material. This stress wave rapidly attenuates because of loss of energy. At some distance within the solid the stress will equal the strength of the material, and at greater distances the material will be elastic, if viscosity and internal friction are neglected. This critical distance has been called the "radius of the equivalent cavity." As previously stated, it is assumed that this radius is equal to the crater depth caused by the impact. This is not to say that an elastic wave detaches itself from the crater, but rather that the shock decays into an elastic wave at approximately this location before the cavity is completely formed.

The boundary condition to be satisfied expresses the equality of the radial component of stress in the medium at the cavity surface to the pressure inside the cavity,

$$\left[ (\lambda + 2\mu) \frac{\partial u}{\partial r} + 2\lambda \left( \frac{u}{r} \right) \right]_{r=r_1} = [p]_{t=0}$$

If the applied pressure is considered to be an impulse which jumps from zero to  $p_1$  at  $t = 0$  and then decays exponentially with time, and is described by the relation

$$p = p_1 e^{-\alpha t}$$

# PROPERTIES OF SPHERICAL SHOCK WAVES

the solution of the wave equation given by Blake (10) is

$$\phi = \frac{p_1 r_1}{\rho r [\omega_o^2 + (\alpha_o - \alpha)^2]} \left\{ -e^{-\alpha \tau} + e^{-\alpha_o \tau} \left[ 1 + \left( \frac{\alpha_o - \alpha}{\omega_o} \right)^2 \right]^{1/2} \right. \\ \left. \cos \left[ \omega_o \tau - \tan^{-1} \left( \frac{\alpha_o - \alpha}{\omega_o} \right) \right] \right\}$$

where

$$\tau = t - \left( \frac{r - r_1}{c} \right)$$

$$\alpha_o = \frac{c}{r_1} \left( \frac{1 - 2\nu}{1 - \nu} \right)$$

and

$$\omega_o = \frac{c}{r_1} \left[ \frac{(1 - 2\nu)^{1/2}}{1 - \nu} \right]^{1/2}$$

This solution satisfies both the wave equation and the boundary condition.

Allen and Goldsmith (11) have employed this solution to give a description of a high-amplitude pulse in steel. In this paper, it was admitted that the form of the forcing function was assumed for mathematical convenience and that it probably did not represent the actual situation.

A pressure pulse more closely simulating the actual forcing function produced by hypervelocity impact may be expressed by the relation

$$p = p_1 (K_1 e^{-\alpha t} + K_2 e^{-2\alpha t} + K_3 e^{-3\alpha t} + \dots + K_n e^{-n\alpha t})$$

Since each term of this expression is of the form  $p = p_1 e^{-\alpha t}$ , a solution of the wave equation may be found for each term

$$(\phi_1, \phi_2, \phi_3, \dots, \phi_n).$$

The sum of these solutions is also a solution; therefore,

$$\phi = \phi_1 + \phi_2 + \phi_3 + \dots + \phi_n$$

## PROPERTIES OF SPHERICAL SHOCK WAVES

The area under the pressure-time curve is the momentum per unit area of this forcing function and is

$$\int_0^{\infty} p dt = p_1 \left( \frac{K_1}{\alpha} + \frac{K_2}{2\alpha} + \frac{K_3}{3\alpha} + \dots + \frac{K_n}{n\alpha} \right) = C_1$$

The total momentum in the forward direction may be expressed as

$$M_s = \pi r_1^2 C_1$$

The momentum of this pulse is a function of the projectile momentum ( $M_p$ ) as well as being dependent upon the target material. As most of the projectile, as well as much of the target material, is ejected as a "back-splash" at a very high velocity, the total forward momentum that must be absorbed by the target may be many times greater than the initial forward momentum of the projectile (12). Measurements of momentum transfer (13) have indicated that the ratio of target momentum to projectile momentum for plastic projectiles impacting aluminum targets is 1.9 for velocities of 25,600 ft/sec. In this study the ratio of the forward momentum of the forcing function to the initial forward momentum of the projectile will be denoted by  $C_2$ .

Previous investigators (14) employing a modified Hopkinson-bar type of experiment have shown that the pressure pulse does jump from zero to a maximum pressure, has a zero slope at that point ( $[dp/dt]_{t=0} = 0$ ), and then decays exponentially. A forcing function producing a pulse of this general shape is generated if the values of  $K_1, K_2, K_3, \dots, K_n$  are determined by solving the following equations for the conditions of zero time:

$$p/p = K_1 + K_2 + K_3 + \dots + K_n = 1$$

$$d(p/p_1)/dt = K_1 + 2K_2 + 3K_3 + \dots + nK_n = 0$$

$$d^2(p/p_1)/dt^2 = K_1 + 4K_2 + 9K_3 + \dots + n^2K_n = 0$$

- - - - -

$$d^{(N-1)}(p/p_1)/dt^{(N-1)} = K_1 + 2^{(N-1)}K_2 + 3^{(N-1)}K_3 + \dots + n^{(N-1)}K_n = 0$$

## PROPERTIES OF SPHERICAL SHOCK WAVES

To solve, the number of equations (N) must equal the number of K-terms (n). The value of  $\alpha$  is given by the relation

$$\alpha = \frac{p_1}{C_1} \left( K_1 + \frac{K_2}{2} + \frac{K_3}{3} + \dots + \frac{K_n}{n} \right)$$

The shape of the forcing function and resulting pressure pulse depends upon the number of terms of the series used. If only the first term is considered, the results are as given by Allen and Goldsmith. The response to a step function of pressure is obtained by setting the decay constant equal to zero.

Table 1 gives the values of  $K_1, K_2, K_3, \dots, K_n$  for values of n ranging from 1 to 15. It will be seen that the values of these coefficients are the same as the binominal coefficients and may be readily expanded for values of n greater than 15. Values of the sum,  $K_1 + K_2/2 + K_3/3 + \dots + K_n/n$ , are also given for various values of n. Figure 5 shows the shape of the forcing function for n having values of 1, 2, 5, 10, and 20, with C remaining constant.

### CONDITIONS AT THE WAVE FRONT

It can be shown that the relations

$$v = \frac{p_1 r_1}{\rho c r} \quad \text{and} \quad \sigma_r = \frac{p_1 r_1}{r} = \rho c v$$

apply at the wave front. These equations imply that the peak particle velocity and peak stresses attenuate at a rate inversely proportional to the radius vector, r. This applies only during the elastic regime or when  $r > r_1$ . For the region  $r_1 > r > r_0$  the attenuation is probably greater than this. At  $r_1$  the peak pressure may be expressed as

$$p_1 = C_3 p_0 \left( \frac{r_0}{r_1} \right)$$

### FRACTURES PRODUCED BY REFLECTED WAVES

The compression pulse diverging from the point of impact is reflected from the rear face of the target as a tension wave and may produce damage at, or near, the rear surface. This damage may appear as a granular fracture at the surface (Fig. 6a), as internal cracks and bulging of the rear surface (Fig. 6b), or as a detachment of the target material (Fig. 6c).

PROPERTIES OF SPHERICAL SHOCK WAVES

Table I  
Values of the Constants  $K_1, K_2, K_3, \dots, K_n$   
and the Sum,  $K_1 + K_2/2 + K_3/3 + \dots, K_n/n = \sigma C_1/p_1$

n	$K_1$	$K_2$	$K_3$	$K_4$	$K_5$	$K_6$	$K_7$	$K_8$	$K_9$	$K_{10}$	$K_{11}$	$K_{12}$	$K_{13}$	$K_{14}$	$K_{15}$	$\sigma C_1/p_1$
1	+	-	+	-	+	-	+	-	+	-	+	-	+	-	+	1.00
2	1	1														1.50
3	3	3	1													1.83
4	4	6	4	1												2.08
5	5	10	10	5	1											2.28
6	6	15	20	15	6	1										2.46
7	7	21	35	35	21	7	1									2.59
8	8	28	56	70	56	28	8	1								2.72
9	9	36	84	126	126	84	36	9	1							2.83
10	10	45	120	210	252	210	120	45	10	1						2.93
11	11	55	165	330	462	462	330	165	55	11	1					3.01
12	12	66	220	495	792	924	792	495	220	66	12	1				3.07
13	13	78	286	715	1287	1716	1716	1287	715	286	78	13	1			3.13
14	14	91	364	1001	2002	3003	3432	3003	2002	1001	364	91	14	1		3.18
15	15	105	455	1365	3003	5005	6435	6435	5005	3003	1365	455	105	15	1	3.23

# PROPERTIES OF SPHERICAL SHOCK WAVES

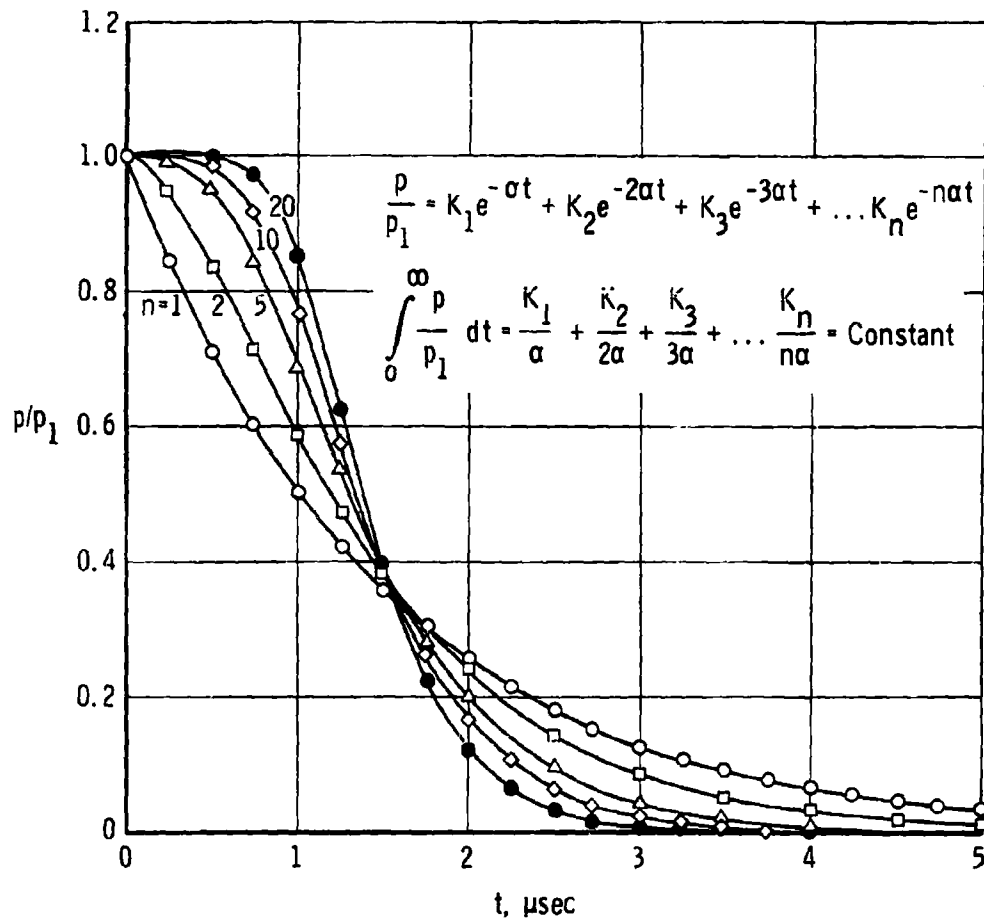


Fig. 5 Various Forcing Functions Having Same Momentum

## PROPERTIES OF SPHERICAL SHOCK WAVES

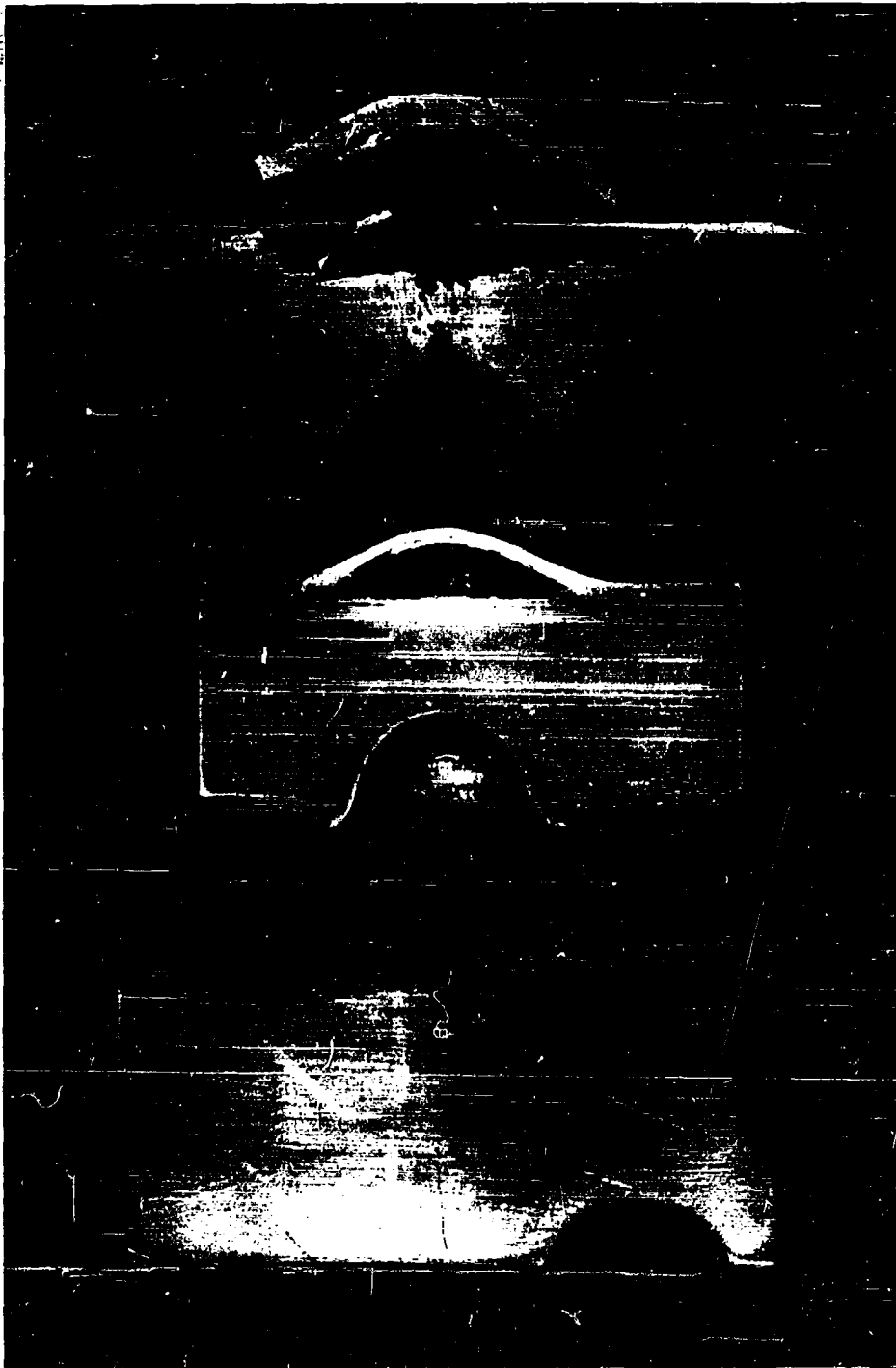


Fig. 6 Types of Fracture Produced by Reflected Shock Waves



## PROPERTIES OF SPHERICAL SHOCK WAVES

That such fractures are formed by the reflected waves is definitely demonstrated by the photographs of the wave reflection and material fracture in the Lucite target shown in Fig. 2. Once a fracture has been produced, the tail of the pulse is reflected as a tensile wave from the new surface so that a series of parallel cracks may be formed.

As each fracture is formed, momentum is trapped between the free surfaces. This momentum may cause a bulge to form on the rear of the target.

### QUANTITATIVE RESULTS

If the values of  $C_2$  and  $C_3$  were known, a quantitative analysis of the effect of hypervelocity impact could be made. An attempt is made to determine these values by applying data obtained by impacting aluminum targets with 0.3 x 0.3-in. cylindrical Lexan projectiles.

The photographs in Fig. 7 show the deformation of the rear surface of a 1.5-in. target as a result of being impacted with a Lexan projectile at a velocity of 24,000 ft/sec. There may be seen what appears to be a shock wave. As the pressure in the range was only 1.4 mm Hg at the time of this shot, together with the fact that the lighting used would not be expected to show even a strong shock, and that its velocity is that of the target surface, it is believed that this is not a shock, but is attributable to particles being knocked from the target surface. Figure 8 is a plot of the material displacement as a function of time. The first part of this time-displacement curve is very similar to those shown by Allen (15). In agreement with that study, it is believed that the curve up to about 4  $\mu$ sec can be associated with elastic deformation. The remaining part of this curve will be discussed later in this paper. The velocity of the rear surface of the target is found to be 1125 ft/sec. According to the Goranson theory (16), the particle velocity in the shock immediately beneath the free surface is one-half the surface velocity, or 0.017 cm/ $\mu$ sec. This value, together with the crater depth of 1.73 cm as determined from Fig. 2, gives a value of 61.5 kilobars (kb) for  $p_1$  by using the relation

$$v = \frac{p_1 r_1}{\rho c r}$$

The value of the attenuation constant,

## PROPERTIES OF SPHERICAL SHOCK WAVES

0.3 x 0.3-in. Cylindrical Lexan Projectile Impacting  
1.5-in. Aluminum Target at Velocity of 24,000 ft/sec

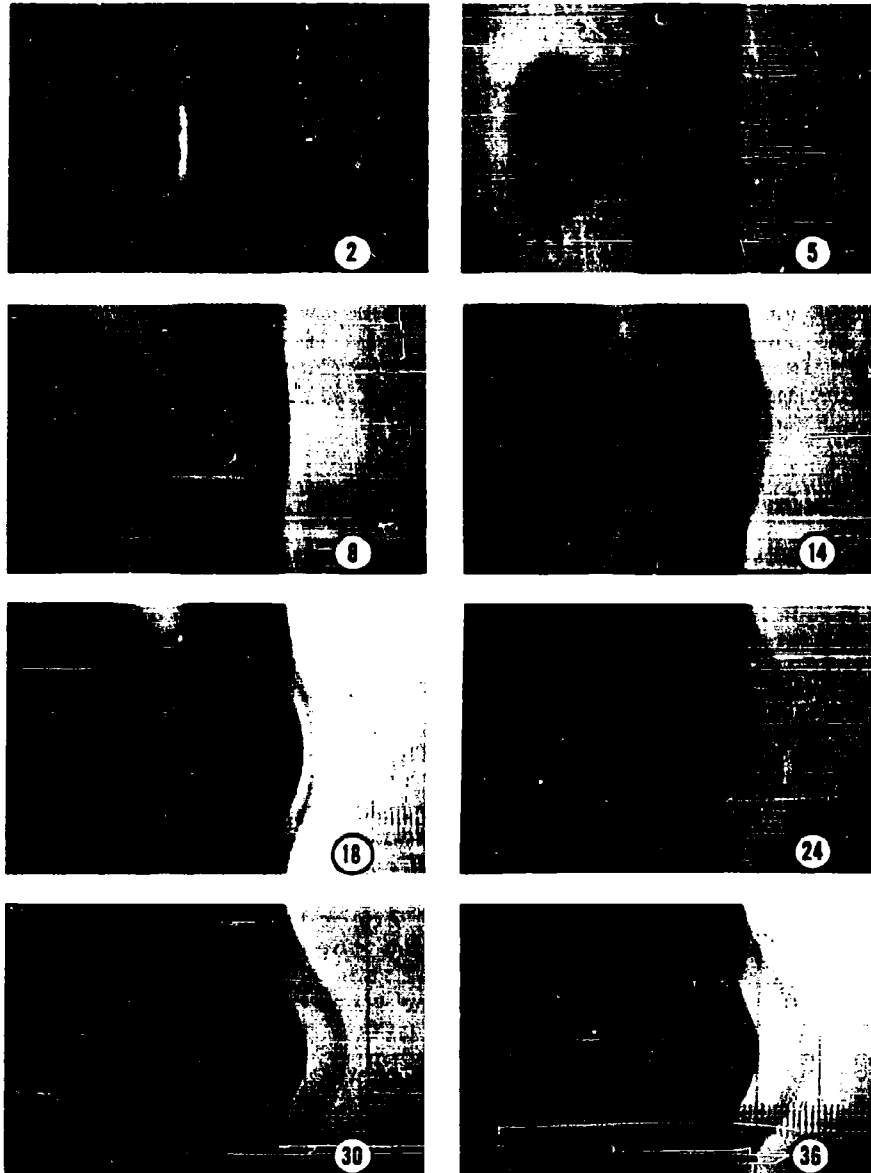


Fig. 7 Photographs Showing Deformation of Rear Surface  
of Aluminum Target

# PROPERTIES OF SPHERICAL SHOCK WAVES

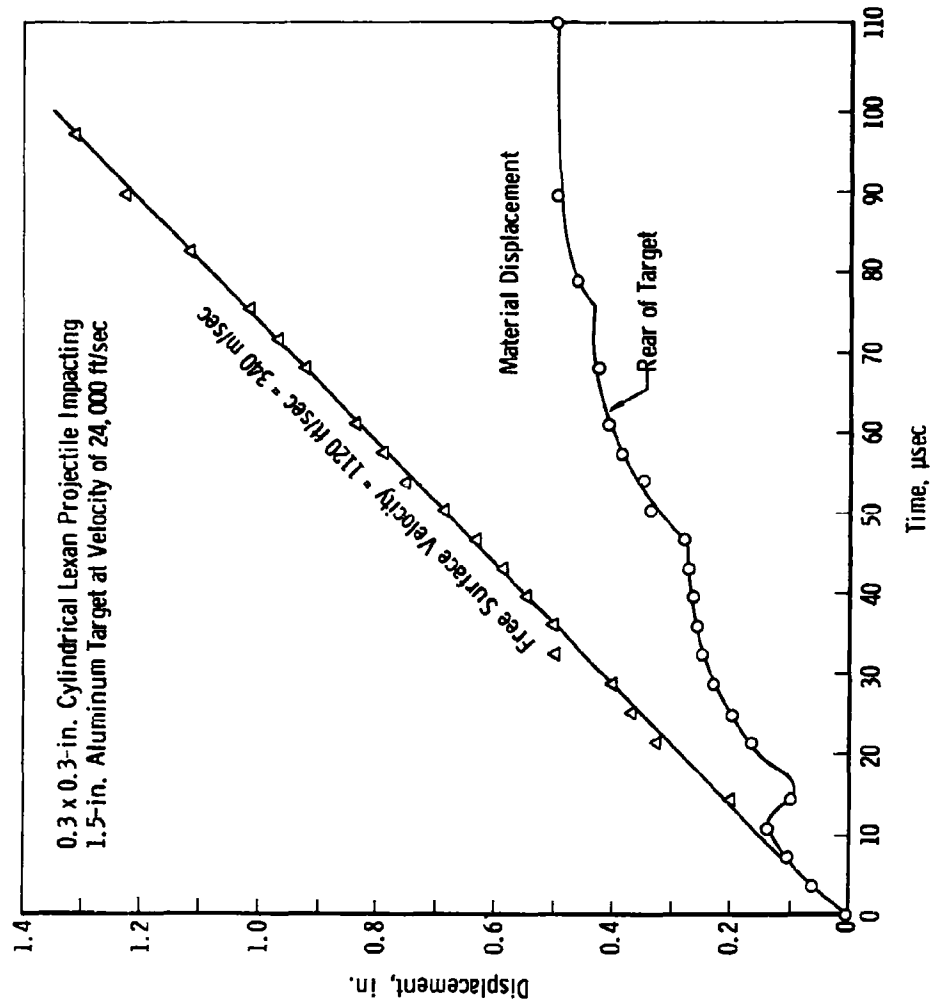


Fig. 8 Displacement of Rear Surface of Target as a Function of Time

## PROPERTIES OF SPHERICAL SHOCK WAVES

$$C_3 = \frac{p_1 r_1}{p_0 r_0}$$

may now be determined. Obtaining the value of  $p_0$ , from Reference 2, based upon the impact pressure of Nylon projectiles and aluminum targets, the value of  $C_3$  is found to be 0.5. This value is dependent upon the value of  $r_0$  assumed earlier. Assuming that this value of  $C_3$  is a constant over the range of conditions being considered, it is now possible to draw the curves shown in Fig. 9.

The shape of the radiating pressure pulse, determined by a solution of the wave equation, depends upon many variables. Figure 10 shows the effect of the target material upon the pulse form. Figure 11 shows the pulse for different values of the decay constant,  $\alpha$ , ranging from 0.1 to 10. Figure 12 shows the pulse shapes for various values of  $n$ ,  $r$ , and  $\alpha$ .

Figure 13 is a photograph of a section of a 1.5-in. aluminum target that has been impacted by a 0.3-in. Lexan projectile at approximately 20,000 ft/sec. Three definite internal fractures near the rear of the target may be seen. These are located at 0.06, 0.11, and 0.15 in. from the rear surface. From Fig. 9, the value of the peak radial stress as the pulse approaches the rear of the target is found to be 19.5 kb. By use of a high-speed digital computer, it was found that a pulse of this magnitude would produce three fractures at these observed locations if the forcing function equation had five terms and the decay constant had a value of 3. It is also indicated that the tensile strength of the target material (99.99% pure aluminum) is about 100,000 psi, or 6.8 kb. This value is somewhat lower than the value of 140,000 psi for 24S-T4 aluminum alloy as determined by Rinehardt (14).

For these conditions, and with these assumptions, the ratio of the forward momentum of the forcing function to the projectile momentum is computed to have a value of 0.97.

Using an IBM 1620 digital computer, various effects of the shock wave upon the target material were determined. Figure 14 shows particle displacement and velocity as the pulse moves through the target. The numbers on each curve indicate the time in microseconds. It is seen that as the wave front reaches any point the material suddenly acquires a velocity which decreases as the front passes, and oscillates with decreasing amplitude and frequency. This is more clearly indicated in Fig. 15, which shows the material displacement as a function of time.

# PROPERTIES OF SPHERICAL SHOCK WAVES

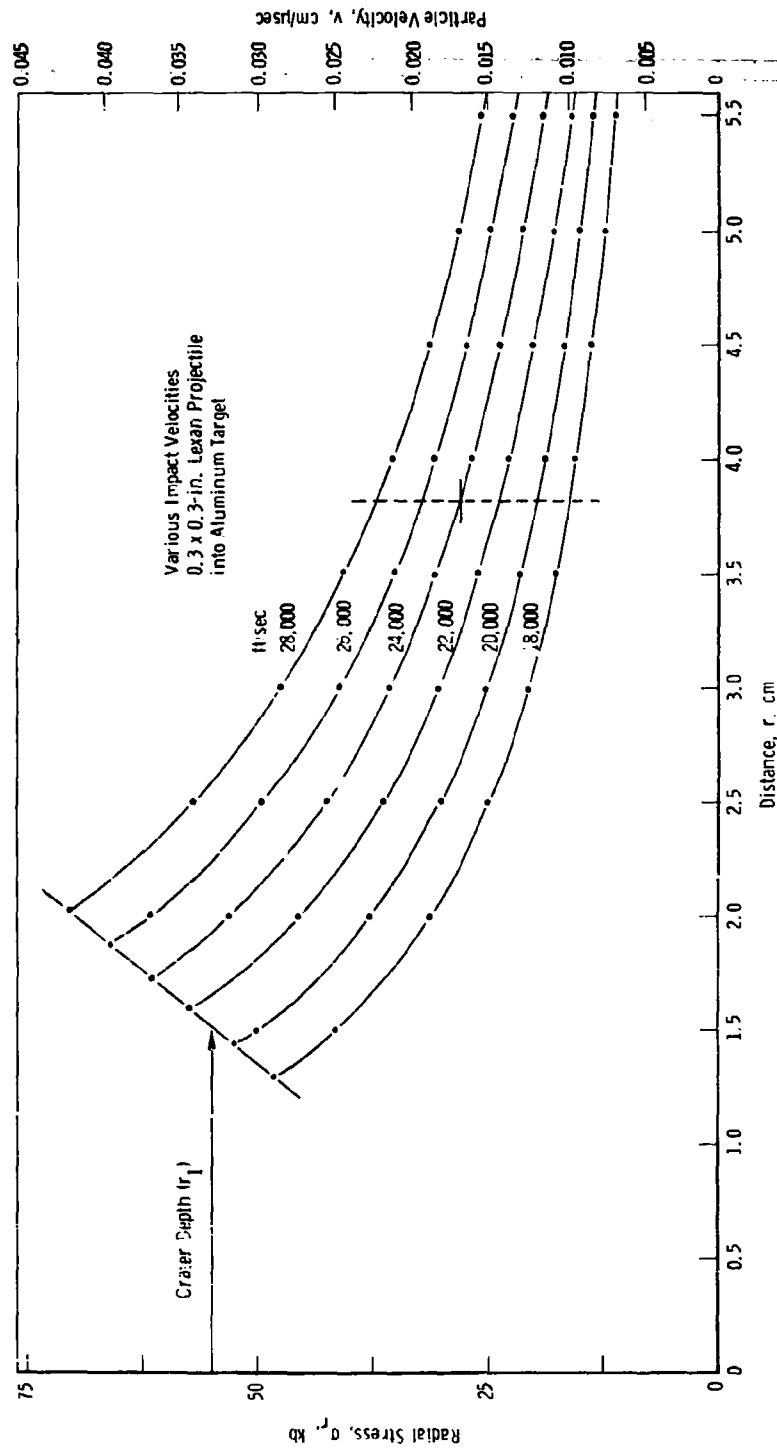


Fig. 9 Peak Stress and Particle Velocity at Wave Front

# PROPERTIES OF SPHERICAL SHOCK WAVES

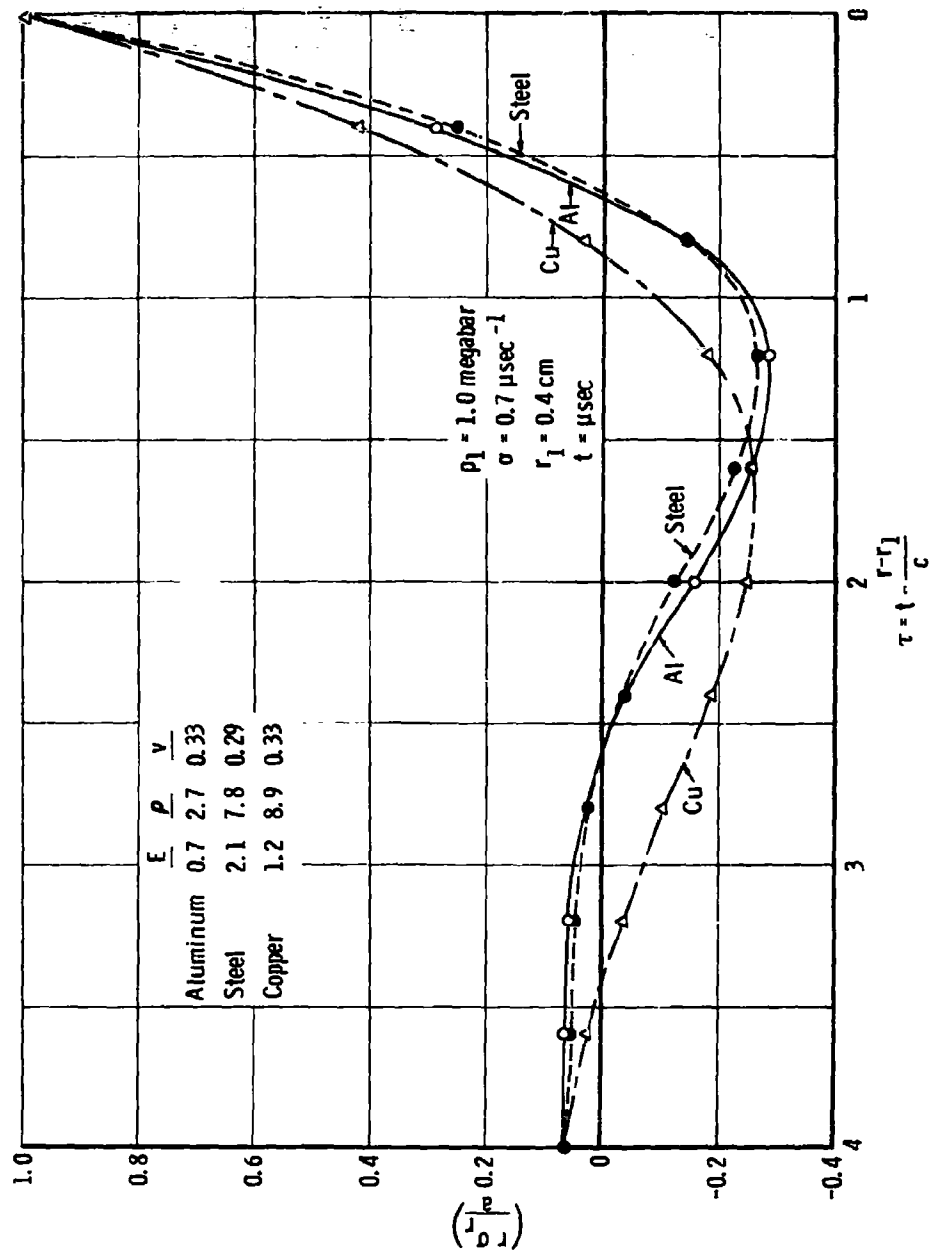


Fig. 10 Dependence of Pulse Form upon Target Material

# PROPERTIES OF SPHERICAL SHOCK WAVES

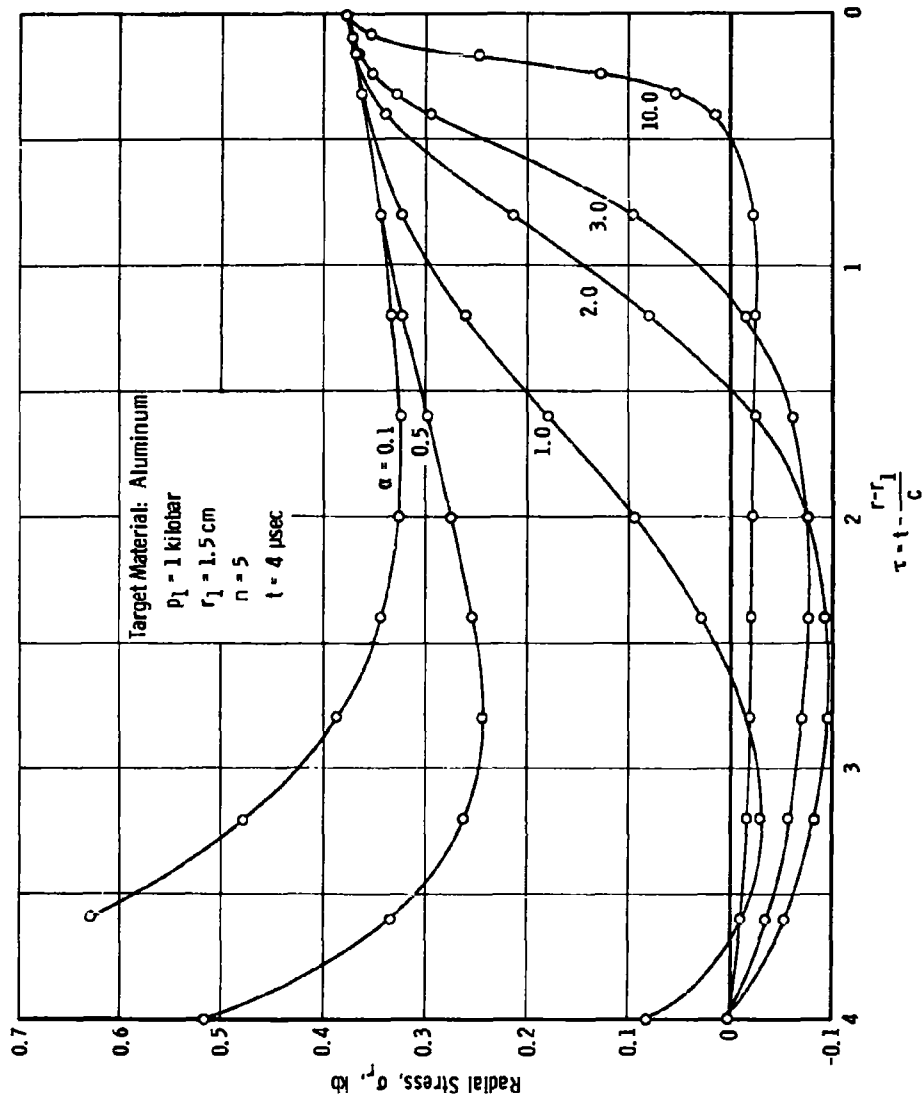


Fig. 11 Effect of the Decay Constant upon Pulse Form

# PROPERTIES OF SPHERICAL SHOCK WAVES

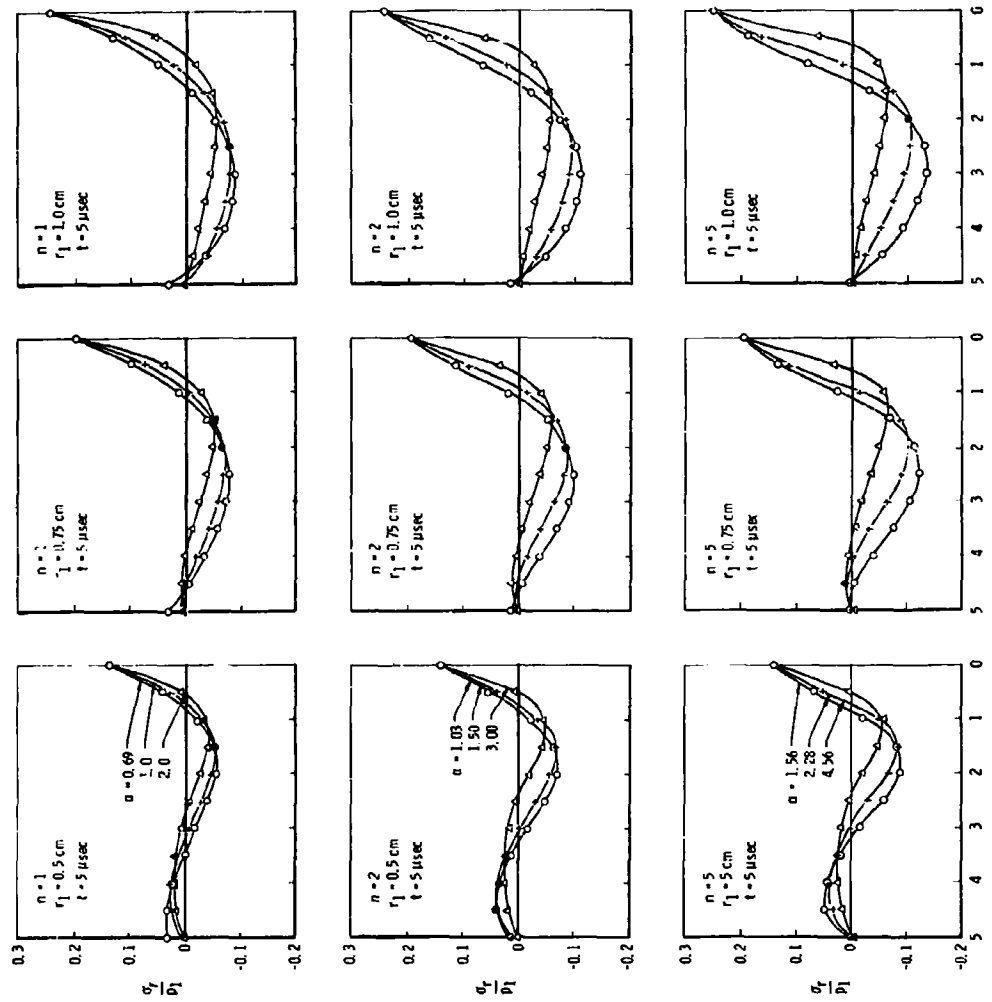


Fig. 12 Pulse Shapes for Various Values of  $n$ ,  $r_1$ , and  $\alpha$



# PROPERTIES OF SPHERICAL SHOCK WAVES

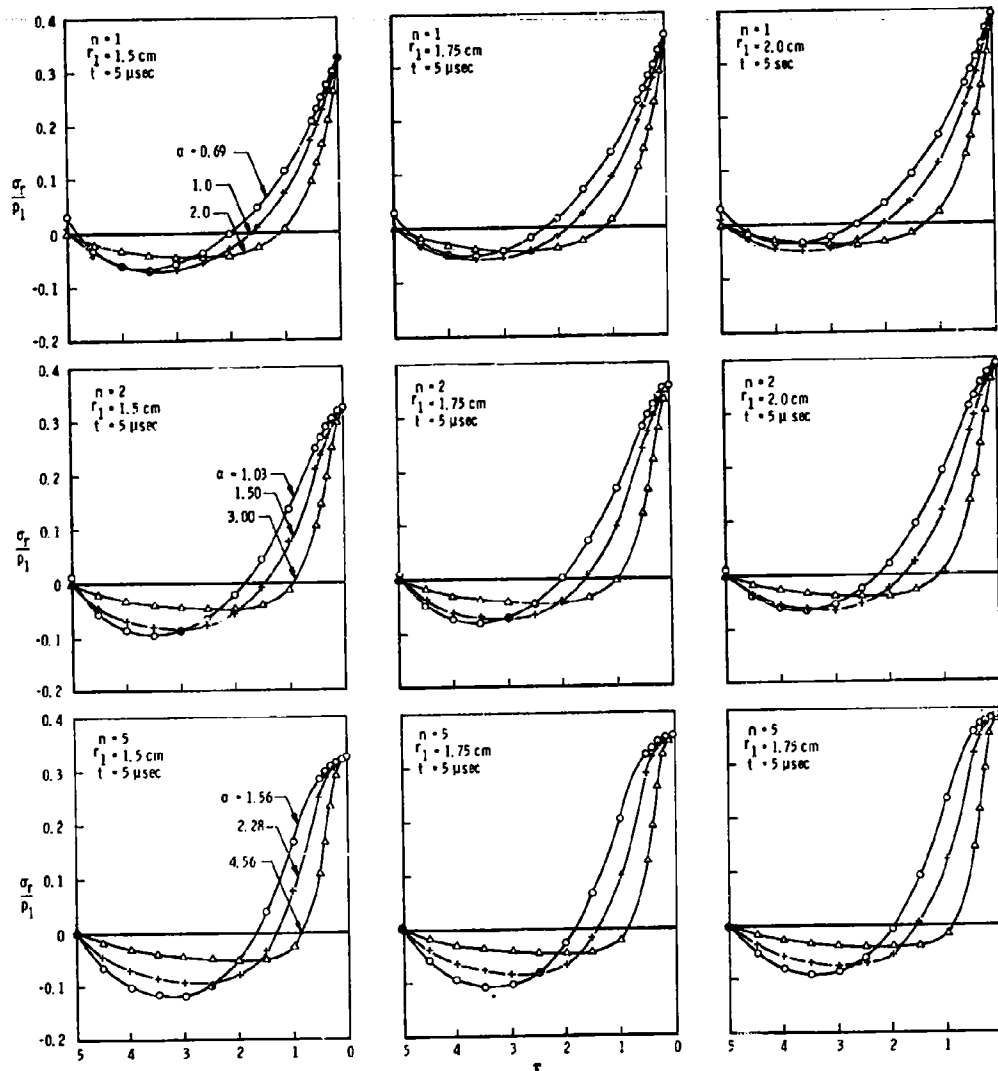
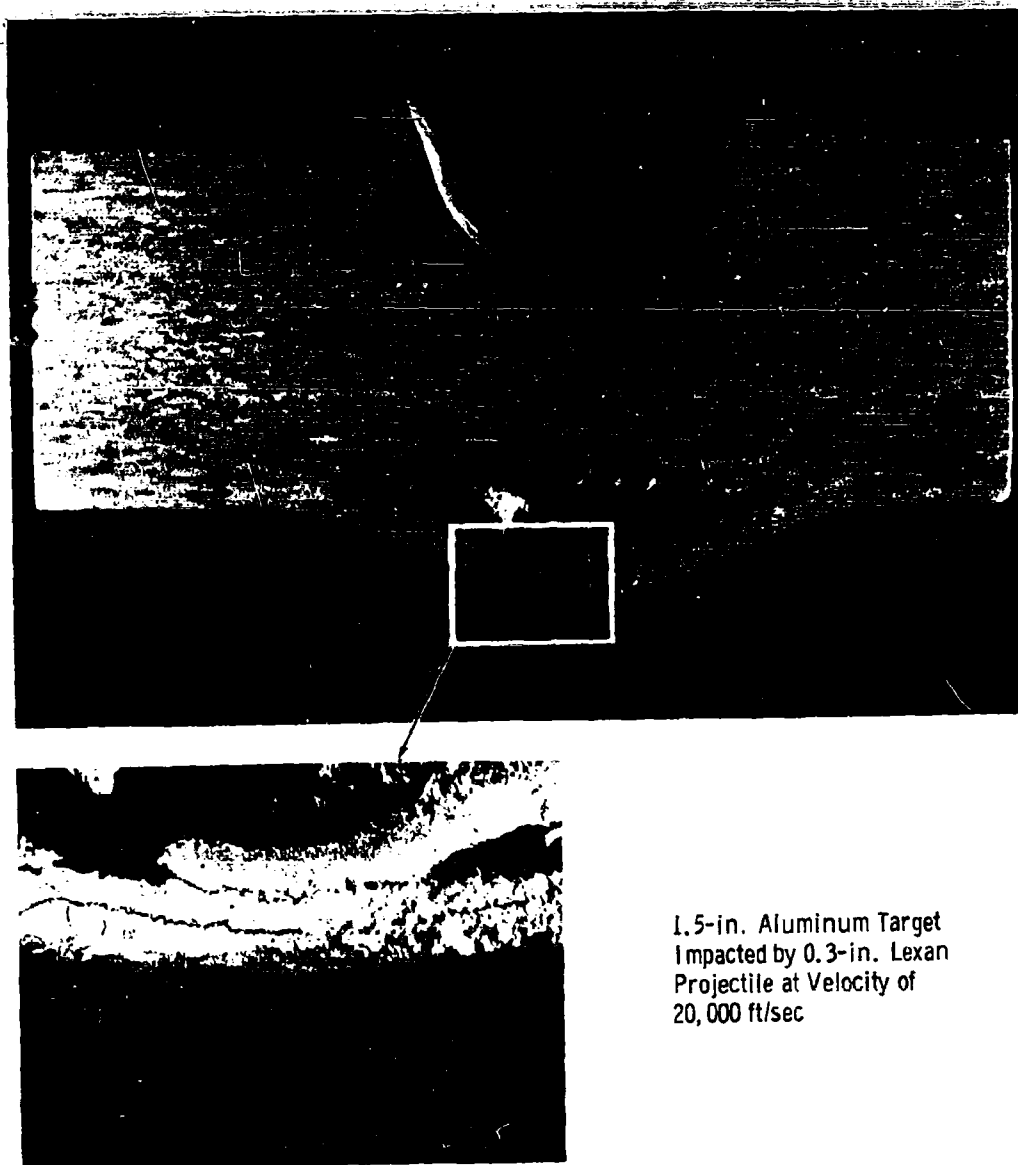


Fig. 12 Concluded

## PROPERTIES OF SPHERICAL SHOCK WAVES



1.5-in. Aluminum Target  
Impacted by 0.3-in. Lexan  
Projectile at Velocity of  
20,000 ft/sec

Fig. 13 Multiple Fractures Near Rear Surface of Aluminum Target

# PROPERTIES OF SPHERICAL SHOCK WAVES

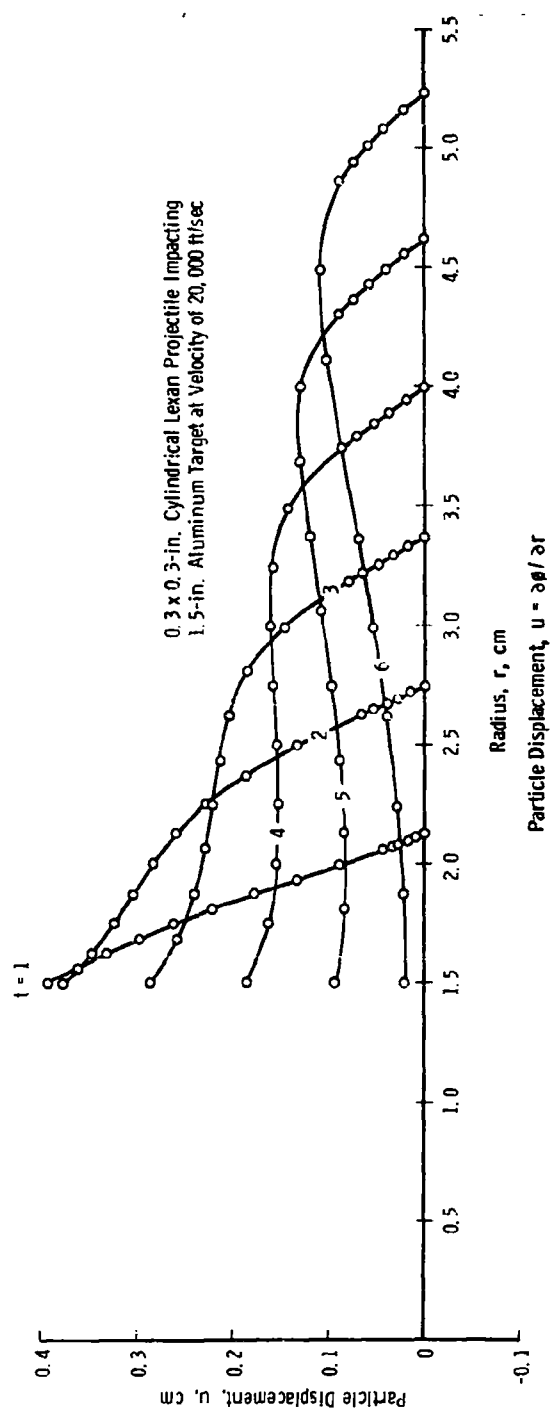
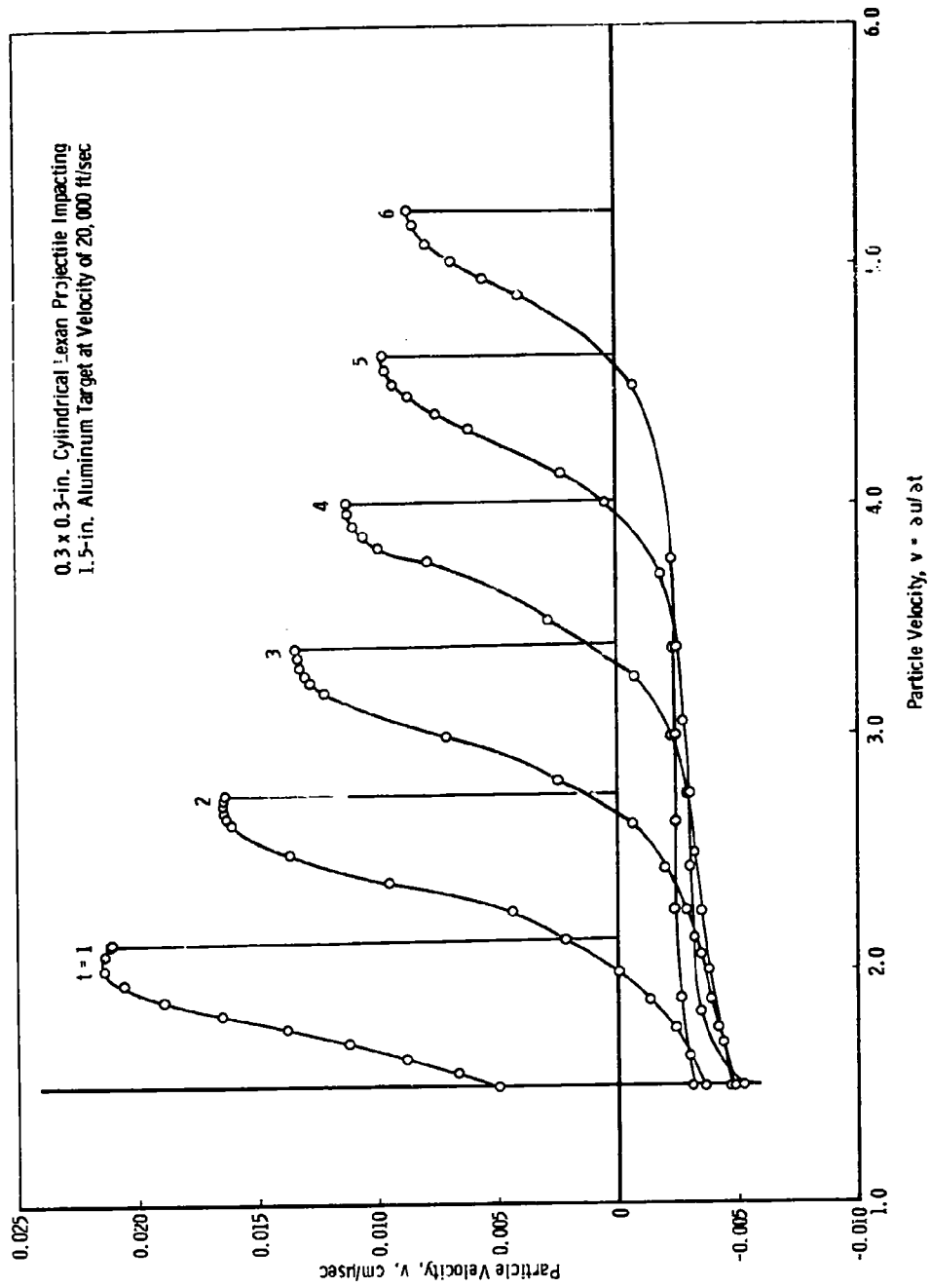


Fig. 14 Particle Displacement and Velocity as Functions of Radius and Time

# PROPERTIES OF SPHERICAL SHOCK WAVES



## PROPERTIES OF SPHERICAL SHOCK WAVES

The values of the principal stresses,  $\sigma_r$  and  $\sigma_\theta$ , are given in Fig. 16. The strong tangential tensile stresses developed near the crater seem to indicate that radial fractures might be expected in this area. These may be seen in Lucite targets. Fractures beneath the crater and parallel to the projectile direction have been observed (17). These may be caused by tangential tensile stresses. These radial fractures occur while the crater is still expanding, and are later subject to very high pressures. They may not occur at all, although the tensile stress is greater than that which produces fractures near the rear of the target, because it has been demonstrated that the resistance of a material to cleavage fracture is increased by the application of hydrostatic pressure (18). Figure 17 shows the calculated values of mean and shear stresses.

The compressive pulse is reflected from the rear target surface as a tensile wave. The development of tensile stress caused by the reflected shock produced by a 1.5-in. aluminum target being impacted by a 0.3-in. Lexan projectile at a velocity of 20,000 ft/sec is shown in Fig. 18. The times ( $t'$ ) given are the number of microseconds elapsed after the compression pulse reached the rear surface. If the tensile stress does not reach the critical fracture strength of the material, this tensile wave begins to decrease in magnitude after about 1  $\mu$ sec. If, however, the stress reaches the fracture strength, a crack parallel to the rear surface is formed. The tail of the forward-moving compression pulse will then be reflected as a tensile wave from the new free surface produced by the material failure and may again reach the fracture strength of the material. Figure 19 shows the formation of the three fractures observed in the aluminum target having a tensile strength of 100,000 psi.

Momentum, corresponding to a portion of the pulse twice the length of the spall thickness, is trapped between the fracture and the target surface. This causes the rear of the target to bulge outward. If additional failures occur, momentum will be trapped between these fractures also, causing additional internal deformations. This deformation of the target surface is seen in Fig. 9 after the initial elastic motion has occurred. It will also be noted that this bulge caused by the trapped momentum is formed at a very non-uniform rate. In fact, the motion practically stops after about 46  $\mu$ sec, moves outward again to slow down after about 76  $\mu$ sec, and then again moves outward to come to its final position after approximately 100  $\mu$ sec. This type of erratic motion of the rear surface may be seen in the data presented by Allen (20), although he attributes it to experimental scatter. The complete explanation is not known. It may be due to the formation of multiple fractures, but it is difficult to

# PROPERTIES OF SPHERICAL SHOCK WAVES

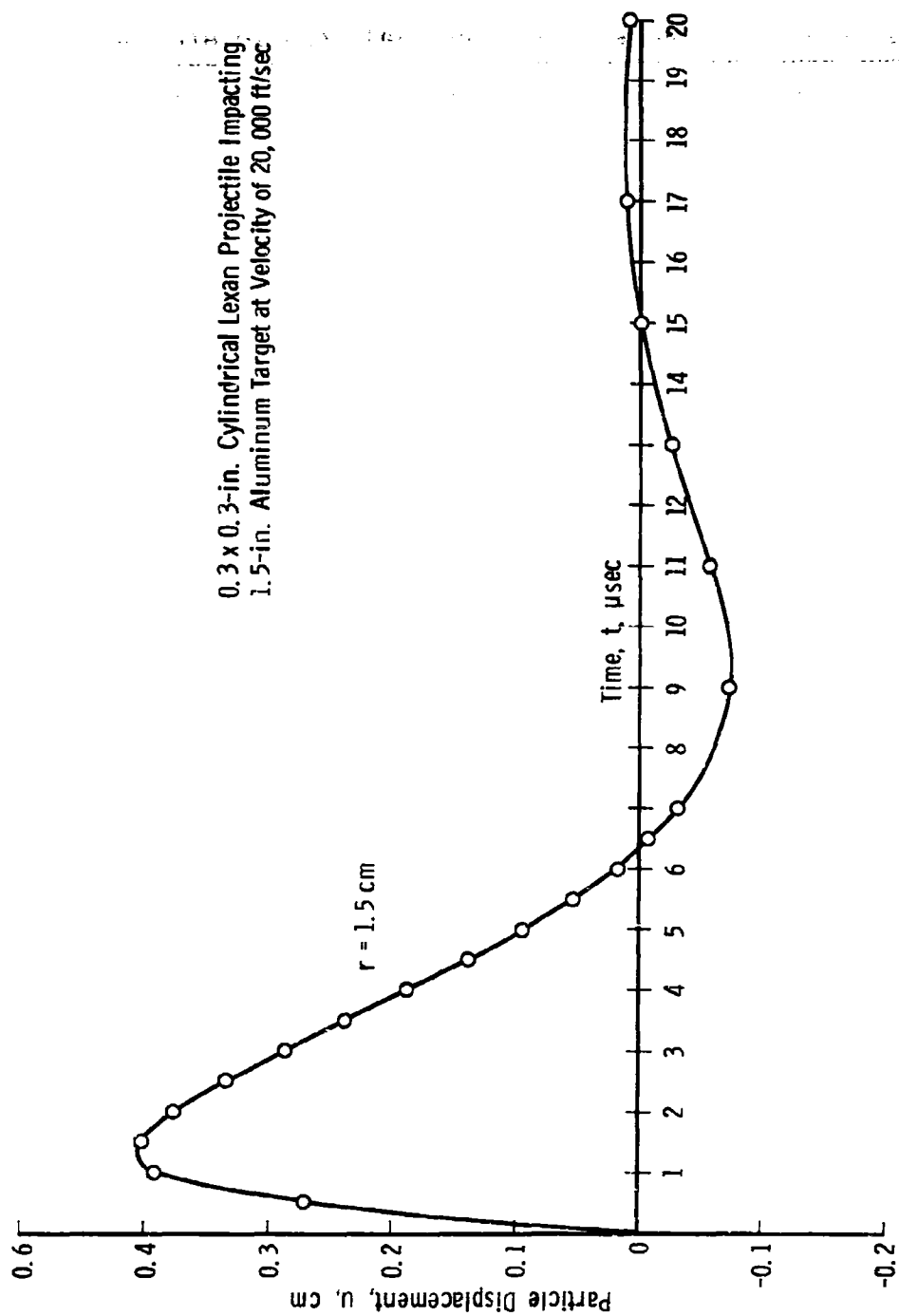
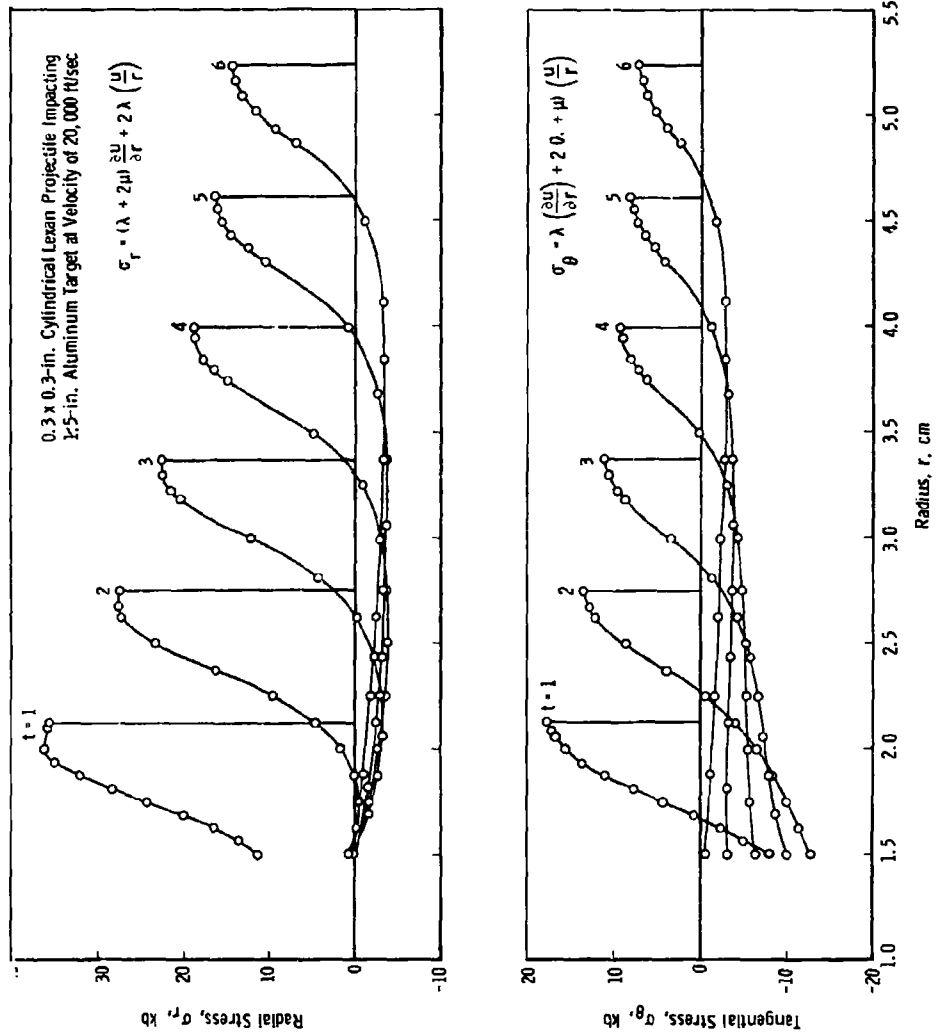


Fig. 15 Particle Displacement as a Function of Time

# PROPERTIES OF SPHERICAL SHOCK WAVES



# PROPERTIES OF SPHERICAL SHOCK WAVES

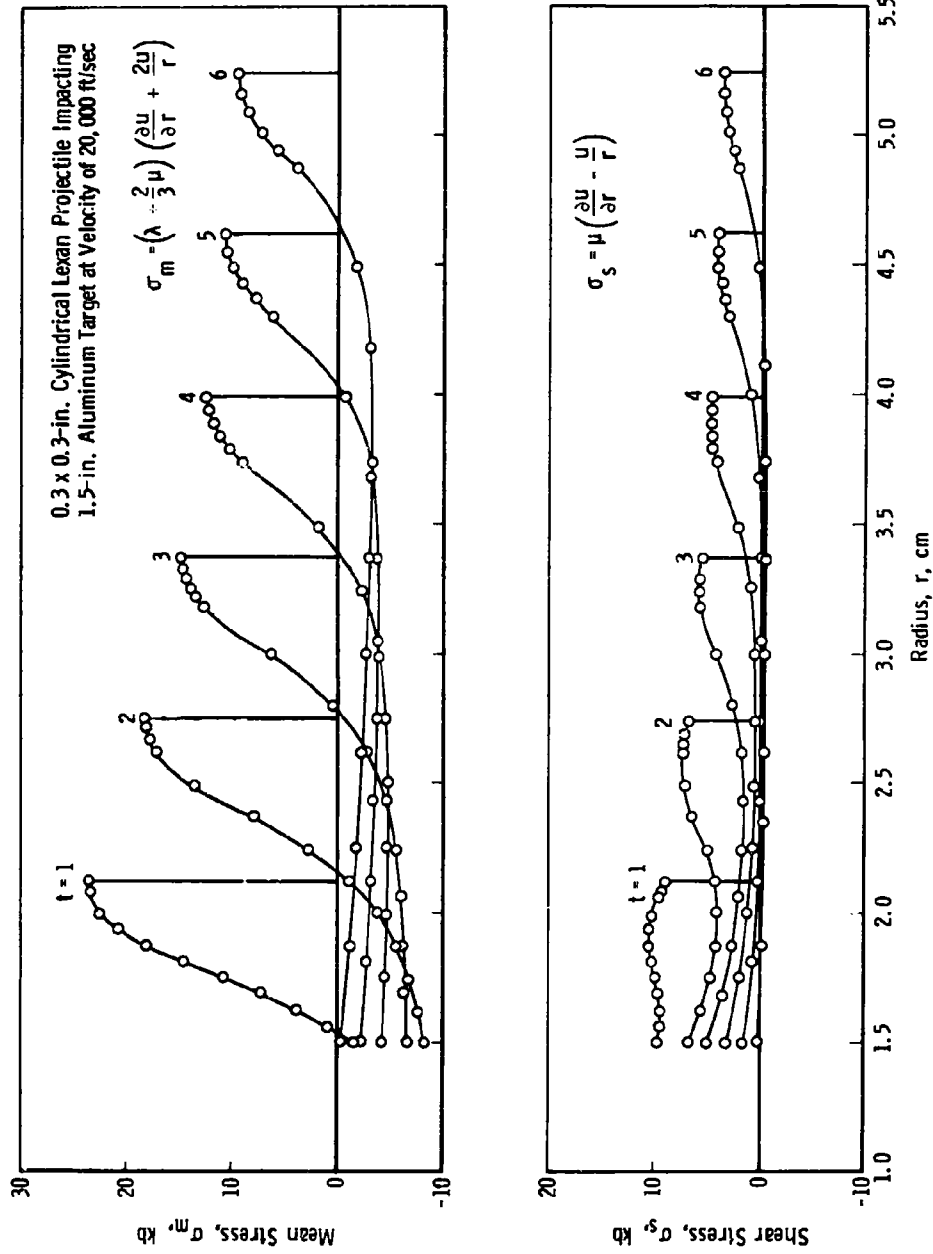


Fig. 17 Mean and Shear Stresses in Target as Functions of Radius and Time



# PROPERTIES OF SPHERICAL SHOCK WAVES

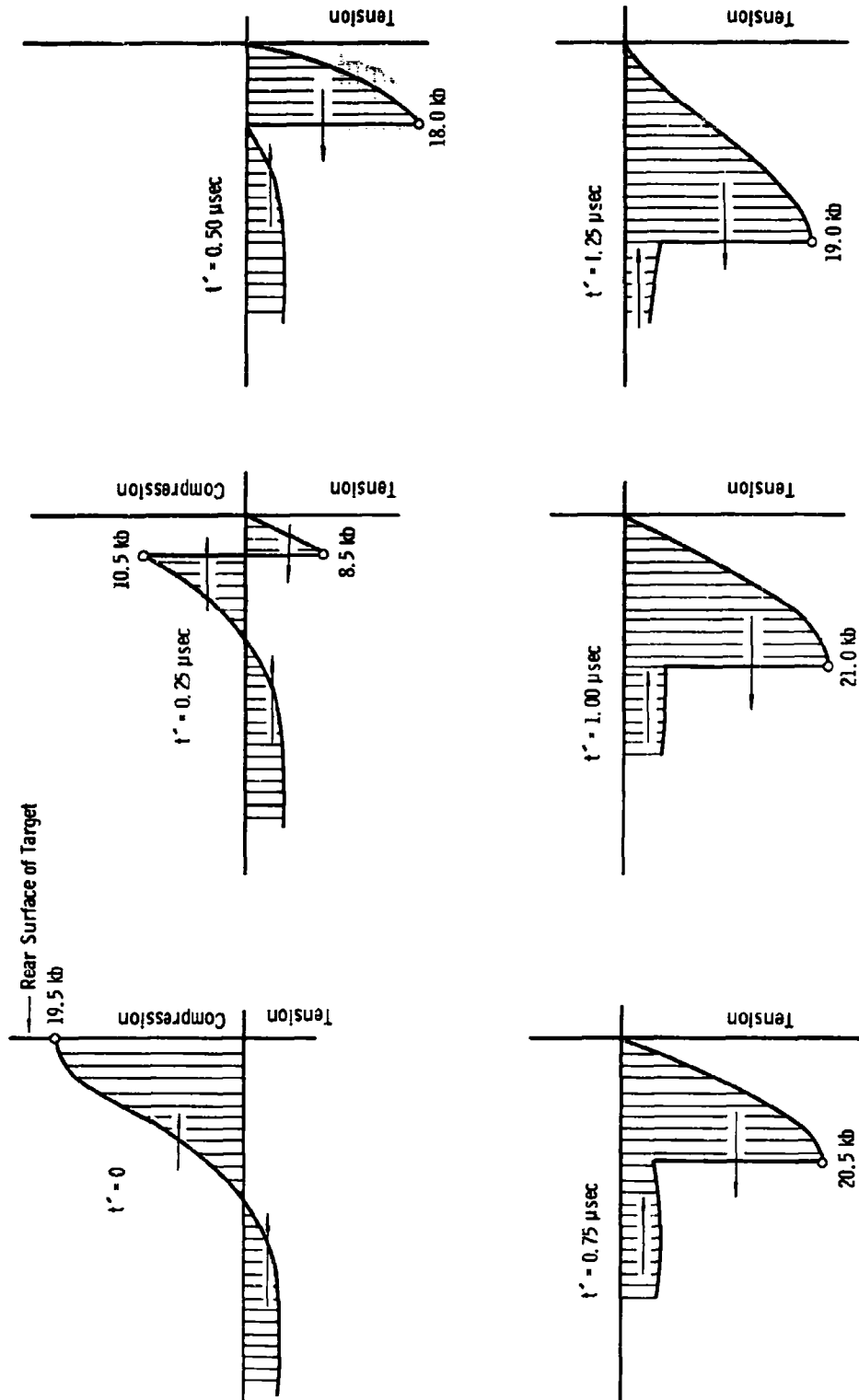


Fig. 18 Development of Radial Tensile Stress Caused by Reflected Shock

# PROPERTIES OF SPHERICAL SHOCK WAVES

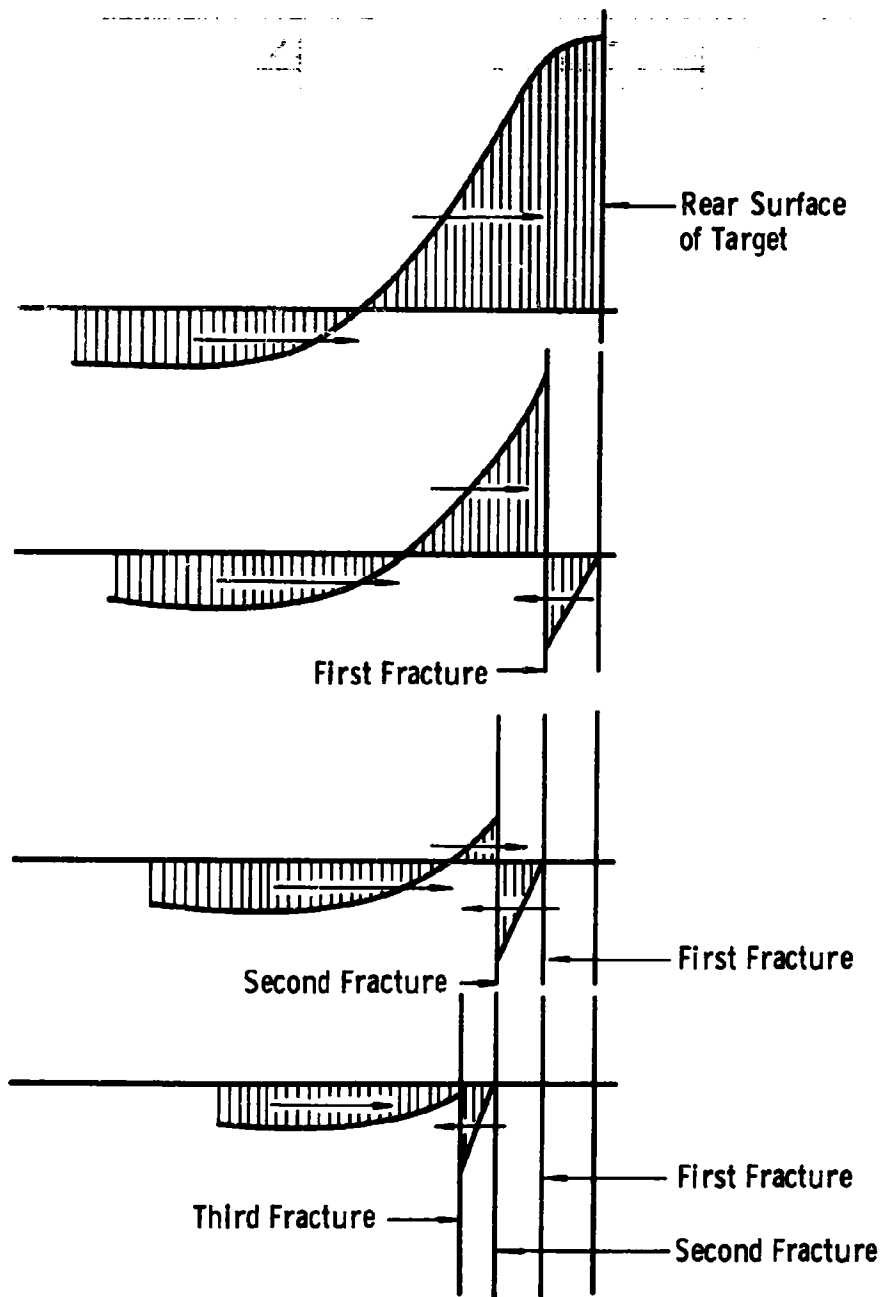


Fig. 19 Formation of Fractures Caused by Reflected Shocks

## PROPERTIES OF SPHERICAL SHOCK WAVES

reconcile the times involved. These impulses occur about 30  $\mu$ sec apart, and the fractures are formed at intervals of less than one microsecond. In addition, this erratic motion may be caused by an oscillation of the material being superimposed upon the bulge formation. If this is the explanation, the frequency of vibration is about 30,000 cycles/sec; this does not agree very closely with its computed natural frequency. A second projectile was fired into a similar target, and the deformation of the rear surface was almost identical with the first.

The final material displacement agrees very closely with the computed value if the portion of the target between the fracture and the target surface is treated as a plate, clamped at its edges, and subjected to an impulsive load equal to the trapped momentum.

Pressure pulses in aluminum caused by impact velocities of Lexan ranging from 18,000 to 28,000 ft/sec are shown in Fig. 20. These are shown as the pulses approach the rear surface of 1, 1.5, and 2-in. targets.

There has been some disagreement whether the spall increases or decreases with an increase in plate thickness with constant impact velocities (17) (19). Figure 21 shows the spall thickness (distance of first fracture from rear surface of target) as a function of target thickness and material strength for constant impact velocity. This indicates that the spall thickness may either increase or decrease with an increase in plate thickness, depending upon the fracture strength of the target. Figure 22 gives the computed spall thickness as a function of projectile velocity. These curves indicate that a decrease in spall thickness occurred with an increase in velocity. This is opposite that found by other investigators (17) in the case of aluminum projectiles impacting steel targets.

A test of the validity of the model presented is whether or not it will enable one to predict the target damage caused by hypervelocity impact. Two test shots were made. One was the impacting of an aluminum target with a cylindrical Lexan projectile at a velocity of 25,000 ft/sec, and the second was the impacting of an aluminum target with a spherical aluminum projectile at 9,800 ft/sec.

The values of the decay constants were determined from the relation

$$\alpha = \frac{3.6 p_o r_o r_1}{M_p}$$

# PROPERTIES OF SPHERICAL SHOCK WAVES

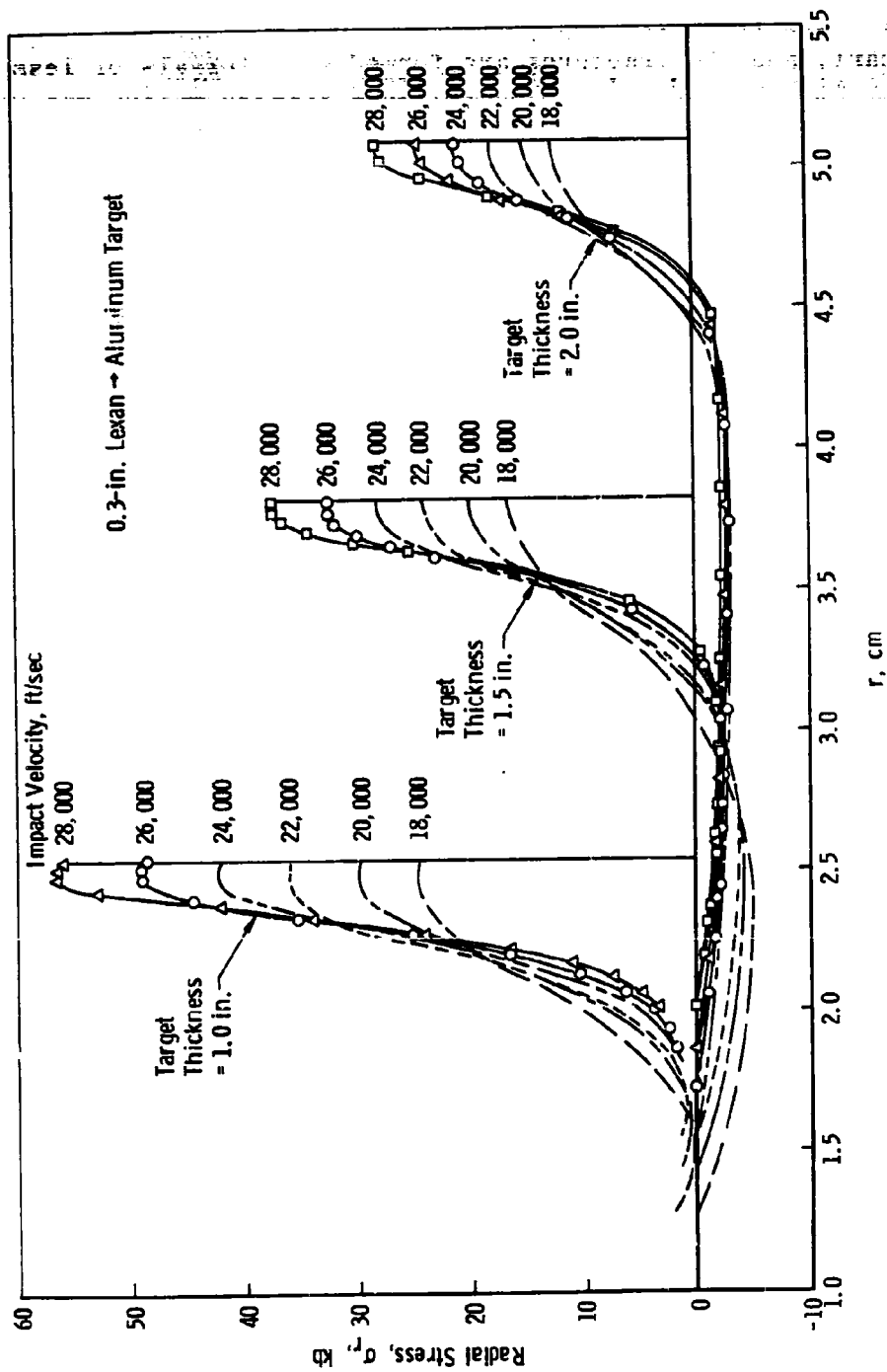


Fig. 20 Radial Stress as a Function of Shock Position for Various Impact Velocities

# PROPERTIES OF SPHERICAL SHOCK WAVES

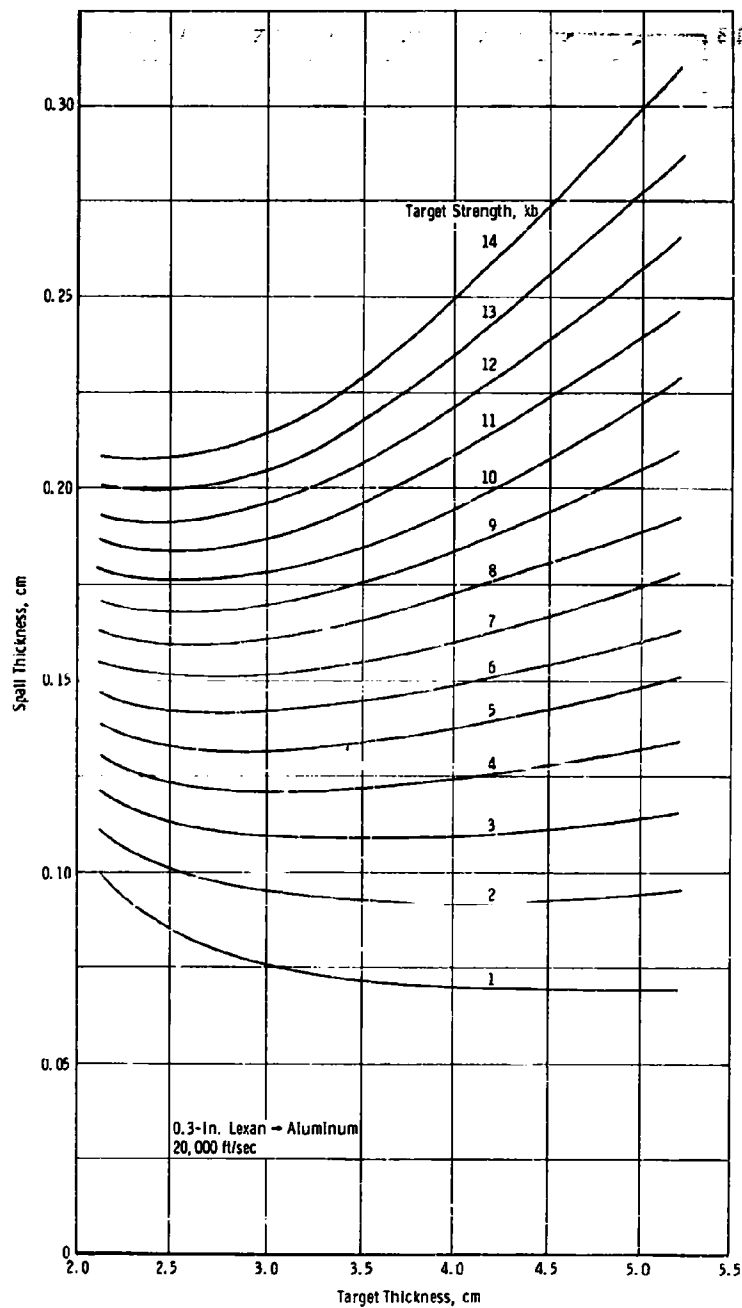


Fig. 21 Spall Thickness as a Function of Target Thickness and Target Strength

# PROPERTIES OF SPHERICAL SHOCK WAVES

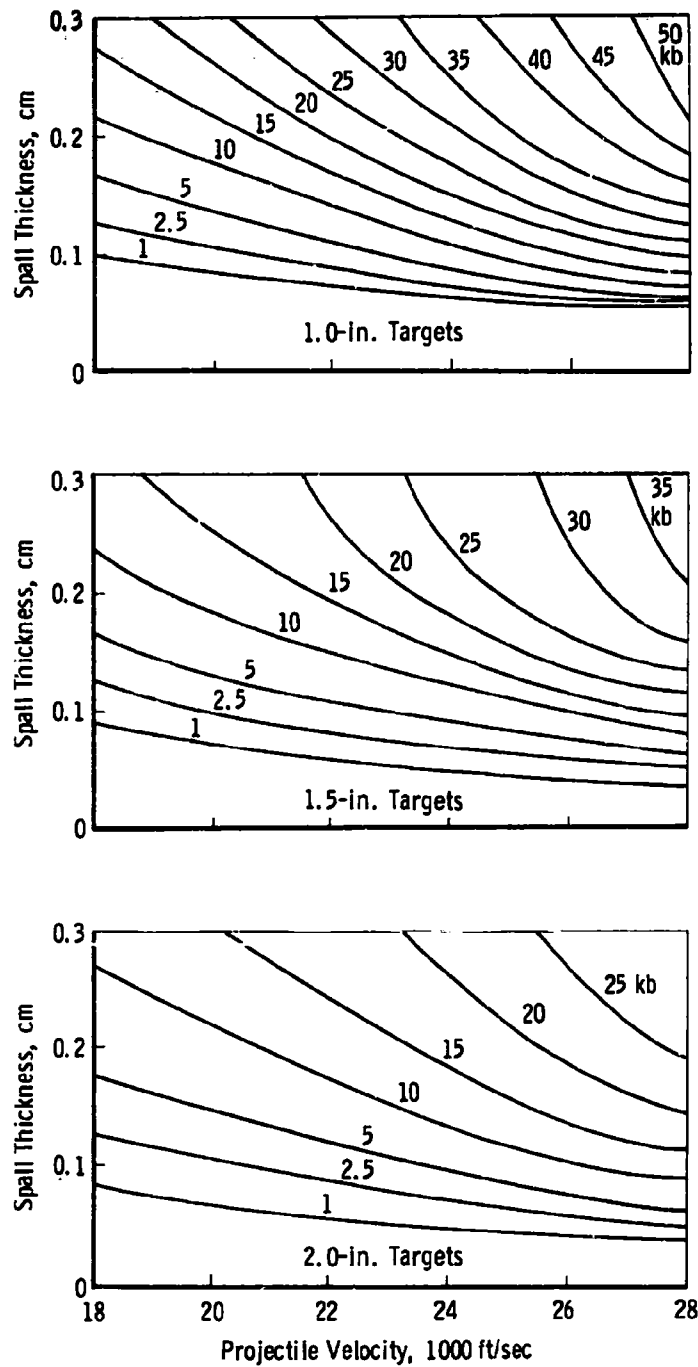


Fig. 22 Spall Thickness as a Function of Target Thickness, Target Strength, and Impact Velocity

## PROPERTIES OF SPHERICAL SHOCK WAVES

The shocks computed for these two shots are shown in Fig. 23. Also shown for comparison is the pulse obtained by impacting an aluminum target with a Lexan projectile at 20,000 ft/sec. From these, the locations of fractures caused by the reflected tensile waves were computed. A comparison of the predicted fractures and the actual fracture locations is given in Fig. 24. For the condition of a Lexan projectile impacting the target at a velocity of 25,000 ft/sec, five fractures were predicted. When the target was sectioned, polished, and etched, six fractures could be seen. It may be seen that the first fracture occurred almost exactly at the location predicted. The distances between the next three were slightly less than predicted, and the distance between the 4th and 5th was greater than the computed value.

If the results of impacting the target with a spherical aluminum projectile could be computed, they would indicate that the projectile shape and density were immaterial, but that only the size and momentum of the target were relevant. However, the results are not conclusive: Two fractures were predicted and two were formed. The location of the first fracture was approximately 15 percent farther from the target surface than predicted; however, the location of the second fracture agreed quite well with its predicted position.

## DISCUSSION

Further experimental work is needed to determine over what range of conditions the ratio of the forward momentum of the forcing function to the momentum of the impacting projectile may be considered constant, and upon what factors this ratio depends. The so-called "attenuation constant" is probably not constant for the regime to which it is applied. It might be more accurate to consider this constant as a power of the radius vector than as a coefficient. More information is needed concerning the particle velocity, especially the cause of the erratic motion of the target's rear surface. For an accurate model, the internal friction and elastic viscosity of the material should be considered.

The values determined in this study apply only to aluminum targets. When an attempt was made to apply these to a copper target, the computed results did not agree with observed locations of fractures. The time decay constant for copper is much less than it is for aluminum. It appears, as would be expected, that the ratio of the shock momentum to the projectile momentum, as well as the attenuation constant, will have entirely different values for targets of other materials. These should be investigated.

# PROPERTIES OF SPHERICAL SHOCK WAVES

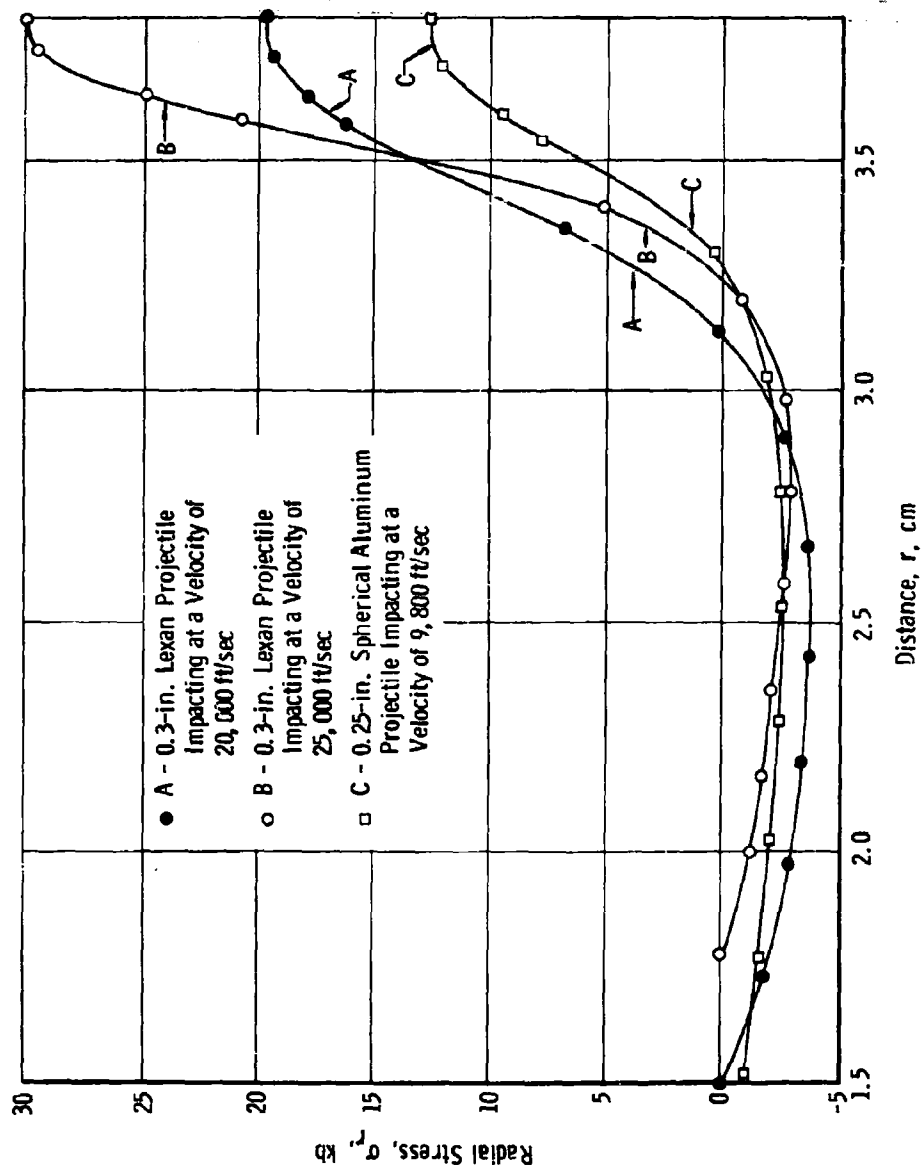


Fig. 23 Comparison of Shocks Caused by Various Impact Conditions



# PROPERTIES OF SPHERICAL SHOCK WAVES

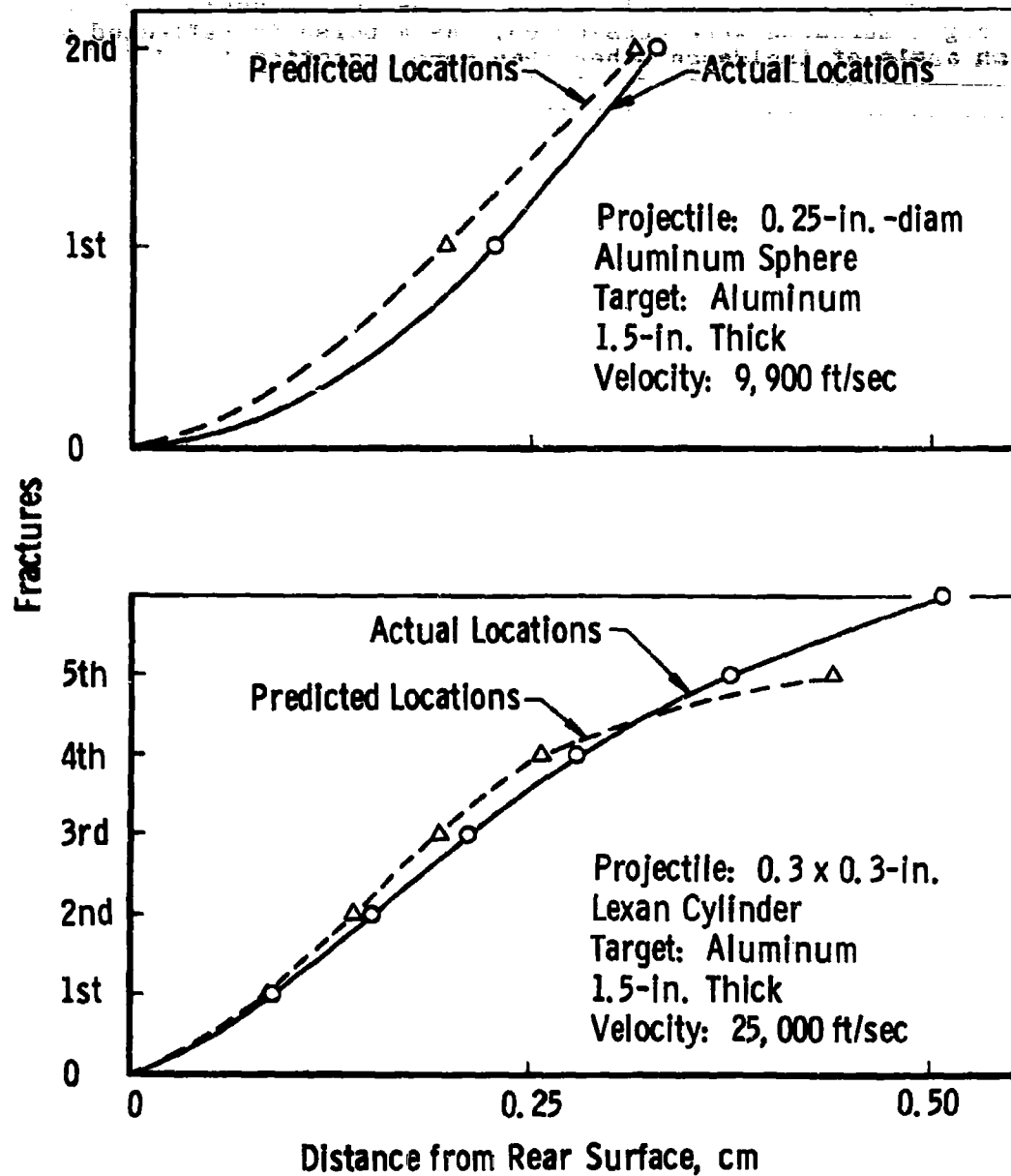


Fig. 24 Comparison of Actual and Predicted Fracture Locations

## PROPERTIES OF SPHERICAL SHOCK WAVES

Only the effects along the radius vector normal to the target surfaces were considered. As a pulse is reflected at an angle of incidence other than zero, rotational and irrotational waves of dilatation are reflected. The interaction of these waves with the compression waves is very complex, but should be analyzed.

In spite of the limitations and assumptions made in this study, the model presented appears to have merit in describing the nature of waves and fractures in solids caused by hypervelocity impact.

## PROPERTIES OF SPHERICAL SHOCK WAVES

### REFERENCES

1. Gehring, J. William, Jr., "Observations of the Phenomena of Hypervelocity Impact," Proceedings of Fourth Symposium on Hypervelocity Impact, Vol. 2, (September 1960).
2. Herrmann, Walter and Jones, Arfon H., "Survey of Hypervelocity Impact Information," ASRL Report No. 99-1 (September 1961).
3. Davids, N. and Haung, Y. K., "Shock Waves in Solid Craters," Journal of the Aerospace Sciences, Vol. 29, (May 1962).
4. Kineke, John H., Jr., "Observations of Crater Formation in Ductile Materials," Proceedings of Fifth Symposium on Hypervelocity Impact, Vol. 1, Part 2, pp. 339-370, (April 1962).
5. Bjork, R. L., "Effects of Meteoroid Impact on Steel and Aluminum in Space," The Rand Corporation, p. 1662, (December 16, 1958).
6. Page, Leigh, Introduction to Theoretical Physics, D. Van Nostrand Company, Inc., New York (1935), p. 181.
7. Love, A. E. H., A Treatise on the Mathematical Theory of Elasticity, Fourth Edition, Dover Publications, New York (1944) p. 142.
8. Kawasumi and Yosiyama, Earthquake Research Institute of Tokyo Bulletin, Vol. 13 (1935), pp. 496-503.
9. Sharpe, Joseph A., "The Production of Elastic Waves by Explosion Pressures. I. Theory and Empirical Field Observations," Geophysics 7, 144 (1942).
10. Blake, F. G., Jr., "Spherical Wave Propagation in Solid Media," Journal of the Acoustical Society of America Vol. 24, Number 2, pp. 211-215 (March 1952).
11. Allen, William A. and Goldsmith, Werner, "Elastic Description of a High-Amplitude Spherical Pulse in Steel," Journal of Applied Physics, Vol. 26, Number 1, pp. 69-74 (January 1955).
12. Eichelberger, R. J. and Gehring, J. W., "Effects of Meteoroid Impacts on Space Vehicles," Ballistic Research Laboratories Report No. 1155 (December 1961).

## PROPERTIES OF SPHERICAL SHOCK WAVES

13. Denardo, Pat B., "Measurements of Momentum Transfer from Plastic Projectiles to Massive Aluminum Targets at Speeds up to 25,600 Feet per Second," NASA Technical Note D-1210, (March 1962).
14. Rinehart, John S., "Some Quantitative Data Bearing on the Scabbing of Metals under Explosive Attack," Journal of Applied Physics, Vol. 22, Number 5, pp. 555-560 (May 1951).
15. Allen, William A., Mapes, Joe M., and Mayfield, Earle B., "Shock Waves in Air Produced by Waves in a Plate," Journal of Applied Physics, Vol. 26, Number 9, pp. 1173-1175 (September 1955).
16. Cook, M. A., Keyes, R. T., and Ursenbach, W. O., "Measurements of Detonation Pressure," Journal of Applied Physics, Vol. 33, Number 12, p. 3414, (December 1962).
17. Maiden, C. J., Charest, J., and Tardif, H. P., "An Investigation of Spalling and Crater Formation by Hypervelocity Projectiles," Proceedings of Fourth Symposium on Hypervelocity Impact, Vol. III (September 1960).
18. Bridgman, P. W., "Fracture and Hydrostatic Pressure," Fracturing of Metals, American Society for Metals (1948), p. 246.
19. Rinehart, J. S. and Pearson, J., "Behavior of Metals under Impulsive Loads," American Society for Metals (1954), p. 127.
20. Allen, William A., "Free Surface Motion Induced by Shock Waves in Steel," Journal of Applied Physics, Volume XXIV, Number 9, pp. 1180-1185, (September 1953).

SHOCK FRONT VARIATION

IN TIME

FOR

HIGH SPEED IMPACT

INTO WATER

James F. Heyda

Space Sciences Laboratory  
Missile and Space Division  
General Electric Company  
Valley Forge, Pennsylvania

## SHOCK FRONT VARIATION IN TIME

### Introduction and Summary

We consider a semi-infinite volume of water bounded by a vertical wall. A small material particle, say a metal sphere of  $1/4$ " diameter traveling at speeds varying from 5,000 to 15,000 feet per second, impacts the water normally through a pre-punched hole in the vertical wall. (The hole is covered, prior to impact, with a thin membrane which offers no resistance to penetration by the particle.) An analytical procedure is desired for determining the fluid particle velocity, density, and pressure behind the shock front and also the time variation of the shock front itself.

The impact problem thus described is axially-symmetric and involves two space variables:  $Z$ , measured along the line of particle penetration and  $R$ , the radial distance normal to this line, (See Figure 1). At time  $t$  since impact at 0 the spherical shock front, centered at 0, has radius  $R(t)$ . This is in keeping with experiments performed at the Lewis Laboratory of the NASA (See Ref. 1) where, using a high speed camera, it is shown that the shock fronts, as represented by shadow graphs viewed through the sides of a water-filled transparent plastic tank, are spheres with centers at the point of particle impact into the water. For the speeds considered here, the material particle stays intact and as it penetrates into the water, a cavity forms behind it. A typical view of the situation ten micro-seconds after impact is sketched in Figure 2.

The excellent data of Reference 1 give, among other things, the shock front position  $R(t)$  and shock front velocity  $\dot{R}(t)$  for equally spaced instants of time since impact. In attempting to find a mathematical model for determining  $R(t)$ , one is tempted to regard the impact problem as an approximate point explosion

## SHOCK FRONT VARIATION IN TIME

since the particle is stopped after penetrating only a few inches. For a point explosion,  $R$  would vary as  $t^{2/5}$  in keeping with Taylor's point blast relations (Ref. 2); this, however, is not at all in agreement with the data. Again, on the assumption that  $R \propto t^N$ , one can of course determine an approximate  $N$  for each set of data; but these exponents vary widely from 0.4 to well over 1.0. Thus, the point explosion explanation offers no promise of a suitable model.

In the present paper, based on the "near separation" of the partial differential equations defining the hydrodynamic behavior of the fluid behind the shock front when similarity variables of the type employed in treating cylindrical and planar blast phenomena are introduced, it is shown that the shock front radius satisfies the differential equation

$$(1) \quad \frac{dR}{dt} = \frac{B}{\sqrt{R}} - \frac{A}{R}, \quad B > A > 0,$$

whose solution is

$$(2) \quad \frac{Bt}{2} = \frac{R^{3/2}}{3} + \frac{kR}{2} + k^2 R^{1/2} + k^3 \ln(R^{1/2} - k) + C.$$

Here  $k = A/B$  and  $C$  is a constant associated with conditions at the time of impact  $t = 0$ .

It is interesting to note that when the constant  $A$  is small relative to the constant  $B$ , equation (2) becomes approximately

$$(3) \quad R = \left( \frac{3B}{2} t \right)^{2/3},$$

since  $C$  is invariably small. Relation (3) defines shock front variation in a planar explosion.

The relation (2) verifies all the data given in Reference 1, extremely closely all the way down to ambience conditions where the shock wave degrades

## SHOCK FRONT VARIATION IN TIME

into an acoustic wave. In fact, relation (1) may be used to determine analytically where this will occur. Putting  $a$  = sonic speed in water, one finds that

$\dot{R} = a$  when

$$(4) \quad \sqrt{R} = \frac{2k}{a} \left( \frac{B}{4k} \right) \left[ 1 \pm \sqrt{1 - \frac{a}{B/4k}} \right],$$

giving two values for  $R$ , one very close to impact using the - sign, the other at the far limit of validity for (1) using the + sign.

The quantity  $B/4k$  defines the maximum shock front speed,

$$(5) \quad \dot{R}_{\text{Max}} = B/4k,$$

which occurs at

$$(6) \quad R = 4k^2, \quad t = \frac{2}{B} \left\{ k^3 \left( \frac{20}{3} + \ln k \right) + C \right\}.$$

Relations (4, 5, 6) also corroborate the experimental data of Reference 1.

Thus,  $k$  is associated with the shock radius  $R^*$  where  $\dot{R}$  is a maximum,

$$(7) \quad k = \frac{1}{2} \sqrt{R^*}$$

and  $B$  is then determined from

$$(8) \quad B = 4k \dot{R}_{\text{Max}}.$$

The more basic characterization of  $A$  and  $B$ , or equivalently  $B$  and  $k$ , in terms of the physical and dynamical characteristics of the impacting particle and parameters associated with water is not available at this writing but will, presumably, fall out naturally when the exact combination of similarity variables renders the defining partial differential equations separable. A "separated" system, based on the heuristic derivation of (1), is available for the determination of  $A$  and  $B$ , but the appropriate formulation of boundary conditions is not clear. The presence of two parameters,  $A$  and  $B$ , will allow both



## SHOCK FRONT VARIATION IN TIME

momentum and energy conservation in a complete treatment of the problem.

The significance of the present result is very great in that possession of the exact differential equation for the shock front makes it plausible that exact separation of the two-dimensional axially symmetric differential equations will be made. If so, it will be the first time a two-dimensional impact problem will have been solved analytically. The application of these results to impact problems involving solid media where the disturbed region behind the shock is treated on the basis of non-viscous fluid dynamics then becomes promising from an analytical standpoint.

### Caloric Equation of State for Water

As caloric equation of state, we use the approximate expression,

$$(9) \quad p = B(S) \cdot \left[ \left( \frac{\rho}{\rho_0} \right)^n - 1 \right],$$

given in Reference 3. Here  $n = 20/3$ ,  $\bar{\rho}_0 = 0.93894 \text{ gm/cm}^3$ ,  $B(S)$  is a slowly varying function of the entropy  $S$ . Pressure and density of the undisturbed water are denoted by  $p_0$ ,  $\rho_0$ .

### Euler's Equations

The radial and axial components,  $V_r$  and  $V_z$ , of the velocity of a water particle behind the axially symmetric shock front satisfy the equations for the conservation of momentum

$$(10) \quad \frac{\partial V_r}{\partial t} + V_r \frac{\partial V_r}{\partial r} + V_z \frac{\partial V_r}{\partial z} = - \frac{1}{\rho} \frac{\partial p}{\partial r}$$

$$(11) \quad \frac{\partial V_z}{\partial t} + V_r \frac{\partial V_z}{\partial r} + V_z \frac{\partial V_z}{\partial z} = - \frac{1}{\rho} \frac{\partial p}{\partial z},$$

conservation of mass

$$(12) \quad \frac{\partial \rho}{\partial t} + \frac{1}{r} \frac{\partial}{\partial r} (\rho r V_r) + \frac{\partial}{\partial z} (\rho V_z) = 0$$

## SHOCK FRONT VARIATION IN TIME

and, assuming that changes in the state of each particle are adiabatic, the additional equation

$$(13) \quad \frac{DS}{Dt} = 0.$$

Since eq. (9) may be inverted for  $S$ , eq. (13) is equivalent to

$$(14) \quad \left( \frac{\partial}{\partial t} + v_r \frac{\partial}{\partial r} + v_z \frac{\partial}{\partial z} \right) \left[ p / \left\{ \left( \frac{\rho}{\rho_0} \right)^n - 1 \right\} \right] = 0.$$

### Introduction of Similarity Variables

Consider the momentum equations (10) and (11). Without the term  $v_z \frac{\partial v_r}{\partial z}$ , eq. (10) describes radially cylindrical flow, while in eq. (11) omission of the term  $v_r \frac{\partial v_z}{\partial r}$  gives an equation applicable to planar flow. It is of interest, therefore, to see how equations (10) and (11) transform with the introduction of first the cylindrical similarity variable  $\eta = r/\bar{R}$  and then the planar similarity variable  $\xi = z/Z$ . These are the variables employed in the study of cylindrical and planar blast waves originating with line and plane explosions, respectively. Here  $\bar{R}$  and  $Z$  are the cylindrical coordinates of a point of the axially symmetric shock front.

Describing the shock front by  $\bar{R} = \bar{R}(\xi, t)$  and introducing the transformations

$$(15) \quad \eta = \frac{r}{\bar{R}}, \quad v_r = \frac{\phi_r(\eta)}{\bar{R}}, \quad v_z = \frac{\phi_z(\eta)}{\bar{R}}, \quad \rho = \bar{\rho}_0 \psi(\eta),$$

$$p = \bar{\rho}_0 \bar{R}^{-2} F(\eta),$$

we find, after numerous computations and simplifications, that equations (10, 11, 12, 14) become:

$$(16) \quad -(\eta \phi_r' + \phi_r) \left( -\frac{\partial \bar{R}}{\partial t} + v_z \frac{\partial \bar{R}}{\partial z} \right) + \bar{R}^{-1} (\phi_r \phi_r' + F'/\psi) = 0$$

# SHOCK FRONT VARIATION IN TIME

$$(17) \quad -(\eta \phi'_z + \phi_z) \left( \frac{\partial \bar{R}}{\partial t} + v_z \frac{\partial \bar{R}}{\partial z} \right) + \bar{R}^{-1} \phi_r \phi'_z - \frac{2F + \eta F'}{\psi} \bar{R}^{-1} \frac{\partial \bar{R}}{\partial z} = 0,$$

$$(18) \quad -\eta \psi' \left( \frac{\partial \bar{R}}{\partial t} + v_z \frac{\partial \bar{R}}{\partial z} \right) + \bar{R}^{-1} \left[ \frac{\phi_r \psi}{\eta} + (\phi_r \psi)' \right] - \psi (\eta \phi'_z + \phi_z) \bar{R}^{-1} \frac{\partial \bar{R}}{\partial z} = 0$$

$$(19) \quad -\{(\psi^n - 1)(2F + \eta F') - n\eta F \psi^{n-1} \psi'\} \left( \frac{\partial \bar{R}}{\partial t} + v_z \frac{\partial \bar{R}}{\partial z} \right) + \phi_r \{F'(\psi^n - 1) - nF \psi^{n-1} \psi'\} \bar{R}^{-1} = 0,$$

where primes indicate differentiation with respect to  $\eta$ .

These equations are linear in the quantities

$$(20) \quad \frac{\partial \bar{R}}{\partial t} + v_z \frac{\partial \bar{R}}{\partial z}, \quad \bar{R}^{-1}, \quad \bar{R}^{-1} \frac{\partial \bar{R}}{\partial z}$$

and would allow separation of variables if  $v_z$  did not depend on  $\eta$ . Since the shock front is spherical,  $\frac{\partial \bar{R}}{\partial z}$  will be constant, as the shock moves outward, along a fixed direction from the point of impact since  $\frac{\partial \bar{R}}{\partial z}$  measures the slope of the front at a given time. However, if one moves along such a fixed direction,  $\bar{R}$  will be proportional to  $R$  and  $\frac{\partial \bar{R}}{\partial t}$  to  $\dot{R}$ . As  $\eta \rightarrow 1$ ,  $v_z$  would behave as some function of  $R$ , so that the shock front would satisfy a differential equation of the form

$$(21) \quad \dot{R} = G(R) - AR^{-1}.$$

where  $G(R)$  is to be determined and  $A$  is a constant.

If instead of the transformation (15) we had introduced the transformation

$$(22) \quad \xi = \frac{z}{Z^{1/2}}, \quad v_r = \frac{\phi_r(\xi)}{Z^{1/2}}, \quad v_z = \frac{\phi_z(\xi)}{Z^{1/2}}, \quad \rho = \bar{\rho}_0 \Psi(\xi), \quad p = \bar{p}_0 Z^{-1} f(\xi),$$

where the shock front is now described by  $Z = Z(r, t)$ , equations similar to

(16, 17, 18, 19) would be obtained which are linear in the quantities

$$(23) \quad \frac{\partial Z}{\partial t} + v_r \frac{\partial Z}{\partial r}, \quad Z^{-1/2}, \quad Z^{-1/2} \frac{\partial Z}{\partial r}$$

Reasoning as before one would arrive at an equation corresponding to (21) of

## SHOCK FRONT VARIATION IN TIME

the form

$$(24) \quad \dot{R} = BR^{-1/2} - H(R),$$

where  $H(R)$  is to be determined and  $B$  is a constant.

Since  $G$  derives from  $V_{\infty}$  as  $\eta \rightarrow 1$ , it is natural to identify it with  $BR^{-1/2}$ , consistent with the behavior of the velocity of a planar front; similarly, as  $\xi \rightarrow 1$ , one would identify  $H$  with  $AR^{-1}$ , since it originates with  $V_r$  and is consistent with the velocity of a cylindrically radial front. Following this heuristic reasoning, we write the differential equation of the front in the form

$$(25) \quad \frac{dR}{dt} = \frac{B}{\sqrt{R}} - \frac{A}{R}$$

The solution of eq. (25) is

$$(2) \quad \frac{Bt}{2} = \frac{R^{3/2}}{3} + \frac{kR}{2} + k^2 R^{1/2} + k^3 \ln(R^{1/2} - k) + C,$$

where  $k = A/B$  and  $C$  is a constant.

Since  $\dot{R} > 0$  providing  $\sqrt{R} > k$ , the log term in eq. (2) will be real for all  $R > k^2$ ; but since  $t \rightarrow -\infty$  as  $\sqrt{R} \rightarrow k^+$ , the log term will be real for all real  $t$ . The graph of  $R$  vs.  $t$  has the general features shown in Figure 3. As  $t \rightarrow -\infty$ , the curve approaches the line  $R = k^2$  asymptotically from above, crosses the  $R$  axis at  $R(0) > 0$  and reaches a maximum slope at  $R = 4k^2$ , where it has a point of inflexion. To the right of this point, the curve is concave downward. An interesting feature here is the positive value of  $R$  at  $t = 0$ . This, however, is an unimportant anomaly of the mathematical model near the point of impact and is less objectionable, for example, than the infinite shock front speed at  $t = 0$  in the Taylor model of a point explosion.

## SHOCK FRONT VARIATION IN TIME

Lastly, we note down the system of ordinary differential equations separated out of equations (16, 17, 18, 19) when proportionality is demanded of the quantities (20) as  $\eta \rightarrow 1$ . We have,

$$(26) A(\eta \phi'_r + \phi_r) + \phi_r \phi'_r + F'/\psi = 0$$

$$(27) A(\eta \phi'_z + \phi_z) + \phi_r \phi'_z - B(\eta F' + 2F)/\psi = 0$$

$$(28) A\eta\psi' + (\phi_r\psi)' + \frac{1}{\eta}(\phi_r\psi) - B\psi(\eta\phi'_z + \phi_z) = 0$$

$$(29) A\left\{(\psi^n - 1)(\eta F' + 2F) - n\eta F\psi^{n-1}\psi'\right\} + \phi_r\left\{F'(\psi^n - 1) - nF\psi^{n-1}\psi'\right\} = 0.$$

In principle, A and B would be determined from conservation of energy and momentum; then equations (26, 27, 28, 29) would be solved simultaneously for  $\phi_r$ ,  $\phi_z$ ,  $\psi$  and F, using the Rankine-Hugoniot relations at the shock to determine initial conditions for the integration. The shape of the cavity will then be obtained by finding a surface of revolution behind the shock on which  $p = 0$ , i. e.  $F = 0$ .

### Comparison With Experimental Results

In the experiments conducted at the Lewis Research Laboratory of the NASA (Reference 1) impacts were made into a water-filled transparent plastic tank with metal spheres, 7/32" in diameter, of aluminum, steel and tungsten-carbide; in addition, one impact involved a copper slug, six inches long, with hemispherical ends of 7/32" diameter. Measurements were obtained giving, among other things, the shock front position versus time, from which shock front velocities were obtained graphically.

To check the applicability of the shock front differential equation

$$(1) \quad \frac{dR}{dt} = \frac{B}{\sqrt{R}} - \frac{A}{R}, \quad k = A/B$$

## SHOCK FRONT VARIATION IN TIME

and its solution

$$(2) \frac{Bt}{2} = \frac{R^{3/2}}{3} + \frac{kR}{2} + k^2 R^{1/2} + k^3 \ln(R^{1/2} - k) + C$$

with the experimental results, the first two data points for  $(R, \dot{R})$  of the Lewis data for each run were used to determine  $A, B$  in (1); this result was then used in (2) along with the  $t$  value for the first data point to determine  $C$ . Equation (2) was then used to compute  $t$  corresponding to all the experimentally determined  $R$  data, and comparisons were made with the experimentally chosen  $t$ -data. This procedure was the natural one in view of the implicit manner in which (2) involves  $R$  as a function of  $t$ .

We summarize below the results for the six cases for which computations were made. In the data,  $R$  is given in inches and  $t$  in microseconds. Values of  $t$  computed from eq. (2) are denoted by  $t_{\text{comp}}$ .

## SHOCK FRONT VARIATION IN TIME

### Case I

1. Aluminum sphere of diameter 7/32 in.
2. Impact velocity = 7,600 ft/sec.
3.  $A = 19,140 \text{ in.}^2/\text{sec}$  ,  $B = 93,300 \text{ in.}^{3/2}/\text{sec}$   
 $k = 0.20515 \text{ in.}^{1/2}$

R	0.57	0.97	1.33	1.67	2.33	4.15
t	5	10	15	20	30	60
t <sub>comp</sub>	5.0	9.8	15.0	20.4	32.1	71.5

After 20 m-sec., conditions rapidly approach ambiency; the recorded shock front velocity at 30 msec, namely 5,210 ft/sec, is already close to the speed of sound in water, 4,715 ft/sec.

Equations (5) and (6) indicate a maximum shock front velocity at  $R = .168$  in. of 9,500 ft/sec at  $t = 1.21$  msec.

### Case II

1. Aluminum sphere of diameter 7/32 in.
2. Impact velocity = 6,690 ft/sec
3.  $A = 38,226 \text{ in.}^2/\text{sec}$  ,  $B = 110,010 \text{ in.}^{3/2}/\text{sec}$   
 $k = .34748 \text{ in.}^{1/2}$

R	.642	.949	1.24	1.50	1.785	2.077
t	4.16	8.32	12.48	16.64	20.80	24.96
t <sub>comp</sub>	4.16	8.22	12.37	16.70	20.85	25.77

Recorded shock front velocity at  $t = 24.96$  was 5,330 ft/sec.

Equations (5) and (6) indicate:

$$R_{\text{Max}} = 6,600 \text{ ft/sec at } R = .482 \text{ in. , } t = 2.1 \text{ msec}$$

The recorded shock front velocity at  $t = 4.16$  was 6,480 ft/sec and decreased steadily thereafter.

## SHOCK FRONT VARIATION IN TIME

### Case III

1. Aluminum sphere of diameter 7/32 in.
2. Impact velocity = 6,230 ft/sec
3.  $A = 51,378 \text{ in}^2/\text{sec}$ ,  $B = 119,940 \text{ in}^{3/2}/\text{sec}$

$$k = .42835 \text{ in}^{1/2}$$

R	.77	1.11	1.44	1.76	2.38	4.2
t	5	10	15	20	30	60
t <sub>comp</sub>	5.0	9.93	14.93	20.04	30.62	66.50

The recorded value of R at 30 msec was 5,080 ft/sec.

From equations (5) and (6) we have:

$$\dot{R}_{\text{Max}} = 5,833 \text{ ft/sec when } R = .734 \text{ in. and } t = 4.50 \text{ msec.}$$

$$\dot{R} \text{ recorded at } t = 5 \text{ msec was } 5,830 \text{ ft/sec.}$$

### Case IV

1. Steel sphere of diameter 7/32 in.
2. Impact velocity = 6,130 ft/sec
3.  $A = 27,206 \text{ in}^2/\text{sec}$ ,  $B = 89,638 \text{ in}^{3/2}/\text{sec}$

$$k = .30351 \text{ in}^{1/2}$$

R	.275	.62	.97	1.31	1.99	3.87
t	5	10	15	20	30	60
t <sub>comp</sub>	5.0	9.76	15.03	20.69	33.44	77.0

Recorded  $\dot{R}$  at  $t = 30 \text{ msec}$  was 5,420 ft/sec.

From equations (5), (6) we have:

$$\dot{R}_{\text{Max}} = 6,150 \text{ ft/sec when } R = .368 \text{ in., } t = 6.26 \text{ msec.}$$

At 5 msec, the recorded value of  $\dot{R}$  was 6,000 ft/sec.



# SHOCK FRONT VARIATION IN TIME

## Case V

1. Copper slug, 6 in. long and 7/32" diam.
2. Impact velocity not recorded.
3.  $A = 25,807 \text{ in}^2/\text{sec}$ ,  $B = 91,708 \text{ in}^{3/2}/\text{sec}$   
 $k = .28141 \text{ in}^{1/2}$

R	.705	1.05	1.27	1.53	1.80	2.06
t	8.22	12.33	16.44	20.55	24.66	28.77
t <sub>comp</sub>	7.84	12.88	16.38	20.31	25.63	30.57

Ambiency conditions prevail shortly beyond 24 msec.

From equations (5), (6) we obtain:

$$\dot{R}_{\text{Max}} = 6,790 \text{ ft/sec when } R = .482 \text{ and } t = 2.83 \text{ msec.}$$

At 5 msec, the recorded value of  $\dot{R}$  was 6,550 ft/sec.

## Case VI

1. Tungsten-carbide sphere of diameter 7/32".
2. Impact velocity = 4,615 ft/sec
3.  $A = 52,600 \text{ in}^2/\text{sec}$ ,  $B = 129,080 \text{ in}^{3/2}/\text{sec}$   
 $k = .40751 \text{ in}^{1/2}$

R	.74	1.12	1.47	1.81	2.45	4.2
t	5	10	15	20	30	60
t <sub>comp</sub>	5.0	9.92	14.7	19.7	29.7	61.5

Ambiency conditions prevail at t = 30 msec.

From equations (5), (6) we obtain:

$$\dot{R}_{\text{Max}} = 6,600 \text{ ft/sec when } R = .665 \text{ in. and } t = 4.05 \text{ msec.}$$

At 5 msec the recorded value of  $\dot{R}$  was 6,580 ft/sec.

# SHOCK FRONT VARIATION IN TIME

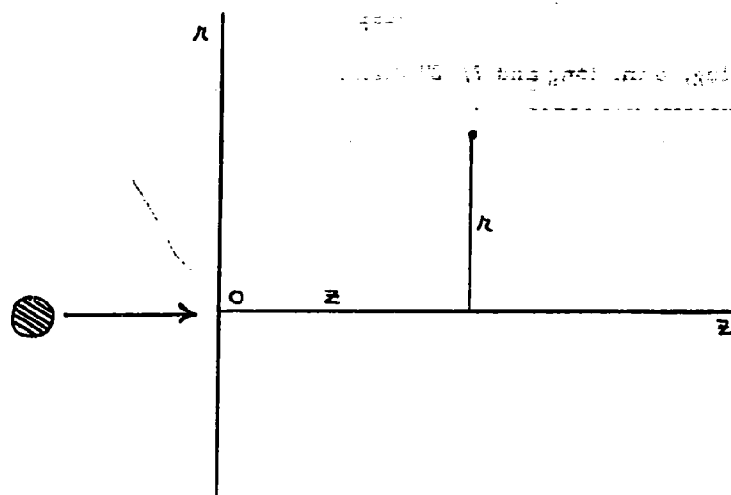


Figure 1

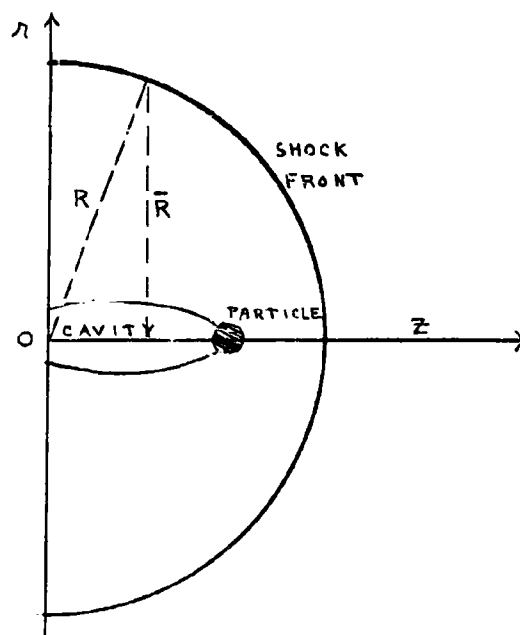


Figure 2

# SHOCK FRONT VARIATION IN TIME

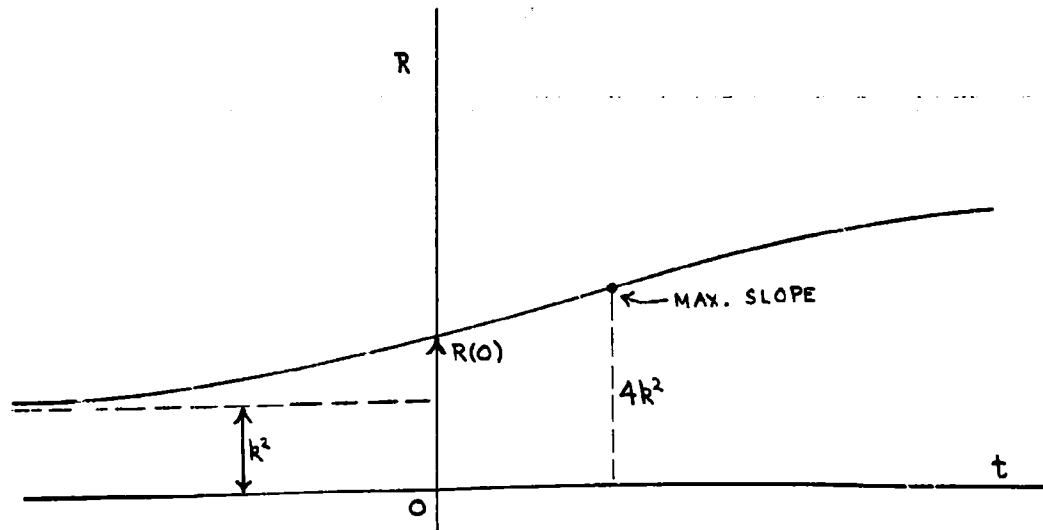


Figure 3

## SHOCK FRONT VARIATION IN TIME

### References

1. Stepka, F. S., Morse, C. R., "Preliminary Investigation of Catastrophic Fracture of Liquid Filled Tanks Impacted by High Velocity Particles," NASA TND-1537.
2. Taylor, G. I., "The Formation of a Blast Wave by a Very Intense Explosion," Proc. Roy. Soc. (London), ser. A, Vol. 201, (1950), 159-174.